

University of Eastern Piedmont

“Amedeo Avogadro”

Department of Sciences and Technological Innovation

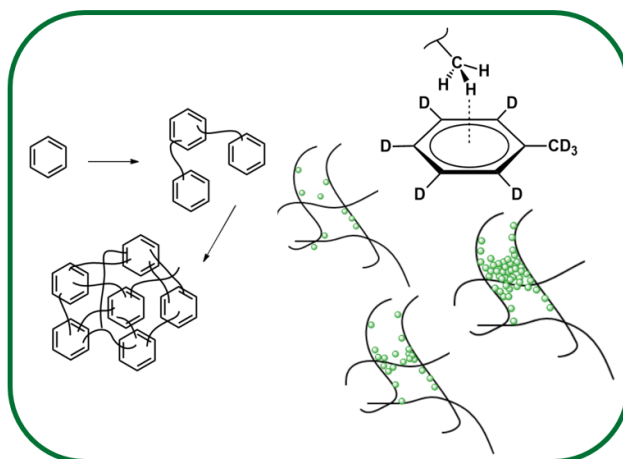
Ph.D. Program in “Chemistry & Biology”

Cycle XXXIII, a.y. 2017-2020

Chemical methodologies for new molecules and nanomaterials (CHIM02)

*Development of Hyper Cross-linked
Polymers for environmental applications*

Federico Begni



Supervised by: Prof. Giorgio Gatti

Ph.D. Program Co-Ordinator: Prof. Gian Cesare Tron

University of Eastern Piedmont

“Amedeo Avogadro”

Department of Sciences and Technological Innovation

Ph.D. Program in “Chemistry & Biology”

Cycle XXXIII, a.y. 2017-2020

***Development of Hyper Cross-linked
Polymers for environmental
applications***

Federico Begni

Supervised by: Prof. Giorgio Gatti

Ph.D. Program Co-Ordinator: Prof. Gian Cesare Tron

DECLARATION AND AUTHORISATION TO ANTIPLAGIARISM DETECTION

The undersigned student of the Chemistry & Biology Ph.D. course (**XXXIII** Cycle)

Declares:

- to be aware that the University has adopted a web-based service to detect plagiarism through a software system called “Turnit.in”,
- his/~~her~~ Ph.D. thesis was submitted to Turnit.in scan and reasonably it resulted an original document, which correctly cites the literature;

Acknowledges:

- his/~~her~~ Ph.D. thesis can be verified by his/~~her~~ Ph.D. tutor and/~~or~~ Ph.D. Coordinator in order to confirm its originality.

Date: **13/01/2020**

Signature:

A handwritten signature in black ink, appearing to read "Federico Pao", written on a light blue background.

Table of Contents

<i>Development of Hyper Cross-linked Polymers for environmental applications</i>	2
DECLARATION AND AUTHORISATION TO ANTIPLAGIARISM DETECTION	3
Chapter I.....	7
1.1 Introduction: motivating the need for solid sorbents	7
1.2 Classes of solid sorbents	13
1.2.1 Zeolites.....	14
1.2.2 Synthetic clays	15
1.2.3 Porous carbons	18
1.2.4 Metal – Organic Frameworks (MOFs)	19
1.2.5 Covalent Organic Frameworks (COFs)	21
1.2.6 Porous Organic Polymers (POPs).....	25
Outline.....	58
Chapter II	60
2.1 Introduction.....	60
2.2 Friedel – Crafts alkylation reaction.....	60
2.3 Synthesis of mPAF Hyper Cross-linked Polymers	62
2.4 Synthesis of Hyper Cross-linked Polymers	63
2.4.1 ABT materials.....	64
2.4.2 TPMTTC material	65
2.4.3 DIXYT materials	67
2.4.4 PS-1.3 material.....	69
2.5 Synthesis of synthetic clays: saponites	70
2.5.1 SAP110 and SAP-OP materials	71
2.6 References.....	73
Chapter III.....	75
3.1 Introduction.....	75
3.2 Characterization of HCP materials	75

3.2.1 Morphological analysis of HCP materials	76
3.2.2 Textural properties of HCP materials	85
3.2.3 FT-IR analysis of HCP materials	101
3.2.4 SS-NMR analysis of HCP materials	117
3.2.5 Thermogravimetric analysis of HCP materials	125
3.3 Characterization of saponite materials	127
3.3.1 Morphological analysis of saponite materials	128
3.3.2 X-Ray powder diffraction analysis	129
3.3.3 Textural properties of saponite materials	130
3.3.4 FT-IR analysis of saponite materials	134
3.3.5 SS-NMR analysis of saponite materials	137
3.3.6 Thermogravimetric analysis of saponite materials	139
3.4 Conclusions	141
3.5 References	142
Chapter IV	147
4.1 Introduction	147
4.1.1 HSZ-Y N ₂ physisorption analysis	149
4.2 Volumetric adsorption of toluene on mPAF materials and HSZ-Y	151
4.3 FT-IR study of toluene-d ₈ adsorption on mPAF materials	155
4.3.1 Toluene-d ₈ adsorption on mPAF-1/16	156
4.3.2 Toluene-d ₈ adsorption on mPAF materials	164
4.4 SS-NMR study of BTX adsorption on mPAF materials	170
4.4.1 Toluene-d ₈ adsorption on mPAF-1/16	170
4.4.2 BTX adsorption on mPAF-1/16	174
4.5 Computational studies of the adsorption of toluene and n-hexane on mPAF materials	177
4.6 Conclusions	181
4.7 References	183
Chapter V	187
5.1 Introduction	187
5.2 Membranes preparation	189
5.3 Permeation measurements	191

5.2 Membranes characterization	193
5.3 Membranes permeability measurements.....	195
5.4 T1 relaxation times membranes measurements	200
5.5 Conclusions.....	205
5.6 References.....	207
Chapter VI.....	212
6.1 Introduction.....	212
6.2 Membranes preparation	214
6.3 Permeation measurements	215
6.2.1 PIM1 + ABT materials	215
6.2.2 PIM1 + DIXYT materials	222
6.2.3 Comparison between the PIM1 membrane and the best performing MMMs	228
6.4 Conclusions.....	233
6.5 References.....	235
Chapter VII	239
7.1 VOC adsorption on mPAF materials	239
7.2 Measurements performed on saponites, PIM1 and PIM1 + saponites MMM samples.....	241
7.3 Measurements performed on the synthesized HCPs, PIM1 and PIM1 + HCPs MMM samples	245
Chapter VIII.....	247
Acknowledgements.....	252

Chapter I

Adsorbent materials and their applications

1.1 Introduction: motivating the need for solid sorbents

There is no doubt that anthropogenic pollution has become one of the most pressing issues of today's society¹. Only recently, we have come to realize that humanity is indeed a planetary force. The constant increase in the energy demands, as a result of population and technological growth, is having a serious impact worldwide on the delicate balance between Earth ecosystems. The term "anthropogenic pollution" is referring to the multitude of environmental contaminations with man – made origin, which are often related to a disproportionate production with respect to their natural abundance. Among the various species which constitute anthropogenic pollution, greenhouse gasses such as CO₂ and CH₄, air pollutants such as NO_x and SO_x and VOC (Volatile Organic Compounds) are among the most abundant and for this reason, probably the most dangerous². Greenhouse gasses are thought to be responsible for the progressive global increase in temperatures, known as global warming^{3,4,5}. Greenhouse gasses are capable of trapping Earth thermal radiation by acting as a blanket over the entire planet⁶. A fraction of the radiation coming from

the Sun is re – emitted outward as radiation with wavelength in the infrared region (700 nm – 1 mm) which can be absorbed by infrared sensitive species such as CO₂ and CH₄. Being CO₂ a byproduct of all combustion reactions its concentration in the atmosphere is still rapidly increasing because of the constant use of fossil fuel, as it is seen by the graph reported in Figure 1.

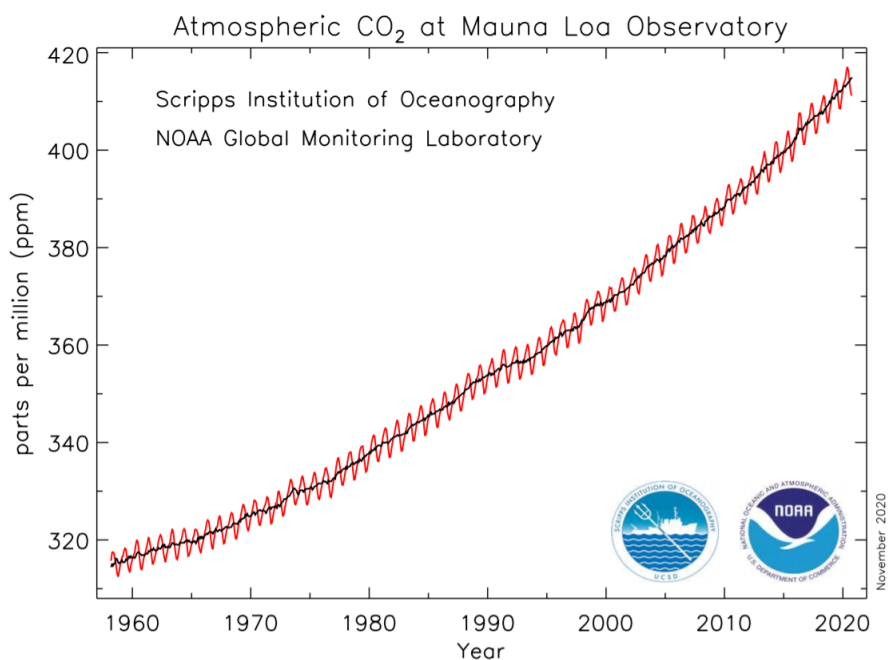


Figure 1. Monthly mean carbon dioxide concentration between 1958 and 2020. Adapted from: <https://www.esrl.noaa.gov>.

While greenhouse gasses are responsible for indirect consequences to humans, air pollutants such as NO_x are directly linked with negative respiratory effects, in addition to be responsible, along SO_x, for acid rains. NO_x and SO_x are generated by road transport, combustion processes and reagents typically employed at an industrial level⁷. In particular SO_x are mainly produced through the combustion of solid products containing sulfur such as coal while NO_x are typically produced in

combustion engines via high temperature reactions with atmospheric and fuel nitrogen with oxygen⁷.

Like air pollutants, VOCs represents a class of harmful species both for humans and the environment. VOCs are species characterized by high vapor pressure, which is a consequence of the weak intermolecular forces holding the molecules together⁸. VOCs are introduced in the environment through a vast number of human activities above all industrial processes such as the production of paints, and in general they are by products associated with the petrochemical industry⁹.

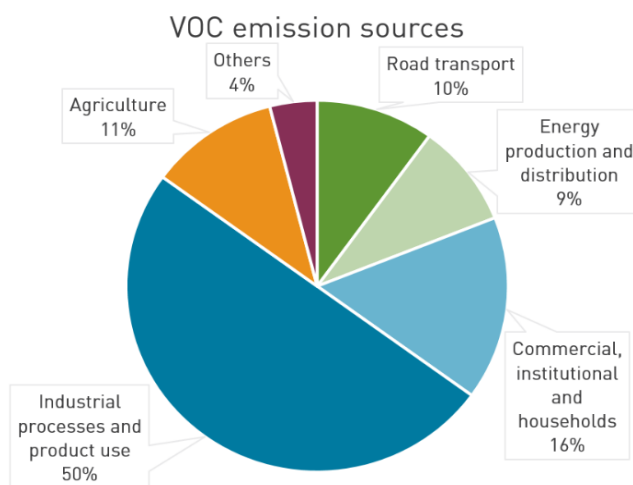


Figure 2. Main sources of VOC emission¹⁰.

VOCs comprise a vast number of compounds including amides, esters, halogenated hydrocarbons, phenols, aliphatic and aromatic hydrocarbons. Aliphatic and aromatic VOCs are often associated with the employment of fossil fuel.

Aliphatic VOCs are a significant fraction of petroleum derivatives and often used as fuel. Among those, methane, propane, hexane and cyclohexane are the most common

along with aliphatic compounds such as alkenes and alkynes and non – aromatic cyclic compounds. In Figure 3, some molecular structures of aliphatic VOCs are reported⁹.

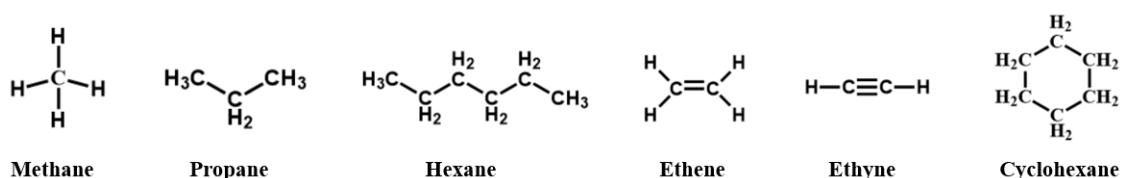


Figure 3. Structures of selected aliphatic VOC. From left to right: methane, propane, hexane, ethene, ethyne and cyclohexane.

Aromatic VOCs are molecules possessing one or more aromatic rings usually conferring stability and consequently resulting in high persistency in the environment which leads to biomagnification and accumulation⁹. Among aromatic VOCs, benzene, toluene and xylene and PAHs (Polycyclic Aromatic Hydrocarbons) such as naphthalene, anthracene and pyrene are the most common. Aromatic compounds are often linked with carcinogenic and/or teratogenic effects⁹. In Figure 4, some molecular structures of aromatic VOCs are reported.

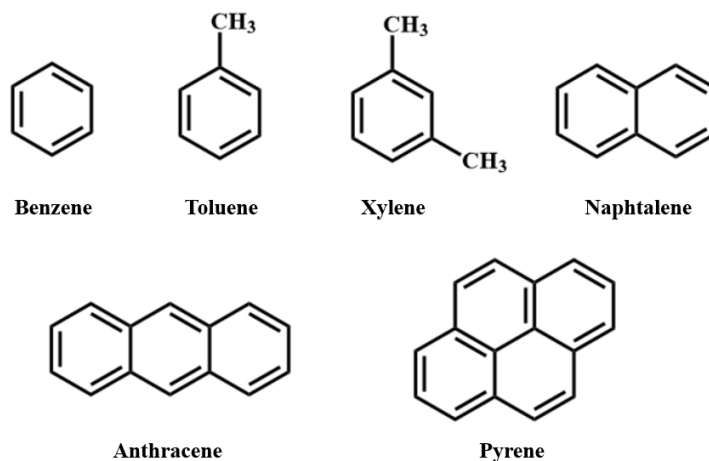


Figure 4. Structures of selected aromatic VOC. From left to right: benzene, toluene, xylene naphtalene, anthracene and pyrene.

All the pollutants mentioned so far are in some way related to the production and/or combustion of fossil fuels. There is a growing need for the development of clean energy solutions and, as of today, alternatives to fossil fuels are being actively explored such as solar, wind, geothermal and fusion power^{11,12,13}. These alternatives rely on renewable energy sources and are not plagued with the emission of large quantities of harmful byproducts^{14,15}. However, it is becoming evident that the pace at which clean energy technologies are being developed, is not sufficient to promptly tackle the environmental problems at hand. The need of fossil fuel is still present due to the necessity of meeting the planetary energy demands¹⁶. Even when the rate of fossil fuel exploitation will drop, pollutants production will continue for the foreseeable future. It is urgent the need of parallel endeavors addressing the development of more readily available solutions. Hence the second - best option to tackle environmental pollution is to try to remove the desired species from the environment whenever possible.

Pollutants removal can be achieved through the use of substances or materials which are able to attract and retain the target molecules. These substances are called

“sorbents” and they can be obtained in both the liquid and solid state¹⁷. Liquid – phase absorption is a process already implemented at an industrial level which mainly deals with CO₂ removal from both natural and flue gas^{18,19}. It is a post – combustion technology, meaning the fuel is combusted and at the end of the process the CO₂ is removed. Post – combustion technologies are usually preferred to pre – combustion ones because of easier implementation at an industrial level since they do not require significant modifications of the already existing implant²⁰. CO₂ liquid – phase absorption relies on amine – based solvents²¹, which can trap carbon dioxide through a process called chemical adsorption, or chemisorption. Chemisorption is the capture of molecules by another species through the formation of a chemical bond. Hence, it is not a reversible process and, in the specific case of amine – based solvents, costly regeneration steps have to be performed in order for the liquid – phase to be able to efficiently repeat the capture of additional CO₂²². This constitutes a problem for liquid – phase absorption since the energy requirement for the solvent regeneration is around 3.5 GJ per ton of CO₂²³. Amines are also corrosive which leads to serious plant durability issues and indeed plant corrosion is a known problem for CO₂ capture via amine – based solvent technology²⁴. In addition, the high temperatures associated with flue gas can lead to amine degradation and the production of species such as NO_x and SO_x which can be released in the atmosphere or can cause poisoning of the solvent itself²⁵. Due to the aforementioned problems, it is often preferred to search for technologies associated with lower costs and ease of operation. Solid sorbents represent a promising alternative because of lower costs of regeneration, greater temperature range of operation, the possibility of fine – tuning the interactions between the material and the adsorbate, longer stability and lower risks for the environment when disposal of the material is needed²⁶. In addition, solid sorbents can operate via both chemisorption and physical adsorption, namely physisorption. Physisorption relies on weak interactions, usually Van der Waals forces, electrostatic interactions, dipole – dipole et cetera to retain the target species via adhesion with the material’s surface. The magnitude of the weak

interactions at play allow for more mild regeneration conditions which in turn is reflected in the longer period of operation of the same material²⁷. For solid sorbents to be effective they require high porosity, and consequently high surface area, in order to maximize the surface interactions and the volume at disposal of the adsorbate²⁶. Pores are defined as a function of their dimensions. Specifically, “micropores” are pores with diameter under 2 nm, “mesopores” possess pore diameter between 2 and 50 nm while pores with diameter greater than 50 nm are named “macropores”²⁶. Solid sorbents displaying both micro and mesopores are named “hierarchical” materials²⁶. However, in order to be classified as a true hierarchical material, the solely presence of the two classes of pores is not a sufficient condition. In fact, a certain degree of interconnection within the porous framework needs to be present in order to allow access to both types of porosities²⁶. A vast number of solid sorbents have been developed in recent years and in the next section a brief overview of the main categories will be presented.

1.2 Classes of solid sorbents

Adsorbent materials can be classified on the basis of their structure and chemical composition. Porous materials range from completely inorganic to inorganic – organic hybrid to completely organic. They can be subdivided in:

- Inorganic porous materials (Zeolites, synthetic clays)
- Porous carbons
- Inorganic – organic hybrid materials (Metal Organic Frameworks, MOFs)
- Organic materials (Covalent Organic Frameworks, COFs)

- Porous organic polymers (Conjugated Microporous Polymers, CMPs; Porous Aromatic Frameworks, PAFs; Polymers of Intrinsic Microporosity, PIMs, Hyper Cross – Linked Polymers, HCPs and others)

1.2.1 Zeolites

Zeolites are crystalline and microporous tectosilicates, in which all central atoms T (Si, Al, ...) are in tetrahedral coordination, and all oxygen atoms are shared by two tetrahedral TO₄ units. Therefore the inorganic framework is composed of [SiO_{4/2}] and [AlO_{4/2}]- tetrahedra, in addition to metals such as Ti, Zn, Sn. Tetracoordinated atoms with oxidation states lower than +4 (e.g. Al³⁺, Fe³⁺, Zn²⁺) impart a negative charge to the crystalline framework, which is compensated by non-framework cations in the pores. Zeolites are also found in nature where volcanic debris react with alkaline groundwater under high pressures²⁸. Natural zeolites are characterized by high Al content, limited composition variability and a high level of impurities. Synthetic approaches have been developed to produce zeolites with wider composition ranges, higher purity²⁹ as well as new zeolites not existing in nature. In Figure 5 it is reported a scheme representing some zeolitic frameworks and porous structures. Zeolites frameworks are composed of channels and cavities which can host adsorbed species or can be used to selectively sort molecules based on their dimension; for this last property zeolites are also called “molecular sieves”³⁰. Zeolites have been successfully employed at an industrial level as catalysts, especially in the petrochemical industry where they manage to surpass in performances amorphous silica in fluid catalytic cracking (FCC) processes³¹. It has been estimated that the global cost of petroleum refining would be higher by at least 10 billion US dollars per year if zeolites have not been implemented³¹. Among the advantages of this class of materials the high thermal stability³² associated with the

inorganic framework, the low cost of production and the vast number of possible structures, have allowed zeolites to be established as one of the most effective solid sorbents³³. However, as it is the case for every material destined to fulfill a practical application, there are intrinsic drawbacks. Zeolites tend to preferably adsorb water. This becomes problematic when in the presence of a mixture of gases and water, due to the resulting limited adsorption capacity³³. Zeolites also display relatively low Specific Surface Area (SSA), usually $< 1000 \text{ m}^2 \text{ g}^{-1}$ ³¹.

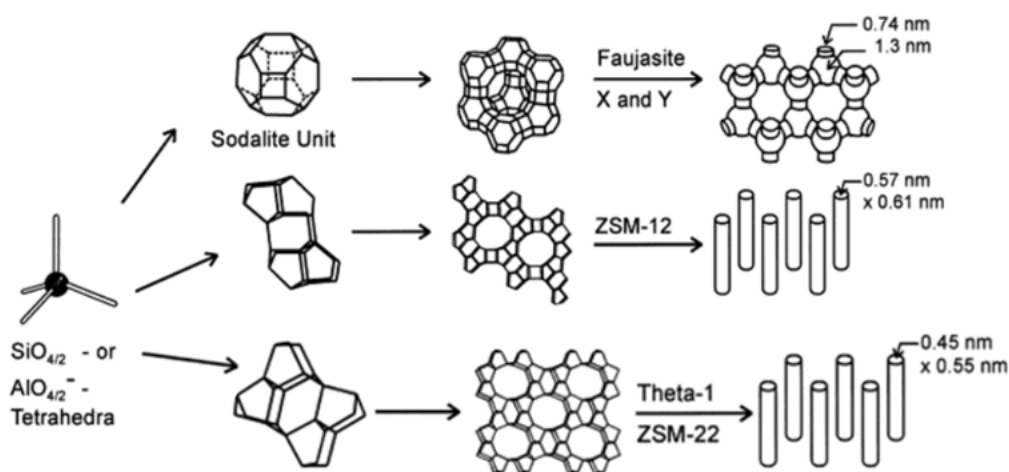


Figure 5. Selected zeolites with associated framework and micropore structures. Adapted from [29].

1.2.2 Synthetic clays

Clays are minerals named phyllosilicates which display a layered structure. Each sheet is referred to as tetrahedral (T) or octahedral (O) depending on the arrangement of the building blocks. Sheets consist of tetrahedra of silicon oxide and octahedra of

aluminum hydroxide^{34,35}. The TO_4 tetrahedral (T) sheets sites are usually occupied by Si^{4+} , Al^{3+} or Fe^{3+} cations interconnected by three vertices, which combine themselves into pseudo-hexagons $(\text{TO}_4)_6$ ^{34,35}. This tetrahedral sheet is always bonded to an octahedral sheet composed of octahedral (O) sites, usually occupied by Al^{3+} , Fe^{3+} , Mg^{2+} or Fe^{2+} cations^{34,35}. The T:O ratio of the layered structure is used to classify phyllosilicates into: (TO) when the each layer is composed by an octahedral and a tetrahedral sheet and 2:1 (TOT) layer types when the octahedral sheet is sandwiched between two tetrahedral sheets³⁵. The layers of the phyllosilicates can display an excess negative charge which is compensated by the insertion of cations in the interlayer space both inorganic³⁴ and organic^{36,37} in nature. Clay minerals are named dioctahedral if 2/3 of octahedral sites are filled by trivalent cations (such as montmorillonite) or trioctahedral if all octahedral sites are filled by divalent cations (such as saponite)³⁵. In Figure 6 TO and TOT type clay structures are reported.

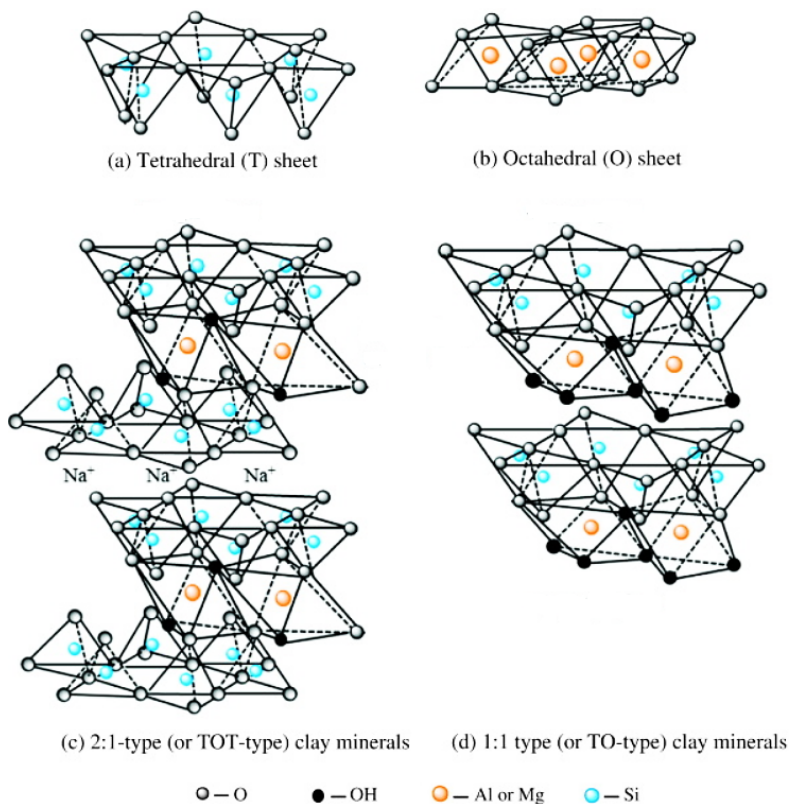


Figure 6. Schematic view of the structures of (a) the tetrahedral sheet, (b) the octahedral sheet, (c) 2:1-type clay mineral and (d) 1:1-type clay mineral.

Natural clays have been the subject of intensive studies in recent years thanks to their physicochemical properties and thanks to their associated low cost and large accessibility³⁸. Because of their intrinsic layered structure and the dimensions associated with the interlayer space, clay minerals can act as natural occurring nanomaterials and for this reason, in recent years they have been the subject of intense studies³⁸. However, impurities and heterogeneity associated with the structure of natural occurring clays, has forced the development of synthetic methods³⁹. Synthetic clays find applications in agriculture and surface coatings, for environmental purposes especially as adsorbents, ion exchangers and in water decontamination applications³⁴. Among the family of smectite clays, saponite has

been extensively studied thanks to properties such its high specific surface area which can surpass $300 \text{ m}^2 \text{ g}^{-1}$, surface acidity which is well exploited for catalytic purposes and thermal stability⁴⁰.

1.2.3 Porous carbons

Porous carbons, or activated carbons, are a class carbon – based inorganic porous materials possessing both micro and mesoporosity. From a chemical point of view they can be thought as graphite – like materials possessing structural defects and packing irregularities⁴¹. Porous carbons can be obtained via physical or chemical activation process. Physical activation consists of steam, air or CO_2 thermal treatment while chemical activation requires the use of compounds such as ZnCl_2 or KOH ⁴². Usually, chemical activation is preferred over physical activation since it faster, it requires lower activation temperatures and it usually leads to materials with higher specific surface areas⁴². In particular, KOH treatments require temperatures ranging from 673 to 1100 K^{42,43}. During chemical activation the following reactions take place:

- 1) $\text{C} + 2\text{KOH} \rightarrow 2\text{K} + \text{H}_2 + \text{CO}_2$
- 2) $\text{C} + 2\text{KOH} \rightarrow 2\text{K} + \text{H}_2\text{O} + \text{CO}$
- 3) $\text{CO}_2 + 2\text{KOH} \rightarrow \text{K}_2\text{CO}_3 + \text{H}_2\text{O}$

Mesopores and micropores are formed as a consequence of the intercalation of potassium within the carbon network during the activation process⁴³. Porous carbons display very high specific surface areas, easily reaching $>3500 \text{ m}^2 \text{ g}^{-1}$ and high pore

volumes⁴⁴. Another important advantage of porous carbons over other porous materials is the possibility to use low – cost starting materials such as plant – based precursors for example walnut shells, peanut or grape seeds or bamboo waste^{42, 44}. The very high physicochemical stability in addition to the excellent textural properties allow porous carbons to be excellent solid sorbents for gas adsorption and storage and for catalytic applications⁴⁴. However, the intrinsic very low density of the material, as for example displayed by the commercial carbon Maxsorb®, 0.37 g/cm³, result in lower performances when a fixed volume of the material has to be used⁴⁵.

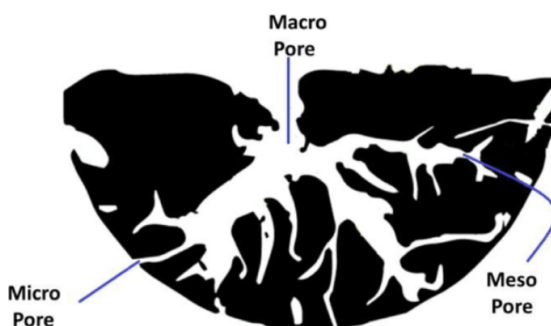
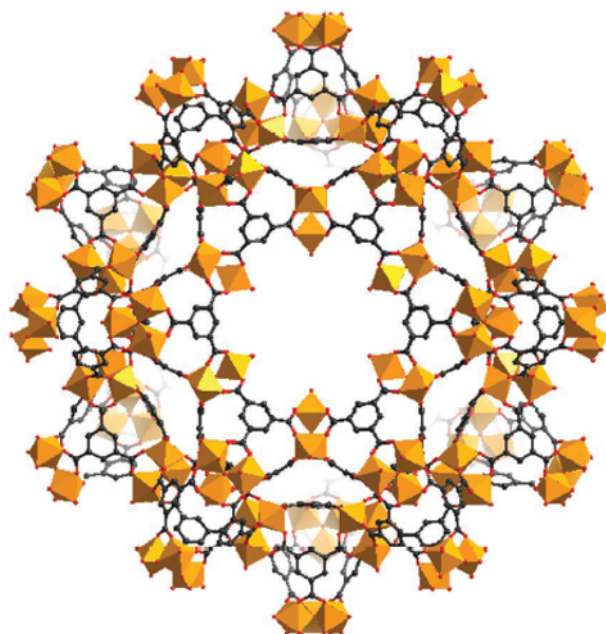


Figure 7. Schematic representation of the porous structure of an activated carbon.

1.2.4 Metal – Organic Frameworks (MOFs)

Metal organic frameworks are a class of porous materials which represents a fusion between an inorganic and organic material. MOFs consist of metal ions or clusters bonded to organic ligands to form one, two or three – dimensional structures. They can be viewed as coordination polymers. The coordination network displays high

through – space order which often results in excellent textural properties⁴⁶. MOFs have been reported to show BET SSA assessed at more than 7000 m² g⁻¹⁴⁷ and it has been demonstrated theoretically that MOFs can achieve SSA as high as 14000 m² g⁻¹⁴⁷. In Figure 8 an example of MOF structure is reported.



MOF: MIL-100

Figure 8. An example of MOF composed of $[Al_3(\mu_3-O)(COO)_6]$ clusters and tricarboxylate linkers. Adapted from [46].

The exceptional textural properties in addition to functional tunability are among the advantages of this class of porous materials which allow these solid sorbents to have applications in a vast number of fields such as hydrogen storage, carbon capture, catalysis, electrocatalysis, biological imaging and sensing, ion separation and as semiconductors⁴⁶. However, the intrinsic weakness of the coordination bond does

not result in high physicochemical stability⁴⁶. In particular, the presence of water has been observed to be detrimental for MOFs stability^{46,48}. Instability of the metal - organic framework has been also evidenced in the context of catalytic applications in the presence of acidic/basic aqueous solutions or coordinating anions⁴⁶. Water is usually present in industrial processes and for this reason, great effort by the scientific community has been directed toward finding strategies for increasing the framework stability either via improving the thermodynamic stability of the metal – ligand bond or by protecting the metal – ligand bond site via steric hindrance⁴⁶. In Figure 9 the proposed mechanism for MOFs decomposition in the presence of water is reported.



Figure 9. Proposed mechanism for the decomposition of the metal – organic framework in the presence of water [46].

1.2.5 Covalent Organic Frameworks (COFs)

Covalent Organic Frameworks are a class of 2D / 3D crystalline porous polymers in which the building blocks are linked together by covalent bonds. The elements composing the framework are mainly carbon, nitrogen, oxygen, hydrogen and boron. The strength of this type of material is the great control over the resulting periodic structure. Prediction over the final framework topology can be made through the use of diagrams like the one shown in Figure 10⁴⁹.

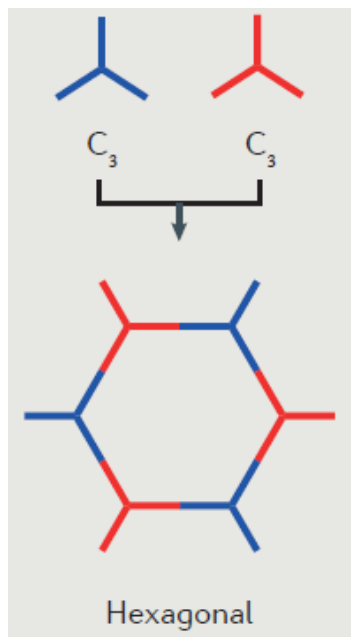


Figure 10. Topology diagram for a 2D COF. Adapted from [49].

To synthesize periodic structures with precision, reaction reversibility is needed in order to counter the presence of possible defects by allowing the growing framework to re-adjust its structure⁴⁹. Condensation reactions are the ones employed for the synthesis of COFs. For instance, condensation of boronate ester, condensation between aldehydes and amine / hydrazines, between squaric acids and amine or self-condensation of aromatic nitriles at high temperatures (673 K) and others⁴⁹ are among the synthetic pathways employed thus far for the synthesis of covalent organic frameworks. An example of condensation reaction between an aldehyde and an amine is reported in Figure 11.



Figure 11. Scheme of the condensation reaction between an aldehyde and an amine.

Covalent organic frameworks are promising candidates for important technological applications such as hydrogen and methane storage, optical materials thanks to the π conjugation exhibited by some COFs⁴⁹, as semiconductors with tunable band – gaps⁵⁰, proton conduction, carbon capture, electrocatalysis and medicine⁴⁹. In Figure 12 it is reported the structure of a proton conductive COF obtained via reaction of triformylphloroglucinol (Tp) and 4,4'-azodianiline (Azo). The resulting material is named Tp-Azo.

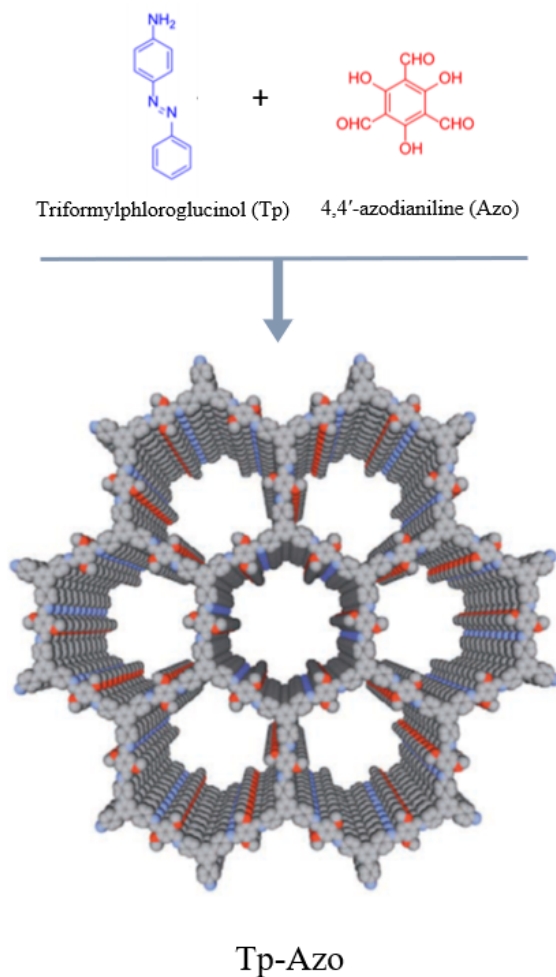


Figure 12. Reaction scheme and final structure of the proton conducting COF Tp-Azo [51]. Adapted from [49] [51].

COFs can be synthesized showing SSA as high as $1500 \text{ m}^2 \text{ g}^{-1}$ ⁴⁹. Reversible reactions are both the strength and the drawback of this kind of systems, because of associated instability in the presence of water, acids and alcohols⁴⁹. However, efforts have been made in recent years to enhance the structural stability of COFs such as employing imine linkages, derived from the condensation of aldehydes and amines, even though the crystallinity of the resulting materials is reduced⁴⁹.

1.2.6 Porous Organic Polymers (POPs)

Porous organic polymers are porous sorbents whose framework is entirely built on covalent bonds. The nature of the chemical bonds involved, in addition to the immense versatility offered by organic chemistry, allow for the incredible diversity of the possible resulting polymeric structures and functionalities, in addition with excellent chemical stability⁵². In Table 1 the main strengths of POPs with respect to other classes of solid sorbents are reported.

Table 1. Properties of different solid sorbents. [52]

Properties	Porous polymers	Zeolites	Porous carbons	MOFs
Pore size	Micro-, meso-, and macropores	Micro-, meso-, and macropores	Micro-, meso-, and macropores	Micro-, meso-, and macropores
Crystallinity	Amorphous, but typically high for COFs	Typically high	Typically amorphous	Typically high
Thermal stability	Medium to high	High	High	Low to medium
Chemical stability	Medium to excellent	Good, but can be acid/base sensitive	Excellent	Poor to good
Chemical diversity	Very high	Medium	Low to medium	Very high
Structural diversity	Very high	High	High	Very high
Processing	Good, with exception of insoluble powder	Insoluble, but technologies for films, composites, and pellets	Insoluble, but technologies for films, composites, and pellets	Insoluble, but many examples of composites and films
Unique selling points	Low density, simultaneous synthesis and processing, commercially proven technology	Low cost, widely used in refinery operations	Good conductivity, commercially proven technology	Structural and chemical control for a diverse range of materials

Porous polymers have applications in a vast number of technological fields such as gas adsorption, carbon capture, pollutants removal, molecular separation, catalysis, electrochemical energy storage, drug delivery, photoenergy conversion in solar cell, proton conduction, sensors, quantum dots and as semiconductors^{52,53, 54,55,56,57,58,59}. The possibility of fine tuning the desired properties in the realization of a tailored and a priori – designed material is one of the main strengths of this class of solid sorbents, which accounts for their widespread applications. In particular, the ability to adjust the pore structures, namely pores dimension, shape and surface

functionalities, is crucial for practical applications. In terms of pore dimensions for example, micropores control is exerted via reticular chemistry, namely the extensive linking of organic building blocks, while mesopores control can be achieved via supramolecular chemistry techniques such as self – assembly and finally macropores can be generated via phase separation⁵².

In terms of functionalities, it is possible to integrate the desired properties in the resulting material via either direct synthesis, which also comprises the possibility of polymerization of functional building blocks, in addition to post – synthesis methods⁵³. In general, the incredible diversity and opportunities offered by organic chemistry are endlessly exploited in the synthesis of new polymeric structures⁵².

In addition to the aforementioned properties, the possibility of macroscopically engineering the final form of the resulting product is also possible for some polymeric materials. Polymers can be processed resulting in monoliths, fibers, beads or separation membranes in the case of polymers composed of linear polymeric chains^{52,60}.

Based on their properties and structures, POPs can be subdivided in various classes.

1.2.6.1 Porous Aromatic Frameworks (PAFs)

Porous Aromatic Frameworks or PAFs, are a class of porous organic solids with exceptional textural properties and physicochemical stability. They differ from COFs in that they are entirely built on strong covalent bonds formed by the direct link of aromatic monomers via coupling reactions between aromatic units. The first PAF, PAF-1, was obtained by in 2009 by Profs. T. Ben, S. Qiu, G. Zhu et al, via a Yamamoto – type Ullman cross - coupling reaction between tetrahedral monomers, namely tetrakis (4-bromophenyl)methane, using a nickel (0) catalyst⁶¹. The reaction

is selective toward para substitution on the aromatic ring thus creating close – range order in the polymeric structure. The resulting material appeared as a white powder insoluble in common organic solvents⁶¹. In Figure 13, the reaction mechanism of a Yamamoto – type cross coupling reaction is reported.

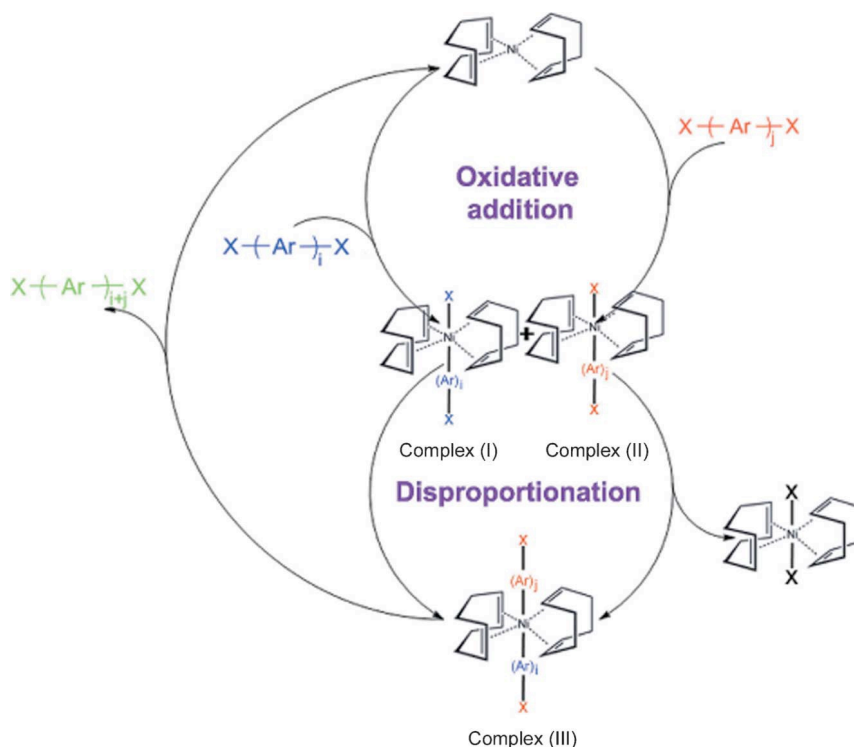


Figure 13. Mechanism of a Yamamoto – type reaction. Adapted from [62].

The idea behind the structure of PAF-1 was derived from a computational work where the structure of diamond was expanded by insertion between C-C bonds of phenyl rings, thus trying to obtain an interconnected porous framework with high physicochemical stability^{61,62}. This led to the choice of the monomer and the resulting polymeric structure which showed BET SSA of $5600 \text{ m}^2 \text{ g}^{-1}$ ⁶¹. Along with the exceptional textural properties, experiments have also demonstrated PAF-1 good

adsorption capacities, for instance 29.5 mmol g^{-1} of carbon dioxide could be stored at 298 K and at a pressure of 40 bar or 75.3 mg g^{-1} of hydrogen at 77 K at 48 bar⁶³. By employing the same synthetic strategy different porous aromatic frameworks could be obtained by changing the monomer and the number and configuration of the phenyl rings making up the “diamond cage”⁶³ as shown in Figure 14.

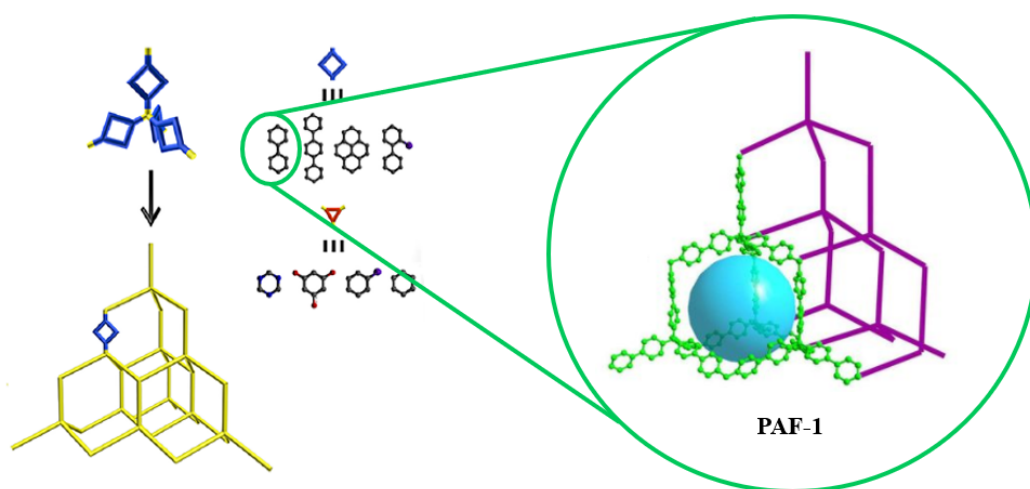


Figure 14. Schematic representation of possible PAF materials. Adapted from [63] [64].

PAF materials have been employed in various technological areas such as gas storage, catalysis and carbon capture as other solid sorbents. However, among other applications, PAF-1 was functionalized with thioether groups and was successfully employed for the selective capture of copper ions from biological fluids⁶³. Functionalized PAF-1 with poly(acrylonitrile) via atom transfer radical polymerization and subsequent KOH treatment was employed for the removal of uranium from seawater showing a maximum uptake capacity of 4.81 mg g^{-1} after 42 days of operation⁶³.

1.2.6.2 Conjugated Microporous Polymers (CMPs)

Conjugated Microporous Polymers are a class of porous organic sorbents in which the desired textural properties of high surface areas and pore volume are combined with an extended π delocalization over the entire framework. First introduced by Cooper et al in 2007⁶⁵ as poly(aryleneethynylene) networks, since then the CMP field has grown thanks to the contribution of a vast number of publications as evidenced in Figure 15.

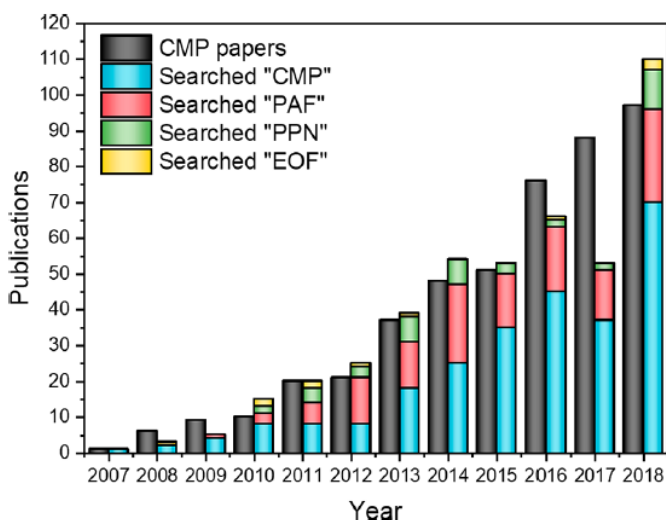


Figure 15. Number of publications per year associated with CMPs and related materials. Adapted from [66].

CMPs are usually obtained via homocoupling reactions. Direct linkage between aromatic units is usually obtained via Pd (0), Ni (0) or Cu (0) catalyzed reactions such as Sonogashira – Hagihara, Suzuki – Miyaura or Yamamoto coupling⁶⁶. In this

regard CMPs present similarities with PAFs having para – selective reactions generating the polymeric framework. However, the presence of a quaternary carbon in PAFs material, disrupt the extended π delocalization⁶⁶. In Figure 16 some synthetic routes for the synthesis of CMPs are presented. With respect to PAFs, CMPs show lower SSA ranging from 500 to approximately 1000 m² g⁻¹⁶⁶.

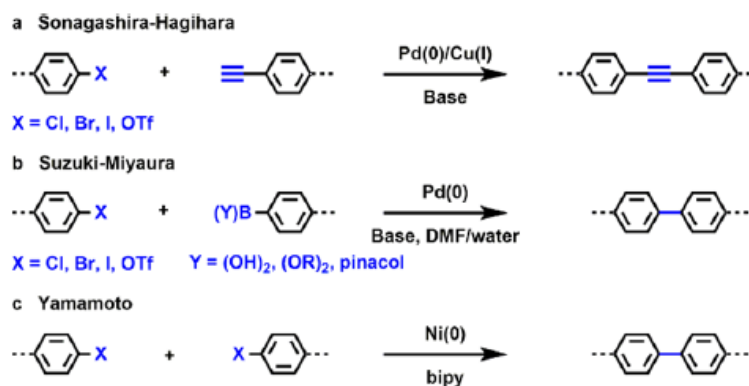


Figure 16. Reaction schemes for the synthesis of CMPs. Adapted from [66].

CMPs have potential applications in gas storage and separations, photoredox catalysis, light emittance, chemosensing^{66,67,68}. Among the previously mentioned applications, the possibility of producing luminescent materials is one of the key applications of CMPs. Due to the presence of rigid building blocks, the light emitting properties are not quenched as it is seen in linear polymeric materials⁶⁶. In addition, thanks to the multiple possibilities offered by organic chemistry, the band gap is tunable which enables control over the luminescent properties as it is summarized in Figure 17⁶⁶.

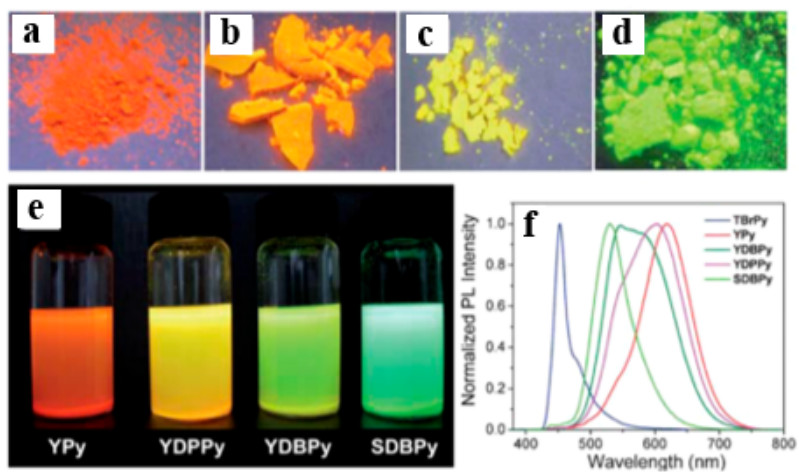
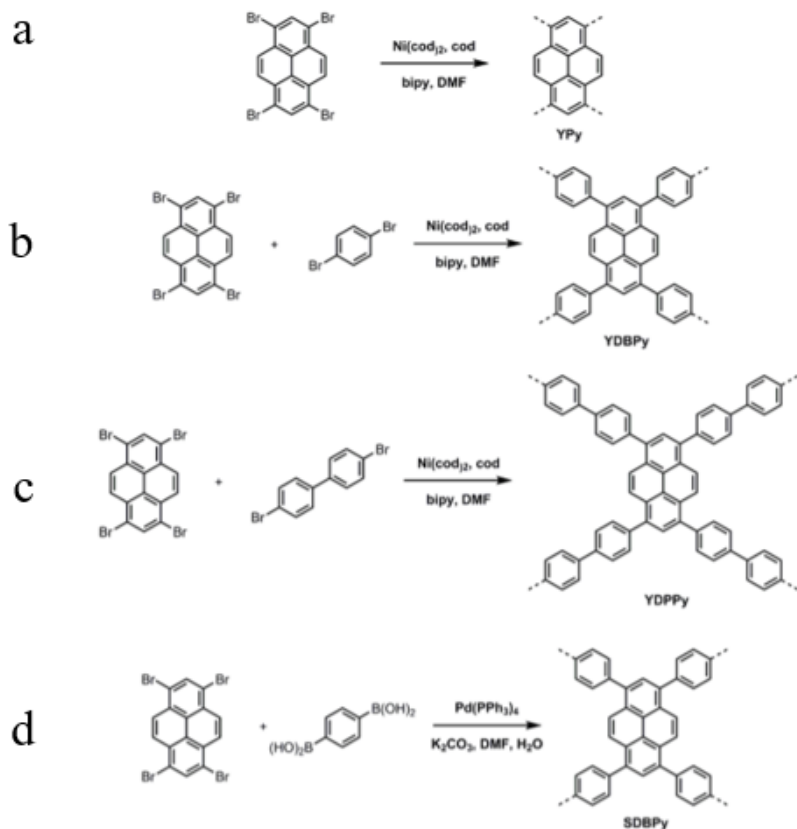


Figure 17. Schemes for the synthesis of pyrene – based CMPs and pictures of the relative suspensions in THF (10 mg / 10 ml). Adapted from [66].

1.2.6.3 Polymers of Intrinsic Microporosity (PIM)

Polymers of intrinsic microporosity, or PIMs, were first obtained by Prof. Neil McKeown and co-workers in the 1990s⁶⁹, in the context of works based on phthalocyanine materials. The discovery of the PIM polymer was somewhat accidental⁷⁰, in that the group designed a solution-processable material to determine phthalocyanine formation efficiency, via the dibenzodioxin polymerization of spirocyclic 5,5,6,6-tetrahydroxy - 3,3,3,3 - tetramethylspirobisindane and 2,3,5,6-tetrafluoroterephthalonitrile⁶⁹. The resulting material showed a BET SSA of 800 m² g⁻¹ and thereafter named PIM1⁶⁹. PIM are defined as polymers possessing a “continuous network of interconnected intermolecular voids”⁶⁹ which are generated by the shape and rigidity of the building blocks of the polymeric chains. The aromatic units in the PIM1 backbone have the effect of hindering rotation along the backbone axis, while the spirocenters help to generate inefficient packing of the polymeric chains⁷⁰. These molecular features result in a rigid and contorted structure composed of linear polymeric chains, meaning PIM polymers are not polymeric networks. The presence of spirocenters is introduced in the molecular structure via spirobisindane groups such as those reported in Figure 18. These functionalities allow for the generation of the microporosity⁷⁰. To further reduce the already hindered rotation of the aromatic rings, bulky lateral groups can be added to the molecular structure^{70,71}.

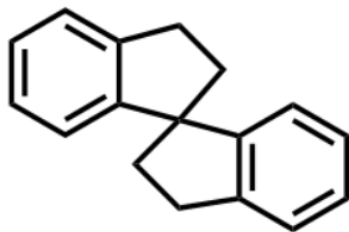


Figure 18. An example of spirobisindane group where the six – member aromatic rings are directly linked with five membered carbon rings linked together by a spirocenter.

PIM1 is synthesized via a nucleophilic aromatic substitution reaction between a hydroxylated aromatic monomers and fluorinated aromatic monomers⁷⁰, as reported in the scheme in Figure 19. The resulting material present itself as a bright yellow powder.

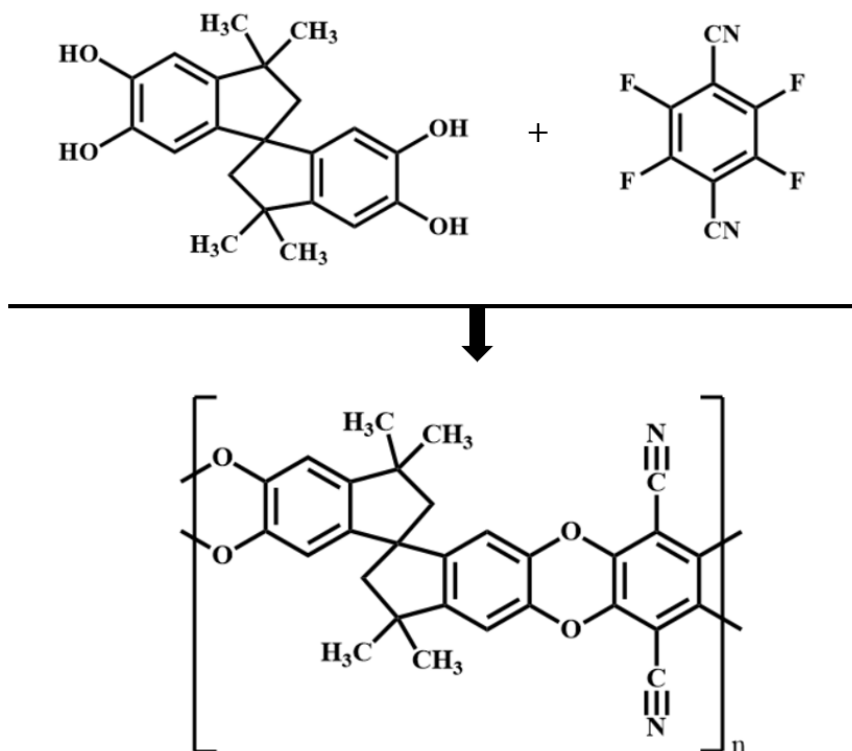


Figure 19. Reaction scheme for the synthesis of PIM1.

It was soon realized that PIM1 could be processed in the form of membranes. The first application concerned the separation of water / phenol mixture⁷², however, PIM1 membranes were soon applied to gas separation⁷³. The performances exhibited by PIM1 in gas separation even managed to surpass the tradeoff between permeability and selectivity, known as Robeson upper – bound⁷³. Usually, polymeric membranes show good permeability and low selectivity while inorganic membranes show the opposite trend, good selectivity and low permeability⁷⁰. The Robeson upper bound is since then progressively surpassed and is constantly moved upward as new PIM and other materials are constantly developed⁷⁰.

For polymeric membranes, the solution – diffusion model is usually used to describe the mass transport within the membrane, namely the gas diffusion is governed by

chemical potential differences within the membrane⁷⁴. Separation of the gas mixture is obtained via solubility and diffusion differences of the single gas components. The gas permeability P is defined as the product between the solubility and the diffusivity as reported in Equation 1.

$$P = D \square S \quad \text{Equation 1}$$

The typical unit of permeability is named barrer and is defined as:

$$1 \text{ barrer} = 10^{-10} \frac{\text{cm}_{STP}^3 * \text{cm}}{\text{cm}^2 * \text{s} * \text{cmHg}}$$

Even though PIM1 is a promising material for gas separation applications, its performances are not stable over time⁷⁰. The decay in the gas permeation rate is called aging. Aging is a general term referring to a thermodynamic driven process associated with the relaxation of glassy frameworks over time^{70,75}. Glassy polymers are materials where the glass transition temperature (T_g) is higher with respect to the temperature of operation and for the case of PIM1, the T_g has recently been assessed at 715 K (442 °C)⁷⁶, which is way above the temperature of operation for gas separation applications. The fact that PIM1 is glassy at room temperature implies that its polymeric framework is not in an equilibrium state. This means that the polymeric chains tend to move and rearrange themselves trying to occupy the intermolecular free volume. The collapse of the internal voids results in decreased permeability performances over time. For PIM1 it is observed that after 1 year the CO₂ permeability decreases approximately by 80% with respect to the initial value^{77,78}. To mitigate aging effects various strategies have been developed by researchers

in recent years including modifying the molecular structure of PIM1 aiming to suppress chains movements by adding rigid and / or bulky groups. Among the novel PIM molecular structures, some are reported in Figure 20.

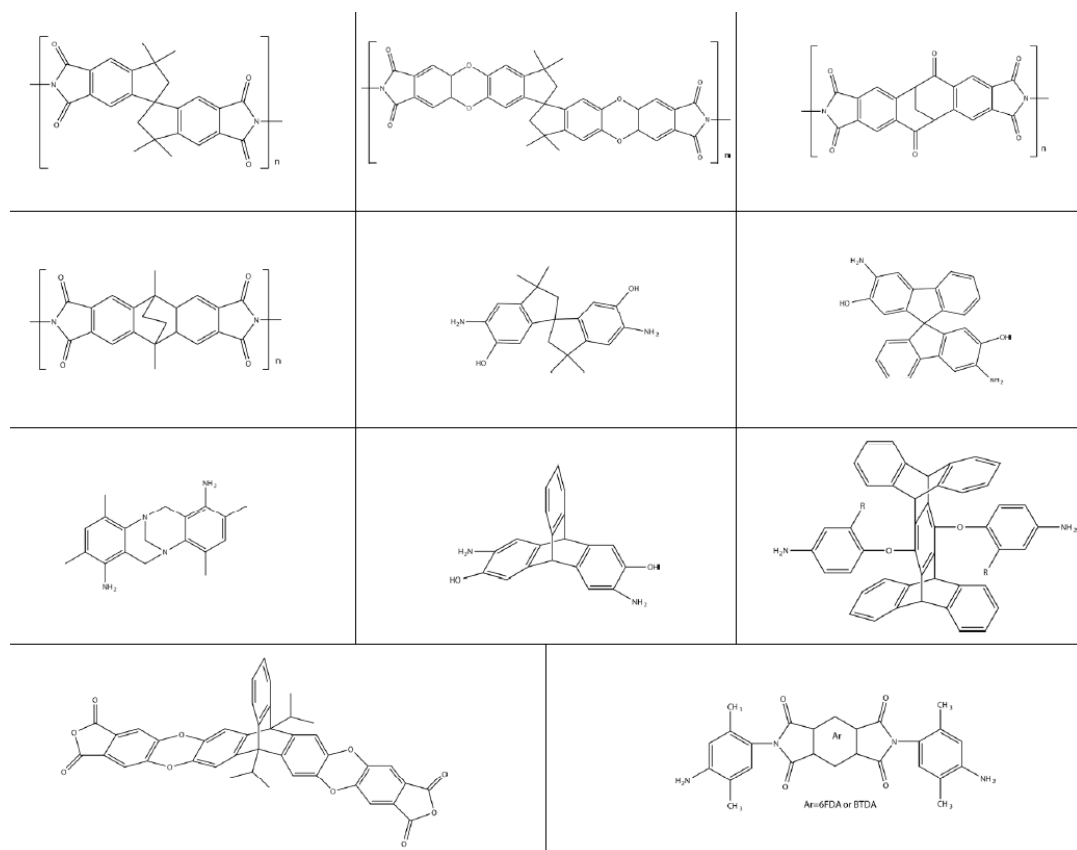


Figure 20. Alternative PIM and monomers molecular structures. Adapted from [70].

In addition to trying to obtain more stable PIM materials, other approaches aimed to mitigate aging effects have been tried such as UV treatment, thermal cross – linking and the addition of fillers, usually porous in nature⁷⁰. This last strategy has been extensively pursued and a multitude of materials have been tested as additives, ranging from inorganic materials such as porous silica, zeolites, graphene and porous

carbons to inorganic – organic hybrid such as MOFs to completely organic such PAFs and Hyper Cross – Linked Polymers (HCPs)^{79,80,81,82,83,84,85}. When fillers are added to the PIM1 matrix the resulting membrane is called Mixed Matrix Membrane (MMM). Among the previously mentioned fillers one of the most effective in reducing aging effects has been PAF-1^{84,85}. This strategy was successfully employed by Lau et al.⁸⁴ in 2014 where the addition of 10 wt % of PAF-1 to the PIM1 matrix resulted in a 7 % drop in CO₂ permeability after 240 days of aging as seen in Figure 21. The positive effects of filler addition are related to a reduced rate of collapse of internal free volume due to the presence of the filler particles, to the porous nature of the PAF-1 filler where its exceptional textural properties provide additional gas diffusion pathways, in addition to the possible partial polymeric chains diffusion within the pores of the filler, thus hindering further chains movements⁸⁴.

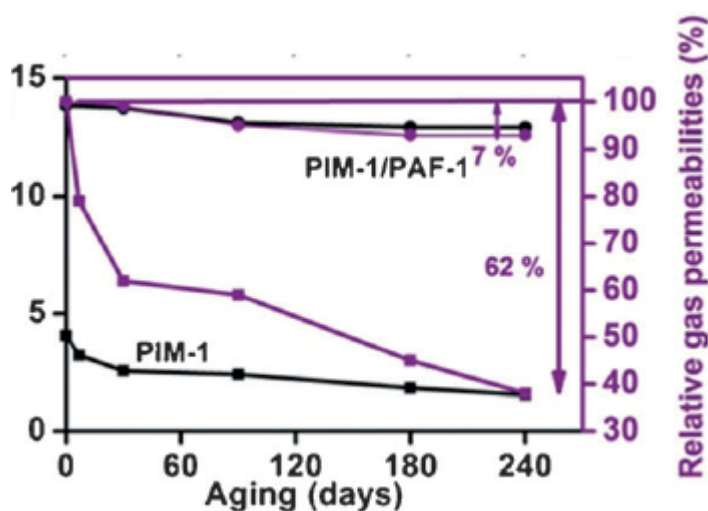


Figure 21. Graph relating the aging of the pure PIM1 membrane and the PIM1 + PAF-1 MMM with the CO₂ permeability. Adapted from [84].

1.2.6.4 Hyper Cross – Linked Polymers (HCPs)

Hyper Cross – linked polymers are a class of sorbents first introduced in 1930s and as of today still the focus of great research interest⁸⁶. HCPs are composed of a highly interconnected network, where each monomer unit is linked to each other via chemical bridges. The high degree of interconnectivity results in a permanent and highly stable nanoporous structure⁸⁷. HCPs are usually based on Friedel – Crafts chemistry⁸⁷, where a metal halide is used to generate the carbocationic sites which reacts to form chemical bridges between aromatic monomer units. A scheme of the Friedel – Crafts alkylation reaction is reported in Figure 22.

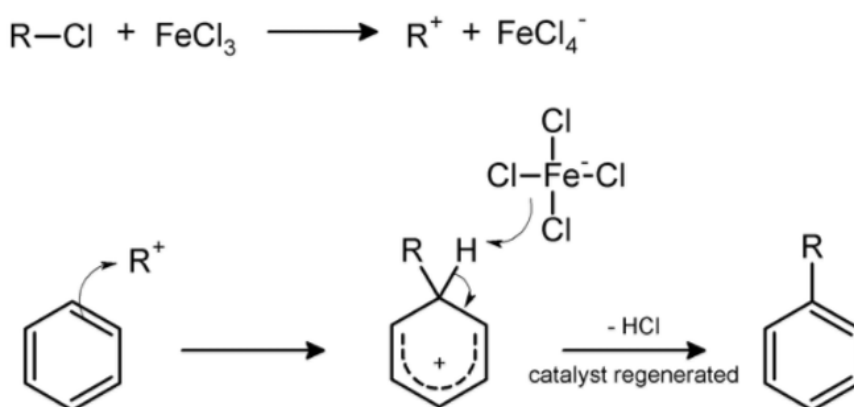


Figure 22. Friedel – Crafts alkylation reaction scheme.

Thanks to the fast kinetic and the simple and versatile synthetic approach, it is possible to obtain porous polymers with good textural properties in a fast and economic manner⁸⁷. In particular, no anhydrous conditions are required, the catalysts are often cheap and non – toxic and non - expensive monomers can be selected. The highly cross – linked network often results in the formation of both micro and

mesoporosity, usually well interconnected by pore channels, hence giving HCP hierarchical properties.

The first type of cross – linked polymer was synthesized as a cross – linked polystyrene, obtained by Staudinger and Heuer in the 1930s where divinylbenzene was used as a cross – linker⁸⁶. The resulting polymer was a gel with a 5 – 8 % content of divinylbenzene⁸⁶. The first application was to use the cross – linked polystyrene as matrix for the synthesis of ion – exchange resins via functionalization of the material with sulfonic groups or ammonium groups⁸⁸. However, the material showed poor permeability. The textural properties were not investigated for these first cross – linked polymers. However, even at early stages of research it was reported the ability of these type of polymeric networks to swell when put in contact with non – polar organic solvents⁸⁹.

The first synthesis of a “modern” HCP was reported by Davankov and Tsyurupa in the 1970s⁹⁰ where a cross – linking degree of more than 40% was achieved, thus resulting in a true Hyper Cross – linked polymer. For this material, the dissolution of a linear polymer (polystyrene) was obtained in dichloroethane and the cross – linking between linear chains was achieved via a FeCl₃ catalyzed Friedel – Crafts reaction with chloro - functionalized divinylbenzene. When the linear polymer is put in a thermodynamic compatible solvent, the polymer swells creating free space between the polymeric chains. Then the cross – linking reaction takes place, which forms a network retaining some of the free space previously generated, so that when the solvent is removed the porosity remained in the form of a rigid and stable polymeric network. A scheme showing this mechanism is reported in Figure 23. The resulting materials showed SSA ranging from 600 to 2000 m² g⁻¹⁹¹.

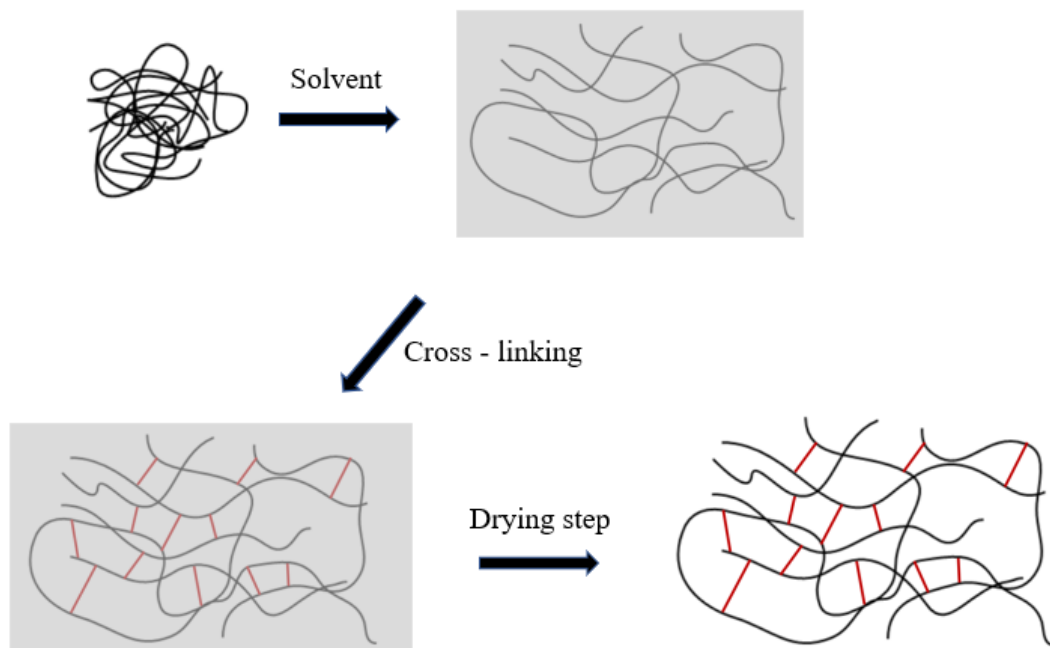


Figure 23. Scheme of the post – cross – linking route to HCPs.

Sherrington and co – workers have obtained a series of vinylbenzyl chloride–divinylbenzene copolymers by adjusting the synthetic parameters by employing different solvents and different catalysts such as AlCl_3 or SnCl_4 ⁹². However, among these polymers, the best textural properties were found for samples obtained using FeCl_3 as catalyst and dichloroethane as solvent, for which the SSA was assessed at $2090 \text{ m}^2 \text{ g}^{-1}$ ⁹².

The post – cross – linking strategy is dependent on the nature of the polymer used as precursor and even though early efforts have focused the attention on this strategy, the number of polymers suited for both the synthesis of the polymer itself and the subsequent role as Friedel – Crafts precursors is limited^{87,93}. It is possible to employ an aromatic cross – linker with chloro – aliphatic functionalities to obtain the cross – linking of cross – linker units. This strategy was employed by Cooper and co –

workers to obtain an HCP via “one – step condensation” of bis(chloromethyl)anthracene^{94,95} as reported in the scheme of Figure 24.

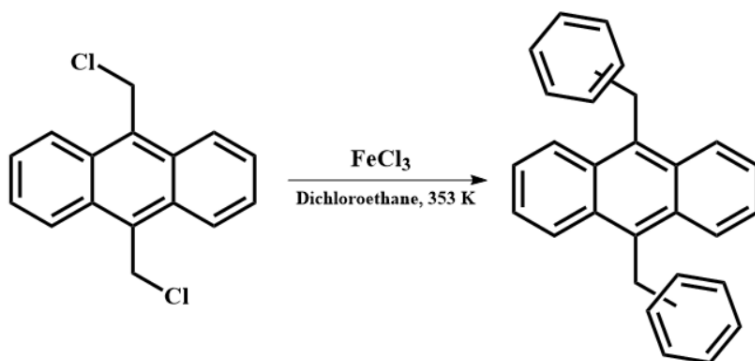


Figure 24. Scheme for the synthesis of bis(chloromethyl)anthracene – based HCP.

The resulting material showed a SSA of $991 \text{ m}^2 \text{ g}^{-1}$. However, by employing bis(chloromethyl)biphenyl for the “one – step condensation” the surface area of the resulting material was assessed at $1874 \text{ m}^2 \text{ g}^{-1}$. The reaction scheme is reported in Figure 25. This confirmed that the textural properties of HCPs are controllable and tunable if the proper monomer and / or cross – linker are employed in the synthetic procedure.

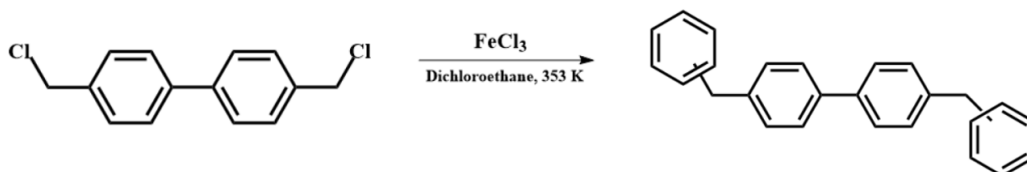


Figure 25. Scheme for the synthesis of bis(chloromethyl) biphenyl – based HCP.

A different and very efficient strategy for the synthesis of HCPs was proposed by Tan and co-workers known as the “knitting method”⁹⁶. Here formaldehyde dimethyl acetal (FDA) is used as cross-linker. The proposed mechanism involves the breaking of carbon-oxygen bonds of the FDA by the Lewis acid, in this case FeCl₃ (Figure 26, a). The carbocations thus produced are responsible for the formation of methoxy groups bonded to the monomeric aromatic species (Figure 26, b). The methoxy groups are again subjected to the attack of the Lewis acid which breaks the C-O bonds (Figure 26, c) with formation of carbations which react with other monomeric aromatic species (Figure 26, d) creating the polymeric network (Figure 26, e). The reaction scheme is reported in Figure 26.

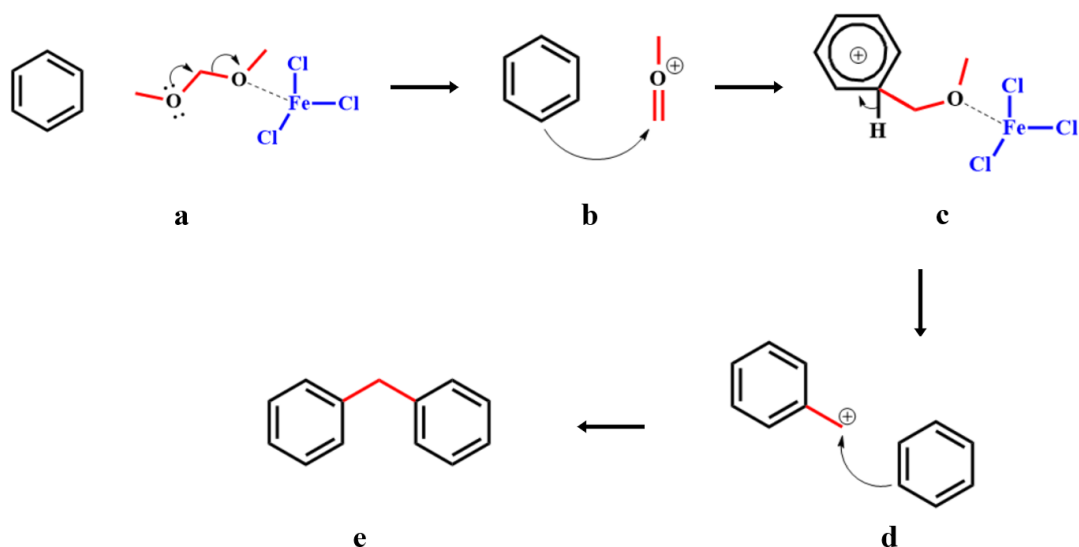


Figure 26. Proposed mechanism for the “knitting method” Friedel – Crafts reaction for the synthesis of HCPs.

An example of reaction scheme involving the knitting method is reported in Figure 27.

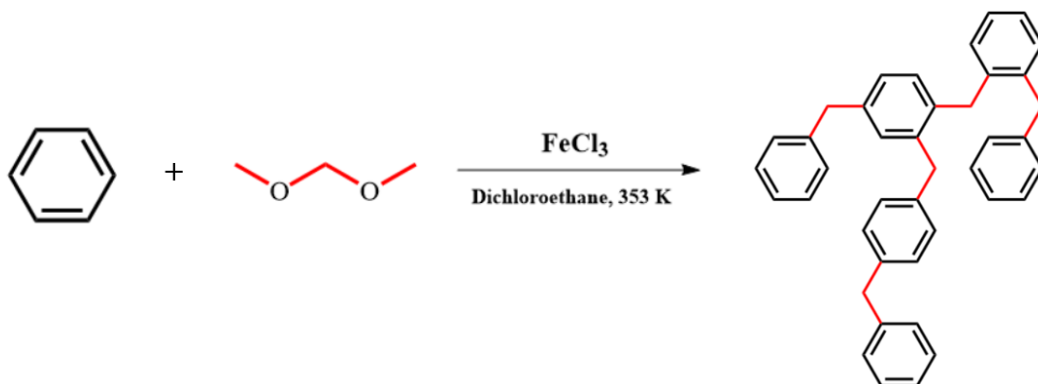


Figure 27. Reaction scheme for the synthesis of HCP via knitting method.

The knitting method allows for the tailoring of the textural properties by variation of the molar ration between the reagents, in addition to the choice of suitable monomers for the desired textural and physicochemical properties. By employing benzene as monomer with a 3/1 cross – linker / monomer ratio the resulting material showed a SSA of $1391 \text{ m}^2 \text{ g}^{-1}$ which decreased to $897 \text{ m}^2 \text{ g}^{-1}$ when a 1:1 molar ration was used. Cooper and co – workers reported in 2011⁹⁷ the synthesis of a HCP based on the monomer usually employed for PAF materials, namely tetraphenyl methane (TPM) and FDA as cross – linker, with FeCl_3 used as catalyst. The resulting material showed a SSA of $1470 \text{ m}^2 \text{ g}^{-1}$. Our group expanded on the knowledge regarding this type of HCP by exploring the effect of different molar ratio between the monomer, TPM and the cross – linker, FDA, by synthesizing materials named mPAF with 1/3, 1/9, 1/16 and 1/30 TPM/FDA ratios. It was shown that the SSA increases by increasing the molar ration up to 1/16 namely from $948 \text{ m}^2 \text{ g}^{-1}$ of the mPAF-1/3 to $1314 \text{ m}^2 \text{ g}^{-1}$ of the mPAF-1/16⁹⁸. However, a slight decrease in SSA was found when a ratio of 1/30 was used. The same trend was evidenced for the pore volume thus indicating a drop in textural properties when an excessive cross – linking degree is reached⁹⁸.

HCPs have been mostly employed in gas adsorption applications, specifically for CO₂, CH₄ and H₂ storage, displaying good adsorption capacities. For example, Davankov – type HCPs with surface area around 1450 m² g⁻¹ display H₂ adsorption capacities around 3 wt % at 77 K and 15 Bar⁸⁷. Unfortunately, it is far from reaching the US Department of Energy (DOE) target of 6.5 wt %. Methane storage on HCPs obtained from one – step condensation of bis(chloromethyl)biphenyl, displaying SSA around 1900 m² g⁻¹, was assessed at 8.3 wt % at 20 bar and 298 K^{87,95}. Carbon dioxide capture was assessed at 13 wt % for TPM – based HCPs obtained via knitting method, however uptakes as high as 20 wt % were obtained on HCPs where heteroatoms were introduced in the framework⁸⁷. This is possible via selection of the desired monomers / cross – linkers where heteroatoms are already present.

HCPs are also employed in pollutants removal and especially interesting results have been achieved in the context of organic pollutants removal. The chemical similarities between the host framework and the organic pollutant guest molecules result in high uptake capacities. For example, Wang and co – workers have explored the adsorption capacities of polystyrene – based HCPs toward dichloromethane and 2 – butanone, resulting in the capture of 1345.3 and 853 mg g⁻¹ respectively⁹⁹ at 308 K, which is almost 1.8 times higher with respect to the performances displayed by commercial solid sorbents at the same conditions. Liu and co – workers developed HCPs based on the knitting of benzylchloride and tested the materials for the adsorption of benzene vapor from humid streams obtaining 1480 mg g⁻¹ as the highest adsorption capacity for the HCP displaying SSA of 1394 m² g⁻¹ ¹⁰⁰. When dynamic adsorption of benzene vapor under dry and humid conditions up to 80% relative humidity was explored by Liu and co – workers it was found that the ability to retain the aromatic species by benzylchloride – based HCPs was not influenced by the humidity content. This is associated with the favorable π/π interactions between the host and the guest in addition to the presence of hydrophobic effects.

The fact that HCPs are easy to synthesize, non – expensive and display an incredible diversity of possible obtainable structures in addition to favorable host – guest interactions toward organic species and the possibility of fine-tuning surface interactions toward guest molecules, makes HCPs one of the promising candidates for future applications where a key role is played by host – guest interactions.

1.3 References

- [1] Anthropogenic pollution of aquatic ecosystems: Emerging problems with global implications. Häder, Donat-P.; Banaszak, A. T.; Villafañe, V. E.; Narvarte, M. A.; González, R. A.; Helbling, E. H. *Sci. Total Environ.* 713, 2020, 136586.
- [2] Anthropogenic pollutants: a threat to ecosystem sustainability? Rhind, S. M.; *Philos. Trans. R. Soc. Lond. B Biol. Sci.* 2009. 364, 3391–3401.
- [3] Relative contributions of greenhouse gas emissions to global warming. Lashof, D. A.; Ahuja, D. H. *Nature.* 344. 1990.
- [4] Intergovernmental Panel on Climate Change, Working Group I Contribution to the IPCC Fifth Assessment Report (AR5); Stocker, T. F.; Qin, D.; Plattner, G.-K.; Tignor, M.; Allen, S. K.; Boschung, J.; Nauels, A.; Xia, Y.; Bex, V.; Midgley, P. M. *Climate Change 2013: The Physical Science Basis.* Cambridge University Press: New York, 2013.
- [5] Review of Recent Advances in Carbon Dioxide Separation and Capture Kenarsari, S. D.; Yang, D.; Jiang, G.; Zhang, S.; Wang, J.; Russell, A. G.; Wei, Q.; Fan, M.. *RSC Adv.* 2013, 3 (45), 22739–22773.
- [6] Reports on Progress in Physics Global warming. Houghton, John. *Rep. Prog. Phys.* 2005. 68. 6.
- [7] NO_x and SO_x emissions from fossil fuels: A global distribution. Dignon, J. *Atmos. Environ., Part A.* 1992. 26, 6, 1157 – 1163.
- [8] Characterization and assessment of volatile organic compound (VOCs) emission from typical industries. Wang Hai Lin, Nie Lie, Li Jing, Wang Yu Fei, Wang Gang, Wang Jun Hui, Hao Zheng Ping. *Chin. Sci. Bull.* 2013. 58, 724-730.

[9] Risk assessment of exposure to volatile organic compounds in different indoor environments. H. Guo, H.; Lee, S. C.; Chan, L. Y.; Li, W. M. Environ. Res. J. 2004. 94, 57 – 66.

[10] <http://www.epa.gov/indoor-air-quality-iaq/volatile-organic-compounds-impact-indoor-air-quality>.

[11] Towards global sustainability: Education on environmentally clean energy Technologies. Nowotny, J.; Dodson, J.; Fiechter, S.; Gür, T. M.; Kennedy, B.; Macyk, Q.; Bak, T.; Sigmund, W.; Yamawaki, M.; Rahman, K. A. Renewable Sustainable Energy Rev. 2018. 81, 2541 – 2551.

[12] Energy Efficiency Indicators. World Energy Council; 2016. <http://www.worldenergy.org/data/efficiency-indicators>.

[13] Hori M. Nuclear Production of Hydrogen [60526]. USA: International Nuclear Societies Council. La Grange Park, IL; 2004.

[14] The afterlives of solar power: Waste and repair off the grid in Kenya. Cross, J.; Murray, D.; Energy research & social science. 2018. 44, 100 – 109.

[15] Nuclear fusion: Status report and future prospects. Ongena, J.; Ogawa, Y.; Energy Policy. 2016. 96, 770 – 778.

[16] Energy storage: The route to liberation from the fossil fuel economy? Energy Policy. 2008. 36, 12, 4363 – 4367.

[17] CO₂ capture by solid adsorbents and their applications: current status and new trends. Wang, Q.; Luo, J.; Zhong Z.; Borgna, A. Energy Environ. Sci., 2011, 4, 42.

[18] Amine-Based CO₂ Capture Technology Development from the Beginning of 2013: A Review. Dutcher, B.; Fan, M.; Russell, A. G. ACS Appl. Mater. Interfaces 2015. 7, 2137–2148.

- [19] CO₂ Removal from Natural Gas by employing amine absorption and membrane technology - A technical and economical analysis. Peters, L.; Hussain, A.; Follmann, M.; Melin, T.; Hägg, M. B. *Chem. Eng. J.* 2011, 172, 952–960.
- [20] Post-combustion CO₂ capture with chemical absorption: A state-of-the-art review. Wanga, M.; Lawal, A.; Stephenson, P.; Sidders, J.; Ramshaw, C. *Chem. Eng. Res. Des.* 2011. 89, 9, 1609 – 1624.
- [21] Experience with CO₂ capture from coal flue gas in pilot-scale: Testing of different amine solvents. Knudsen, J. N.; Jensen, J. N.; Vilhelmsen, P. J.; Biede, O. *Energy Procedia.* 2009. 1, 783 – 790.
- [22] Pushing the limits of intensified CO₂ post-combustion capture by gas–liquid absorption through a membrane contactor. Chabanon, E.; Bounaceur, R.; Castel, C.; Rode, S.; Roizard, D.; Favre, E. *Chem. Eng. Process.* 2015. 91, 7–22.
- [23] CO₂ Capture and Storage: Closing the Knowing – Doing Gap. *Chem. Eng. Res. Des.* Steeneveldt, R.; Berger, B.; Torp, T. A. 2006. 84, 9, 739 – 763.
- [24] The effect of CO₂-loaded amine solvents on the corrosion of a carbonsteel stripper. Kyra L. Sedransk Campbell, K. L. S.; Zhao, Y.; Hall, J. J.; Williams, D. R.
- [25] Technology and pilot plant results of the advanced amine process. Frederic Vitse, F.; Baburao, B.; Dugas. R.; Czarnecki, L.; Schubert, C. 2011. 4, 5527 – 5533.
- [26] Recent advances in solid sorbents for CO₂ capture and new development trends Wang, J.; Huang, L.; Yang, R.; Zhang, Z.; Wu, J.; Gao, Y.; Wang, Q.; O'Hare, D.; Zhong, Z. *Energy Environ. Sci.*, 2014. 7, 3478-3518.
- [27] Adsorption — from theory to practice. Dąbrowski, A. *Adv. Colloid Interface Sci.* 2001. 1 – 3, 93, 135 – 224.
- [28] Mineralogy and Geology of Natural Zeolites. *Reviews in Mineralogy & Geochemistry*, 4. Edited by: Fred A. Mumpton. De Gruyter, 1977.

- [29] Zeolites and catalysis. Weitkamp, J.; *Solid state ionics*. 2000. 131, 175 – 188.
- [30] Molecular Sieves. D. W.; J. V. Smith, J. V. *Scientific American*. 1959. 200, 85 – 96.
- [31] Zeolites and related microporous materials: state of the art 1994, studies in surface science and catalysis. Naber, J. E.; de Jong, K. P.; Stork, W. H. J.; Kuipers, H. P. C. E.; Post, M. F. M.; in: Weitkamp, J.; Karge, H. G.; Pfeifer, H.; Holderich, W.; (Eds). Elsevier. 1994. 84, 2197 part C.
- [32] Zeolites upon heating: Factors governing their thermal stability and structural changes. Cruciani, G. *J. Phys. Chem. Solids*. 2006. 67, 1973 – 1994.
- [33] Industrial application of solid acid - base catalysts. Tanabea, K.; Holderich. W. F. *Appl. Catal., A*. 1999. 181, 399 – 434.
- [34] Synthesis of clay minerals. Zhang, D.; Zhou, C. H.; Lin, C. X.; Tong, D. S.; Yu, W. H. *Appl. Clay Sci*. 2010. 50, 1 – 11.
- [35] Handbook of Clay Science (Developments in Clay Science, 1). F. Bergaya, B. K. G. Theng and G. Lagaly, 2006, Elsevier Science.
- [36] Synthesis and Physicochemical Properties of an Organo-Modified Saponite Clay. Bisio, C.; Carniato, F.; Paul, G.; Gatti, G.; Boccaleri, E.; Marchese, L. *One-Pot. Langmuir* 2011, 27, 7250–7257.
- [37] Sodium montmorillonite silylation: Unexpected effect of the aminosilane chain length. Piscitelli, F.; Posocco, O.; Toth, R.; Fermeglia, M.; Pricl, S.; Mensitieri, G.; Lavorgna, M. *J. Colloid Interface Sci*. 2010. 351, 108.
- [38] Chapter 1 General Introduction: Clays, Clay Minerals, and Clay Science. *Dev. Clay Sci*. Bergaya, F.; Lagaly, G. 2006. 1, 1 – 18.
- [39] Chapter 7.1 - Purification of Natural Clays. Bergaya, F.; Lagaly, G. *Dev. Clay Sci*. 2013. 5, 213 – 222.

- [40] The effect of synthesis gel dilution on the physico chemical properties of acid saponite clays. Costenaro, D.; Gatti, G.; Carniato, F.; Paul, G.; Bisio, C.; Marchese, L. *Microporous Mesoporous Mater.* 2012, 162, 159–167.
- [41] Porous carbons. Manocha, S. M. Sadhana. 2003. 28, 335–348.
- [42] Potassium hydroxide activation of activated carbon: a commentary. Hui, T. S.; Abbas, M.; Zaini, A.; *Carbon Letters.* 2015. 16, 4, 275 - 280.
- [43] Toward a molecular design of porous carbon materials. Borchardt, L.; Zhu, Q. L.; Casco, M. E.; Berger, R.; Zhuang, X.; Kaskel, S.; Feng, X.; Xu, Q. *Mater. Today.* 2017. 20, 10.
- [44] Ultra-High Surface Area Activated Porous Asphalt for CO₂ Capture through Competitive Adsorption at High Pressures. Jalilov, A. J.; Li, Y.; Tian, J.; Tour, J. M. *Adv. Energy Mater.* 2017, 7, 1600693.
- [45] Production and adsorption characteristics of MAXSORB: High-surface-area active carbon. Otowa, T.; Tanibata, R.; Itoh, M. *Gas Sep. Purif.* 1993. 7, 4, 241 – 245.
- [46] Stable Metal–Organic Frameworks: Design, Synthesis, and Applications. Yuan, S.; Feng, L.; Wang, K.; Pang, J.; Bosch, M.; Lollar, C.; Sun, Y.; Qin, J.; Yang, X.; Zhang, P.; Wang, Q.; Zou, L.; Zhang, Y.; Zhang, L.; Fang, Y.; Li, J.; Zhou, H. C. *Adv. Mater.* 2018, 1704303.
- [47] Metal–Organic Framework Materials with Ultrahigh Surface Areas: Is the Sky the Limit? Farha, O. K.; Eryazici, I.; Jeong, N. C.; Hauser, B. G.; Wilmer, C. E.; Sarjeant, A. A.; Snurr, R. Q.; Nguyen, S. N.; Yazaydin, Ö. A.; Hupp, J. H. *J. Am. Chem. Soc.* 2012, 134, 15016 – 15021.

- [48] Understanding and controlling water stability of MOF-74. Zuluaga, S.; Fuentes-Fernandez, E. M. A.; Tan, K.; Xu, F.; Li, J.; Chabal, Y. J.; Thonhauser, T. J. *Mater. Chem. A*, 2016. 4, 5176 – 5183.
- [49] Covalent organic frameworks: a materials platform for structural and functional designs. Huang, N.; Wang, P.; Jiang, D. *Nature reviews*. 2016. 1, 1 – 19.
- [50] Few-layer, large-area, 2D covalent organic framework semiconductor thin films. Feldblyum, J. I.; McCreery, C. H.; Andrews, S. C.; Kurosawa, T.; Santos, E. J. G.; Duong, V.; Fang, L.; Ayzner, A. L.; Bao, Z. *Chem. Commun.* 2015. 51, 13894 – 13897.
- [51] Proton conduction in crystalline and porous covalent organic frameworks. Xu, H.; Tao, S.; Jiang, D.; *Nat. Mater.* 2016. 15, 722–726.
- [52] Porous Polymers as Multifunctional Material Platforms toward Task-Specific Applications. Wu, J.; Xu, F.; Li, S.; Ma, P.; Zhang, X.; Liu, Q.; Fu, R.; Wu, D. *Adv. Mater.* 2019. 31, 1802922
- [53] Function-led design of new porous materials. Anna G. Slater, A. G.; Cooper, A. I. *Science*. 2015. 348, 6238.
- [54] The photoluminescence mechanism in carbon dots (graphene quantum dots, carbon nanodots, and polymer dots): Current state and future perspective. Zhu, S.; Song, Y.; Zhao, X.; Shao, J.; Zhang, J.; Yang, B. *Nano Research*. 2015, 8, 2, 355 – 381.
- [55] Proton conduction in acid doped polybenzimidazole. Bouchet, R.; Siebert, E. *Solid State Ionics*. 1999. 118, 3 – 4, 287 – 299.
- [56] Polymers for Drug Delivery Systems. Liechty, W. B.; Kryscio, D. R.; Slaughter, B. V.; Peppas, N. A. *Annu. Rev. Chem. Biomol. Eng.* 2010. 1, 149 – 73.

- [57] Electrochemically Active Polymers for Electrochemical Energy Storage: Opportunities and Challenges. Mike, J. F.; Lutkenhaus, J. L. *ACS Macro Lett.* 2013, 2, 9, 839 – 844.
- [58] Development of polymeric and polymer-based hybrid adsorbents for pollutants removal from waters. Pan, B.; Pan, B.; Zhang, W.; Lv, L.; Zhang, Q.; Zheng, S. *Chem. Eng. J.* 2009. 151, 1 -13, 19 – 29.
- [59] Gas Storage in Nanoporous Materials. Morris, R. E.; Paul S. Wheatley, P. S. 2008. 47, 4966 – 4981.
- [60] CMP Aerogels: Ultrahigh- Surface- Area Carbon- Based Monolithic Materials with Superb Sorption Performance. Du, R.; Zhang, N.; Xu, H.; Mao, N.; Duan, W.; Wang, J.; Zhao, Q.; Liu, Z.; Zhang, J.; *Adv. Mater.* 2014. 26, 8053.
- [61] Targeted Synthesis of a Porous Aromatic Framework with High Stability and Exceptionally High Surface Area. Ben, T.; Ren, H.; Ma, S.; Cao, D.; Lan, J.; Jing, X.; Wang, W.; Xu, J.; Deng, F.; Simmons, J. M.; Qiu, S.; Zhu, G. *Angew. Chem.* 2009. 121, 9621 – 9624.
- [62] Porous aromatic frameworks: Synthesis, structure and functions. Ben, T.; Qiu, S. *Cryst. Eng. Comm.* 2013. 15, 17.
- [63] Porous Aromatic Frameworks as a Platform for Multifunctional Applications. Yuan, Y.; Zhu, G. *ACS Cent. Sci.* 2019. 5, 409 – 418.
- [64] PAF-derived nitrogen-doped 3D Carbon Materials for Efficient Energy Conversion and Storage. Xiang, Z.; Wang, D.; Xue, Y.; Dai, L.; Chen, J. F.; Cao, D. *Scientific Reports.* 2015. 5, 8307.
- [65] Conjugated Microporous Poly(Aryleneethynylene) Networks. Jiang, J.-X.; Su, F.; Trewin, A.; Wood, C. D.; Campbell, N. L.; Niu, H.; Dickinson, C.; Ganin, A. Y.; Rosseinsky, M. J.; Khimyak, Y. Z.; *Angew. Chem., Int. Ed.* 2007. 46, 8574 – 8578.

- [66] Advances in Conjugated Microporous Polymers. Jet-Sing M. Lee, J. S. M.; Cooper, I. A. *Chem. Rev.* 2020. 120, 2171 – 2214.
- [67] Conjugated microporous polymers: design, synthesis and application. Xu, Y.; Jin, S.; Xu, H.; Nagai, A.; Jiang, D. *Chem. Soc. Rev.* 2013. 42, 8012 – 8031.
- [68] Conjugated Microporous Polymers. I. Cooper, I. A. *Adv. Mater.* 2009. 21, 12.
- [69] Polymers of Intrinsic Microporosity. Neil B. McKeown. *ISRN Materials Science.* 2012, 1.
- [70] Polymers of Intrinsic Microporosity (PIMs) Gas Separation Membranes: A mini Review. Ma, C.; Urban, J. J. *Proceedings of the Nature Research Society.* 2018. 2, 02002.
- [71] A spirobifluorene-based polymer of intrinsic microporosity with improved performance for gas separation. C. G. Bezzu; M. Carta; A. Tonkins; J. C. Jansen; P. Bernardo; F. Bazzarelli; N. B. McKeown. *Adv Mater.* 2012. 24, 44, 5930.
- [72] Solution-processed, organophilic membrane derived from a polymer of intrinsic microporosity. P. M. Budd; E. S. Elabas; B. S. Ghanem; S. Makhseed; N. B. McKeown; K. J. Msayib; C. E. Tattershall; D. Wang. *Advanced Materials.* 2004. 16, 5, 456.
- [73] Gas separation membranes from polymers of intrinsic microporosity. Budd, P. M.; Msayib, K. J.; Tattershall, C. E.; Ghanem, B. S.; Reynolds, K. J.; McKeown, N. B.; Detlev Fritsch, D. J. *Membr. Sci.* 2005. 251, 1 – 2, 263 – 269.
- [74] Ester-Cross-linkable Composite Hollow Fiber Membranes for CO₂ Removal from Natural Gas. Canghai Ma; Koros, W. J. *Industrial & Engineering Chemistry Research.* 2013. 52, 31, 10495.
- [75] On relaxations and aging of various glasses. Amira, A.; Oreg, Y.; Imry, Y. *PNAS.* 2012. 109, 61850 – 1855.

- [76] First Clear-Cut Experimental Evidence of a Glass Transition in a Polymer with Intrinsic Microporosity: PIM-1. Yin, H.; Chua, Y. Z.; Yang, B.; Schick, C.; Harrison, W. J.; Budd, P. M.; Böhning, M.; Schönhals, A. *J. Phys. Chem. Lett.* 2018. 9, 8, 2003 – 2008.
- [77] Gas permeation parameters and other physicochemical properties of a polymer of intrinsic microporosity: Polybenzodioxane PIM-1. Budd, P.; McKeown, N.; Ghanem, B.; Msayib, K.; Fritsch, D.; Starannikova, L.; Belov, N.; Sanfirova, O.; Yampolskii, Y.; Shantarovich, V. *J. Membr. Sci.* 2008. 325, 2, 851.
- [78] Effect of physical aging on the gas transport and sorption in PIM-1 membranes. Bernardo, P.; Bazzarelli, F.; Tasselli, F.; Clarizia, G.; Mason, C. R.; Maynard-Atem, L.; Budd, P. M.; Lanč, M.; Pilnáček, K.; Vopička, O.; Friess, K.; Fritsch, D.; Yampolskii, Y. P.; Shantarovich, V.; J. C. Jansen, J. C. *Polymer*. 2017. 113, 283.
- [79] Gas transport behavior of mixed-matrix membranes composed of silica nanoparticles in a polymer of intrinsic microporosity (PIM-1). Ahn, J.; Chung, W.-J.; Pinnau, I.; Song, J.; Du, N.; Robertson, G. P.; Guiver, M. D. *J. Membr. Sci.* 2010. 346, 2, 280.
- [80] Khan, M. M.; Filiz, V.; Bengtson, G.; Shishatskiy, S.; Rahman, M.; Abetz, V. Functionalized carbon nanotubes mixed matrix membranes of polymers of intrinsic microporosity for gas separation. *Nanoscale Res. Lett.* 2014. 9, 7, 504.
- [81] Post-synthetic Ti exchanged UiO-66 metal-organic frameworks that deliver exceptional gas permeability in mixed matrix membranes. Smith, S. J.; Ladewig, B. P.; Hill, A. J.; Lau, C. H.; Hill, M. R. *Sci Rep.* 2015. 5, 7823.
- [82] Mixed matrix membranes comprising polymers of intrinsic microporosity and covalent organic framework for gas separation. Wu, X.; Tian, Z.; Wang, S.; Peng, D.; Yang, L.; Wu, Y.; Xin, Q.; Wu, H.; Jiang, Z. *J. Membr. Sci.* 2017. 528, 273.

- [83] PIM-1 mixed matrix membranes for gas separations using cost-effective hypercrosslinked nanoparticle fillers. Mitra, T.; Bhavsar, R. S.; Adams, D. J.; Budd, P. M.; Cooper, A. I.; Chem. Commun. 2016. 52, 5581 – 5584.
- [84] Ending Aging in Super Glassy Polymer Membranes. Lau, C. H.; Nguyen, P. T.; Hill, M. R.; Thornton, A. W.; Konstas, K.; Doherty, C. M.; Mulder, R. J.; Bourgeois, L.; Liu, A. C. Y.; Sprouster, D. J.; Sullivan, J. P.; Bastow, T. J.; Hill, A. J.; Gin, D. L.; Noble, R. D. Angew. Chem., Int. Ed. 2014, 53, 5322 – 5326.
- [85] Gas- Separation Membranes Loaded with Porous Aromatic Frameworks that Improve with Age. Lau, C. H.; Konstas, K.; Thornton, A. W.; Liu, A. C. Y.; Mudie, S.; Kennedy, D. F.; Howard, S. C.; Hill, A. J.; Hill, M. R. Angew. Chem., Int. Ed. 2015, 54, 2669 – 2673.
- [86] “Über hochpolymere Verbindungen, 93. Mitteil.: Über das Zerreißen der Faden - Molekdinger, H., - styrols”. Staudinger, H.; Heuer, W. Berichte der deutschen chemischen Gesellschaft (A and B Series) 1934. 67, 7, 1159 – 1164.
- [87] Hypercrosslinked porous polymer materials: design, synthesis, and applications. Tan, L.; Tan, B. Chem. Soc. Rev. 2017. 46, 3322 — 3356.
- [88] Production of synthetic polymeric compositions comprising sulphonated polymerizates of poly-vinyl aryl compounds and treatment of liquid media therewith. D’Alelio, G. F. U.S. Patent 2, 366, 007, 1944.
- [89] Hypercross-linked polystyrene and its potentials for liquid chromatography: A mini-review”. Davankov, V.; Tsyurupa, M.; Ilyin, M.; Pavlova, L. J. Chromatogr. A. 2002. 965, 1, 65 – 73.
- [90] Macronet polystyrene structures for ionites and method of producing same. Davankov, V.; Rogozhin, V.; Tsjurupa, M. US Patent: 1973.

- [91] Nanoporous polymers for hydrogen storage. Germain, J.; Fréchet, J. M. J.; Svec, F. *Small*. 2009, 5, 10, 1098 – 1111.
- [92] Rapid generation and control of microporosity, bimodal pore size distribution, and surface area in Davankov-type hyper-cross-linked resins. *Macromolecules*. Ahn, J.-H.; Jang, J.-E.; Oh, C.-G.; Ihm, S.-K.; Cortez, J.; Sherrington, D. C. 2006. 39, 2, 627 – 632.
- [93] Hypercrosslinked Polymers: A Review. Jing Huang, J.; Turner, S. R. *Polymer Reviews*. 2018. 58, 1, 1 – 41.
- [94] Hydrogen Storage in Microporous Hypercrosslinked Organic Polymer Networks. Wood, C. D.; Tan, B.; Trewin, A.; Niu, H.; Bradshaw, D.; Rosseinsky, M. J.; Khimyak, Y. Z.; Campbell, N. L.; Kirk, R.; Stöckel, E.; Cooper, A. I. *Chem. Mater.* 2007. 19, 8, 2034 – 2048.
- [95] Microporous Organic Polymers for Methane Storage. Wood, C. D.; Tan, B.; Trewin, A.; Su, F.; Rosseinsky, M. J.; Bradshaw, D.; Sun, Y.; Zhou, L.; Cooper, A. I. *Adv. Mater.* 2008. 20,10, 1916 – 1921.
- [96] A New Strategy to Microporous Polymers: Knitting Rigid Aromatic Building Blocks by External Cross-Linker. Li, B.; Gong, R.; Wang, W.; Huang, X.; Zhang, W.; Li, H.; Hu, C.; Tan, B. *Macromolecules*. 2011. 44, 8, 2410 – 2414.
- [97] Microporous Organic Polymers for Carbon Dioxide Capture. Dawson, R.; Stöckel, E.; Holst, J. R.; Adams, D. J.; Cooper, A. I. *Energy Environ. Sci.* 2011. 4, 10, 4239 – 4245.
- [98] Microporous Hyper-Cross-Linked Aromatic Polymers Designed for Methane and Carbon Dioxide Adsorption. Errahali, M.; Gatti, G.; Tei, L.; Paul, G.; Rolla, G. A.; Canti, L.; Fraccarollo, A.; Cossi, M.; Comotti, A.; Sozzani, P.; Marchese, L. J. *Phys. Chem. C*. 2014. 118, 49, 28699 – 28710.

[99] Enhanced adsorption and desorption of VOCs vapor on novel micro-mesoporous polymeric adsorbents. Shuangshuang, W.; Zhang L.; Long, C.; Li, A. J. *Colloid Sci.* 2014. 428, 185 – 190.

[100] Synthesis of novel hyper-cross-linked polymers as adsorbent for removing organic pollutants from humid streams. Wang, W.-Q.; Wang, J.; Chen, J. G.; Fan, X.-S.; Liu, Z.-T.; Liu, Z.-W.; Jiang, J.; Hao, Z. *Chem. Eng. J.* 2015. 281 34 – 41.

Outline

The Ph.D. thesis' work is focused on developing solid sorbents aimed to address problems associated with environmental pollution. Two main technological fields were selected, namely pollutants removal and gas separation, with particular attention toward the mixture CO₂/N₂.

The development of solid sorbents was centered on the production of low – cost porous materials. Two classes of porous solids were selected, namely synthetic clays and hyper cross – linked polymers. From the synthetic clays family, saponite was chosen and synthesized in both inorganic and as a novel organo – functionalized hybrid material. With respect to hyper cross – linked polymers a total of nine different porous polymers were obtained. Among the nine HCPs, five are novel materials not previously published in the literature. The synthesized materials were characterized via a multi – technique approach, namely via scanning and transmission electron microscopies, N₂ physisorption at 77 K, FT – IR and SS – NMR spectroscopies, thermogravimetric analysis and XRD diffraction,

Pollutants associated with the VOC class was addressed by studying the adsorption capacities of selected HCPs toward the toluene that is representative of the aromatic VOC family. A volumetric adsorption approach was employed to investigate the materials' adsorption capacities. The host – guest interactions between the aromatic pollutant and the materials' framework were studied by following the adsorption process via FT-IR and SS-NMR spectroscopy. To further investigate on these interactions at play the adsorptions of benzene, xylene and *n* – hexane on a selected HCP material were studied via SS-NMR spectroscopy. Finally, a computational study was conducted in order to further elucidate the SS-NMR results.

Synthetic clays and selected HCPs were employed for gas separations applications. Gas separation via polymeric membranes obtained from a processed polymer of intrinsic microporosity (PIM1) has become a promising alternative for gas separations technologies. The need to increase the stability of the gas separation performances over time of PIM1 has recently been addressed via production of PIM1 membranes with the addition of porous solids as additives. In this regard, saponite clays and selected HCPs were tested as additives for a period of approximately one year. Eight mixed matrix membranes (MMMs) were obtained in addition to one of pure PIM1 for comparison, namely two MMMs made of PIM1 and saponite particles and six MMMs made of PIM1 + selected HCPs. The gas separations performances were tested via single gas permeation experiments performed on a custom - made permeation rig. The interactions over time between the PIM1 polymeric matrix and the additives were studied via SS - NMR ^{13}C spin-lattice relaxation times (T1). This project was conducted in collaboration with the department of Chemical Engineering of the University of Edinburgh under the supervision of Prof. Maria – Chiara Ferrari.

In conclusion in this Ph.D. work novel porous solids were designed, synthesized and studied in the context of technological applications for environmental purposes.

Chapter II

Synthesis of HCP and saponites materials

2.1 Introduction

This chapter will be devoted to the presentation of the methods employed for the synthesis of Hyper Cross-linked Polymers and saponite materials.

2.2 Friedel – Crafts alkylation reaction

Hyper Cross-linked polymers were obtained via Friedel-Crafts alkylation reaction.

The Friedel – Crafts alkylation is an electrophilic aromatic substitution, involving the substitution of a hydrogen atom on the aromatic ring with an electrophile, while releasing a proton. The starting mechanism involves the interaction between a Lewis acid, usually a metal halide, which acts as the catalyst, and a Lewis base typically a halogen atom of an alkyl halide.

The attack of the Lewis acid on the halogen atom induces heterolysis of the C-halogen bond. Formation of the Lewis acid-base complex turns the halogen into a better leaving group. The carbenium ion formed is a strong electrophile which reacts with the π cloud of the aromatic ring. Subsequent deprotonation gives the final

product. The mechanism of the Friedel – Crafts alkylation is reported in Figure 1. Here the metal halide is AlCl_3 which is a common Lewis acid employed in the Friedel Crafts alkylation, along with BF_3 , SbCl_5 , SnCl_4 , FeCl_3 , AlBr_3 , FeBr_3 and others^{1,2}.

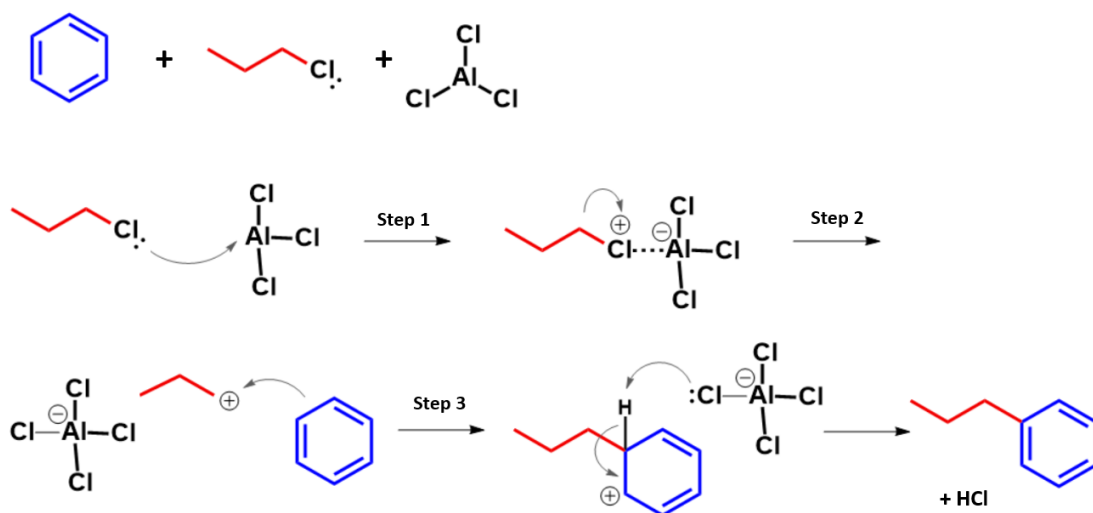


Figure 1. An example of the mechanism of the Friedel – Crafts alkylation reaction.

Modifications to the Friedel – Crafts alkylation for the synthesis of HCPs, by employment of a different type of cross-linker, have been reported by A. Cooper and coworkers³. Here the cross-linker is formaldehyde dimethylacetal (FDA). The reaction mechanism differs from the classic Friedel – Crafts alkylation in that the Lewis acid causes the scission of the carbon - oxygen bonds of the FDA with subsequent formation of a carbocation of the type reported in Figure 2.

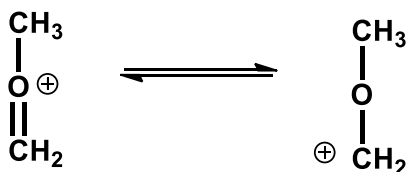


Figure 2. Resonance structures of the carbocation derived from the cross-linker FDA.

During the Ph.D. work, synthetic procedures based on alkyl halide cross-linkers have resulted in five different hyper cross-linked polymers, namely ABT01, ABT02, TPMTc, DIXYT01 and DIXYT02. Synthetic procedures based on FDA as a cross-linker have resulted in four materials, namely mPAF-1/9, mPAF-1/16, mPAF-1/30 and PS-1.3.

2.3 Synthesis of mPAF Hyper Cross-linked Polymers

Hyper cross-link polymers named mPAF (micro Porous Aromatic Frameworks) were synthesized following the synthetic procedure developed by A. Cooper et al. The ratios monomer/FDA/catalyst have been optimized in our laboratories prior to this Ph.D. project⁴ and are used in the name of the materials as mPAF-1/n, where 1/n is the molar ratio between the monomer (1) and the cross-linker/catalyst (n). Below it is reported the synthetic procedure of the material mPAF-1/16 as representative.

The mPAF-1/16 is synthesized as follow: in a 250 ml three necked round bottom flask, 1g (3.12×10^{-3} mol) of the monomer tetraphenyl methane (TPM) is suspended in 90 ml of dichloroethane (DCE) at room temperature. 8.10 g (5×10^{-2} mol) of iron (III) chloride are then added to reaction mixture which is left under stirring for 10 minutes. 4.42 ml of formaldehyde dimethyl acetal (FDA) are then added dropwise. The reaction mixture is left under stirring for approximately 20 minutes at room

temperature and then heated under reflux over night at 80 °C. The resulting mixture is a dark brown gel. The gel is then cooled and washed plenty with ethanol and water and then put in oven at 70 °C for 24 h. The resulting material is a brown powder. The reaction scheme associated with the synthesis of mPAF materials is reported in Figure 3. Here the desired product is represented by the red methylene bridge connecting two monomer units, while in purple, blue and green possible additional substitutions deriving from secondary reactions are shown.

Three mPAF materials have been synthesized namely mPAF-1/9, mPAF-1/16 and mPAF-1/30.

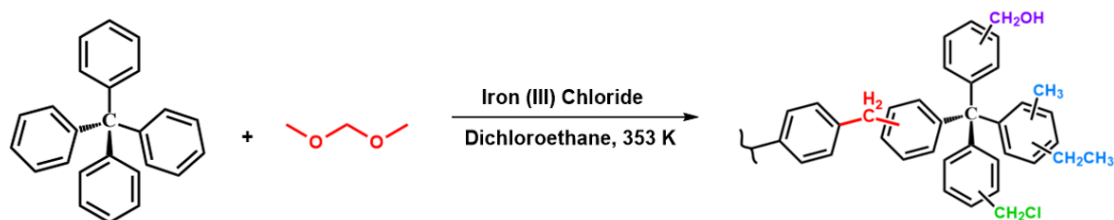


Figure 3. Reaction scheme for the synthesis of mPAF hyper cross-linked polymers. In red the methylene bridge connecting two monomer units while the blue, green and purple groups represent possible additional substitution on the aromatic ring.

2.4 Synthesis of Hyper Cross-linked Polymers

Hyper Cross-linked Polymers with different structures, textural properties and functional groups were obtained through the employment of different monomers, cross-linkers and catalysts resulting in novel materials, with the exception of the material named PS-1.3 where a patent has been deposited by our research group prior to this PhD project⁵.

2.4.1 ABT materials

As a first approach in the synthesis of novel materials, tetraphenyl methane was still used as monomer, while 1,3,5-tris(bromomethyl)benzene was employed as a cross-linking agent and AlBr_3 as catalyst. The choice of employing a cross-linker with the possibility of bridging three monomer units was made to investigate how the textural properties are affected by a higher degree of reticulation. It is worth mentioning that the employment of a cross-linking agent with an aromatic ring in its molecular structure can cause auto-reticulation of the cross-linker itself, meaning the carbocation species can attack both the monomer and other cross-linker molecules. However, by having three total substitutions namely in para (1) and meta position (2) should somewhat prevent extensive reticulation of the cross-linker itself. Another possible issue is the possibility of having more than one attack on the monomer unit by the same cross-linker species. For this reason, we used a monomer/cross-linker ratio of 1/9. The use of a metal bromide as catalyst, AlBr_3 , was dictated by the presence of bromine in the cross-linker. Two materials were obtained, namely ABT01 and ABT02 (AB from aluminum bromide and T from tetraphenyl methane). The first was synthesized in dichloromethane at 35 °C and the second one in dichloroethane at 80 °C. For the sake of brevity, here we report the synthetic procedure for ABT01 being the procedure for the synthesis of ABT02 identical with the exception of the choice of the solvent and the temperature the reaction mixture.

The ABT01 material is synthesized as follow: in a 250 ml three necked round bottom flask, 1g (3.12×10^{-3} mol) of the monomer tetraphenyl methane (TPM) is suspended in 90 ml of dichloromethane (DCM) at room temperature. 7.46 g (2.8×10^{-2} mol) of Aluminum (III) Bromide are then added to reaction mixture which is left under stirring for 10 minutes. 10.02 g (2.8×10^{-2} mol) of 1,3,5-tris(bromomethyl)benzene is then added to the reaction mixture which is left under stirring for approximately

20 minutes at room temperature and then heated under reflux over night at 35 °C. The resulting mixture is a dark brown gel. The gel is then cooled and washed plenty with ethanol and water and then put in oven at 343 K for 24 h. The resulting material is a brown powder. The reaction scheme associated with the synthesis of ABT materials is reported in Figure 4.

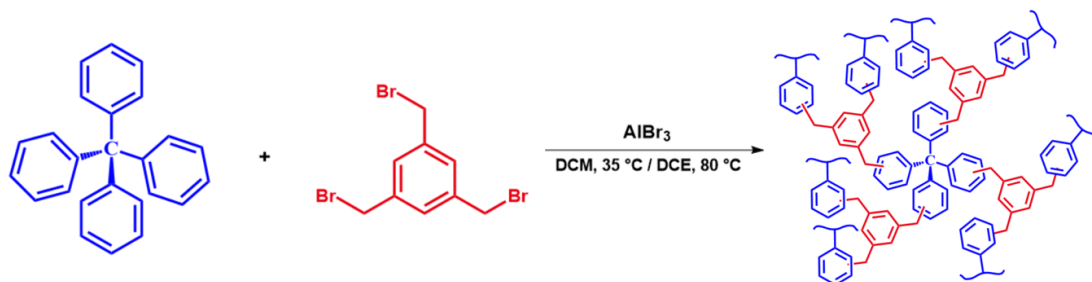


Figure 4. Reaction scheme for the synthesis of ABT hyper cross-linked polymers.

2.4.2 TPMTC material

Friedel – Crafts alkylation is not selective towards specific aromatic substitutions, meaning attack on the aromatic ring by the carbocation can theoretically happen on every position, leaving steric hindrance as major guidance for the preferred product. As reported by G. Olah and coworkers² the choice of the catalyst can have an important role in the resulting aromatic substitution which is then found in the material's polymeric framework. Substitution in para position on the aromatic rings can, for example, results in a more ordered polymeric framework^{5,6} which is a desirable property in the quest for materials with higher specific surface areas and pore volume. It was reported for the benzylation of benzene with methylbenzyl chlorides² that, among various metal halides, TiCl_4 gives for the vast majority, products with abundance of para position substitution. Since TiCl_4 is consider a weak

catalyst, its lack of reactivity is compensated by higher selectivity, as is often the case. On the contrary, AlBr_3 used for ABT materials is more reactive², hence less selectivity towards a specific product should be expected.

To increase the chances of para substitution, titanium (IV) chloride was used for the synthesis of a novel HCP. It is worth mentioning that TiCl_4 is also an inexpensive reagent. The use of a catalyst with the tendency of favoring a specific substituent orientation allows to employ an aromatic cross-linker with less probability of incurring in self-reticulation. Tetraphenyl methane was used as monomer while α,α' -dichloro-p-xylene was used as cross-linker, in addition to TiCl_4 as catalyst and dichloroethane as solvent. A ratio of 1/9 between the monomer and the cross-linker/catalyst was used.

The TPMTTC material is synthesized as follow: in a 250 ml three necked round bottom flask, 1g ($3.12 \cdot 10^{-3}$ mol) of the monomer tetraphenyl methane (TPM) is suspended in 90 ml of dichloroethane (DCE) at room temperature. 4.9 g ($2.8 \cdot 10^{-2}$ mol) of α,α' -dichloro-p-xylene are then added to reaction mixture which is left under stirring for 10 minutes. 3.07 ml ($2.8 \cdot 10^{-2}$ mol) of TiCl_4 are then added to the reaction mixture which is left under stirring for approximately 20 minutes at room temperature and then heated under reflux over night at 80 °C. The resulting mixture is a brown gel. The gel is then cooled and washed plenty with ethanol and water and then put in oven at 70 °C for 24 h. The resulting material is a brown powder. The reaction scheme associated with the synthesis of TPMTTC material is reported in Figure 5.

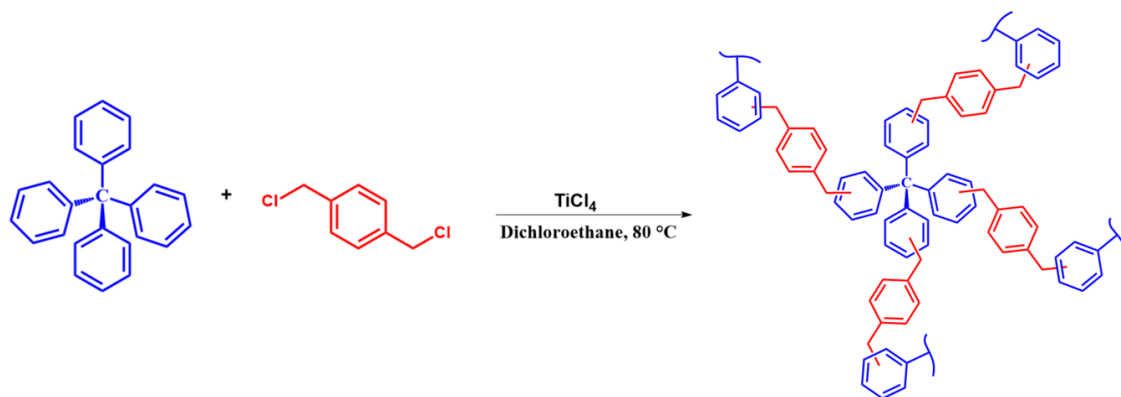


Figure 5. Reaction scheme for the synthesis of TPMTC hyper cross-linked polymer.

2.4.3 DIXYT materials

The insertion of heteroatoms within the polymeric framework can extend the realm of possible interactions between the material and guest molecules. The presence of lone pairs on heteroatoms can increase the affinity towards polarizable guest molecules, for example CH_4 and CO_2 . This strategy was here exploited to obtain HCPs with enhanced affinity towards polarizable guest molecules. In the context of the Friedel-Crafts alkylation the easiest way to obtain a polymeric framework containing heteroatoms in its molecular structure is to start with a monomer already possessing the heteroatom. We focus our attention on diphenyl sulfide because of its low toxicity, low cost of production, high resonance energy (for luminescent properties) and flexibility (for a swellable structure). α,α' -dichloro-*p*-xylene was used as cross-linker and TiCl_4 as catalyst. Two materials were synthesized namely DIXYT01 and DIXYT02. DI from diphenyl sulfide, XY from α,α' -dichloro-*p*-xylene and T from TiCl_4 . DIXYT01 was obtained using dichloromethane as solvent and $35\text{ }^\circ\text{C}$ as reaction temperature while DIXYT02 was synthesized in dichloroethane at $80\text{ }^\circ\text{C}$

°C. For the sake of brevity, here we report the synthetic procedure for DIXYT01 being the procedure for the synthesis of DIXYT02 identical with the exception of the choice of the solvent and the temperature of the reaction mixture.

DIXYT01 material was synthesized as follow: in a 250 ml three necked round bottom flask, 1ml (4.78×10^{-3} mol) of the monomer diphenyl sulfide is suspended in 90 ml of dichloromethane (DCM) at room temperature. 6.66 g (3.8×10^{-2} mol) of α,α' -dichloro-p-xylene are then added to the reaction mixture which is left under stirring for 10 minutes. 4.16 ml (3.8×10^{-2} mol) of TiCl_4 are then added to the reaction mixture which is left under stirring for approximately 20 minutes at room temperature and then heated under reflux over night at 35 °C. The resulting mixture is a yellow gel. The gel is then cooled and washed plenty with ethanol and water and then put in oven at 70 °C for 24 h. The resulting material is a yellow powder. The reaction scheme associated with the synthesis of DIXYT materials is reported in Figure 6.

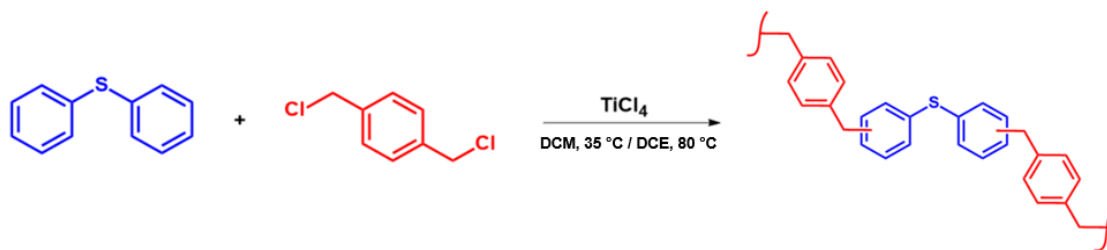


Figure 6. Reaction scheme for the synthesis of DIXYT hyper cross-linked polymers.

2.4.4 PS-1.3 material

Hyper cross-linked polymers are insoluble⁷. The materials presented in this work have been observed to be insoluble in common organic solvents and even in very acidic or basic solutions. This raises questions about the fate of the polymeric material when it needs to be discarded or replaced. In order to address this issue, a different approach for the obtaining of an HCP has been taken. Instead of using a monomer as a starting building block we decided to turn our attention to discarded polymeric materials, specifically polystyrene. Chips of pure polystyrene, commonly used in packaging, are recovered and used as a starting building block. Instead of having single monomers species linked together, polystyrene chains are cross-linked using FDA. Polymeric chains of the starting material are unrolled by the solvent, dichloroethane, which allows for the cross-linking to take place efficiently⁹.

The PS-1.3 material was synthesized as follow: in a 250 ml three necked round bottom flask, 1 g of polystyrene chips are dropped in 90 ml of dichloroethane (DCE) at room temperature. 3.11 g (1.92×10^{-2} mol) of FeCl_3 are then added to the reaction mixture which is left under stirring for 10 minutes. 1.7 ml (1.92×10^{-2} mol) of FDA are then added to the reaction mixture which is left under stirring for approximately 20 minutes at room temperature and then heated under reflux over night at 80 °C. The resulting mixture is a dark brown gel. The gel is then cooled and washed plenty with ethanol and water and then put in oven at 70 °C for 24 h. The resulting material is a brown powder. The reaction scheme associated with the synthesis of PS-1.3 material is reported in Figure 7.

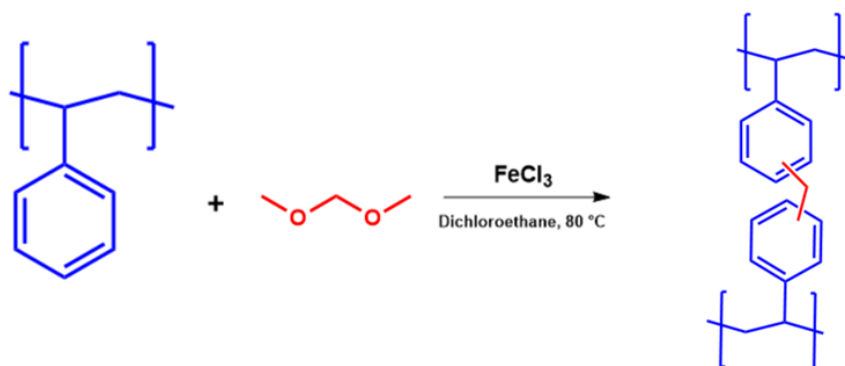


Figure 7. Reaction scheme for the synthesis of PS-1.3 hyper cross-linked polymer.

2.5 Synthesis of synthetic clays: saponites

Synthetic clays can be obtained via sol-gel and hydrothermal methods^{10,11,12}. However, as was reported by Kloprogge and coworkers¹³ hydrothermal approaches result in products with higher purity degree because of more favorable nucleation and growth of saponite materials by means of higher hydrolysis rates of the octahedral cations precursors at high temperature. In this work, synthetic clays are obtained via hydrothermal techniques. Hydrothermal methods consist in the preparation of the synthesis gel which is put in a sealed container, usually an autoclave, which is then heated at temperatures ranging from 100 to 250 °C, thus allowing the hydrolysis reaction to take place.

2.5.1 SAP110 and SAP-OP materials

The synthetic saponite named SAP110 material is obtained as follow: saponite synthesis gel with composition 1.0 SiO₂ : 0.835 MgO : 0.056 Al₂O₃ : 0.056 Na₂O : 110 H₂O was obtained from NaOH (>98 wt % Carlo Erba), SiO₂ (SiO₂ 99.8 wt %, Sigma Aldrich), Mg(CH₃COO)₂·4H₂O (>99%, Sigma Aldrich) and Al[OCH(CH₃)₂]₃ (>98%, Sigma Aldrich). 0.34 g of NaOH were added to 106.77 g of deionized water. 3.98 g of amorphous silica are then added to the solution. The gel is then left under stirring for 30 minutes. 11.95 g of Mg(CH₃COO)₂·4H₂O, 1.58 g of Al[OCH(CH₃)₂]₃ and 30 g of deionized water are then added to the reaction mixture which is left under stirring for 3 hours. The resulting gel was poured in autoclave at 240 °C for 72 hours. The material obtained was then washed with deionized water until a neutral pH was reached and then dried at 80 °C for 24 hours. The sample is hereafter named SAP110, where 110 is the ratio between H₂O and SiO₂ used for the preparation of the synthesis gel.

The hybrid organic-inorganic sample was prepared through a one-pot approach adapting a procedure already optimized in our laboratories¹⁴ that foresees the direct addition of hexadecyltrimethylammonium bromide (CTABr) to the reaction mixture. In detail, to a synthesis gel with the same composition indicated above for the preparation of SAP110 sample, a quantity of CTABr (>98%, Sigma Aldrich) equal to twice the cation exchange capacity was added; the measured CEC of SAP110 was 59.7 mequiv/100 g. The gel was then put in autoclave at 200 °C K for 72 hours and then washed and dried with the same procedure adopted for SAP110. The resulting material is named SAP-OP.

In Figure 8, representations of the structures of saponite materials are reported.

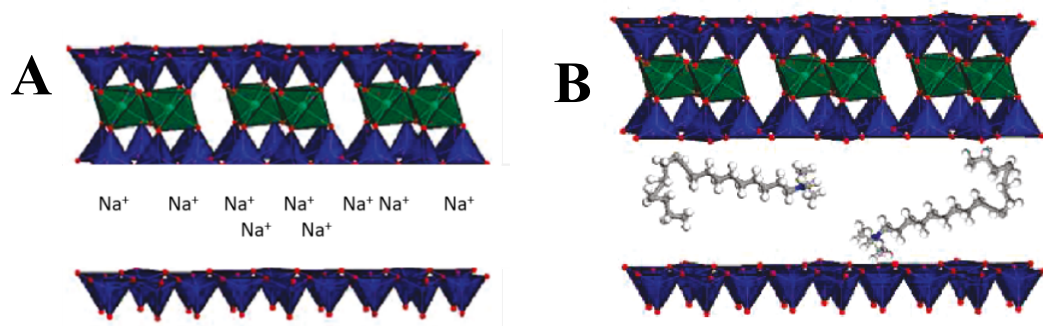


Figure 8. Structure representation of SAP110 (A) and SAP-OP (B). Adapted from [14].

2.6 References

- [1] A review of new developments in the Friedel–Crafts alkylation – From green chemistry to asymmetric catalysis. M. Rueping; B. J. Nachtsheim. *Beilstein Journal of Organic Chemistry* 2010, 6, 6.
- [2] Aromatic Substitution. XXX.1 23Friedel-Crafts Benzoylation of Benzene and Toluene with Benzyl and Substituted Benzyl Halides. G. A. Olah; S. Kobayashi; M. Tashiro. *Journal of the American Chemical Society*, 94, 21, 1972.
- [3] R. Dawson; E. Stöckel; J. R. Holst; D. J. Adams; A. I. Cooper. *Microporous Organic Polymers for Carbon Dioxide Capture. Energy Environ. Sci.* 2011, 4, 10, 4239–4245.
- [4] M. Errahali; G. Gatti; L. Tei; G. Paul; G. A. Rolla; L. Canti; A. Fraccarollo; M. Cossi; A. Comotti; P. Sozzani; L. Marchese. *Microporous Hyper-Cross-Linked Aromatic Polymers Designed for Methane and Carbon Dioxide Adsorption. J. Phys. Chem. C.* 2014, 118, 49, 28699–28710.
- [5] SOL S.p.A.; Inventors: Marchese L., Errahali M., Gatti G., Tei L., Cossi M, Valtolina D. “A method of preparing a gas-adsorbing micro- and meso-porous carbon material and the gas-adsorbing micro- and meso-porous carbon material thereby obtained” European Patent application N°: EP3421126; Date of publication: 02.01.2019
- [6] Gas storage in porous aromatic frameworks (PAFs) T. Ben; C. Pei; D. Zhang; J. Xu; F. Deng; X. Jing, S. Qiu. *Energy Environ. Sci.*, 2011, 4, 3991.

[7] Function-led design of new porous materials. Slater, A. G.; Cooper, A. I. *Science*. 2015. 348, 6238.

[8] Porous aromatic frameworks: Synthesis, structure and functions. T. Ben; S. Qiu. *CrystEngComm*, 2013, 15, 17–26, 17.

[9] Hypercrosslinked porous polymer materials: design, synthesis, and applications. Tan, L.; Tan, B. *Chem. Soc. Rev.* 2017. 46, 3322 — 3356.

[10] H. Suquet; J.T. Iiyama; H. Kodama; H. Perezat; *Clays Clay Miner.* 25, 1977, 231–242.

[11] J.T. Klopogge; J. Breukelaar; J.B.H. Jansen; J.W. Geus; *Clays Clay Miner.* 41, 1993, 103–110.

[12] I. Vincent; P. Salagre; Y. Cesteros; F. Medina; J.E. Sueiras; *Appl. Clay Sci.* 48, 2010, 26–31.

[13] J.T. Klopogge; S. Komarneni; J.E. Amonette; *Clays Clay Miner.* 47, 1999, 529–554.

[14] One-Pot Synthesis and Physicochemical Properties of an Organo-Modified Saponite Clay. Bisio, C.; Carniato, F.; Paul, G.; Gatti, G.; Boccaleri, E.; Marchese, L. *Langmuir* 2011, 27, 7250–7257.

Chapter III

Characterization of HCP and Saponite materials

3.1 Introduction

This chapter is focused to the study of the structural properties of the synthesized materials presented in Chapter II. The chapter is divided in two sections, the first is devoted to the characterization of HCP materials while the second will related to the characterization of synthetic clays.

3.2 Characterization of HCP materials

The synthesized HCPs were characterized using multiple techniques, namely, via Scanning Electron Microscopy (SEM) to observe the morphology, via N₂ physisorption analysis at -196 °C to study the textural properties, through a spectroscopic approach via FT-IR and SS-NMR spectroscopy to gain structural information, and via Thermogravimetric Analysis (TGA) to study the thermal stability. Each characterization technique is presented in its own section to allow for better comparison between materials.

3.2.1 Morphological analysis of HCP materials

SEM images of the synthesized HCPs are reported below. A thin film of gold (20 nm) was deposited on the materials' surface to achieve better resolutions, since HCPs are poor conducting materials. EDX data are shown normalized with respect to the atomic weight of the element under consideration.

In Figure 1 SEM images at 30000x magnification of the three mPAF materials are reported.

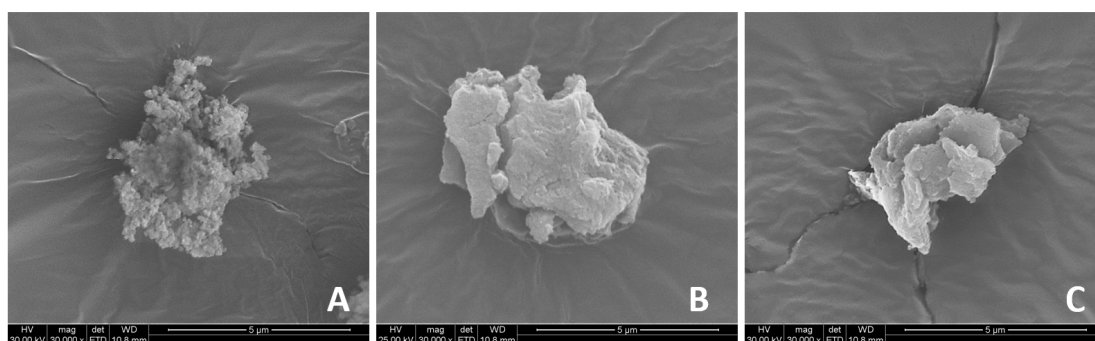


Figure 1. SEM images of HCPs mPAF-1/9 (A), mPAF-1/16 (B) and mPAF-1/30 (C) at 30000x magnification. A thin film of 20 nm was deposited on the materials' surface.

Among the three mPAF materials, it is seen that mPAF-1/9 possess a more heterogenous morphology which resembles an aggregation of small round particles. mPAF-1/16 and mPAF-1/30 display a similar morphology namely a more uniform surface.

Elemental analysis on the three mPAF samples was perform via EDX spectroscopy and the results are reported in Table 1. Five spot measurements were performed for any material and the mean values are reported.

Table 1. Elemental analysis performed via EDX spectroscopy on mPAF-1/9, mPAF-1/16 and mPAF-1/30. Five spot measurements were performed on any of each sample and the mean values are here reported.

Element	mPAF-1/9 (At %)	mPAF-1/16 (At %)	mPAF-1/30 (At %)
C	98.17 ± 0.21	94.93 ± 6.01	98.28 ± 0.38
O	1.83 ± 0.21	1.14 ± 0.30	1.71 ± 0.39
Fe	/	0.33 ± 0.2	/
Cl	/	0.12 ± 0.08	/

From the elemental analysis performed on the three samples it can be seen that the materials are composed for the vast majority of carbon. This is expected since the monomer do not possess heteroatoms and the cross-linker should transform in -CH₂-bridges between monomer units. It is however observed the presence of oxygen within the polymeric framework in all three samples. Oxygen is contained both in the cross-linker and during the synthetic procedure as atmospheric oxygen, since the Friedel – Crafts alkylation does not require an inert atmosphere. The presence of oxygen in the final material can be attributed to the occurrence of side reactions during the synthetic procedure. For the sample of mPAF-1/16 it is also observed the presence of Cl and Fe. Chlorine can be present as a side reaction groups and in catalyst form, FeCl₃, trapped inside the porous structure of the HCP after the washing step. The presence of Fe can be attributed to both oxidized iron and unreacted catalyst.

In Figure 2, SEM images at 50000x magnification of ABT materials are reported. A film of 50 nm of gold was deposited on the samples surface.

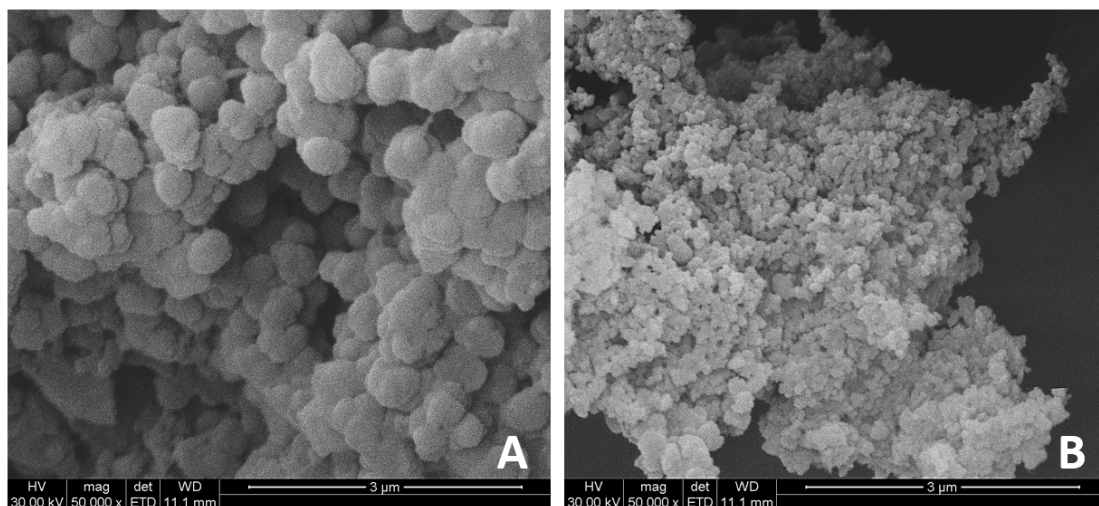


Figure 2. SEM images at 50000x magnification of ABT01 (A) and ABT02 (B). A film of 50 nm of gold was deposited on the samples' surface.

ABT materials present themselves as an aggregation of seemingly flat and circular particles. Particles dimension in ABT01 are of the range of 500 nm while for ABT02 particles diameter is of the order of 100 nm. In Table 2 the EDX elemental analysis is reported. An EDX analysis with a full frame scan was performed and the corresponding mean values are reported.

Table 2. Elemental analysis performed via EDX spectroscopy on ABT01 and ABT02 materials. A full frame analysis was performed on each sample.

Element	ABT01 (at %)	ABT02 (at %)
C	81.86	94.18
O	2.85	1.80
Al	7.36	1.35
Cl	2.75	2.21
Br	5.18	0.46

From the elemental analysis performed on ABT materials it is seen that the HCPs are composed for the vast majority of carbon, as expected. A fair amount of bromine and aluminum have been detected. The presence of aluminum can be explained by the presence of residual catalyst trapped within the porous structure of the ABT materials. The presence of bromine can be due to unreacted cross – linker species. The presence of both chlorine and oxygen could be due to side reactions products.

In Figure 3 a SEM image of the TPMTTC material is reported.

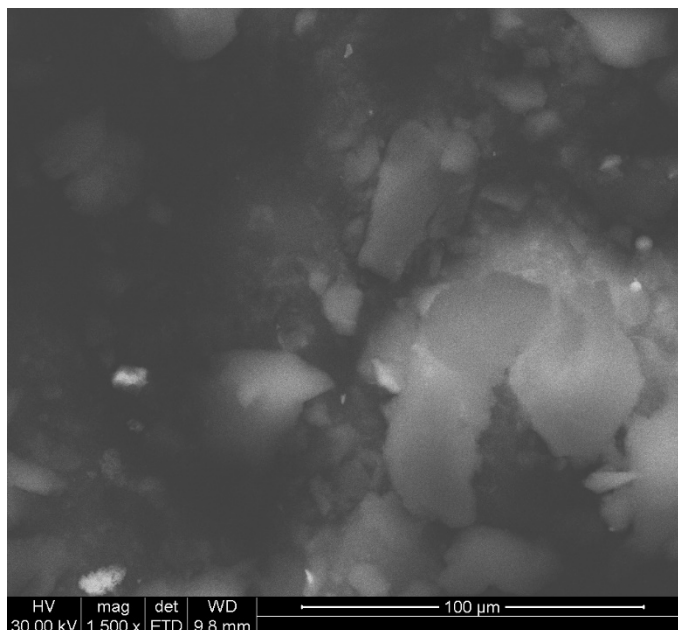


Figure 3. SEM images at 1500x magnification of TPMTC. A film of 20 nm of gold was deposited on the samples' surface.

The TPMTC sample appears to be composed of particles of heterogeneous size and shapes. Sharp edges characterize the particles' morphology which may be an indication of brittleness of the particles. In Table 3 the EDX analysis of TPMTC is reported.

Table 3. Elemental analysis performed via EDX spectroscopy on the TPMTC material. A full frame analysis was performed on the sample.

Element	TPMTC (At %)
C	92.30
Ti	0.90
O	1.05
Cl	1.87

In Figure 4 SEM images at 10000x magnification of DIXYT materials are reported. A thin film of 20 nm of gold was deposited on the samples.

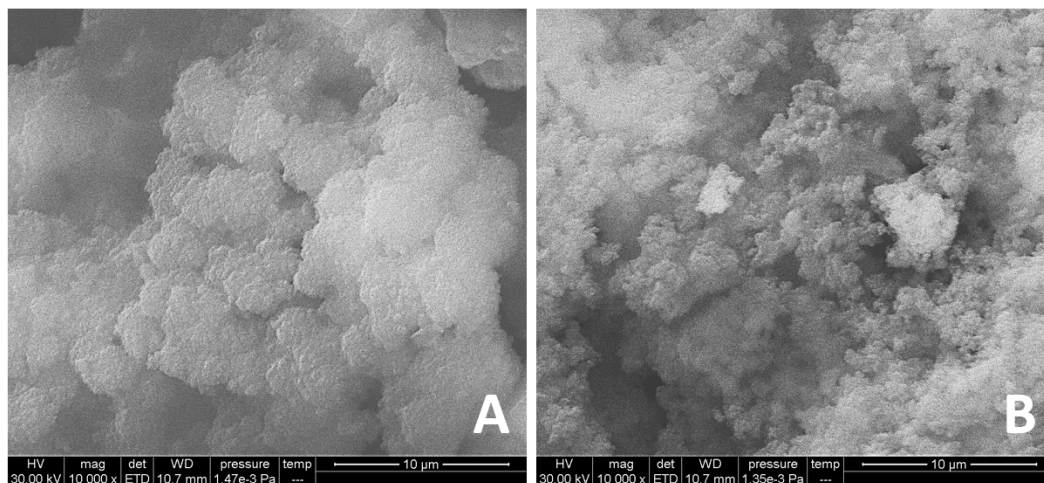


Figure 4. SEM images at 10000x magnification of DIXYT01 (A) and DIXYT02 (B). A film of 20 nm of gold was deposited on the samples' surface.

The morphology of DIXYT materials is comparable to that observed for ABT materials, namely the materials present themselves as aggregates of round-shape particles. DIXYT01, obtained in dichloromethane at 35 °C is the one displaying particles size greater with respect to the one displayed by DIXYT02, obtained in dichloroethane at 80 °C.

It is interesting to note that for both ABT and DIXYT materials, the resulting HCP obtained in dichloroethane, hence at higher temperatures, displays particles dimension smaller than the corresponding HCP obtained in dichloromethane at lower temperatures. In Table 4 the EDX elemental analysis of DIXYT materials is reported. A full frame analysis was performed on each sample.

Table 4. Elemental analysis performed via EDX spectroscopy on DIXYT01 and DIXYT02 materials. A full frame analysis was performed on each sample.

Element	DIXYT01 (At %)	DIXYT02 (At %)
C	97.04	90.78
O	0.29	1.94
S	1.12	1.92
Cl	0.73	1.85
Ti	0.82	3.51

From the elemental analysis it is observed that DIXYT materials are mainly composed of carbon, which is expected. A small amount of oxygen, 0.29 At %, is detected for DIXYT01 while for DIXYT02 the amount of oxygen is assessed around 1.92 At %. Sulfur is present for both samples, as expected. The presence of the carbon conducting tape prevent an accurate assessment of the C/S ratios.

In Figure 5 a SEM image at 6000x magnification of the PS-1.3 material is reported. A thin film of 20 nm of gold was deposited on the sample.

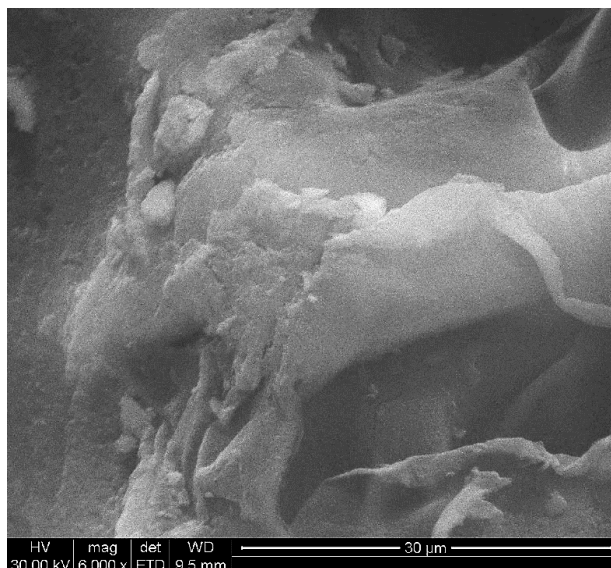


Figure 5. SEM image at 6000x magnification of the PS-1.3 material. A film of 20 nm of gold was deposited on the sample's surface.

The morphology of the PS-1.3 material appears to be not well defined and somewhat more similar to mPAF materials. No aggregation of particles has been detected. In Table 5 the EDX elemental analysis of PS-1.3 is reported.

Table 5. Elemental analysis performed via EDX spectroscopy on the PS-1.3 material. A full frame analysis was performed on the sample.

<i>Element</i>	<i>PS-1.3 (At %)</i>
C	98.81
O	0.50
Cl	0.67

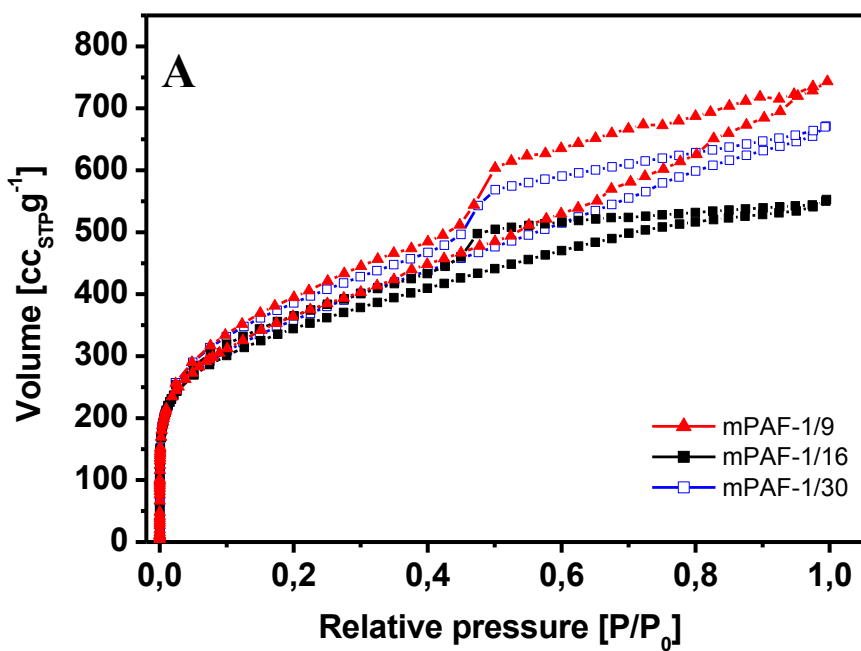
From the EDX analysis it is seen that the material PS-1.3 is almost entirely composed of carbon with the addition of small amounts of oxygen, 0.5 At % and chlorine, 0.67 At %. The presence of oxygen, as with the other materials is probably due to side reactions groups, formed as consequence of both the implementation of FDA as catalyst and the presence of atmospheric oxygen inside the reaction flask. The presence of chlorine alone without the simultaneous presence of iron may indicates that side reactions groups are responsible for detection of chlorine.

3.2.2 Textural properties of HCP materials

The textural properties of HCPs were assessed via N₂ physisorption analysis performed at -196 °C. All HCP samples were degassed at 150 °C for 3 hours to remove adsorbed species, except DIXYT01 which was treated at 90 °C for 6 hours (see section 3.2.5 for the thermogravimetric analysis). The BET method was used for the evaluation of the surface area in the range of 0.05 – 0.3 P/P₀ while the NLDFT

method was used for the pore size distribution for all materials discussed this section. It needs to be kept in mind that calculated Specific Surface Areas are to be treated as “apparent” surface areas, when concerning hierarchical materials possessing a significant fraction of micropores. This is due to the difficulty in separating the process of mono/multi-layer adsorption and the filling of micropores^{[1],[2]}.

In Figure 6, N₂ physisorption isotherms and pore size distributions of mPAF materials are reported, while the main textural properties are reported in Table 6.



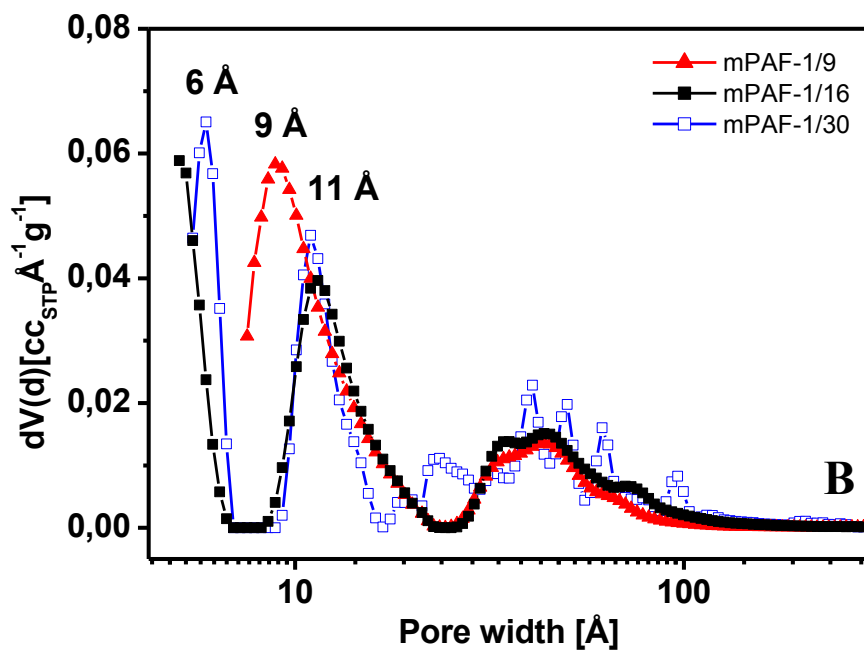


Figure 6. N₂ physisorption isotherms at -196 °C (A) and pore size distribution (B) of mPAF-1/9 ▲, mPAF-1/16 ■ and mPAF-1/30 □.

Table 6. Textural properties of mPAF materials, assessed via N₂ physisorption analysis performed at -196 °C.

Sample	SSA _{BET} [m ² /g]	V _{Tot} [cc/g]	V _{micro} [cc/g]			V _{meso} [cc/g]
			Total	<7Å	7<Å<20	
mPAF-1/9	1236	0.78	0.33	--	0.33	0.45
mPAF-1/16	1289	0.96	0.30	0.09	0.21	0.66
mPAF-1/30	1318	1.06	0.23	0.07	0.16	0.83

As it can be seen from the data reported in Figure 6 mPAFs' isotherms can be classified as type IV with H₂ hysteresis loops indicating the presence of both micro and mesopores^{1,3}. It is worth noting that hysteresis loops for all three materials extend up to very low (0.01) relative pressures, which is a possible indication of the presence of swelling effects of the polymeric frameworks². The superposition of the adsorption and desorption branches below 0.01 P/P₀ is indication of the presence of an interconnected pore network, which allows the complete desorption of N₂ up to the equilibrium values, on the time scale of the measurements⁸. mPAF materials are characterized by high surface areas and high pore volumes (Table 6). Higher amounts of cross-linker results in slightly higher surface areas, ranging from 1236 m²/g for mPAF-1/9 to 1289 m²/g for mPAF-1/16 to 1318 for mPAF-1/30.

The total pore volume follows the same trend, because of increasing fraction of mesopores when a higher quantity of cross-linker is used (0.45 cc/g for mPAF-1/9 to 0.83 cc/g for mPAF1/30). However, the volume associated with micropores shows the opposite trend, decreasing from 0.33 cc/g for mPAF-1/9 to 0.23 cc/g for mPAF-1/30, when higher content of FDA is employed in the synthetic procedure. This can be due to a higher number of side reactions groups which tend to have an occluding effect^{3,8}.

In Figure 7 N₂ physisorption isotherms and pore size distributions of ABT materials are reported, while the main textural properties are reported in Table 7.

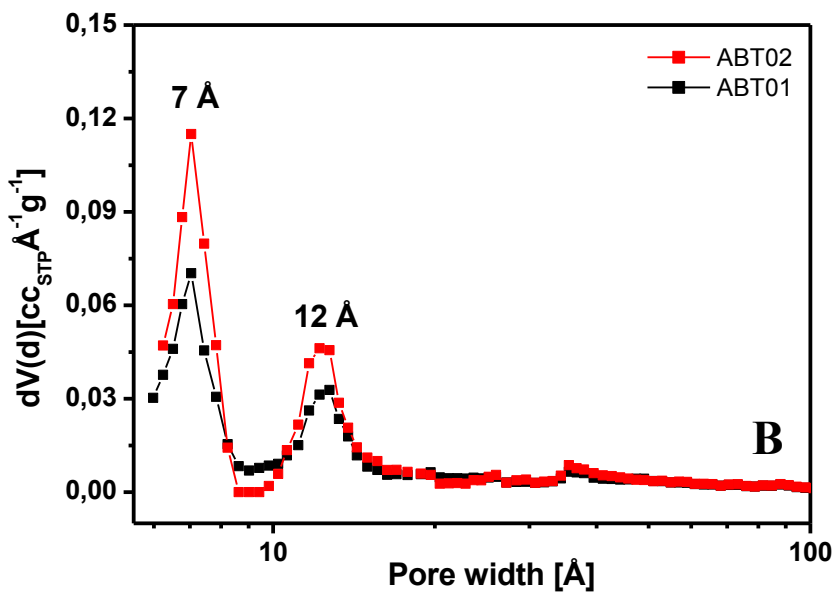
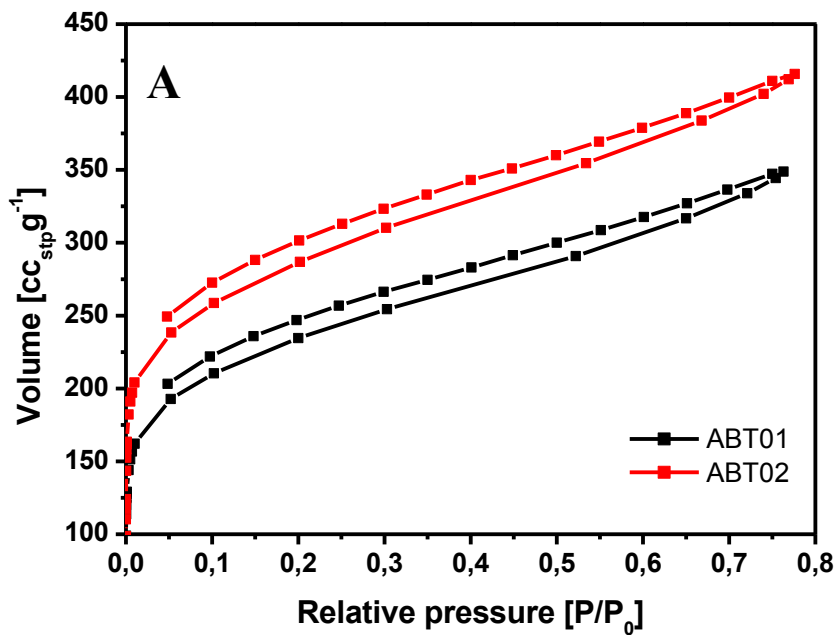


Figure 7. N₂ physisorption isotherms at -196 °C (A) and pore size distribution (B) of ABT01 and ABT02.

Table 7. Textural properties of ABT materials, assessed via N₂ physisorption analysis performed at -196 °C.

Sample	SSA _{BET} [m ² /g]	V _{Tot} [cc/g]	V _{micro} [cc/g]			V _{meso} [cc/g]
			Total	<7Å	7<Å<20	20< Å<100
ABT01	823	0.52	0.28	0.08	0.20	0.24
ABT02	990	0.61	0.35	0.10	0.25	0.26

As it can be seen in Figure 7, ABT isotherms (with upper pressure of only 0.76 - 0.77) do not show a horizontal plateau after the initial filling of the micropores, therefore a clear classification of the isotherms cannot be made. In particular, a distinction between type I and II is not possible. A fair amount of gas (>200 cm³/g) is adsorbed at low relative pressures (up to 0.1 P/P₀), indicating permanent microporosity for both materials. Towards higher values of P/P₀ it is observed a gradual increase in the amount of adsorbed nitrogen indicating the filling of mesopores in the range between 0.45-0.8 P/P₀, which could be interpreted as loose packing induced by inter-particulate voids in the samples¹. Open hysteresis loops for both materials are observed for the whole desorption branch, which is consistent with swelling effects of the polymeric network, due to gas sorption². The non-reversible desorption at low relative pressures indicates that N₂ could be trapped in pockets or free volume elements with a size comparable to the one of the N₂ molecule, and/or that the swelling of ABT is locking some of those pockets or free volume elements on the time scale of the experiments. From the data reported in Table 7 it can be seen that ABT02 possess higher surface area with respect to ABT01, namely 990 m²/g versus 823 m²/g; in addition, pore volume values associated with both micro and mesoporosities are slightly higher in ABT02, which is probably a solvent – induced

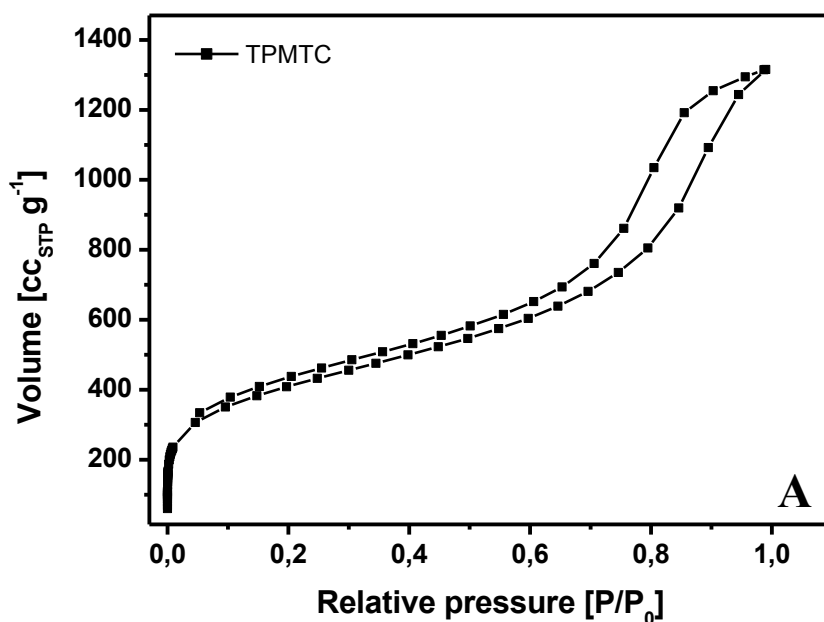
effect since dichloroethane is known to be a particularly suited solvent for the development of high porosity degree in hyper cross-linked polymers⁹.

If a comparison is made between mPAF and ABT materials, it is seen that the employment of a different cross-linker (FDA for mPAF vs 1,3,5-tris(bromomethyl)benzene) visibly affects the resulting textural properties. From the shape of the N₂ physisorption isotherms, especially the hysteresis loops, it is seen that for ABT materials the overall material is composed of plate-like particles which indicate that even in the presence of a three-dimensional monomer, the cross-linker is capable of inducing a two-dimensional effect on the final polymeric network. This effect was not observed for mPAF, where the linker is an entirely sp³ hybridized chemical bridge, meaning a -CH₂- group.

In Figure 8 N₂ physisorption isotherms and pore size distributions of TPMTC are reported, while the main textural properties are reported in Table 8.

The physisorption isotherm of TPMTC displays characteristics of both type I and IV_a^{1,2} namely adsorption in the low relative pressure range associated with the presence of micropores and a hysteresis loop associated with the presence of mesopores, with a final saturation plateau. The fact that both adsorption and desorption branches display the same steepness can be an indication of capillary condensation in open pores where desorption does not occur via nucleation, but via a receding meniscus, meaning equilibrium exists in the vapor – liquid transition¹. Usually, cylindrical pores are responsible for these features¹, but it should be stressed that HCPs are disordered materials, therefore “cylindrical-like” shape should be used as a more correct term. The steepness of the adsorption-desorption branches in the hysteresis loop can also give information about the connectivity of the porous network and information about the accessibility of the mesopores can be obtained¹. For TPMTC, parallel adsorption – desorption branches of the hysteresis loop are seen, which is a possible indication of freely accessible mesopores¹. Superposition

of the adsorption and desorption branches below 0.01 P/P_0 is seen which suggests the presence of an interconnected pore network^{1,2}. Swelling effects are also present, as evidenced by the open hysteresis loop up to low relative pressures². For TPMTC the calculated BET SSA is 1455 m^2/g , which is higher with respect to the previously characterized materials where tetraphenyl methane was used as monomer. A significant volume of adsorbed N_2 is observed in the micropores range of approximately 240 cc/g indicating the presence of a good fraction of micropores, as also evidenced by the pore size distribution (Fig. X (B)). The pore size distribution shows the presence of several pore families, specifically at 7, 14, 17, 30, 55, 75 and 105 Å, additional evidence of the bimodal nature of TPMTC. The total pore volume is assessed at 1.92 cc/g , with 1.53 cc/g being due to mesopores.



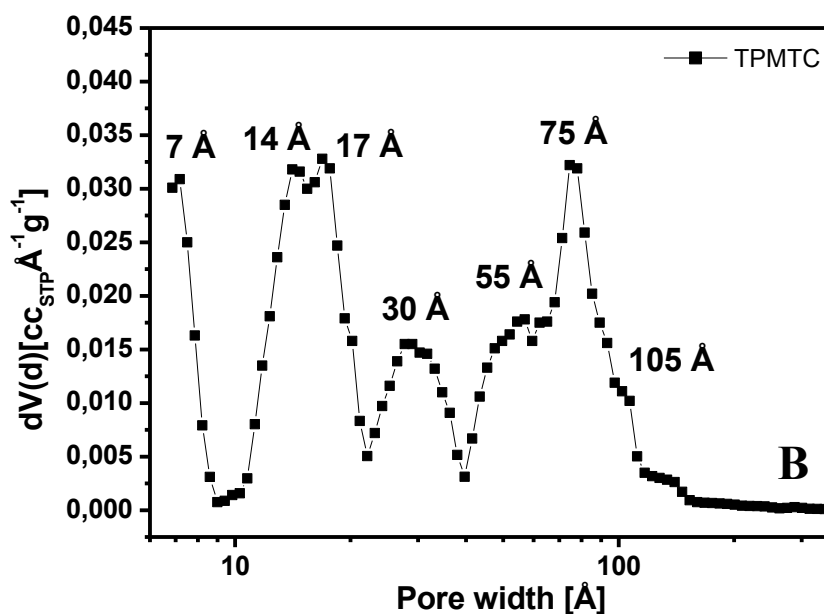


Figure 8. N₂ physisorption isotherms at -196 °C (A) and pore size distribution (B) of TPMTc —■—.

Table 8. Textural properties of TPMTc, assessed via N₂ physisorption analysis performed at -196 °C.

Sample	SSA _{BET} [m ² /g]	V _{Tot} [cc/g]	V _{micro} [cc/g]			V _{meso} [cc/g]
			Total	<7Å	7<Å<20	20< Å<358
TPMTc	1455	1.92	0.39	0.07	0.32	1.53

In Figure 9 N₂ physisorption isotherms and pore size distributions of DIXYT materials are reported, while the main textural properties are reported in Table 9.

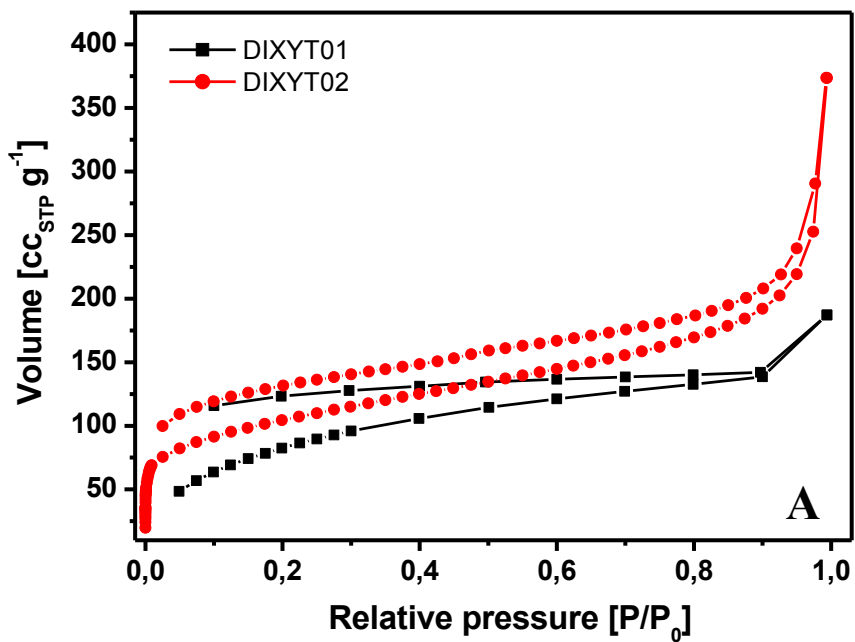
The N₂ physisorption isotherm associated with DIXYT01 had to be recorded with a lower number of points and from a starting relative pressure of 10⁻⁴ P/P₀ to exclude

ultra and micropores probing. This was done to avoid difficulties encountered during sample analysis specifically extremely long analysis times in the micropores range and consequently failure in recording equilibrated physisorption isotherms. A possible explanation could be the presence of a significant fraction of micro and/or ultra-microporosity. N₂ physisorption is known to be somewhat unsatisfactory for assessing pore size distribution of pores with dimension <1 nm^{1,10,11}; the presence of a quadrupole moment in the N₂ molecule can cause interactions of the adsorbate with the adsorbent's surface, thus creating an orienting effect which can alter the micropores filling pressure¹. By employing N₂ as an adsorbate for micropore size evaluation, physisorption can start at very low relative pressures where the rate of diffusion is extremely low, possibly leading to equilibrium problems¹.

N₂ physisorption isotherm of the material DIXYT02, cannot be easily classified. It is interesting to note that the hysteresis loop remains visibly open for the entirety of the desorption process. This can be due to marked swelling effects of the polymeric framework². The formation of hysteresis loops is probably due to the same effects at play in the ABT materials: pockets or free volume elements with a size comparable to the N₂ molecule, and/or locking of N₂ on the time scale of the experiments. The BET SSA for DIXYT02 is assessed at 367 m²/g while the total pore volume is 0.41 cc/g with 0.17 cc/g being due to micropores.

The physisorption isotherm associated with DIXYT01, even if it is not a complete set of data, can still provide information about the textural properties of the corresponding material. The hysteresis loop remains open for the entire desorption process. The material seems to contain a network structure of micropores with narrow constrictions leading to larger cavities, and where the penetrant may cause the material to swell. The overall quantity of adsorbed N₂ is lower for DIXYT01 with respect to DIXYT02 as seen by inspection of the physisorption isotherm. The calculated BET SSA is found to be 315 m²/g, which is lower with respect to DIXYT02; however, even though the total pore volume and the volume associated

with mesopores is much lower with respect to DIXYT02, the micropore volume is found to be 0.19 cc/g versus 0.17 cc/g found for DIXYT02.



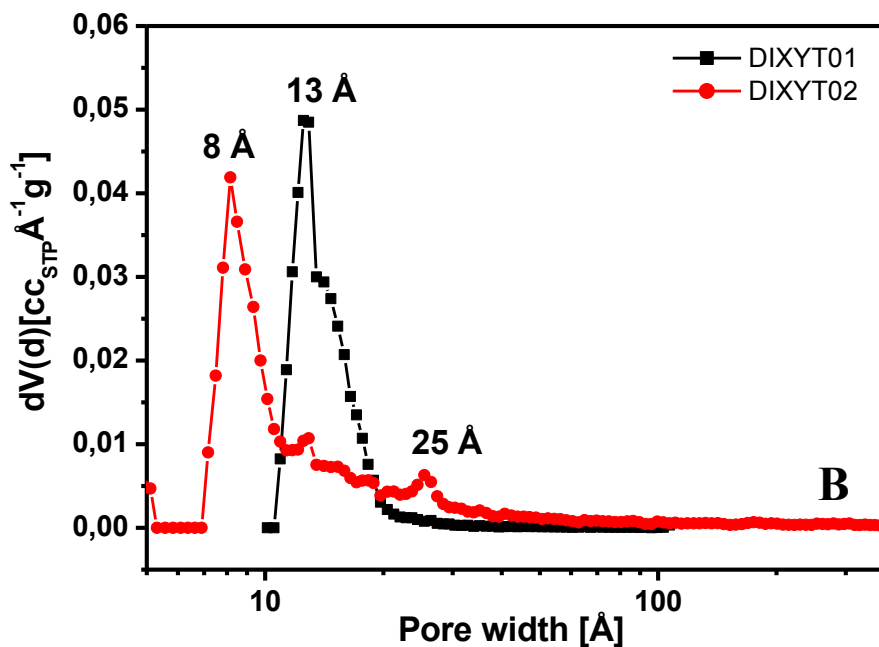


Figure 9. N₂ physisorption isotherms at -196 °C (A) and pore size distribution (B) of DIXYT01 —■— and DIXYT02 —●—.

Table 9. Textural properties of DIXYT materials, assessed via N₂ physisorption analysis performed at -196 °C.

Sample	SSA _{BET} [m ² /g]	V _{Tot} [cc/g]	V _{micro} [cc/g]			V _{meso} [cc/g] 20< Å<377
			Total	<7Å	7<Å<20	
DIXYT01	315	0.21	0.19	---	0.19	0.02
DIXYT02	367	0.41	0.17	0.02	0.15	0.24

In Figure 10 N₂ physisorption isotherms and pore size distributions of PS-1.3 are reported, while the main textural properties are reported in Table 10.

The N₂ physisorption isotherm of PS-1.3 closely resembles the physisorption isotherms already found for mPAF materials. It is to be kept in mind that both PS-1.3 and mPAF materials were obtained via a modified Friedel – Crafts reaction employing FDA as cross-linker and FeCl₃ as catalyst. PS-1.3 isotherm can be classified as type IV with H₂ hysteresis loop^{1,3}. Superposition of the adsorption and desorption branch is seen below 0.01 P/P₀ which indicates the presence of an interconnected pore network¹. A rapid increase in the adsorption branch below 0.1 P/P₀ is indicative of micropore filling; in particular a considerable amount of N₂, almost up to 200 cc/g, is retained by the material implying the presence of a good fraction of micropores as also evidenced by the pore size distribution (Figure 10, B). The hierarchical nature of PS-1.3 is evident from the pore size distribution, namely a family of micropores is found around 11 Å and a broad distribution of mesopores is found between 30 and 100 Å with a peak around 44 Å. Approximately 1/3 of the pore volume is associated with micropores, naming 0.22 cc/g of the total 0.65 cc/g, while the SSA_{BET} is found to be 845 m²/g. It is worth noting that a porous polymer displaying good textural properties, specifically moderately high surface area and pore volumes, is obtained from a waste material through a low - cost approach.

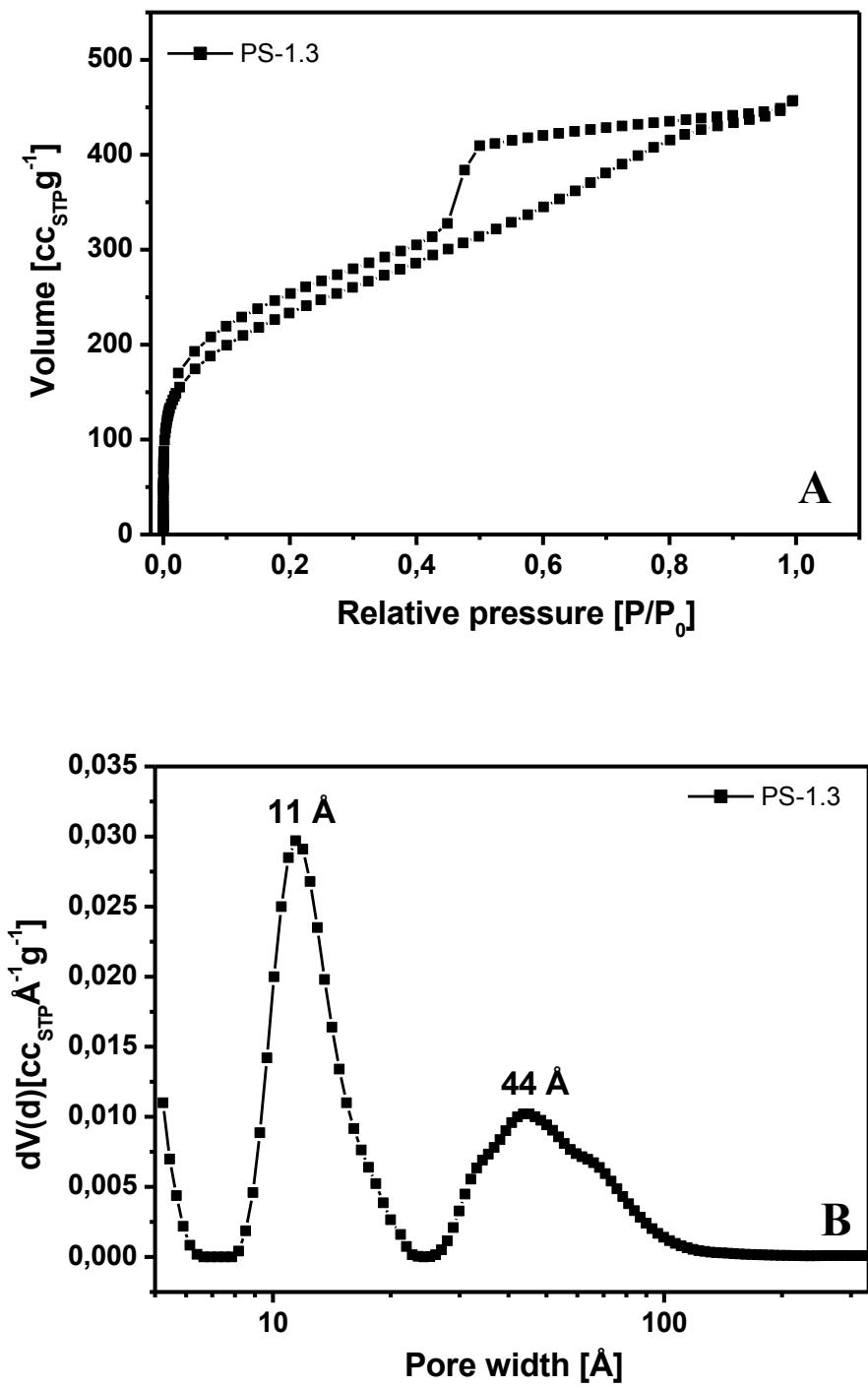


Figure 10. N₂ physisorption isotherms at -196 °C (A) and pore size distribution (B) of PS-1.3 —■—.

Table 10. Textural properties of PS-1.3, assessed via N₂ physisorption analysis performed at -196 °C.

Sample	SSA _{BET} [m ² /g]	V _{Tot} [cc/g]	V _{micro} [cc/g]			V _{meso} [cc/g]
			Total	<7Å	7<Å<20	
PS-1.3	845	0.65	0.22	0.03	0.19	0.43

In Figure 11 a comparison between the N₂ physisorption isotherms of all types of materials is reported. For each class of HCP only one material has been chosen.

All materials present open hysteresis loops (or up to 0.01 P/P₀) which indicates that all synthesized hyper cross-linked polymers seem to experience swelling effects². When the hysteresis loops remain open, up to low relative pressure, it is an indication of the expansion of the polymeric network already happening during the filling of micropores. This means that micropores are not filled completely when the material starts to expand. The ability of this type of adsorbents to expand their framework is particularly useful in the context of storage applications and pollutants removal⁸. Other important aspects characterizing porous solids, in addition to surface area and pore volume, are accessibility and connectivity of the pores. To facilitate mass transfer within the porous framework, there need to be interplay between the internal volumes of the material. In this regard, mPAF materials and TPMTTC seem to possess more accessible and interconnected pore volumes with respect to the other materials. TPMTTC exhibits a symmetric hysteresis loop which is indication of cylindrical – like pores giving rise to an equilibrated desorption process while mPAF materials possess high surface areas and pore volumes which seem to be well interconnected as evidenced by the superposition of the adsorption and desorption branches at low relative pressures.

Between mPAF materials and TPMTC it is seen that the employment of a α,α' -dichloro-p-xylene as a cross-linker in addition to a more para – orienting catalyst, TiCl_4 , results in a material possessing higher surface areas ($1318 \text{ m}^2/\text{g}$ of mPAF-1/30 vs $1455 \text{ m}^2/\text{g}$ of TPMTC) and almost twice the total pore volume (1.03 cc/g of mPAF-1/30 vs 1.92 cc/g of TPMTC). α,α' -dichloro-p-xylene is a bigger molecule with respect to a $-\text{CH}_2-$ bridge encountered in the case of mPAF and PS materials, hence a more open porous structure is expected¹².

It is interesting to compare ABT materials and TPMTC, both being synthesized using chemically similar cross-linkers, the main differences being the number of possible carbocationic sites, three for 1,3,5-tris(bromomethyl)benzene and two for α,α' -dichloro-p-xylene and the cross-linkers leaving groups, bromine for ABT materials and chlorine for TPMTC. ABT materials possess significantly lower surface areas and pore volumes with respect to TPMTC. In TPMTC the p-xylylene bridges allow a fair conformational freedom to the crosslinked structure, in addition TiCl_4 selectively directs the alkylation of tetraphenyl methane on the para positions, keeping the alkylating groups more distant from each other, on average, and easing the swelling of the HCP. In ABT materials instead the alkylation in meta position reduces the distance with the alkylating group, and above all the latter can alkylate three different aromatic rings, so that a) a stiffer overall crosslinking is obtained, and b) the mobility of the alkylating moiety is limited by three covalent bonds.

By comparing mPAF materials and PS-1.3 it is seen that the shapes of the physisorption isotherms closely resemble each other, the main difference being the amount of cc/g of N_2 adsorbed. A very similar porous architecture is obtained from both monomeric species and linear polymeric chains. It seems that the good solubility of polystyrene in dichloroethane, coupled to the additional waiting time during the synthetic procedure to allow for the complete dissolution of the polymer, compensated for the lower diffusion of linear polymeric chains in the reaction mixture.

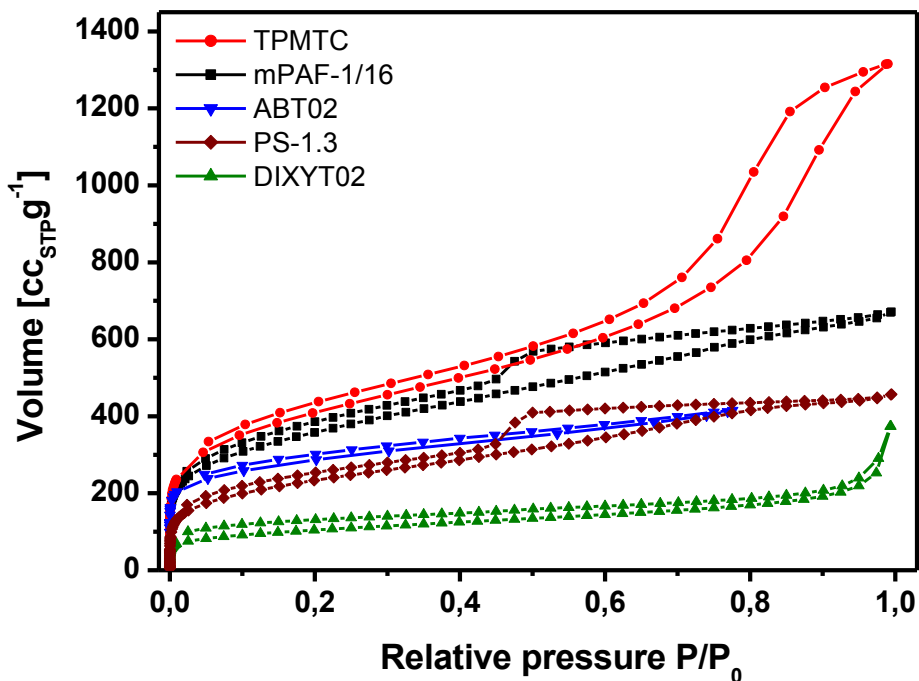


Figure 11. N₂ physisorption isotherms at -196 °C of TPMTc —●—, mPAF-1/16 —■—, ABT02 —▼—, PS-1.3 —◆— and DIXYT02 —▲—.

3.2.3 FT-IR analysis of HCP materials

FT-IR analysis was conducted on all HCPs to gain information about the functional groups and structure of the polymeric framework.

All infrared spectra were recorded under vacuum conditions (10^{-4} mbar) after the samples were thermally treated under vacuum at 150 °C for three hours.

In Figure 12 the IR spectra of mPAF materials are reported.

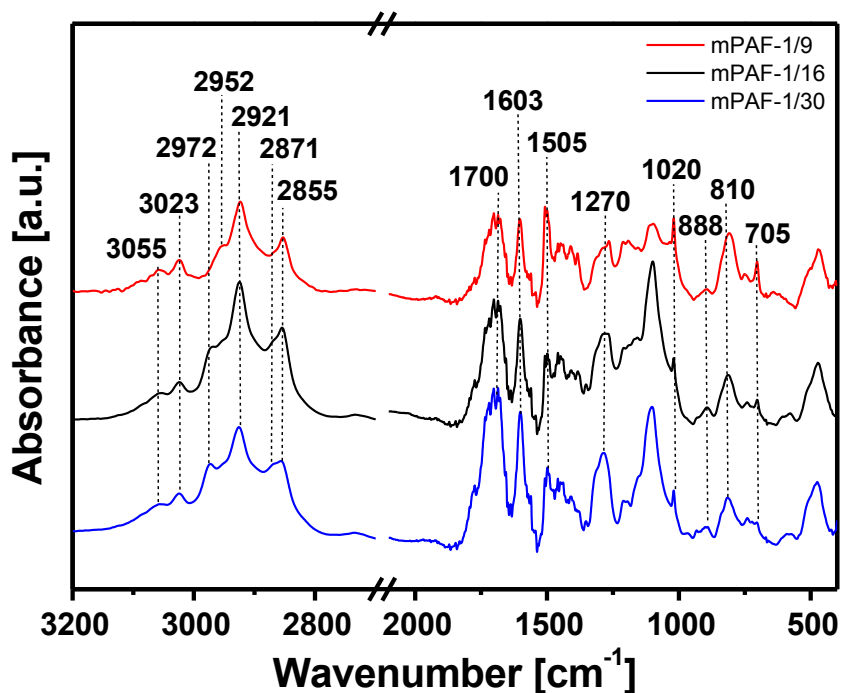


Figure 12. Infrared spectra of mPAF-1/9 —, mPAF-1/16 — and mPAF-1/30 — acquired under vacuum conditions (10^{-4} mbar) and room temperature. Prior to analysis the samples were treated at $150\text{ }^{\circ}\text{C}$ under vacuum for three hours.

The IR spectra of mPAF materials present signals in the ranges $3200 - 2800\text{ cm}^{-1}$ and between 1750 and 400 cm^{-1} .

In the high wavenumbers region, for all three HCPs, signals associated with the stretching of C-H aromatic groups are found at 3055 cm^{-1} and 3023 cm^{-1} respectively due to the asymmetric and symmetric vibrational modes^{13,14}. Between 3000 and 2800 cm^{-1} the signals associated with stretching modes of the aliphatic C-H groups are found^{13,14}. Absorption bands are found at 2972 , 2952 , 2921 , 2871 and 2855 cm^{-1} . The aforementioned signals are respectively due to asymmetric C-H stretching vibrations of the methyl groups probably associated with $-\text{CH}_2\text{CH}_3$ substitution on the aromatic ring, asymmetric C-H stretching vibrations of methyl groups associated

with methylation of the aromatic ring, asymmetric C-H stretching vibrations of $\text{-CH}_2\text{-}$ groups, symmetric stretching vibrations of methyl C-H bonds and finally symmetric stretching vibrations of C-H bonds of $\text{-CH}_2\text{-}$ groups^{3,8,13,14}.

In the low frequency region multiple bands are found and assignments were made for the main absorption bands with position 1700, 1603, 1505, 1270, 1020, 888, 810 and 705 cm^{-1} . Signals found at 1700, 1603, 1505 and 1270 cm^{-1} are associated with asymmetric stretching vibrations of -C=C- groups, meaning vibrations of the aromatic rings^{3,13,14}. The broad band centered at 1700 cm^{-1} is associated with aromatic rings with multiple substitutions and it is found for hyper cross-linked polymers with high degree of interconnectivity within the polymeric framework, specifically in the presence of hindered vibrations of aromatic carbon-carbon bonds¹⁴. As it can be seen in Figure 12, by increasing the concentration of FDA in the synthetic procedure, meaning going from mPAF-1/9 to mPAF-1/30, the relative intensity between the signals associated with stretching of the aromatic C-H groups and the band found at 1700 cm^{-1} , increases in favor of the latter. The signals found between 1603 and 1400 cm^{-1} are associated with ortho, meta and para substitution of the aromatic ring^{13,14}. The sharp peak at 1505 cm^{-1} is indication of ortho and para substitution of the aromatic rings, while the signal at 1603 cm^{-1} is indication of meta substitution^{13,14}. For mPAF-1/9 the band at 1505 cm^{-1} is more pronounced with respect to the other materials, while for mPAF-1/16 and mPAF-1/30 the relative intensity between the bands at 1603 and 1505 cm^{-1} increases in favor of the first. From these observations it can be deduce that the Friedel – Crafts alkylation is not a regioselective reaction, as it is expected. The signal centered at 1270 cm^{-1} is assigned to skeletal -C-C- bond vibrations¹⁴.

In the region between 1020 and 700 cm^{-1} bending modes associated with aromatic C-H groups are found^{13,14}. It is interesting to note a decrease of the signal found at 705 cm^{-1} while increasing the cross-linking degree of the polymeric network. In the range between 900 and 735 cm^{-1} fingerprints associated with the presence of 1,2 /

1,3 / 1,4 substitution on the aromatic rings are found¹⁴. For 1,2 (ortho) substitution absorption bands are typically found in the range between 770 and 735 cm⁻¹, for 1,3 (meta) substitution signals are found in the ranges 810 – 750 and 900 – 860 cm⁻¹ and finally 1,4 (para) substitution is characterized by the presence of signals in the range 860 – 800 cm⁻¹^{13,14}. For mPAF materials it is observed the presence of an intense band centered at 810 cm⁻¹ which falls nicely in the region associated with 1,4 phenyl substitution. However, by increasing the concentration of FDA in the synthetic procedure it is seen an increase in the intensity of the band centered at 888 cm⁻¹, already present for mPAF-1/9. This band falls in the range associated with meta substitution, again confirming the presence of multiple substitution on the aromatic rings as expected for hyper cross-linked polymers.

In Table 11 the assignments of the main IR absorption bands for mPAF materials are reported.

Table 11. Assignments of the main IR absorption bands of mPAF materials.

Bands position [cm⁻¹]	Assignments^{3,8,13,14,15}
3055	v _{as} Aromatic C-H
3033	v _s Aromatic C-H
2972	v _{as} Aliphatic C-H (-CH ₂ CH ₃)
2952	v _{as} Aliphatic C-H (-CH ₃)
2921	v _{as} Aliphatic C-H (-CH ₂ -)
2871	v _s Aliphatic C-H (-CH ₃)
2855	v _s Aliphatic C-H (-CH ₂ -)
1780 – 1200 and 900 - 700	Collective stretching vibrations of poly-substituted benzene rings

In Figure 13 the IR spectra of ABT materials are reported.

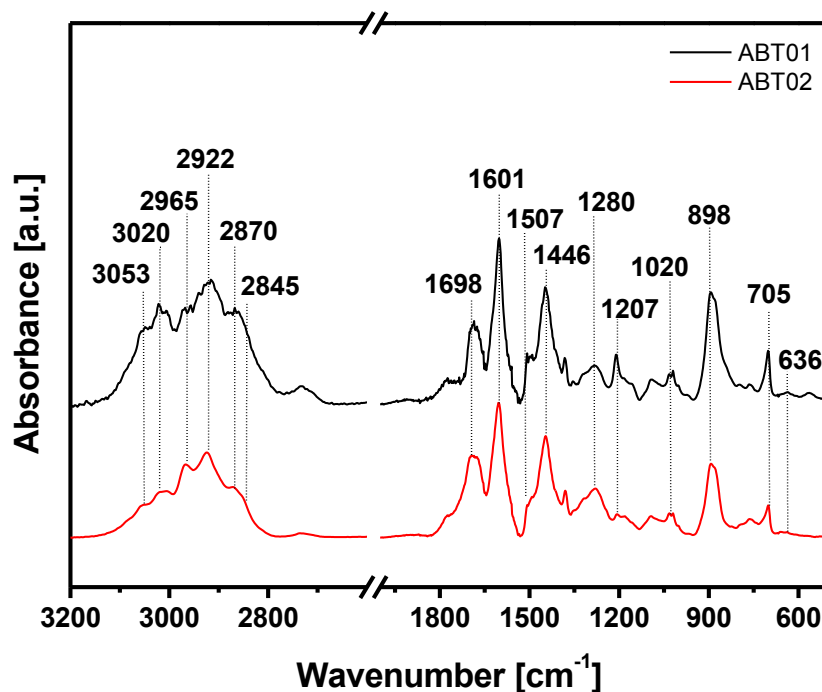


Figure 13. Infrared spectra of ABT01 — and ABT02 — acquired under vacuum conditions (10^{-4} mbar) and room temperature. Prior to analysis the samples were treated at 150 °C under vacuum for three hours.

The IR spectra of ABT materials present signals in the ranges 3200 – 2800 cm⁻¹ and between 1750 and 400 cm⁻¹. In the high wavenumbers region, broad bands centered at 3053, 3020, 2965, 2922 and 2870 cm⁻¹ are found. The signal at 3053 and 3020 cm⁻¹ are respectively assigned to the asymmetric and symmetric aromatic C-H stretching vibrational modes, the band at 2965 cm⁻¹ is assigned to the aliphatic C-H asymmetric stretching modes due to methyl groups, at 2922 cm⁻¹ the signal is due to asymmetric stretching modes of the C-H bonds of -CH₂- groups^{3,13,14}. The corresponding aliphatic C-H symmetric stretching vibrations are found at 2870 cm⁻¹ for the methyl

group and at 2845 cm^{-1} for the methylene group^{8,12,13}. Signals associated with aromatic C-H stretching vibrations are lower in intensity, relative to the aliphatic signals, for ABT02. This can be a sign of a more cross-linked polymeric network with respect to ABT01. In the low frequency region, a series of signals is found, and assignments have been made for the main absorption bands, namely the bands at 1698 , 1601 , 1507 , 1446 , 1270 , 1020 , 898 and 705 cm^{-1} . Between 1700 and approximately 1200 cm^{-1} , signals associated with stretching modes of -C=C- bonds are found^{13,14}. As was already evidenced for mPAF materials, the band at 1698 cm^{-1} is associated with hindered vibrations of the aromatic rings, probably due to extensive cross-linking degree of the polymeric framework¹⁴. The relative intensity of this signal slightly increases for ABT02 with respect to ABT01. This can be linked to higher interconnectivity of the polymeric network of ABT02 probably a consequence of the higher temperature adopted during the synthetic procedure which accelerated the cross-linking reaction. Additional evidence of the higher cross-linking degree for ABT02 is also the lower intensity of the signal at 1207 cm^{-1} assigned to skeletal C-C bonds vibrations¹⁴. The absence of a sharp peak around 1500 cm^{-1} and the presence of the intense signal at 1601 cm^{-1} are indication of possible predominant meta substitution of the aromatic rings, which is expected when AlBr_3 is used in the synthetic procedure^{13,14}.

Between 1225 and 950 cm^{-1} in plane bending modes of aromatic C-H groups are found^{13,14}. In the region between 1020 and 700 cm^{-1} out of plane bending modes associated with aromatic C-H groups are found^{13,14}. A decrease of the signal found at 705 cm^{-1} is observed for ABT02 with respect to ABT01, which can be linked to higher cross-linking degree of the polymeric network. The presence of the intense signal centered at 898 cm^{-1} may be interpreted as a sign of 1,3 substitution of the aromatic ring^{13,14}.

Between 700 and 600 cm^{-1} the stretching vibrations of the C-Br bond are found. For ABT01 a weak signal at 636 cm^{-1} is found, which indicates that a small amount of

bromine is directly linked to the polymeric network, probably as $-\text{CH}_2\text{Br}$ groups, since the aromatic C-Br bond stretching vibrations are found around 680 cm^{-1} ^{13,14}.

In Table 12 the assignments of the main IR absorption bands for ABT materials are reported.

Table 12. Assignments of the main IR absorption bands of ABT materials.

Bands position [cm^{-1}]	Assignments ^{3,8,13,14,15}
3053	ν_{as} Aromatic C-H
3020	ν_{s} Aromatic C-H
2965	ν_{as} Aliphatic C-H ($-\text{CH}_3$)
2922	ν_{as} Aliphatic C-H ($-\text{CH}_2-$)
2870	ν_{s} Aliphatic C-H ($-\text{CH}_3$)
2845	ν_{s} Aliphatic C-H ($-\text{CH}_2-$)
1280	ν skeletal -C-C-
1700 – 1210 and 900 - 700	Collective stretching vibrations of poly-substituted benzene rings
636	ν aliphatic C-Br ($-\text{CH}_2\text{Br}$)

In Figure 14 the IR spectrum of TPMTc is reported.

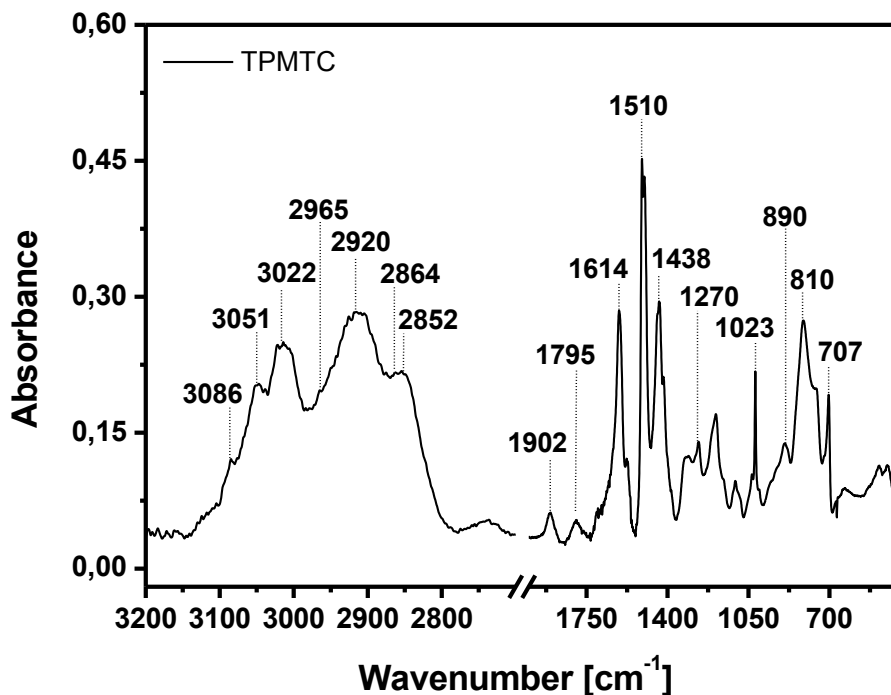


Figure 14. Infrared spectra of TPMTc ——— acquired under vacuum conditions (10^{-4} mbar) and room temperature. Prior to analysis the sample was treated at $150\text{ }^{\circ}\text{C}$ under vacuum for three hours.

The IR spectrum of TPMTc presents signals between 3150 and 2800 cm^{-1} and between 1910 and 400 cm^{-1} . In the high frequency region, signals are found at 3086 cm^{-1} followed by broad bands centered at 3051 , 3022 , 2965 , 2920 , 2864 and 2852 cm^{-1} . The signals at 3086 and 3051 cm^{-1} are assigned to the aromatic asymmetric C-H stretching vibrations while the signal at 3022 cm^{-1} is assigned to the aromatic C-H symmetric stretching vibrations^{13,14}. Between 3000 and 2800 cm^{-1} the aliphatic C-H stretching vibrations are found. The more intense bands are at 2920 cm^{-1} , which is due to the asymmetric C-H stretching vibrations of $-\text{CH}_2-$ groups^{13,14}, while at 2820 cm^{-1} the corresponding symmetric stretching vibrations are found^{13,14}. Signals associated with asymmetric and symmetric stretching vibrations of methyl C-H bonds are respectively found at 2965 and 2864 cm^{-1} ^{8,13,14}, however the weak relative

intensity of these bands suggest a low content of this functional group within the polymeric framework.

In the low frequency region assignments have been made for the main absorption bands which are found at 1902, 1795, 1614, 1510, 1438, 1023, 890, 810 and 707 cm^{-1} . The weak bands centered at 1902 and 1795 cm^{-1} are assigned to combination and overtones of the out-of-plane hydrogen deformations of C-H aromatic bonds^{13,14}. The signals at 1614 and 1510 cm^{-1} , as was evidenced for the previously discussed materials, can be used to gain information about the substitution of aromatic rings¹⁵. For TPMTC, the higher relative intensity of the signal found at 1510 cm^{-1} with respect to the ones centered at 1614 and 1438 cm^{-1} is a possible indication of predominant para substitution^{13,14}. However, the occurrence of absorption bands at 1614 and 1438 cm^{-1} suggests that ortho and meta substitution are still present within the polymeric framework, as was expected given the lack of regioselectivity of the Friedel – Crafts alkylation. Between 1225 and 950 cm^{-1} , signals due to in plane bending modes of the aromatic C-H groups are found^{13,14}. The signal centered at 1023 cm^{-1} is assigned to the in plane bending of the C-H aromatic bond while the out of plane bending are found at 810 and 707 cm^{-1} ^{13,14}. Additional evidence regarding the presence of 1,4 substitution of the aromatic ring can be obtain by inspection of the region 860 – 800 cm^{-1} . The band centered at 810 cm^{-1} may be interpreted as a sign of para substitution while the presence of the signal at 890 cm^{-1} may be due to meta substitution of the aromatic ring^{13,14}.

Table 13. Assignments of the main IR absorption bands of TPMTc.

Bands position [cm⁻¹]	Assignments^{3,8,13,14,15}
3086	v _{as} Aromatic C-H
3051	v _{as} Aromatic C-H
3022	v _s Aromatic C-H
2965	v _{as} Aliphatic C-H (-CH ₃)
2920	v _{as} Aliphatic C-H (-CH ₂ -)
2864	v _s Aliphatic C-H (-CH ₃)
2852	v _s Aliphatic C-H (-CH ₂ -)
1270	v skeletal -C-C-
1700 - 1200	Collective stretching vibrations of poly-substituted benzene rings
900 - 700	Collective bending vibrations of poly-substituted benzene rings
636	v aliphatic C-Br -CH _{2n} Br)

In Figure 15 the IR spectra of DIXYT materials are reported.

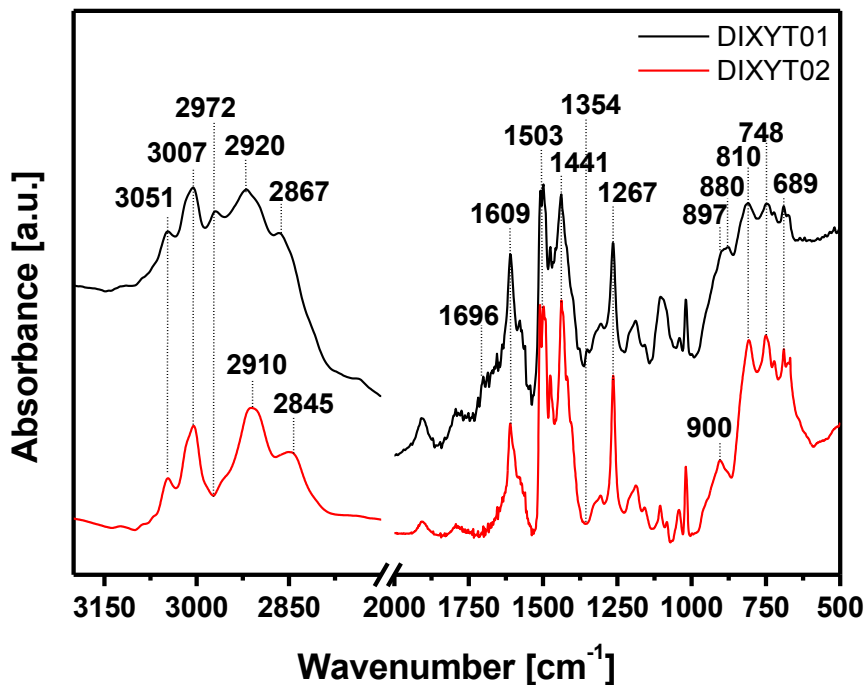


Figure 15. Infrared spectra of DIXYT01 — and DIXYT02 — acquired under vacuum conditions (10^{-4} mbar) and room temperature. Prior to analysis the sample of DIXYT01 was treated at $90\text{ }^{\circ}\text{C}$ under vacuum for four hours while the sample of DIXYT02 was treated at $150\text{ }^{\circ}\text{C}$ under vacuum for three hours.

The IR spectrum of DIXYT01 materials is characterized by absorption bands between 3100 and 2800 cm^{-1} , specifically centered at 3051 , 3007 , 2972 , 2920 , 2867 and 2845 cm^{-1} . The bands at 3051 and 3007 cm^{-1} are respectively assigned to the asymmetric and symmetric stretching vibrations of aromatic C-H groups^{13,14}. The signals centered at 2972 and 2867 cm^{-1} are respectively due to the aliphatic asymmetric and symmetric C-H stretching vibrations associated with CH_3 groups probably associated with $-\text{CH}_2-\text{CH}_3$ groups, while asymmetric and symmetric C-H stretching vibrations associated with $-\text{CH}_2-$ groups are respectively assigned to the bands centered at 2920 and 2845 cm^{-1} ^{8,13,14}.

In the region between 2000 and 500 cm^{-1} several absorption bands are observed, and assignments have been made for the main signals, namely the ones centered at 1696, 1609, 1503, 1441, 1267, 897, 880, 810, 748 and 689 cm^{-1} . The band centered at 1696 cm^{-1} is associated with hindered vibrations of substituted benzene rings¹⁵. The presence of intense signals centered at 1609, 1503 and 1441 cm^{-1} are indication of possible multiple substitution on aromatic rings. The signal found at 1267 cm^{-1} is assigned to skeletal C-C vibrations¹⁴. The weak signal found for DIXYT01 at 1354 cm^{-1} can be assigned to the stretching of the S=O bond found in the sulfonate group $-\text{SO}_3\text{H}$ ^{13,14}. The presence of this functionality suggests that a fraction of the C-S-C bonds formed by the bridging sulfur atom with the two aromatic rings in the monomer unit are broken during the synthetic procedure. The presence of signals centered at 897, 880, 810 and 748 cm^{-1} is an additional evidence of the occurrence within the polymeric framework of 1,2 (ortho), 1,3 (meta) and 1,4 (para) substitution on aromatic rings^{13,14}. The signal at 689 cm^{-1} is tentatively assigned to the stretching of the C-S bond^{13,14}, however it is worth mentioning that C-S bonds are highly polarizable, therefore they are more active in the Raman spectrum than in the infrared spectrum¹³. For this reason, the assignment of the band found at 689 cm^{-1} should be treated with caution.

The IR spectrum of DIXYT02 shows absorption bands in the high frequency region, specifically at 3051, 3007, 2910 and 2845 cm^{-1} . The signals found at 3051 and 3007 cm^{-1} are respectively assigned to asymmetric and symmetric stretching vibrations of aromatic C-H bonds while the aliphatic asymmetric and symmetric stretching vibrations of $-\text{CH}_2-$ groups are respectively assigned to the bands centered at 2910 and 2845 cm^{-1} ^{8,13,14}.

In the low frequency region, between 2000 and 500 cm^{-1} several absorption bands are present, and assignments have been made for the main signals, namely the ones centered at 1609, 1503, 1441, 1354, 1267, 900, 810, 748 and 696 cm^{-1} . The signals found at 1609, 1503 and 1441 cm^{-1} are indication of the presence of multiple

substitution on the aromatic rings^{13,14}. The band centered at 1267 cm⁻¹ is assigned to the skeletal C-C vibrations¹³. The presence of the signals at 900, 810 and 748 cm⁻¹ is indication of ortho, meta and para substitution on the aromatic rings^{13,14}.

From the FT-IR investigation of DIXYT materials, differences about the structure of the two polymeric frameworks emerges. For DIXYT01 ethyl groups (and possibly methyl groups) are present as substitution on the aromatic rings. Evidence of more abundant phenyl substitutions and signs of hindered vibrations of aromatic rings suggest that one of the reasons that DIXYT01 shows lower surface area with respect to DIXYT02 is probably a due to pore occlusion effects caused by side reactions groups.

Table 14. Assignments of the main IR absorption bands of DIXYT materials.

Bands position [cm⁻¹]	Assignments ^{3,8,13,14,15}
3051	v _{As} Aromatic C-H
3007	v _S Aromatic C-H
2972	v _{As} Aliphatic C-H (-CH ₃)
2920	v _{As} Aliphatic C-H (-CH ₂ -)
2867	v _S Aliphatic C-H (-CH ₃)
2845	v _S Aliphatic C-H (-CH ₂ -)
1354	v S=O (-SO ₃ H)
1280	v skeletal -C-C-
1700 - 1210	Collective stretching vibrations of poly-substituted benzene rings
900 - 700	Collective bending vibrations of poly-substituted benzene rings
689	v C-S

In Figure 16 the IR spectra of PS-1.3 and the expanse polystyrene chip are reported.

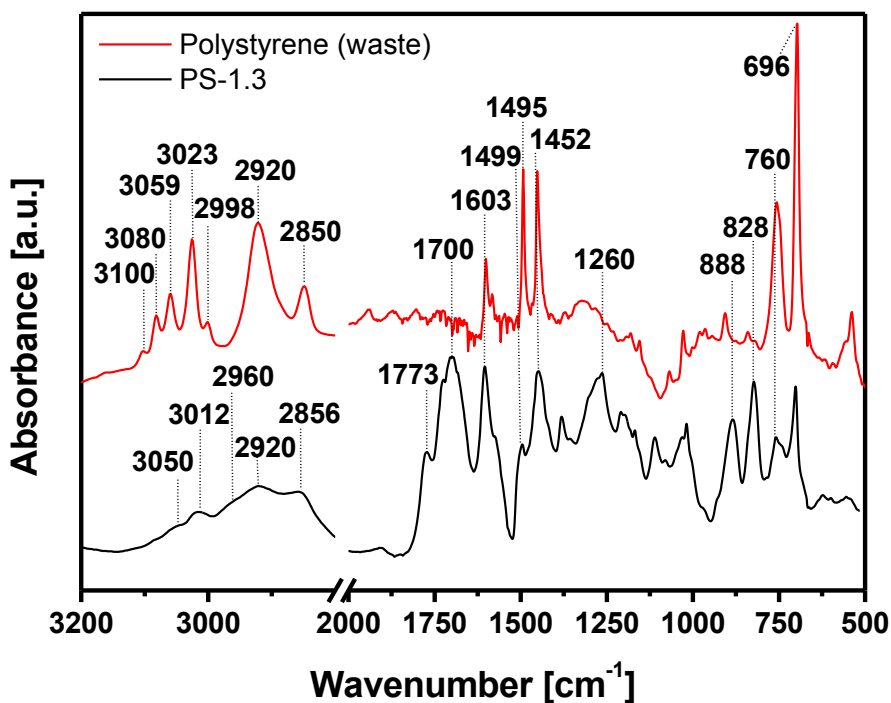


Figure 16. Infrared spectra of polystyrene chip — and PS-1.3 — acquired under vacuum conditions (10^{-4} mbar) and room temperature. Prior to analysis the samples were treated at $150\text{ }^{\circ}\text{C}$ under vacuum for three hours.

The IR spectrum of the polystyrene chip shows the typical signals associated with polystyrene¹⁶. In the high frequency region between 3100 and 3000 cm^{-1} the absorption bands associated with the stretching of aromatic C-H bonds are found^{13,14}. Specifically signals at 3100 , 3080 and 3059 cm^{-1} are associated with asymmetric stretching vibrations of aromatic C-H groups while the signal centered at 3023 cm^{-1} is associated with symmetric stretching vibrations of C-H groups^{13,14}. Between 3000 and 2850 cm^{-1} the aliphatic C-H stretching vibrations are found, which are related with the hydrocarbon backbone^{13,14,15,16}. The signal centered at 3000 cm^{-1} is associated with the asymmetric stretching vibrations of the C-H bond of the tertiary carbon^{13,14}. The band centered at 2920 cm^{-1} is due to the asymmetric stretching vibrations of the $-\text{CH}_2-$ group while at 2850 cm^{-1} the absorption band due to the

corresponding symmetric stretching vibrations are found^{13,14,16}. In the low frequency region assignments have been made for the main absorption bands, namely at 1603, 1495, 1452, 760 and 696 cm^{-1} . The signals centered at 1603, 1452 and 1495 cm^{-1} are due to stretching vibrations of phenyl -C=C- bonds while out of plane aromatic C-H bending modes are associated with the signals found at 760 and 696 cm^{-1} ^{13,14,16}. Between 1225 and 950 cm^{-1} in plane bending modes of aromatic C-H groups are found^{13,14}.

The IR spectrum of the hyper cross-linked polymer derived from the polystyrene chip, PS-1.3, presents several absorption bands in the regions 3100 – 2850 and 1800 – 500 cm^{-1} . In the high frequency region, broad bands are found with peaks centered at 3050, 3012, 2960, 2920 and 2856 cm^{-1} . At 3050 and 3012 cm^{-1} the absorption bands are respectively assigned to asymmetric and symmetric stretching vibrations of aromatic C-H groups^{13,14} while the bands at 2920 and 2856 cm^{-1} are respectively assigned to asymmetric and symmetric stretching vibrations of aliphatic C-H bonds of $\text{-CH}_2\text{-}$ groups^{13,14}. It is also observed the presence of a shoulder approximately centered at 2960 cm^{-1} which falls in the region associated with asymmetric stretching vibrations of C-H bonds associated with methyl groups^{8,13,14}. In the low frequency region assignments have been made for the main absorption bands which are centered at 1773, 1700, 1603, 1499, 1452, 1260, 888, 828, 760 and 696 cm^{-1} . The signals centered at 1773 and 1700 cm^{-1} are assigned to hindered stretching vibrations of the aromatic rings¹⁵ possibly appearing as a consequence of the high interconnectivity of the polymeric chains due to the cross-linking reaction. The signals found at 1603, 1499 and 1452 cm^{-1} are due to stretching vibrations of -C=C- bonds and the presence of these signals is indication of multiple substitutions of the aromatic rings^{13,14}. The band centered at 1260 cm^{-1} is assigned to skeletal -C-C- vibrations¹³. The in - plane bending modes of aromatic C-H groups are found between 1225 and 950 cm^{-1} ^{13,14}. In the region between 900 and 735 cm^{-1} information about the phenyl substitution can be obtained. In particular, the presence of both

signals found at 888 and 828 cm^{-1} is indication of both meta and para substitution which is expected for a Friedel – Crafts cross-linking reaction^{3,15}. The signals found at 760 and 696 cm^{-1} are associated with out of plane bending modes of aromatic C-H bonds^{13,14}. It is observed a decrease in intensity of these two signals when the cross-linking reaction is carried out.

Table 15. Assignments of the main IR absorption bands of waste polystyrene and PS-1.3.

Bands position [cm^{-1}]	Assignments^{3,8,13,14,15}
3100	ν_{As} Aromatic C-H
3080	ν_{As} Aromatic C-H
3059	ν_{As} Aromatic C-H
3050	ν_{As} Aromatic C-H
3023	ν_{S} Aromatic C-H
3012	ν_{S} Aromatic C-H
2998	ν C-H of tertiary carbons
2960	ν_{As} Aliphatic C-H (-CH ₃)
2920	ν_{As} Aliphatic C-H (-CH ₂ -)
2856	ν_{S} Aliphatic C-H (-CH ₂ -)
2850	ν_{S} Aliphatic C-H (-CH ₂ -)
1270	ν skeletal -C-C-
1780 - 1200	Collective stretching vibrations of substituted benzene rings
900 - 700	Collective bending vibrations of poly-substituted benzene rings
696	δ aromatic C-H Out of plane

3.2.4 SS-NMR analysis of HCP materials

SS-NMR spectroscopy was used for the structural characterization of the synthesized HCPs. ^{13}C CPMAS NMR spectra were recorded using a cross-polarization contact time of 10 ms and a MAS rate of 10 kHz.

In Figure 17 ^{13}C CPMAS NMR spectra of mPAF materials are reported and assignments have been made for the main peaks in accordance with previous reports from the literature^{3,8,17,18,19}.

Peaks associated with aromatic carbons are found in the range between 150 and 120 ppm. The peak centered at 144 ppm is assigned to the carbon directly linked to the central quaternary carbon in tetraphenyl methane^{3,8,17,18,19} at 136 ppm the peak is assigned to the methylene substituted carbon while at 128 ppm the aromatic carbons associated with C-H groups are found^{3,8,17}. At 64 ppm the peak is assigned to the central quaternary carbon of the tetraphenyl methane unit^{3,8}. Carbons associated with the methylene bridging groups are found around 35 ppm^{3,8}. The Friedel – Crafts alkylation is known to produce secondary reaction groups as substitution on the aromatic rings^{3,8,18} hence the presence of additional signals. Carbons associated with CH_2OH groups are found at 71 ppm while carbons associated with CH_2Cl groups are found at 43 ppm^{3,8,17,18}. The high amount of FDA in the reaction mixture, in addition with the presence of dichloroethane, can cause the substitution of the aromatic rings by methyl and/or ethyl groups²⁰. Evidence of the presence of these functional groups directly attached to the aromatic rings are the peaks at 17 and 13 ppm which are associated with methyl carbons^{3,8}.

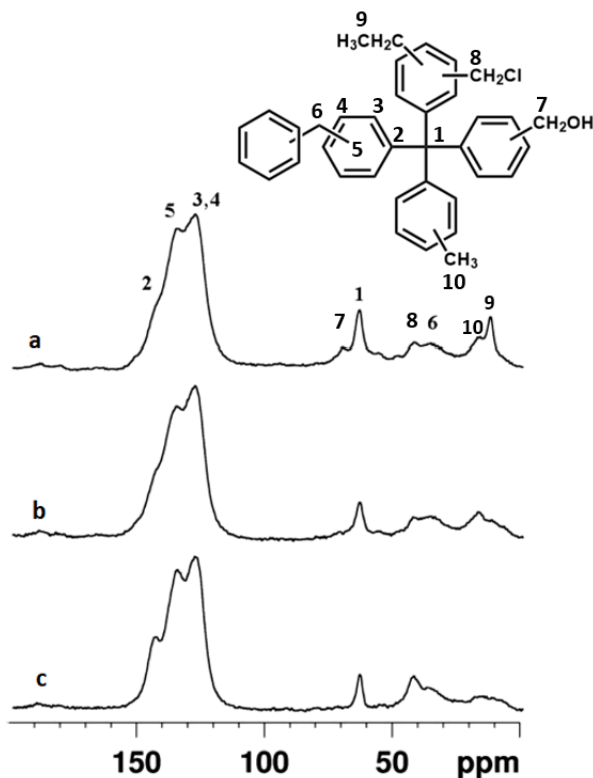


Figure 17. ^{13}C CPMAS NMR spectra of mPAF-1/30 (a), mPAF-1/16 (b) and mPAF-1/9 (c).

In Figure 18 the ^{13}C CPMAS NMR spectra of ABT materials are reported.

Peaks associated with aromatic carbons are found in the region between 150 and 120 ppm. Around 142 ppm the signal is associated with both the carbon directly attached to the central quaternary carbon and the carbon directly attached to the methylene group of the cross-linker^{3,8,17,18,19}. Aromatic carbons associated with C-H groups are found at 134 and 128 ppm^{3,8,17,18,19}. The central quaternary carbon of the monomer unit is found at 58 ppm while around 35 ppm the carbons associated with the methylene group of the cross-linker are found^{3,8,18,19}. As was already found for mPAF materials, carbons associated with methyl groups are detected around 17 and 12 ppm^{3,8}. It is interesting to observe the presence of these functional groups even in the absence of FDA in the synthetic procedure. This data is also confirmed by the

FT-IR analysis (*vide supra*). As a possible explanation, the presence of ethyl groups can be a consequence of a small fraction of dichloroethane molecules reacting with the catalyst while methyl groups can be explained via mechanisms involving the carbocationic sites of the cross-linker.

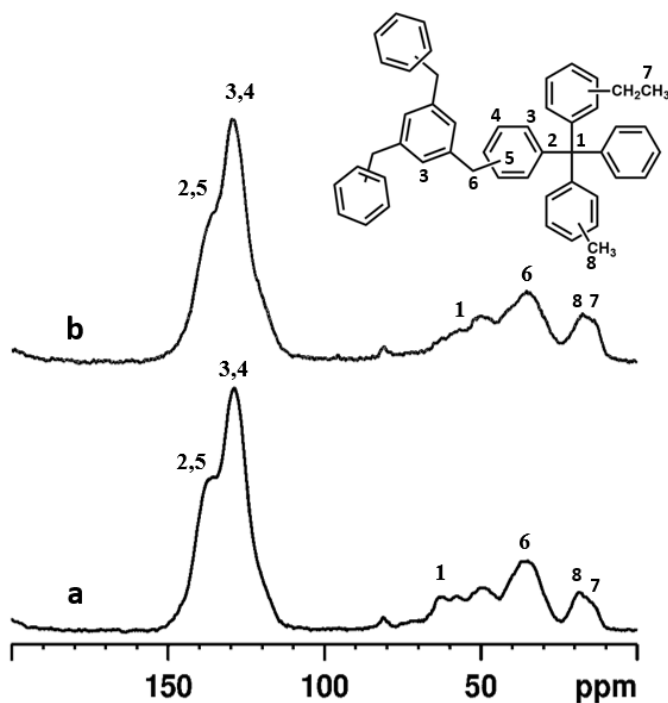


Figure 18. ^{13}C CPMAS NMR spectra of ABT01 (a) and ABT02 (b).

In Figure 19 the ^{13}C CPMAS NMR spectrum of TPMTC is reported.

In the region between 150 and 120 ppm the signals associated with aromatic carbons are recovered. The peak assigned to carbons directly attached to the quaternary carbon of the monomer unit are found at 137 ppm along the carbons directly connected to the cross-linker unit. Aromatic carbons associated with C-H groups are found at 128 ppm^{3,8,17,18,19} Quaternary carbons of the tetraphenyl methane unit are

found at 63 ppm^{3,8,18,19}. The peak centered at 36 ppm is due to aliphatic carbons of the cross-linker unit, namely carbons associated with the -CH₂- group^{3,8,17,18,19}. The broad peak centered at 17 ppm is associated with carbons seen in ethyl and/or methyl groups^{3,8}. The peak centered at 47 ppm may be due to carbons associated with the CH₂Cl group which may be generated by substitution of the aromatic ring in addition to partially unreacted cross-linker species^{3,8}.

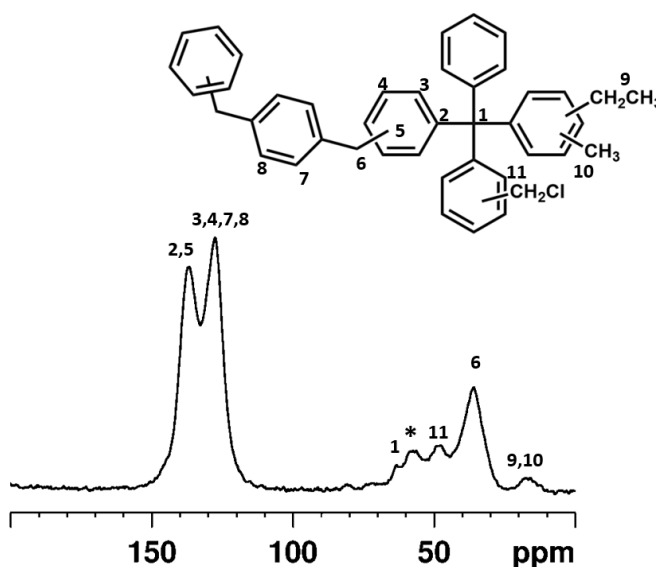


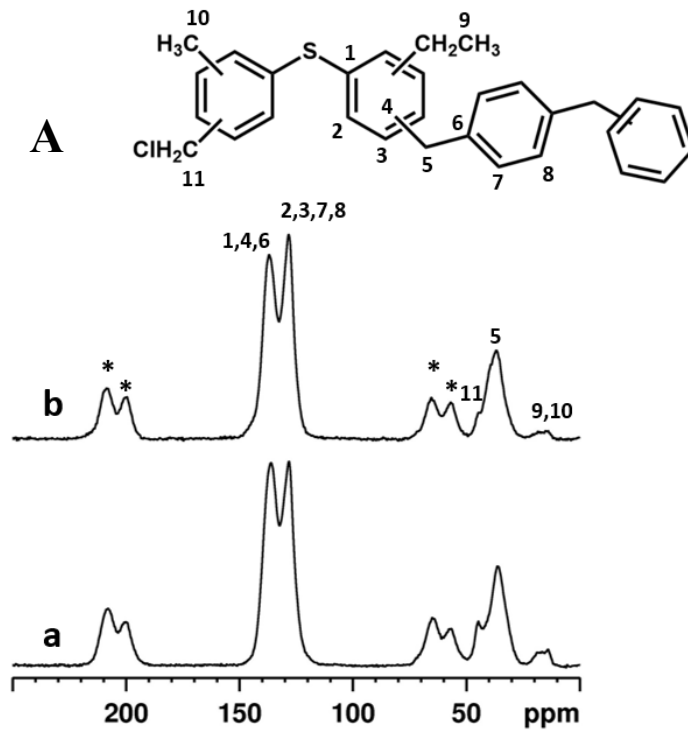
Figure 19. ¹³C CPMAS NMR spectrum of TPMTc. * is used to indicate spinning side bands.

In Figure 20 the ¹³C CPMAS NMR spectra of DIXYT materials are reported.

The signals associated with aromatic carbons are recovered in the region between 150 and 120 ppm. At 136 ppm the peak associated with substituted aromatic carbons is found. At 128 ppm the peak is assigned to aromatic carbons associated with C-H aromatic groups^{3,17,18,19}. The peak centered at 37 ppm is assigned to carbons associated with methylene groups of the cross-linker species^{3,8,18,19}. At 19 ppm the signal can be assigned to methylation of the aromatic ring while methyl carbons

found in ethyl groups may be responsible for the signal around 14 ppm^{3,8}. The signal observed at 45 ppm is assigned to carbons of CH₂Cl groups^{3,8}. It is interesting to note that by changing solvent from dichloromethane (DIXYT01) to dichloroethane (DIXYT02), in addition to the reaction temperature (35 °C, DIXYT01 and 80 °C, DIXYT02), the peaks associated with side reaction groups, namely the ones assigned to CH₂Cl, CH₃ and CH₂CH₃ decrease in intensity, suggesting a lower content of these functionalities for DIXYT02. Pore obstruction effects caused by side reaction groups can be linked to the lower surface area and pore volume of DIXYT01 with respect to DIXYT02, observed in the context of N₂ physisorption analysis (*vide supra*). This effect was not manifested in the ¹³C CPMAS NMR spectra of ABT materials where again an HCP was obtained in dichloromethane at 35 °C and was compared with the one synthesized in dichloroethane at 80 °C.

From the ¹H ECHO NMR spectra the signals of the aromatic protons are observed at 6.7 ppm while around 3 ppm the protons of the -CH₂- groups are found⁸. Alkyl protons are found between 0 and 1.15 ppm⁸. However, it is interesting to note the appearance of the signal at 9.8 ppm for the DIXYT01 material. This resonance is assigned to the proton of the -SO₃H group²¹.



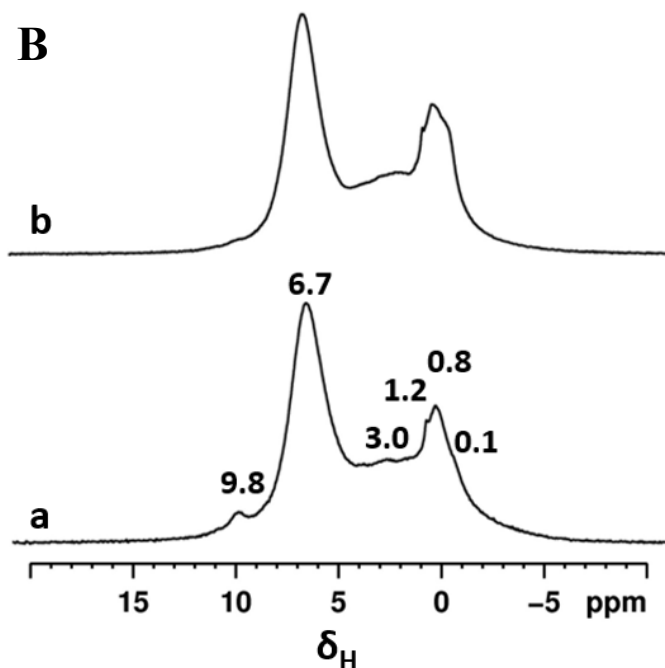


Figure 20. ^{13}C CPMAS NMR (A) and ^1H ECHO NMR (B) spectra of DIXYT01 (a) and DIXYT02 (b). * is used to indicate spinning side bands.

In Figure 21 the ^{13}C CPMAS NMR spectrum of PS-1.3 is reported.

The ^{13}C CPMAS NMR spectrum of PS-1.3 shows signals in the 150 – 120 ppm region which are associated with aromatic carbons^{3,8,18,19}. In particular, a broad band is found in this region with the main peak centered at 129 ppm, presenting a shoulder at 138 ppm, which are respectively assigned to substituted aromatic carbons and aromatic carbons associated with C-H groups^{3,8,18,19}. A broad peak is also found in the region associated with aliphatic carbons, presenting the main peak centered at 41 ppm which is assigned to the $-\text{CH}_2-$ group of the polystyrene back bone polymeric chain^{3,8,18,19}. A small shoulder at 50 ppm is assigned to the methyne carbon of the polystyrene chain. The result of the cross-linking reaction, meaning the generation of methylene bridges between the phenyl rings of the polymeric chains, manifest itself as the presence of a shoulder at 36 ppm^{3,8,18,19}. The occurrence of side reactions

during synthesis is seen though the appearance of peaks centered at 190, 64 and around 19 ppm as a broad peak. The first peak is assigned to the carbonyl group, probably associated with aldehyde groups directly attached to the phenyl ring. The peak centered at 64 ppm is probably due to carbons of the $-\text{CH}_2\text{OH}$ group while around 19 ppm the broad peak is indication of the presence of methylation and/or ethylation of aromatic rings^{3,8,18,19}.

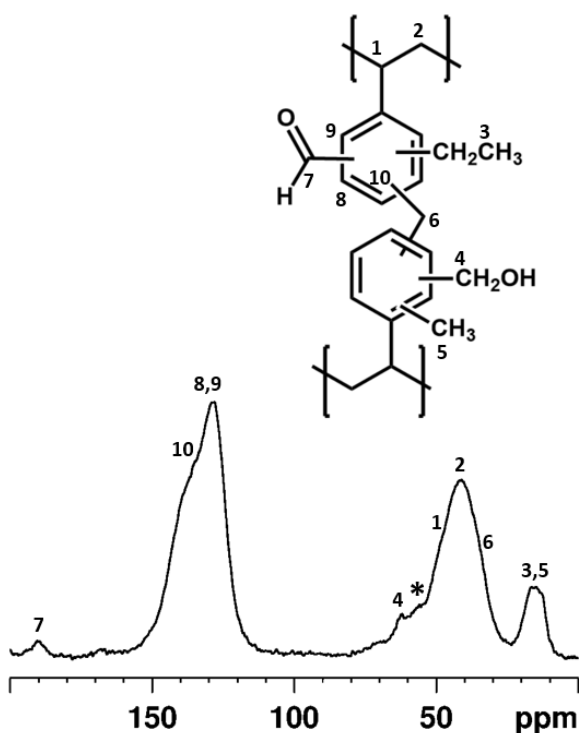


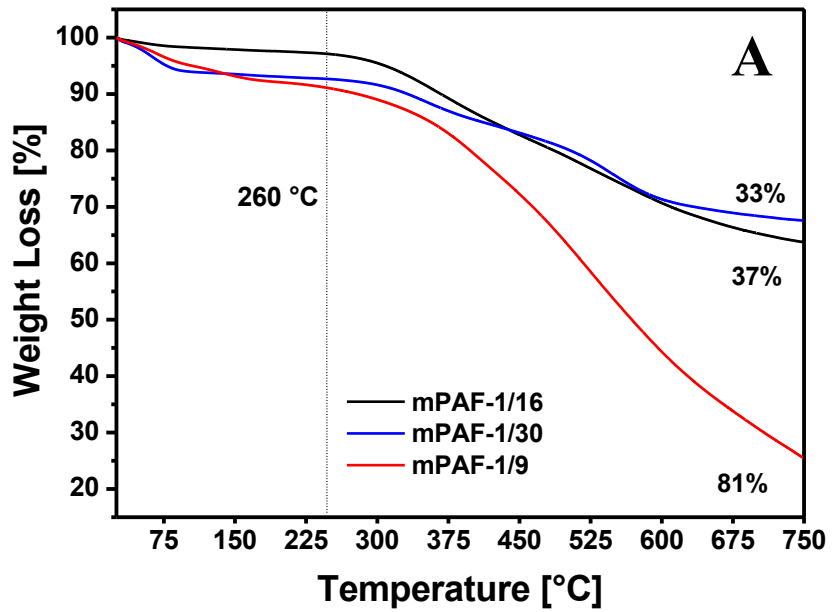
Figure 21. ^{13}C CPMAS NMR spectrum of PS-1.3. * is used to indicate spinning side bands.

3.2.5 Thermogravimetric analysis of HCP materials

In order to assess the thermal stability of the synthesized materials, thermogravimetric analysis was performed. Data were collected under Ar flow (20 ml/min) from 25 to 800 °C with a thermal ramp of 5 °C/min.

In Figure 22 the TGA curves (A) and differential TG curves (B) of mPAF materials are reported.

Up to 260 °C the curves show a weight loss around 5% which can be attributed to physisorbed water, hence the HCPs are thermally stable up to 260 °C. As evidenced by the DTG curves, after 260 °C thermal degradation starts for all HCPs. However, for mPAF-1/16 and mPAF-1/30 a first significant drop in weight is seen around 350 °C while for mPAF-1/9 it is seen around 395 °C. These signs of thermal decomposition may be attributed to degradation of side reactions groups. Around 500 °C thermal degradation of the polymeric framework starts to appear for all mPAF materials. Total weight loss is assessed at 33 and 37% for mPAF-1/30 and mPAF-1/16 respectively, while mPAF-1/9 shows a total weight loss of 81%. This may indicate that by increasing the cross-linking degree more thermally stable HCPs can be obtained.



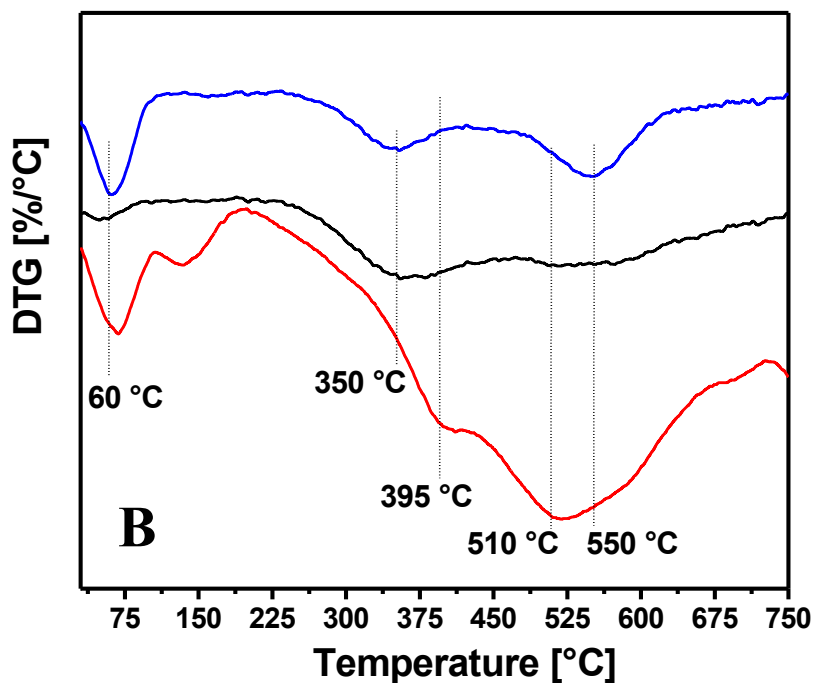


Figure 22. TGA curves (A) and DTG curves (B) of mPAF-1/9 —, mPAF-1/16 — and mPAF-1/30 — collected under Ar flow (20 ml/min) with a thermal ramp of 5 °C/min.

3.3 Characterization of saponite materials

Saponite materials were characterized using multiple techniques, namely, via Scanning Electron Microscopy (SEM) to observe the morphology, via XRPD to assess the resulting structure, via N₂ physisorption analysis at -196 °C to study the textural properties, through a spectroscopic approach via FT-IR and SS-NMR spectroscopy to gain structural information, and via Thermogravimetric Analysis

(TGA) to study the thermal stability. Each characterization technique is presented in its own section to allow for better comparison between materials.

3.3.1 Morphological analysis of saponite materials

SEM images of the synthesized saponite materials are reported in Figure 23. Both saponite materials, namely SAP110 and SAP-OP, show the presence of aggregates made by the packing of sheets of dimensions of approximately 0.5 – 1 μm confirming the layered structure of the clays.

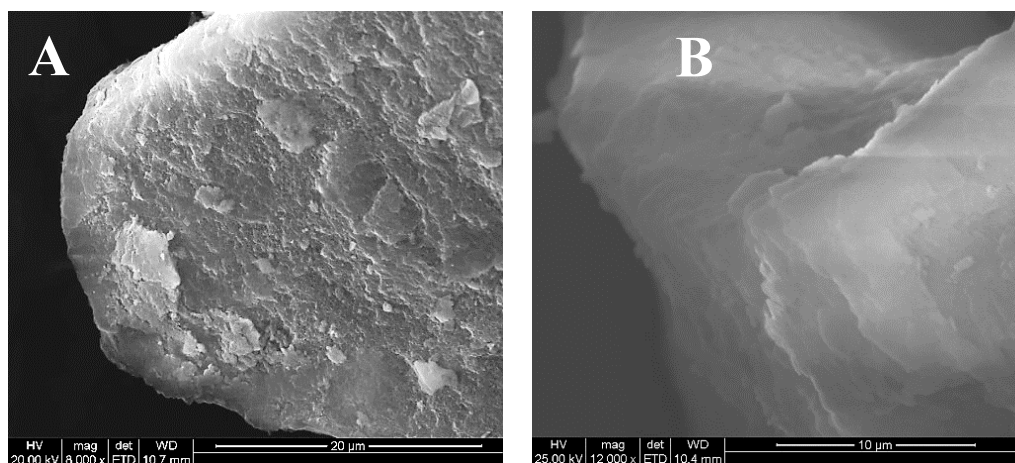


Figure 23. SEM images of SAP110 (A) and SAP-OP (B) respectively at 8000 and 12000x magnification.

3.3.2 X-Ray powder diffraction analysis

XRPD patterns are reported in Figure 24 and were recorded for both saponite materials between 2° and 65° 2θ with a step size of 0.02 with a rate of 1° 2θ /min.

XRPD pattern of SAP110 shows reflections at 8° , 19.5° and 60.5° 2θ which are respectively associated with the (001), (110) and (060) planes, characteristic of the saponite structure^{22,23,24}. The occurrence of a trioctahedral structure is inferred from the appearance of the (060) reflection^{22,23,24}. The XRPD pattern of SAP-OP retains the same profile as the one display by SAP110, suggesting that the resulting material retain the typical saponite structure. However, a small shift from 8° to 6.5° 2θ of the reflection associated with the (001) plane is observed. The (001) plane is associated with the distance between T-O-T sheets^{22,23,24}. The shift suggests a more expanded interlayer space for SAP-OP. Through Bragg's law (Eq. 1) is possible to calculate the interlayer space between lamellar sheets.

$$n\lambda = 2d \sin \theta \qquad d = \frac{n\lambda}{2 \sin \theta} \qquad \text{Equation 1}$$

Where d is the interlayer space, n is a positive integer, λ is the wavelength of the incident X-Ray employed for the analysis, which corresponds to 0.154 nm and θ is the glancing angle.

The calculated d -spacing between lamellar sheets is of 11 Å, for SAP110 and 13.5 Å for SAP-OP. The observed increase in spacing between T-O-T sheets for SAP-OP is probably due to the presence of CTA^+ species. Evidence of d -space expansion, as a consequence of CTA^+ intercalation, was also observed in the context of CTA^+

intercalation through a one-pot approach for a saponite obtained with a H₂O/Si ratio of 20²³.

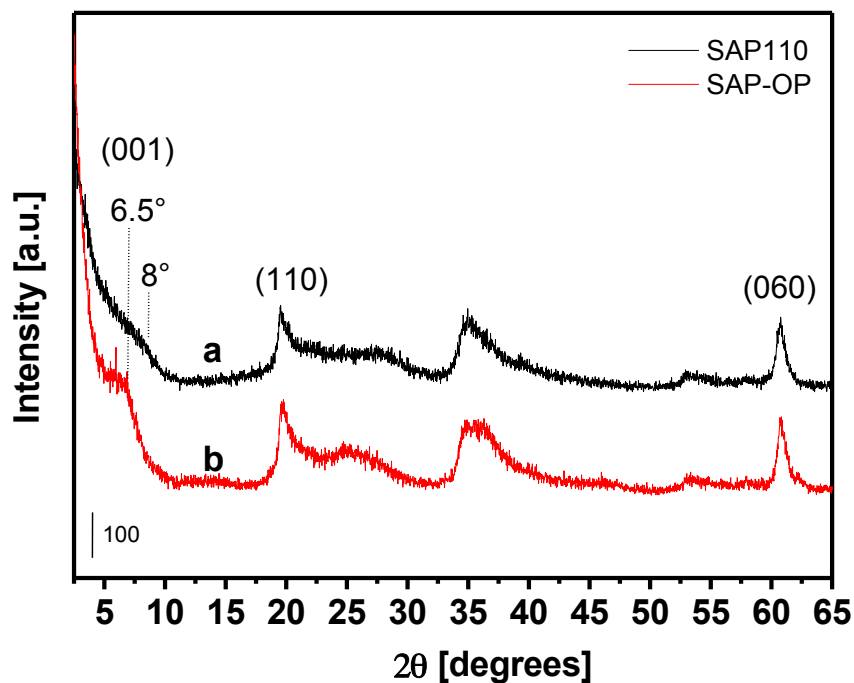


Figure 24. XRD patterns of SAP110 — and SAP-OP — from 2.5 to 65 2theta degree.

3.3.3 Textural properties of saponite materials

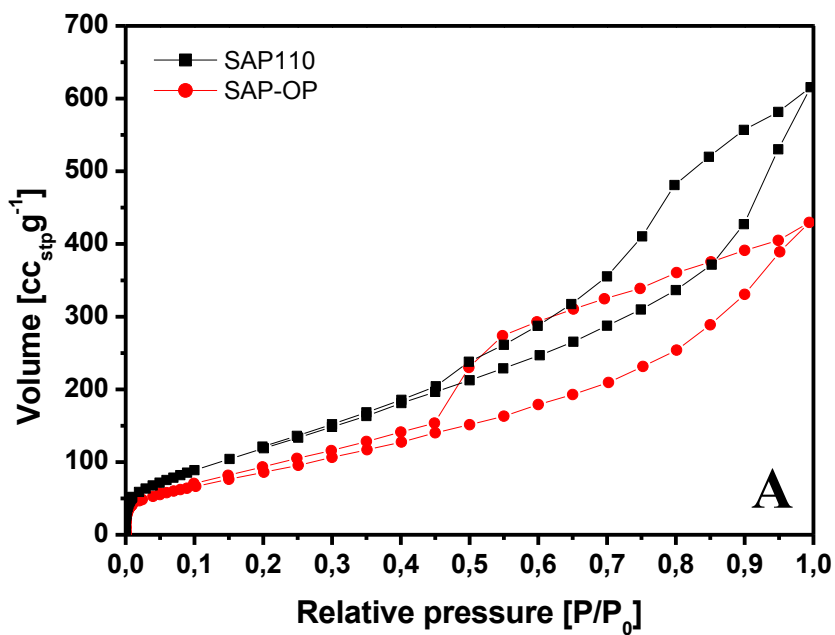
The textural properties of saponite materials were assessed via N₂ physisorption analysis performed at -196 °C. Both saponite samples were degassed at 150 °C for 3 hours to remove adsorbed species. The BET method was used for the evaluation of the surface area in the range of 0.05 – 0.3 P/P₀ while the NLDFT method was used for the pore size distribution. It needs to be kept in mind that calculated Specific Surface Areas are to be treated as “apparent” surface areas, when concerning

hierarchical materials possessing a significant fraction of micropores. This is due to the difficulty in separating the process of mono/multi-layer adsorption and the filling of micropores^{1,2}.

In Figure 25, N₂ physisorption isotherms and pore size distributions of saponite materials are reported, while the main textural properties are reported in Table 16.

N₂ physisorption isotherms can be classified as type IV, with H₃ hysteresis loops. These features are typically associated with hierarchical materials, possessing both micro and mesopores and specifically, H₃ hysteresis loops are associated with formation of plate – like particles, which is expected for saponite materials^{22,23} and are responsible for the generation of mesoporosities. The hysteresis loops are almost closed around 0.45 P/P₀ which would be a sign of rigidity of the framework^{1,2}, however a small gap between the adsorption and desorption branches is seen for SAP-OP up to 0.1 P/P₀ which suggests a small propensity of the framework to expand upon increasing pressure of the adsorbed gas^{1,2}. This is probably associated with the plate – like nature of the saponite particles. SAP110 also shows an open hysteresis loop up to 0.2 P/P₀. For SAP110 the shape of the isotherm is fairly symmetric, implying equilibrium during the desorption process¹. For SAP-OP a clear step down in the desorption branch is seen around 0.45 P/P₀ which is indication of the presence of cavitation effects during the desorption process¹. These effects usually arise when the entrance of the pore is lower than some critical size which depends upon the adsorbent and temperature employed during the experiment, which for N₂ is around 5-6 nm at -196 °C¹. Given the structure of a functionalized saponite, cavitation may be due to occlusion effects caused by the CTA⁺ functionalities which may disrupt the equilibrium of the desorption process in the time scale of the experiment. The calculated SSA_{BET} are 300 and 230 m² for SAP110 and SAP-OP respectively. From the pore size distribution it is seen a small pore family around 15 Å, with the main pore family centered around 20 Å in addition to another broad and small pore family around 37 Å. The micropore volume is assessed at 0.22 cc/g for SAP110 and 0.14

cc/g for SAP-OP while the mesopore volume are 0.37 cc/g for SAP110 and 0.27 cc/g for SAP-OP.



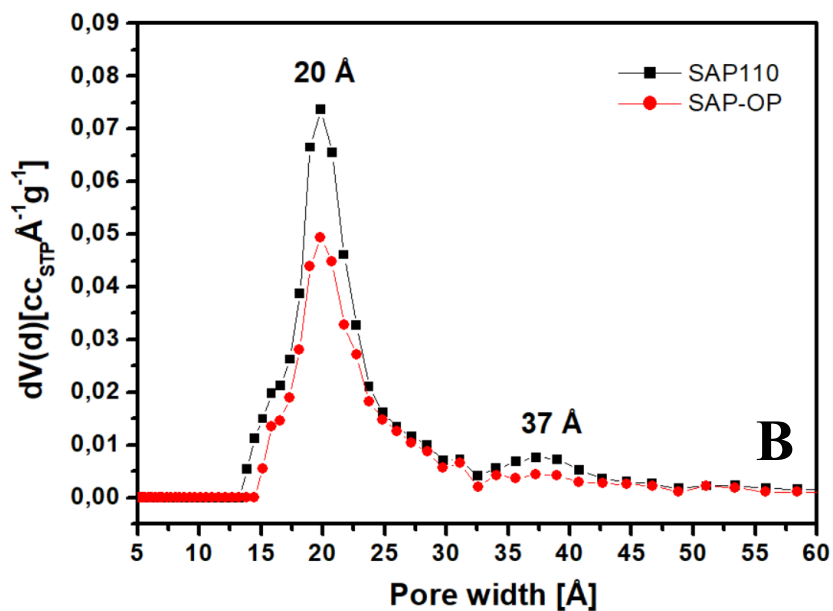


Figure 25. N₂ physisorption isotherms at -196 °C (A) and pore size distribution (B) of SAP110 ● and SAP-OP ■.

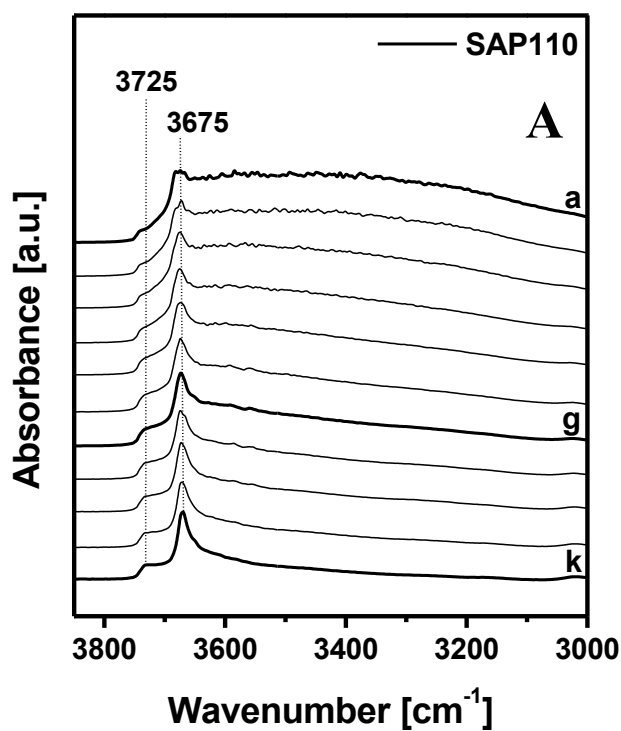
Table 16. Textural properties of saponite materials, assessed via N₂ physisorption analysis performed at -196 °C.

Sample	SSA _{BET} [m ² /g]	V _{Tot} [cc/g]	V _{micro} [cc/g]			V _{meso} [cc/g] 20< Å<100
			Total	<7Å	7<Å<20	
SAP110	300	0.59	0.20	---	0.22	0.37
SAP-OP	230	0.41	0.43	---	0.14	0.27

3.3.4 FT-IR analysis of saponite materials

Variable temperature infrared analysis (VTFT-IR) was conducted on SAP110 and SAP-OP to gain information about functional groups and the framework, their thermal stability in addition to the thermal stability of the organic functionalities of SAP-OP.

VTFT-IR spectra were recorded from room temperature to 500 °C and are shown in Figure 26.



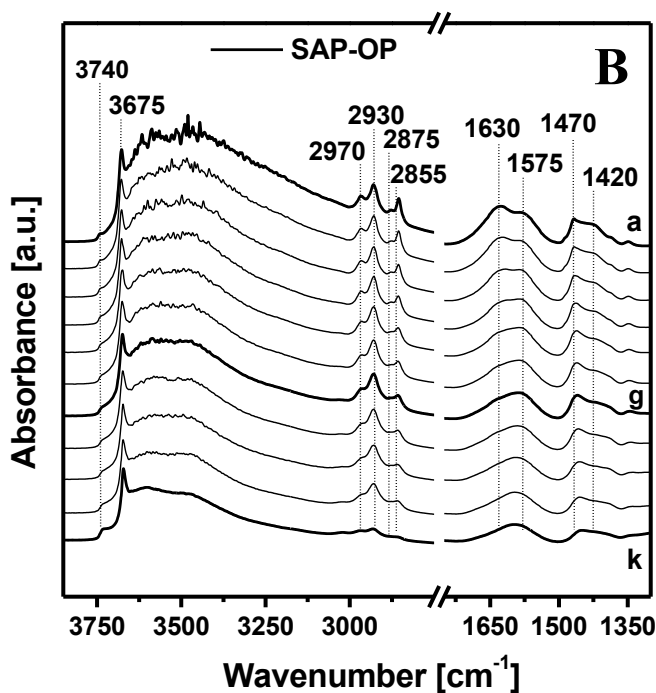


Figure 26. VRFT-IR spectra of SAP110 (A) and SAP-OP (B) recorded at room temperature (a), at 50 °C (b) and then from (b) to (k) every 50 °C up to 500 °C (k).

The IR spectrum of SAP110 collected at room temperature is characterized by the presence of a sharp peak centered at 3675 cm^{-1} and by a broad band between 3600 and 3400 cm^{-1} . The first sharp signal is assigned to the stretching vibrations of the O-H bond due of cathedral Mg²³ while O-H stretching of physisorbed water is found in the range 3600 – 3400 cm^{-1} ^{13,14,22}. The room temperature spectrum of SAP-OP is characterized by the same signals found for SAP110, namely the sharp peak at 3675 cm^{-1} assigned to the stretching vibrations of the $[\text{Mg}]_{\text{oct}}\text{-O-H}$ bond and the broad band between 3600 and 3400 cm^{-1} and between 1650 and 1550 cm^{-1} which is ascribed to physisorbed water^{13,14,22}. In addition, the presence of the CTA^+ species is inferred from the bands appearing between 3000 and 2850 cm^{-1} and from the signals between 1500 and 1300 cm^{-1} . In the high frequency region signals are found 2970, 2930, 2875 and 2855 cm^{-1} which are respectively assigned to asymmetric

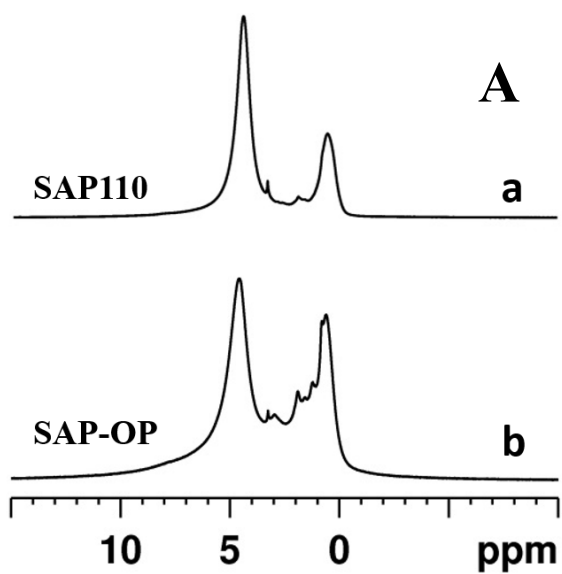
stretching vibrations of the C-H bond of the methyl groups, asymmetric stretching vibrations of C-H bonds of -CH₂- groups and the corresponding symmetric stretching vibrations at 2875 cm⁻¹ for -CH₃ and at 2855 cm⁻¹ for -CH₂-^{13,14,23}. In the low frequency region, the bending modes of the aliphatic C-H groups are found^{13,14,23}.

When the thermal treatment is applied to the SAP110 sample it is observed a progressive sharpening of the signals centered at 3675 and 3725 cm⁻¹, in addition to the disappearing of the broad band between 3600 and 3400 cm⁻¹. These effects are explainable in terms of desorption of physisorbed water^{22,23}. Specifically, the sharpening of the two signals is due to increased vibrational freedom of the O-H groups, bond in one case to the tetrahedral magnesium and for the 3725 cm⁻¹ signal, bonded to Si in isolated silanols groups (Si-O-H)^{22,23}. No signs of thermal degradation are visible up to 500 °C.

In the case of SAP-OP, thermal treatment results in the same effects seen for SAP110, meaning the desorption of physisorbed water exposes surface functional groups resulting in increased intensity of the corresponding IR signals. However, here signs of thermal degradation concerning the organic functionalities are observed. Up to 300 °C (Figure 26, curve “g”) signals associated with C-H aliphatic groups are still clearly visible, however by increasing the temperature further, a progressive decrease in the intensity of the signals centered at 2970, 2930, 2875, 2855, 1470 and 1420 cm⁻¹ is seen. A decrease in signal intensity is also observed for the bands at 1630 and 1575 cm⁻¹ which are ascribed to bending modes of water^{14,22,23}.

3.3.5 SS-NMR analysis of saponite materials

SS-NMR spectroscopy was used to characterize the saponite materials. The nuclei ^1H and ^{28}Si were probed in order to acquire the SAP110 and SAP-OP spectra, which are reported in Figure 27.



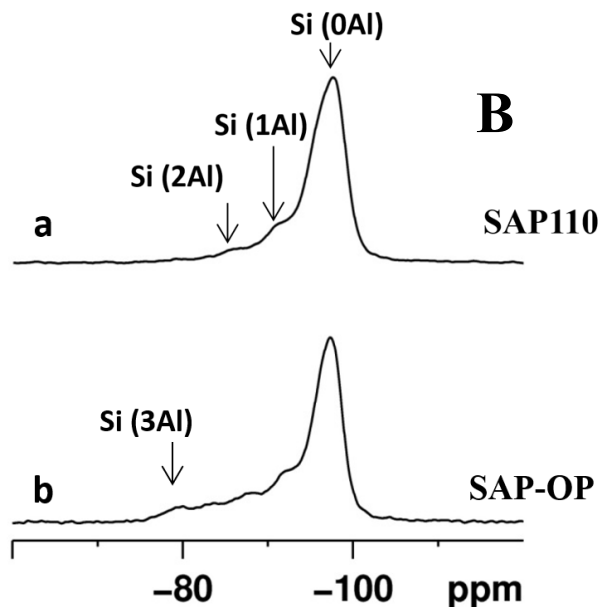


Figure 27. ^1H SS-NMR spectra (A) of SAP110 (a) and SAP-OP (b) and ^{28}Si CPMAS-NMR spectra (B) of SAP110 (a) and SAP-OP (b).

The SAP110 and SAP-OP ^1H SS-NMR spectra (Figure 27, A) show two main peaks centered at 1 and 5 ppm which are ascribed to hydrogens of the Mg-OH and Al-OH groups². The small peak around 4 ppm is assigned to physisorbed water, as it is also seen in the literature²². In the case of SAP-OP additional resonances are seen at 2 and 3 ppm, the latter associated with the hydrogens bonded to the methyl groups which are bonded to the positively charged head of the CTA^+ species, while the first is assigned to hydrogens of the $-\text{CH}_2-$ groups of the CTA^+ chain²³.

^{28}Si CPMAS-NMR spectra (Figure 27, B) of both SAP110 and SAP-OP show resonances at -96, -92 and -86 ppm which are assigned to $[\text{Si}(0\text{Al})]$, $[\text{Si}(1\text{Al})]$, and $[\text{Si}(2\text{Al})]$ species, respectively^{22,23}.

3.3.6 Thermogravimetric analysis of saponite materials

In order to assess the thermal stability of saponite materials, thermogravimetric analysis was performed. Data were collected under Ar flow (20 ml/min) from 25 to 800 °C with a thermal ramp of 5 °C/min.

In Figure 28 the TGA curves (A) and differential TG curves (B) of saponite materials are reported.

By comparing the TGA curves of the two saponite materials it is seen a lower amount of physisorbed water for SAP-OP with respect to SAP110, which is inferred from the lower weight loss up to approximately 200 °C, assessed at 6 wt % for SAP110 and 1.7 wt % for SAP-OP. This effect is explained taking into account the presence of hydrophobic species for SAP-OP, as it is also observed in the literature²³. The functionalization of SAP-OP results in the presence of additional weight losses, with respect to SAP110, in the range 250 – 550 °C which are ascribed to the decomposition of CTA⁺ species²³. Two main degradation events are seen by inspection of the DTG curve in figure 28 (B), at 415 and 485 °C. The amount of CTA⁺ is assessed at 6.3 wt %. It is interesting to note that the temperature range associated with CTA⁺ decomposition is shifted towards higher temperatures with respect to pure CTAb. It is reasonable to assume that CTA⁺ molecules are located within the interlayer, between T-O-T sheets, because of the protecting effects the saponite framework confer to organic species, the CTA⁺ thermal stability appears to be higher²³. The total weight loss is assessed at 10 wt % for SAP110 and at 12 wt % for SAP-OP.

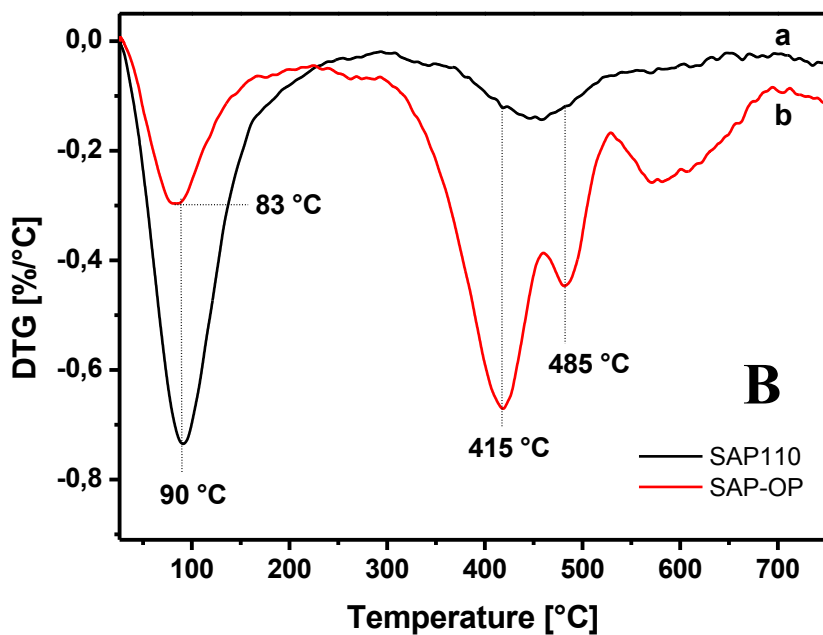
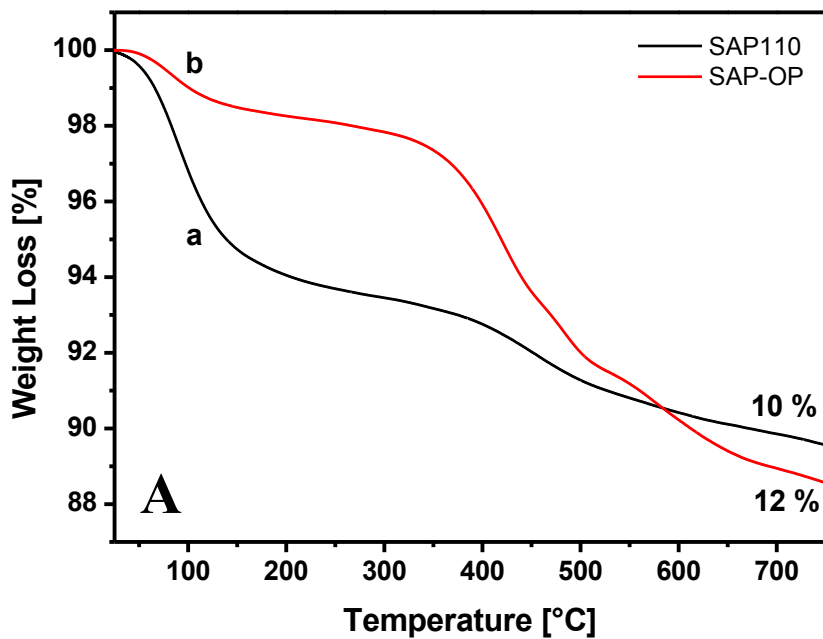


Figure 28. TGA curves (A) and DTG curves (B) of SAP110— and SAP-OP — collected under Ar flow (20 ml/min) with a thermal ramp of 5 °C/min.

3.4 Conclusions

In this chapter the characterization of the synthesized materials have been presented. Modulation of the structure and textural properties of the HCPs were obtained through the employment of different synthetic routes, meaning by changing monomers, cross-linkers and catalysts. Friedel – Crafts alkylation is known to be unselective towards a specific orientation of the substituents. Nonetheless, by carefully choosing the synthetic approach, a certain degree of control over the resulting structure can be achieved. In particular for ABT materials a more macroscopic 2D structure have been obtained through a meta orienting catalyst, AlBr_3 , in addition to the employment of a “planar” cross – linker with three possible carbocationic sites 1,3,5-tris(bromomethyl)benzene. For TPMTC a higher surface area and pore volume were obtained through the employment of a para-orienting catalyst TiCl_4 and a rigid cross-linker, namely α,α' -dichloro-p-xylene. Lower surface areas were obtained for DIXYT materials when a flexible two - dimensional monomer was used, in addition to introducing a sulfur heteroatom in the polymeric framework. Waste materials, namely polystyrene chips were used as starting material to obtain an HCP with good textural properties, thus allowing a wasted product to be useful once again, which is an important result in the context of environmental sustainability.

Two saponite materials were obtained, namely one completely inorganic (SAP110) and a one organo – functionalized through a one-pot approach (SAP-OP), the latter resulting in a framework with a more expanded interlayer space but retaining the same structural features of saponite materials.

3.5 References

[1] Recent advances in the textural characterization of hierarchically structured nanoporous materials. Cychosz, K. A.; Guillet-Nicolas, R.; Martinez, J. G.; Thommes, M.; *Chem. Soc. Rev.* 2017, 46, 389 – 414.

[2] Thommes, M.; Kaneko, K.; Neimark, A. V.; Olivier, J. P.; Rodriguez-Reinoso, F.; Rouquerol, J.; Sing, K. S. W. Physisorption of Gases, with Special Reference to the Evaluation of Surface Area and Pore Size Distribution (IUPAC Technical Report). *Pure Appl. Chem.*, 2015, 87, 1051 – 1069.

[3] Errahali, M.; Gatti, G.; Tei, L.; Paul, G.; Rolla, G. A.; Canti, L.; Fraccarollo, A.; Cossi, M.; Comotti, A.; Sozzani, P.; Marchese, L. Microporous Hyper-Cross-Linked Aromatic Polymers Designed for Methane and Carbon Dioxide Adsorption. *J. Phys. Chem. C* 2014, 118 (49), 28699–28710.

[4] Adsorption Hysteresis of Nitrogen and Argon in Pore Networks and Characterization of Novel Micro- and Mesoporous Silicas. Thommes, M.; Smarsly, B.; Groenewolt, M.; Ravikovitch, P. I.; Neimark, A. V. *Langmuir* 2006, 22, 2, 756 – 764.

[5] Density Functional Theory of Adsorption in Spherical Cavities and Pore Size Characterization of Templated Nanoporous Silicas with Cubic and Three-

Dimensional Hexagonal Structures. Ravikovitch, P. I.; Neimark, A. V. *Langmuir* 2002, 18, 5, 1550 – 1560.

[6] Capillary Condensation in Linear Mesopores of Different Shape. Wallacher, D.; Künzner, N.; Kovalev, D.; Knorr, N.; Knorr, K. *Phys. Rev. Lett.* 2004. 92, 195704.

[7] Experimental Confirmation of Different Mechanisms of Evaporation from Ink-Bottle Type Pores: Equilibrium, Pore Blocking, and Cavitation. Peter I. Ravikovitch, P. I.; Alexander V. Neimark, A. V. *Langmuir* 2002, 18, 25, 9830 – 9837.

[8] Hyper-Cross-Linked Polymers for the Capture of Aromatic Volatile Compounds. Paul, G.; Begni, F.; Melicchio, A.; Golemme, G.; Bisio, C.; Marchi, D.; Cossi, M.; Marchese, L.; Gatti, G. *ACS Appl. Polym. Mater.* 2020, 2, 647 – 658.

[9] Hypercrosslinked polymers: controlled preparation and effective adsorption of aniline. Liu, Y.; Fan, X.; Jia, X.; Zhang, B.; Zhang, H.; Zhang, A.; Zhang, Q. *J. Mater. Sci.* 2016. 51, 8579–8592.

[10] Physical adsorption characterization of nanoporous materials: progress and challenges. Thommes, M.; Cychosz, K. A. *Adsorption.* 2014. 20, 233–250.

[11] Characterization of Activated Carbon Fibers by CO₂ Adsorption. Cazorla-Amorós, D.; Alcañiz-Monge, J.; Linares-Solano, A. *Langmuir.* 1996. 12, 11, 2820–2824.

[12] The Nature of The Chemical Bond and the Structure of Molecules and Crystals: An Introduction to Modern Structural Chemistry. Pauling, L. 1960. 3rd edition. ISBN-13 : 978-0801403330.

[13] Interpretation of Infrared Spectra, A Practical Approach, John Coates, Coates Consulting, Newtown, USA, Encyclopedia of Analytical Chemistry, R.A. Meyers (Ed.) Copyright John Wiley & Sons Ltd.

[14] Infrared and Raman Characteristic Group Frequencies: Tables and Charts, 3rd Edition. Socrates, G. Wiley. 2004. ISBN: 978-0-470-09307-8.

[15] On the nature of “functional groups” in non-functionalized hypercrosslinked polystyrenes. M.P. Tsyurupa, Z.K. Blinnikova, Yu.A. Davidovich, S.E. Lyubimov, A.V. Naumkin, V.A. Davankov. *Reactive & Functional Polymers*. 2012, 72, 973–982.

[16] Infrared spectra of high polymers. VI. Polystyrene. Liang, C. Y.; Krimm, S. *Journal of Polymer Science*. 1958. 27, 115.

[17] Click chemistry produces hyper-cross-linked polymers with tetrahedral Cores. Plietzsch, O.; Schilling, C. I.; Grab, T.; Stephan L. Grage, S. L.; Ulrich, A. S., Comotti, A.; Sozzani, P.; Muller, T.; Brase. *S. New J. Chem.*, 2011, 35, 1577–1581.

[18] Solid-State ^{13}C MAS NMR Studies of Hyper-Cross-Linked Polystyrene Resins. Law, R. V.; Sherrington, D. C.; Snape, C. E.; Ando, I.; Hiromichi Kurosu, H. *Macromolecules* 1996, 29, 19, 6284–6293.

[19] Hydrogen Storage in Microporous Hypercrosslinked Organic Polymer Networks. Wood, C. D.; Tan, B.; Trewin, A.; Niu, H.; Bradshaw, D.; Rosseinsky, M. J.; Khimiyak, Y. Z.; Campbell, N. L.; Kirk, R.; Stöckel, E.; et al. *Chem. Mater.* 2007, 19, 2034–2048.

[20] Hypercrosslinked porous polymer materials: design, synthesis, and applications. Tan, L.; Tan, B. *Chem. Soc. Rev.* 2017, 46, 3322 — 3356.

[21] De Novo Access to SO_3H - Grafted Porous Organic Polymers (POPs@H): Synthesis of Diarylbenzopyrans/Naphthopyrans and Triazoles by Heterogeneous catalytic Cyclocondensation and Cycloaddition Reactions. Yadav, C.; Maka, V. K.; Soumen Payra, S.; Morthy, J. N. *ACS Appl. Polym. Mater.* 2020, 2, 3084–3093.

[22] Costenaro, D.; Gatti, G.; Carniato, F.; Paul, G.; Bisio, C.; Marchese, L. The effect of synthesis gel dilution on the physico chemical properties of acid saponite clays. *Microporous Mesoporous Mater.* 2012, 162, 159–167.

[23] Bisio, C.; Carniato, F.; Paul, G.; Gatti, G.; Boccaleri, E.; Marchese, L. One-Pot Synthesis and Physicochemical Properties of an Organo-Modified Saponite Clay. *Langmuir* 2011, 27, 7250–7257.

[24] Physicochemical and catalytic characterization of non-hydrothermally synthesized Mg-, Ni and Mg–Ni-saponite-like materials. Prihod'ko, R.; Hensen, E. J. M.; Sychev, M.; Stolyarova, I.; Shubina, T. E.; Astrelin, I.; van Santen, R. A. *Microporous Mesoporous Mater.* 2004, 69, 49–63.

Chapter IV

Toluene adsorption on mPAF materials

4.1 Introduction

Hyper cross – linked polymers have attracted great research interest in the last decades as inexpensive and easy to obtain porous materials¹. Based on the versatile Friedel – Crafts alkylation, the properties of these solid sorbents can be easily modulated thanks to the immense diversity offered by organic chemistry^{2,3}, as already stated in Chapter I. An essential aspect in designing a porous network with specific adsorption properties is to understand eventual host – guest interactions. In particular, non - covalent interactions play a crucial role in guiding the uptake of molecules in physisorption processes. A modulation on the selectivity toward target species can be achieved by selection of specific chemical functionalities at the surface⁴. Hyper cross – linked polymers are, in general, composed of aromatic units linked together by aliphatic groups^{1,2}. To gain a broad understanding of the adsorption capacities towards aromatic pollutants and to study the interactions between aromatic species and the HCP's surface, we chose toluene as representative of the aromatic VOC family and mPAF materials as representatives of the HCPs family, given their textural properties and the chemical nature of the polymeric framework.

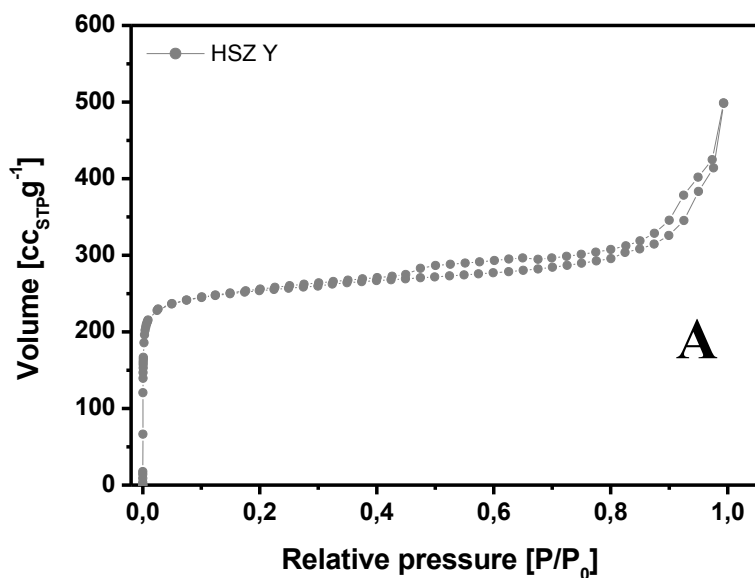
The system mPAFs / toluene is analyzed through a volumetric approach to obtain information on the overall adsorption capacities of the mPAF materials. This approach also allows to obtain information on how the textural properties influence the amount of adsorbed toluene. The data obtained are compared with those of Y zeolite (HSZ-Y) which is widely used in this field of applications. The Y zeolite is an ultra-stable Y (USY) produced by Tosoh through dealumination of zeolite Y (HSZ-390HUA), with $\text{SiO}_2/\text{Al}_2\text{O}_3 = 200$.

A spectroscopic approach was used to study the interactions at play between mPAFs and the adsorbed toluene molecules; in particular, the adsorption process was monitored by FT-IR and SS-NMR spectroscopy. All volumetric adsorption experiments were performed at 35 °C, to allow a direct comparison with the FT-IR investigation, in which the temperature of the material under the action of the IR beam is about the same. Finally, considering the information obtained from the spectroscopic techniques as a starting point, the host - guest interactions were studied through a computational approach. The findings reported in this section have been published in the journal ACS Applied Polymer Materials with the title Hyper-Cross-Linked Polymers for the Capture of Aromatic Volatile Compounds, authored by G. Paul, F. Begni, A. Melicchio, G. Golemme, C. Bisio, D. Marchi, M. Cossi, L. Marchese, G. Gatti (ACS Appl. Polym. Mater. 2020, 2, 647–658).

Before discussing toluene adsorption, a brief discussion of the textural properties of HSZ-Y is needed, since a comparison between the toluene adsorption capacities of mPAF materials and Y zeolite is proposed in this section.

4.1.1 HSZ-Y N₂ physisorption analysis

N₂ physisorption analysis on HSZ-Y was performed at -196 °C. The sample was degassed for 3 hours at 150 °C in order to remove adsorbed species. N₂ physisorption isotherm and pore size distribution are reported in Figure 1.



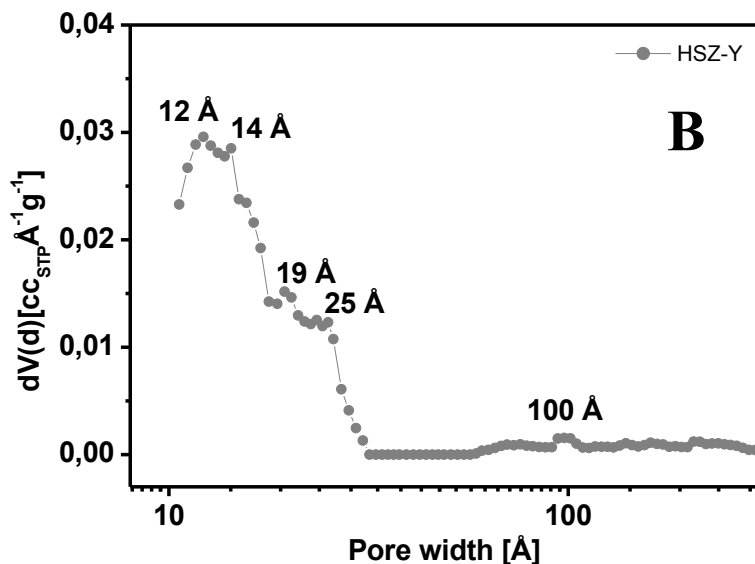



Figure 1. N₂ physisorption isotherms at -196 °C (A) and pore size distribution (B) of HSZ-Y .

N₂ physisorption isotherm can be classified as type I, which is associated with microporous materials. However, it is seen the presence of a small hysteresis loop. This can be due to the dealumination process⁵ generating mesoporosities, hence the formation of a metastable state upon N₂ adsorption within mesopores.

The distribution of the pores indicates the presence of three different families. The first microporous with a porosity between about 10 and 18 Å, a second mesoporous with pores between about 20 and 30 Å and finally a third family of macropores with pore sizes ranging between about 50 and 100 Å also present, probably due to the dealumination process. The main textural properties are reported in Table 1.

Table 1. Textural properties of HSZ-Y, assessed via N₂ physisorption analysis performed at -196 °C.

Sample	SSA _{BET} [m ² /g]	V _{Tot} [cc/g]	V _{micro} [cc/g]			V _{meso} [cc/g]
			Total	<7Å	7<Å<20	20< Å<300
HSZ-Y	991	0.68	0.28	---	0.28	0.40

4.2 Volumetric adsorption of toluene on mPAF materials and HSZ-Y

Toluene adsorption isotherms were obtained at 35 °C on HSZ-Y and mPAF materials by employing a volumetric analysis of vapor sorption in an Autosorb iQ MP-XR equipped with a cryocooler (Quantachrome Instruments). Prior to the adsorption measurements all samples were outgassed for 30 min at 50 °C, 30 min at 80 °C, 2 h at 120 °C, and 2 h at 150 °C in order to remove possible adsorbed species. For the mPAF materials a final treatment for 12 h at 200 °C under high-vacuum conditions (final pressure 7×10^{-4} mbar) was adopted. Toluene adsorption isotherms are reported in Figure 2. Weights of adsorbed toluene were calculated from volumetric data by dividing the volume of adsorbed toluene by the molar volume of an ideal gas at STP conditions. The obtained moles of adsorbed gas were multiplied by the molar mass of the toluene molecule. Toluene uptakes Q[%] were calculated via Eq. 1

$$Q[\%] = \frac{W_{tolads}}{W_{sample}} * 100 \quad (1)$$

where W_{tolads} is the weight of the adsorbed toluene and W_{sample} is the weight of the sample before the adsorption.

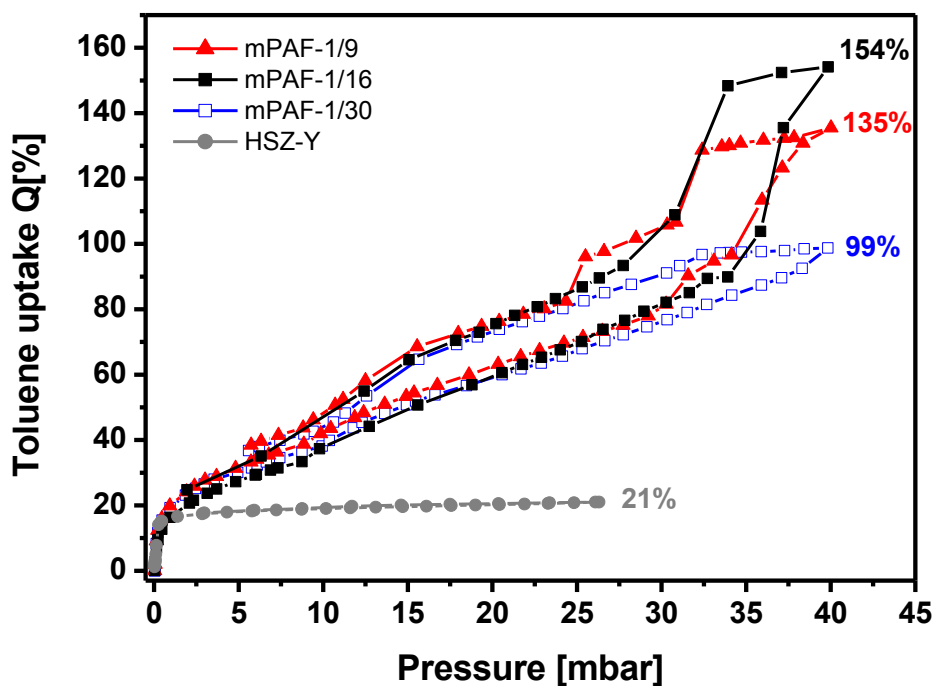


Figure 2. Toluene volumetric adsorption isotherms at 35 °C of mPAF-1/9 ▲, mPAF-1/16 ■, mPAF-1/30 □ and HSZ-Y ●.

For all volumetric adsorption isotherms, a rapid absorption of toluene up to about 0.4 mbar is observed, due to the filling of the respective micropores. For HSZ-Y zeolite a further increase in toluene pressure does not result in a significant increase

in toluene uptake. This is due to the low fraction of available volume associated with larger pores, as meso and macropores⁵. In particular, up to 0.4 mbar the amount of toluene retained in the porous structure of the zeolite is estimated at 15 Q[%]. After 0.4 mbar of toluene pressure, the zeolite Y isotherm shows a drastic slowdown in toluene absorption, reaching a final toluene adsorption capacity of 21 Q[%], at 27 mbar of toluene pressure. Up to 0.4 mbar the adsorption profile displayed by mPAF materials is similar across all polymers, with mPAF-1/30 and mPAF-1/9 slightly above mPAF-1/16 in terms of 3 Q[%]. The real difference in adsorption capacities is observed above 1 mbar of toluene pressure.

In fact, at this pressure the HSZ-Y adsorption curve has almost reached its saturation point, while mPAF adsorption isotherms show a clear gradual increase in toluene uptake upon increasing toluene pressure. The final adsorption capacities are evaluated at 99 Q[%] for mPAF-1/30, 135 Q[%] for mPAF-1/9 and finally at 154 Q[%] for mPAF-1/16. By evaluation of the textural properties (Chapter III, Table 6) it is seen that the amount of toluene retained in the polymeric framework by mPAF materials, is much higher with respect to the one expected by only taking into account the amount of pore volume at disposal. Furthermore, for the adsorption isotherms of toluene it is observed that for all HCPs the desorption branch does not close for the entire desorption process. This is associated with the swelling of the polymeric framework^{5,6}. It is interesting to note that for mPAF-1/9 and mPAF-1/16 different steps in the desorption branch are seen. For mPAF-1/9, two steps are observed, at 32 and 25 mbar respectively, while for mPAF-1/16 a single step at 33 mbar is observed. This feature is associated with expansion of the polymeric framework, which confers additional free volume, available for hosting guest molecules⁵. It is interesting to compare the pore volume measured via N₂ physisorption analysis with the one occupied by toluene at 40 mbar, which is the toluene saturation pressure at 35 °C, hence allowing a comparison with N₂ physisorption values of P/P₀ up to 1. In Table 2 the toluene volumes (C7) in mPAF materials calculated by dividing the adsorbed

toluene mass (per gram of sample) by the toluene density (0.853 g cm^{-3}) at $35 \text{ }^\circ\text{C}$ are reported.

Table 2. Comparison of Pore Volume of mPAF materials and HSZ-Y Zeolite Obtained from N_2 Physisorption at $-196 \text{ }^\circ\text{C}$ and from Toluene Sorption at $35 \text{ }^\circ\text{C}$.

Sample	SSA_{BET} [m²g⁻¹]	V_{Tot} [ccg⁻¹]	V_{tot}[C7] [ccg⁻¹]	V_{C7}/V_{N2}
HSZ-Y	991	0.68	0.25	0.36
mPAF-1/9	1236	0.78	1.58	2.03
mPAF-1/16	1289	0.96	1.81	1.88
mPAF-1/30	1318	1.06	1.16	1.09

For HSZ-Y it is seen that only 36% of the total pore volume is occupied by toluene. This may be due to inefficient stacking of the toluene molecules in the rigid framework of the Y zeolite⁵. All mPAF materials, however, are seen to retain higher toluene volume at $35 \text{ }^\circ\text{C}$ with respect to nitrogen at $-196 \text{ }^\circ\text{C}$. In other words, the pore volume assessed via toluene uptake is higher with respect to the one assessed via N_2 physisorption analysis. This indicates the propensity for a hyper cross-linked polymeric framework, such as the one of mPAF materials, to expand in the presence of affine solvents, in this case toluene⁵. For two of the three mPAF materials (mPAF-1/9 and mPAF-1/16), the swelling effect is quite severe, resulting in almost a factor of about two in the amount of pore volume gained, specifically a factor of 2.03 for mPAF-1/9 and 1.88 for mPAF-1/16. It is interesting to note that for the material displaying the higher cross-linking degree, namely mPAF-1/30, the swelling effect is assessed at 1.09 of the initial pore volume. This is an indication of the fact that an

overly cross-linked framework, loses the swelling capacity in favor of rigidity, which for pollutants removal applications is a clear drawback⁵.

From the data presented in this section it is seen that mPAF-1/16 is the material displaying the higher toluene adsorption capacity. This fact is not solely due to its textural properties, but is a fine combination of textural properties and structural features, such as the cross-linking degree. It is evident that, for the hyper-crosslinked polymers mPAF presented here, it is necessary to achieve a balance between the textural properties and the rigidity of the structures if the adsorbent with the maximum adsorption capacity is to be obtained.

4.3 FT-IR study of toluene-d₈ adsorption on mPAF materials

The process of adsorption of toluene on mPAF materials was studied via FT-IR spectroscopy to investigate on the possible interactions between the material's surface and the guest molecules. Fully deuterated toluene (toluene-d₈) was used to avoid signals overlap. Toluene-d₈ was dosed on the materials until saturation (27 mbar) and then gradually remove from the apparatus. To simplify the exposition, spectra are discussed from low to high toluene pressure. The analysis was performed on self-supported pellets which were treated under vacuum conditions (10⁻⁴ mbar) at 150 °C for 3 hours prior to analysis in order to remove possible adsorbed species. The data are presented first on mPAF-1/16 in section 4.3.1 and then on all mPAF materials in section 4.3.2.

4.3.1 Toluene-d₈ adsorption on mPAF-1/16

The IR assignments of the absorption bands of mPAF materials are reported in Chapter III, section 3.2.3 and in Table 11, however the main signals with the corresponding assignments are here summarized in Table 3. In Figure 3 it is reported the full process of toluene-d₈ adsorption on mPAF-1/16 in the high frequency region.

Upon admission of small doses of toluene-d₈ no apparent changes are seen in the spectral profile of mPAF-1/16 up to approximately 6 mbar of pressure (Figure 3 curve “f”). When the toluene-d₈ pressure is increased up to 27.1 mbar, a shoulder appears at 2965 cm⁻¹. This band has been interpreted as a red-shifted signal associated with the asymmetric stretching vibrations of the C-H bonds of the methyl of -CH₂CH₃ groups of the polymeric framework^{5,7,8}. The shift towards lower frequencies can be generated by the attractive force exerted on the methyl functional group by the interacting guest molecule. The hydrogen of the C-H bond of the material's methyl groups is pulled toward the guest molecule, thus elongating (or temporary weakening) the bond and consequently lowering its stretching frequency^{9,10,11}. The magnitude of the observed red-shift, 7 cm⁻¹, is consistent with the presence of the weak C-H/π interactions, as it is observed in the literature for other scenarios involving C-H/π interactions between methyl groups or methane with aromatic molecules such as benzene and toluene^{12,13}. The weakness of the interactions at play is explainable in terms of the acidity of the hydrogen atom subjected to the interactions. For a methyl group C-H bond, the carbon adopt an sp³ hybridization, which means that the amount of s character is lower with respect to sp² and sp C-H bonds. Since the s orbital is characterized by the presence of electron density at the nucleus, while p orbitals have a node at the nucleus, a C(sp³)-H have less electron density concentrated at the carbon nucleus¹⁰. The ability of a nucleus to retain its electrons is also viewed as electronegativity, thus an hydrogen in an sp³ hybridized

C-H bond is less acidic with respect to an sp^2 hybridized C-H bond, and consequently, higher acidity is indeed observed for the hydrogen of an sp hybridized C-H bond¹⁰. In the context of C-H/ π interactions, which are a somewhat special case of hydrogen bond, the more acidic the hydrogen atom involved in the interaction, the stronger the attraction⁹. Here is a clear information of how small is the host – guest interaction between a methyl group and a toluene molecule, since only a 7 cm^{-1} red shift is observed; in this situation, dispersion forces are predominantly responsible for the attraction between the species, meaning the stronger electrostatic forces, which are the main source of conventional hydrogen bonds, are not present due the lack of charge separation between the sp^3 carbon and the hydrogen atom⁹.

In the case of the presence of an electrostatic component in the interactions involved, as for example in a study on the interactions between zeolites (HSZ-Y and ZSM-5) and toluene¹⁴, a red shift of 150 cm^{-1} was observed for the interaction [Si] -OH / π . It should be pointed out however that the presence of a quadrupole moment of the aromatic ring could confer additional intensity to the interaction between a C(sp^3)-H and a π system, meaning dispersion forces, even though predominant, are not the only energy component to the CH/ π interaction⁹. It is interesting to note that no signs of π/π interactions are here seen, meaning no shift is observed for the signals associated with the aromatic C-H bonds of the material's framework. It is also worth noting that bridging methylene groups seem to not participate in the interactions characterizing the adsorption of toluene- d_8 on the HCP, since no alteration of the corresponding IR bands is seen. A careful investigation of the interactions at play between mPAF-1/16 and aromatic molecules (benzene, toluene, xylene [BTX]) will be presented in the context of the SS-NMR analysis.

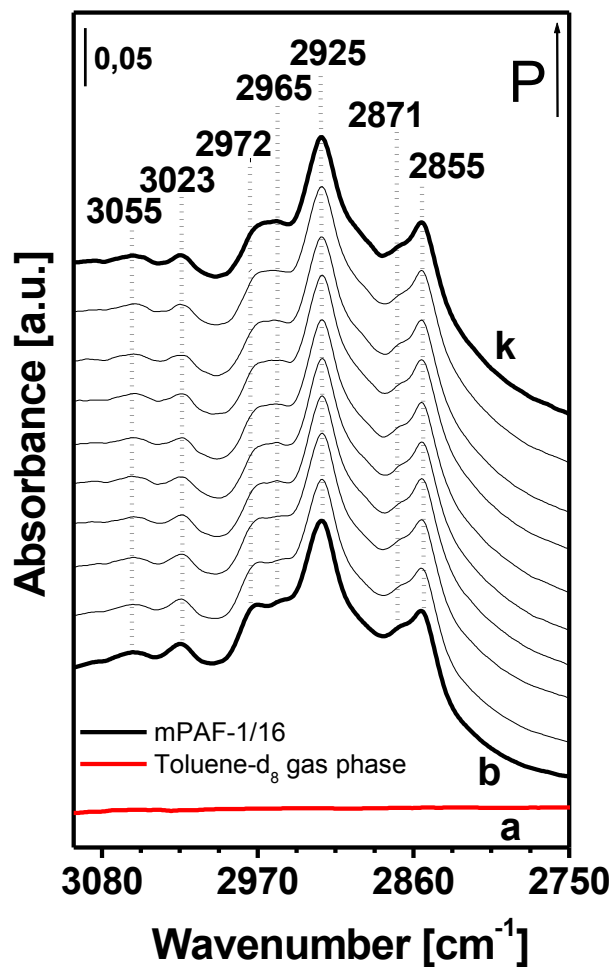


Figure 3. High frequency region IR spectra of toluene- d_8 adsorbed on mPAF-1/16 at beam temperature (bt). (a) is the gas-phase spectrum of toluene- d_8 (b) is recorded under vacuum conditions ($1 \cdot 10^{-4}$ mbar) after treating the sample at $150 \text{ }^\circ\text{C}$ for 3 hours. Spectra from (c) to (k) are associated with the admission of 0.2 (c), 0.9 (d), 2.1 (e), 6.1 (f), 10.1 (g), 14.1 (h), 22.1 (i), 26.1 (j), and 27.1 mbar (k) of toluene- d_8 .

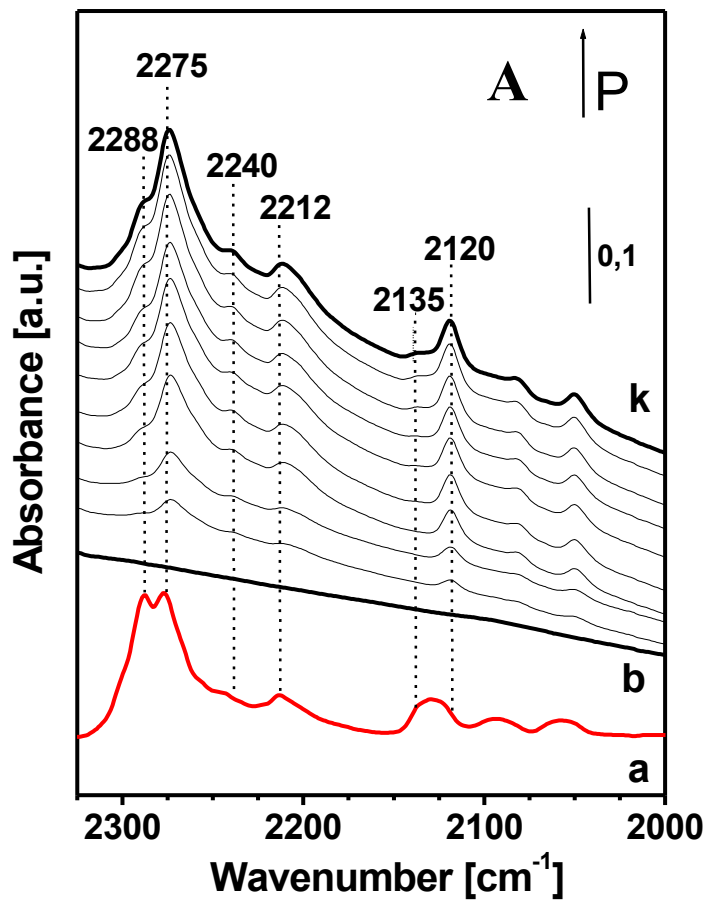
Table 3. Assignments of the main IR absorption bands of mPAF materials.

Bands position [cm⁻¹]	Assignments [7],[8]
3055	ν_{As} Aromatic C-H
3023	ν_S Aromatic C-H
2972	ν_{As} Aliphatic C-H (-CH ₂ CH ₃)
2952	ν_{As} Aliphatic C-H (-CH ₃)
2921	ν_{As} Aliphatic C-H (-CH ₂ -)
2871	ν_S Aliphatic C-H (-CH ₃)
2855	ν_S Aliphatic C-H (-CH ₂ -)
900 - 700	Collective bending vibrations of poly-substituted benzene rings

In Figure 4 the full adsorption of toluene-d₈ on mPAF-1/16 is reported between 2325 and 2000 cm⁻¹ (panel A) and between 900 and 780 cm⁻¹ (panel B) while in Figure 5 the gas phase and liquid phase spectra of toluene-d₈ are reported. The toluene-d₈ spectra of Figure 5 were recorded at 27 mbar for the gas phase and with a 1:2 volume dilution in CCl₄ for the liquid phase.

When toluene-d₈ is admitted in the sample cell, a new series of bands appear centered at 2275, 2240, 2212, 2120, 880, 869, 838 and 819 cm⁻¹. The bands at 2275 and 2240 cm⁻¹ are assigned to stretching modes of aromatic C-D groups, while the bands at 2212 and 2120 cm⁻¹ are assigned to stretching modes of the aliphatic C-D bonds of the toluene-d₈ -CD₃ group¹⁵. The peak at 880 cm⁻¹ is assigned to scissoring modes of the aromatic C-D group while the signal at 869 cm⁻¹ is assigned to asymmetric rocking modes of the aromatic C-D group¹⁵. Bending modes associated with aromatic C-D bonds are centered at 838 and 819 cm⁻¹¹⁵. Upon adsorption of toluene-d₈ on mPAF-1/16 it is seen the appearance of the IR bands characteristic of toluene-d₈ in the liquid phase. In particular, in the higher frequency region (Figure 4, panel A) the presence of the signal at 2275 cm⁻¹ and the simultaneous absence of the band at 2288 cm⁻¹, the presence of the peak at 2120 cm⁻¹ and the absence of the broad band

around 2130 cm^{-1} and in the lower frequency region the presence of the two signals at 880 and 869 cm^{-1} in addition to the presence of the two intense bands centered at 838 and 819 cm^{-1} . This indicates that even at low toluene- d_8 pressures, namely already at 0.2 mbar, confinement effects within the material's micropores result in the formation of a metastable state (liquid-like) of the toluene- d_8 molecules. This is an indication of the high affinity between the HCP surface and the guest molecules. The presence of a liquid-like state is seen up to 27.1 mbar of toluene- d_8 pressure. However, above 6.1 mbar it is seen the appearance of weak signals associated with toluene- d_8 in the gas phase, in particular the signals centered at 2288 and 2135 cm^{-1} , which indicates the presence of both liquid – like and gas phase within the material and sample cell¹⁵. The detection of a liquid – like state in the context of the IR investigation is additional confirmation of the findings reported in section 4.2 on the volumetric adsorption of toluene on mPAF materials.



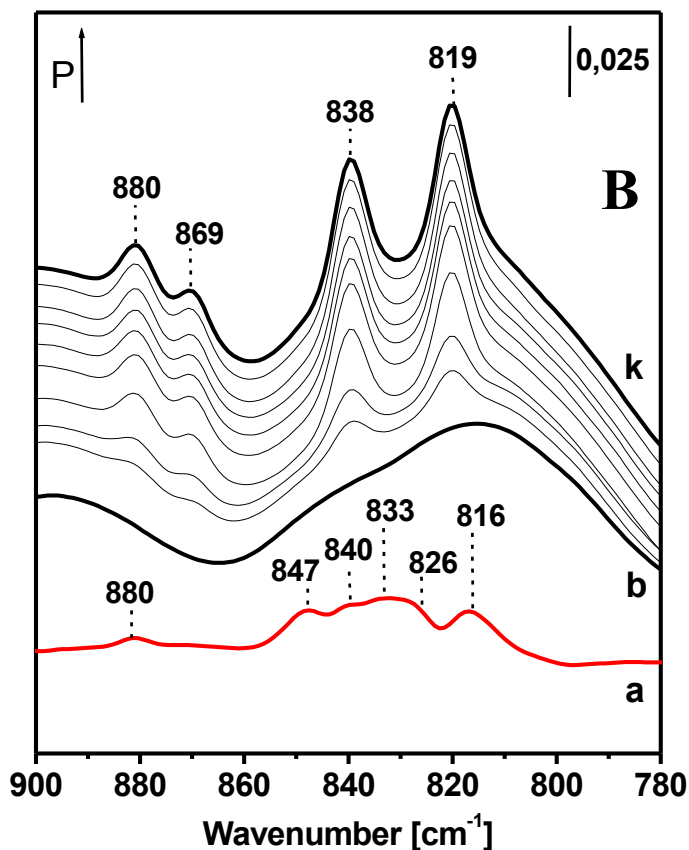
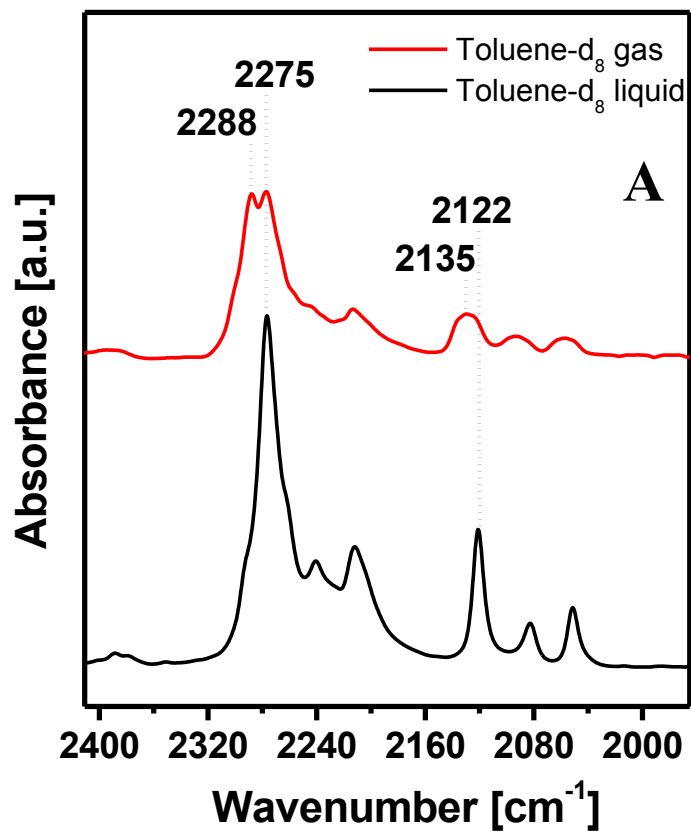


Figure 4. IR spectra of toluene- d_8 adsorbed on mPAF-1/16 at beam temperature (bt) in the 2325 – 2000 cm^{-1} region (panel A) and in the lower frequency region 900 – 780 cm^{-1} (panel B). (a) is the gas-phase spectrum of toluene- d_8 (b) is recorded under vacuum conditions ($1 \cdot 10^{-4}$ mbar) after treating the sample at 150 $^{\circ}\text{C}$ for 3 hours. Spectra from (c) to (k) are associated with the admission of 0.2 (c), 0.9 (d), 2.1 (e), 6.1 (f), 10.1 (g), 14.1 (h), 22.1 (i), 26.1 (j), and 27.1 mbar (k) of toluene- d_8 .



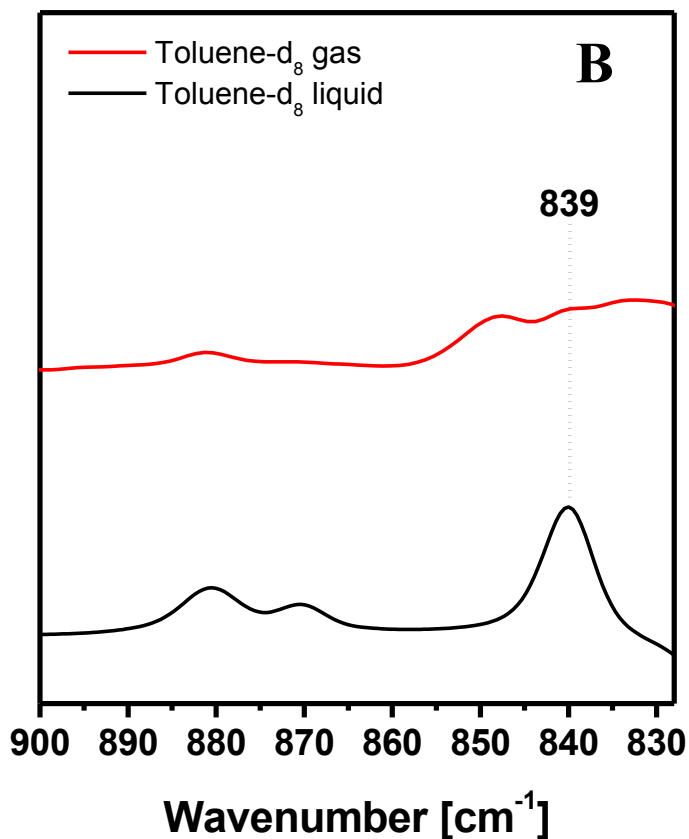


Figure 5. IR spectra of toluene-d₈ in the gas and liquid phase in the 2410 – 1965 cm⁻¹ frequency region (panel A) and in the 900 – 830 cm⁻¹ frequency region (panel B). The gas phase spectrum was recorded at a pressure of 27 mbar and the liquid phase spectrum was recorded with a 1:2 volume dilution in CCl₄.

4.3.2 Toluene-d₈ adsorption on mPAF materials

In Figures 6 and 7 selected adsorption pressure steps of toluene-d₈ on all mPAF materials are reported.

In the high frequency region (Figure 6), upon adsorption of toluene-d₈, it is seen for mPAF-1/30 the red shift of the band centered at 2974 cm⁻¹ to 2967 cm⁻¹. The corresponding 7 cm⁻¹ shift toward lower frequencies is associated with host – guest interactions between the material's methyl groups of -CH₂CH₃ functionalities and the toluene-d₈ molecules, which was already encountered for mPAF-1/16 (section 4.3.1) as it is also seen here for the (b) curves. As was previously observed for mPAF-1/16, no signs of π/π interactions for mPAF-1/30 are detected as well as no indication of interaction between the guest molecules and the bridging methylene groups. For mPAF-1/9 a lower amount of -CH₂CH₃ is observed, hence no appreciable effects on the spectral profile are observed.

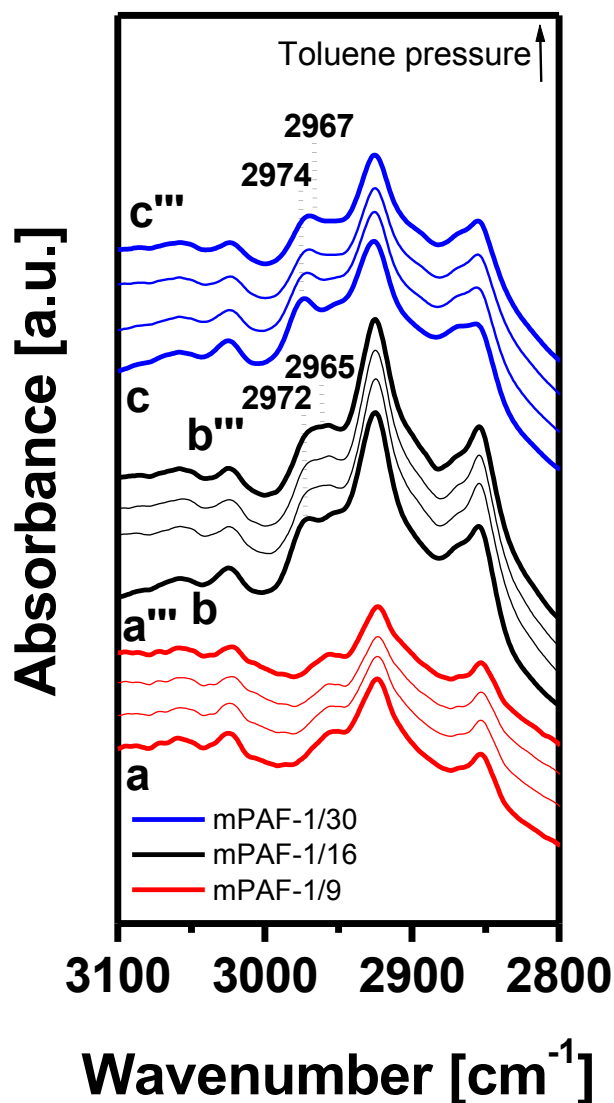
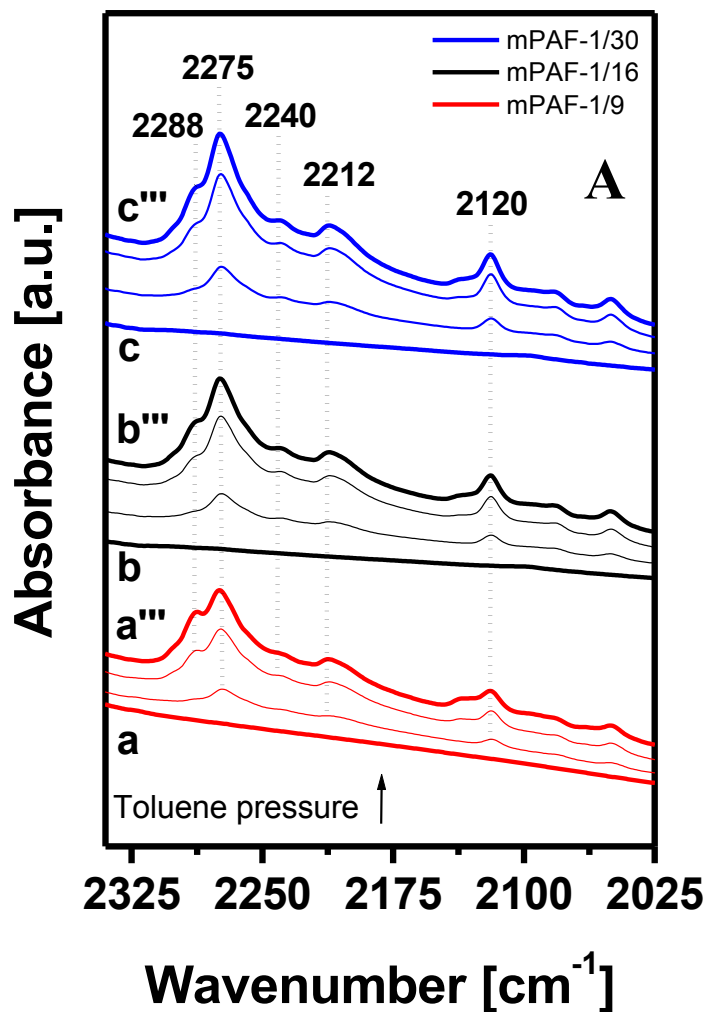


Figure 6. IR spectra of toluene- d_8 adsorbed on mPAF materials at beam temperature (bt) in the high frequency region. (a), (b) and (c) are the mPAFs spectra recorded under vacuum conditions ($1 \cdot 10^{-4}$ mbar) after treating the sample at 150 °C for 3 hours. (a'), (b') and (c') are the mPAFs spectra recorded after admission of 2.1 mbar of toluene- d_8 . (a''), (b'') and (c'') are the mPAF spectra recorded after admission of 16.1 mbar of toluene- d_8 . (a'''), (b''') and (c''') are the mPAF spectra recorded after admission of 27.1 mbar of toluene- d_8 . The spectra are respectively associated with (a): — mPAF-1/9, (b) — mPAF-1/16 and (c) — mPAF-1/30.

The adsorption of toluene-d₈ on mPAF materials result in the formation of the same bands, previously discussed for mPAF-1/16, in the 2335 – 2025 cm⁻¹ region (Figure 7, panel A). However it is worth noting that the relative intensity between the 2288 cm⁻¹ and 2275 cm⁻¹ band increases in favor of the first when a lower FDA concentration is used in the synthetic procedure, meaning ranging from mPAF-1/30 to mPAF-1/9. This effect is explainable by considering the amount of micro and mesoporosity of the materials. In particular, higher amounts of mesopores result in larger quantities of liquid – like toluene-d₈, hence the higher intensity of the gas – phase signal, centered at 2288 cm⁻¹ for the mPAF-1/9 which possess 0.45 cc/g of mesopores versus 0.66 and 0.83 cc/g of mesopores volume displayed by mPAF-1/16 and mPAF-1/30 respectively⁵. Higher amounts of toluene-d₈ in the liquid – like phase are also seen in the low frequency region, when the amount of FDA is increased in the reaction mixture, by inspection of the intensities of the bands centered at 839 and 819 cm⁻¹. Specifically, progressively higher intensity is observed from mPAF-1/9 to mPAF-1/30.



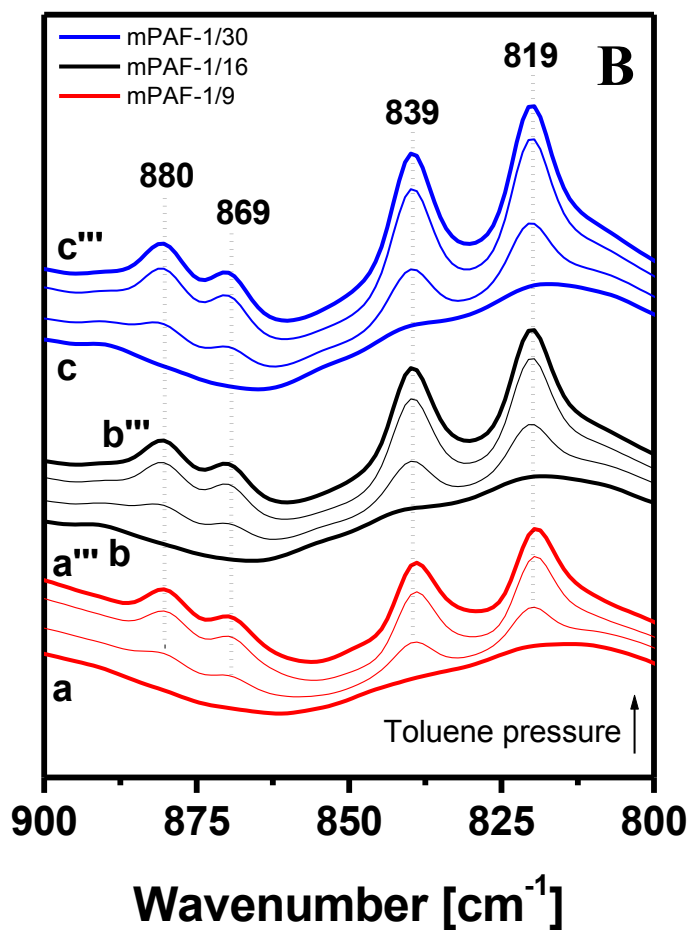


Figure 7. IR spectra of toluene-d₈ adsorbed on mPAF materials at beam temperature (bt) in the 2335 – 2025 cm⁻¹ region (panel A) and in the 900 – 800 cm⁻¹ region (panel B). (a), (b) and (c) are the mPAFs spectra recorded under vacuum conditions ($1 \cdot 10^{-4}$ mbar) after treating the sample at 150 °C for 3 hours. (a'), (b') and (c') are the mPAFs spectra recorded after admission of 2.1 mbar of toluene-d₈. (a''), (b'') and (c'') are the mPAF spectra recorded after admission of 16.1 mbar of toluene-d₈. (a'''), (b''') and (c''') are the mPAF spectra recorded after admission of 27.1 mbar of toluene-d₈. The spectra are respectively associated with (a): — mPAF-1/9, (b) — mPAF-1/16 and (c) — mPAF-1/30.

4.4 SS-NMR study of BTX adsorption on mPAF materials

SS-NMR spectroscopy has been used to obtain deeper insights into the process of the adsorption of toluene- d_8 on mPAF-1/16. Additionally, to acquire general information about host – guest interactions between the HCP and aromatic species, BTX (benzene, toluene, xylene) adsorption was study using the same experimental conditions. Finally, *n*-hexane adsorption was study in order to compare the findings associated with BTX adsorption to the ones related with the adsorption of an aliphatic molecule. mPAF-1/16 sample was degassed under vacuum conditions (1×10^{-4} mbar) prior to adsorption of 19 mbar of the aromatic / aliphatic species. The adsorption was conducted on the sample by means of a homemade cell in which the NMR rotor was placed. After waiting for the equilibrium adsorption (1.5 hours), the rotor was closed with a zirconia cap using a piston attached to the cell. The rotor was then extracted from the cell and submitted for solid state NMR experiments.

4.4.1 Toluene- d_8 adsorption on mPAF-1/16

In Figure 8, the ^{13}C CPMAS NMR spectra and ^1H spin-echo NMR spectra of mPAF-1/16 and mPAF-1/16 with adsorbed toluene- d_8 are reported. The full assignments of the resonance peaks are reported in Chapter 3, section 3.2.4, however for the sake of clarity the main peaks are here summarized.

In the ^{13}C CPMAS NMR spectrum of the bare material, the peak at 14.4 ppm is associated with the carbon of the methyl group of the $-\text{CH}_2\text{CH}_3$ aromatic functionality, while the resonance peak at 17 ppm is associated with the carbon of the methyl group directly attached to the aromatic ring¹⁶. Upon adsorption of toluene- d_8 it is seen the appearance of a signal centered at 20.3 ppm and a shift

toward higher ppm of the signal associated with the $-\text{CH}_2\text{CH}_3$ methyl group. The basis of a CPMAS NMR experiment is the through - space magnetization transfer between ^1H and ^{13}C via heteronuclear dipolar couplings. Consequently, ^{13}C species in close proximities to proton nuclei are visible in the CPMAS spectra. For the toluene- d_8 molecules no ^1H nuclei are present since the molecule is fully deuterated, hence no signals associated with toluene- d_8 carbons should be visible. However, when toluene- d_8 is adsorbed on mPAF-1/16, a sharp peak centered at 20.3 ppm is seen, which is assigned to the carbon of the toluene- d_8 methyl group⁵. This effect is explainable in terms of close proximity between the toluene- d_8 methyl group and the mPAF polymeric framework when host – guest interactions occur⁵. The toluene- d_8 molecules generating the 20.3 ppm resonance, should be close enough to the protons of the HCP surface to generate the cross – polarization between the ^{13}C -D carbons and the C- ^1H protons, necessary for the appearance of the NMR signal.

The observed 1.6 ppm downfield shift of the 14.4 resonance peak is related to the net magnetic field experienced by the methyl carbons of the ethyl functionalities produced by side reactions of the Friedel – Crafts alkylation⁵. When a downfield shift is observed in the presence of an aromatic ring current, it implies that the circulating π electrons induce a magnetic field which is added to the applied NMR magnetic field, causing the carbons located near the edges of the aromatic molecule to experience an overall stronger magnetic field. Here, the downfield shift on the materials methyl carbons is interpreted as having the methyl carbons in the vicinity of the edges of a toluene- d_8 aromatic ring, interacting with the mPAF-1/16 polymeric framework⁵.

In the ^1H spin-echo NMR spectra of the bare material it is seen the presence of a broad peak centered at 0.84 ppm which is assigned to the methyl carbon of the $-\text{CH}_2\text{CH}_3$ generated by ethylation of aromatic rings. Upon adsorption of toluene- d_8 it is seen the splitting of this signal into two resonances, corresponding with the appearance of an intense peak at 0.94 ppm and a shoulder at 0.54 ppm. In addition,

the appearance of a sharp peak at -0.24 ppm is observed. Since no signals associated with toluene-d₈ are present, the appearance of the signal at -0.24 ppm can be attributed to structural features of the mPAF-1/16 polymeric framework. It is interesting to note that the signal is found at negative ppm, hence an upfield shift should be responsible for its appearance. Upfield shifts are caused by ring current effects, which are well reported in the literature^{17,18}. Opposed to what was found in the context of the ¹³C CPMAS NMR spectra, upfield shifts associated with aromatic rings affect nuclei which are positioned either above or below the aromatic ring and pointing toward the center of the ring. In this case, the π electrons movements generate a magnetic field opposite to the one applied by the NMR instrument. The net result is that the nucleus subjected to the ring current, experience a lower intensity magnetic field, hence shifting the corresponding resonance to lower ppm. This is an indication of the fact that the adsorbed toluene-d₈ molecules interact with the methyl protons by facing them with the center of the ring. This orientation can be induced by the shape of the quadrupole moment of the phenyl ring, having two lobes protruding outside the plane of the ring, one above and one below¹⁰.

SS-NMR has thus proven to be effective in giving information about the geometry of the interaction involved in the system mPAF-1/16 – toluene-d₈. The presence of opposite shifts associated with carbons nuclei and protons will be investigated further in the context of the computational studies (section 4.5).

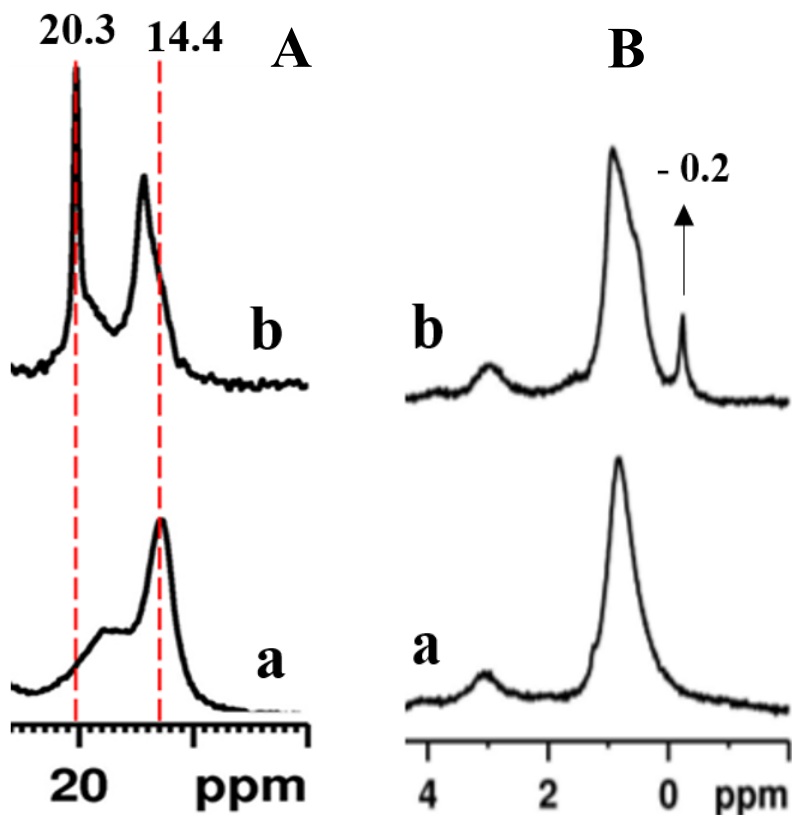


Figure 8. ^{13}C CPMAS NMR spectra (panel A) and ^1H spin-echo NMR spectra (panel B) of mPAF-1/16 before (a) and after adsorption of 19 mbar of fully deuterated toluene (b). Spectra were recorded using a cross-polarization contact time of 10 ms and a MAS rate of 10 kHz.

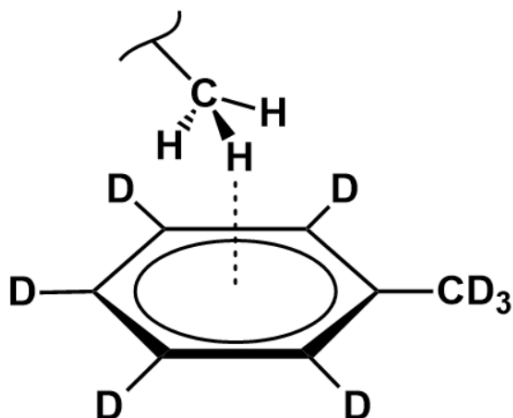


Figure 9. Schematic representation of the geometry associated with the CH/ π interaction established between toluene- d_8 molecules and the methyl group of the mPAF-1/16 polymeric framework.

4.4.2 BTX adsorption on mPAF-1/16

In order to confirm that the observed NMR shifts associated with the material methyl group are indeed caused by π electrons effects on the functional group, the adsorption of benzene, *p*-xylene and *n*-hexane was performed on mPAF-1/16 and the data are reported in Figure 10.

Upon adsorption of aromatic species the same features encountered during the adsorption of toluene- d_8 are here observed. In particular it is seen the downfield shift associated with methyl carbons and the upfield shift associated with methyl protons of the polymeric framework. These features are present for both benzene and *p*-xylene, even though for this last aromatic molecule the intensity of the upfield shifted resonance is lower with respect to the benzene and toluene cases. Interestingly, no apparent changes in the spectral profile are observed when *n*-hexane is adsorbed on

the HCP. This has been interpreted as additional confirmation of the fact that host - guest CH/ π interactions are indeed present between the adsorbed aromatic species and the alkyl methyl groups of the material's framework⁵.

It is observed that not all methyl groups signals display observable shifts when aromatic species are adsorbed. For instance, the shoulder at 0.54 ppm in the ¹H spin-echo NMR spectra might be associated with effects caused by the metastable phase of the adsorbed aromatic molecules within mesopores. In addition, a significant fraction of methyl protons seem to experience a different environment with respect to the one experienced in the bare material. This is probably a consequence of the framework expansion upon contact with a chemically similar solvent. This last effect may be associated with the appearance of the signal at 0.94 ppm⁵.

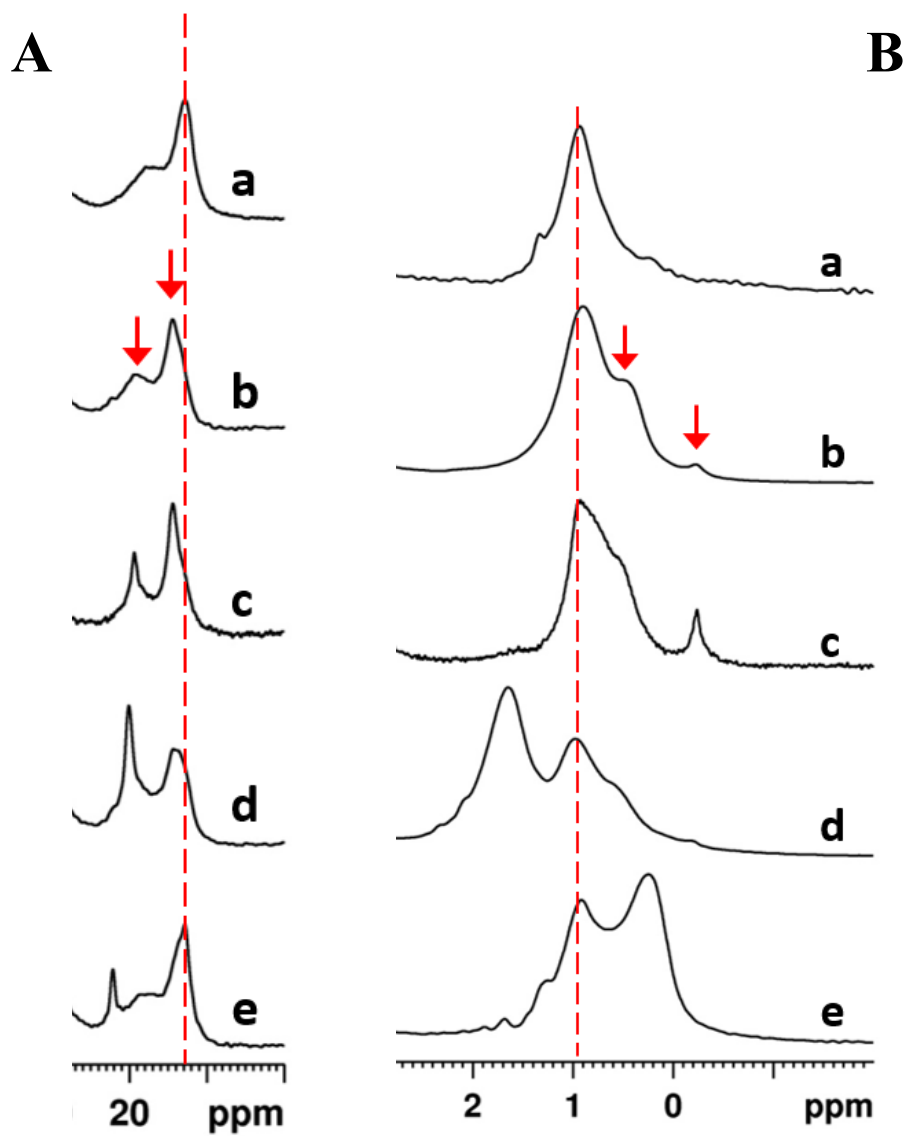


Figure 10. ^{13}C CPMAS NMR spectra (panel A) and ^1H spin-echo NMR spectra (panel B) of the bare mPAF-1/16 (a) and mPAF-1/16 with adsorbed 19 mbar of benzene (b), toluene- d_8 (c), p-xylene (d) and n-hexane (e).

4.5 Computational studies of the adsorption of toluene and *n*-hexane on mPAF materials

In order to gain deeper insights into the nature of the interactions at play between the host polymeric framework of the mPAF materials and the guest toluene molecules, molecular dynamics (MD) and *ab initio* calculations were performed on a small model represented by three monomer units, two of which are linked together in para positions by methylene units. One ethyl group per monomer has been added to allow for the presence of CH/ π interactions of the type detected in the context of the spectroscopic investigations. In Figure 11 the results of the computational studies are reported.

First one guest molecule was added to the system, either toluene or *n*-hexane, and the geometries were optimized at the DFT level. The phenyl rings were kept frozen in position while letting the side chains to adjust, Figure 11, (b) for *n*-hexane and (c) for toluene. For *n*-hexane only weak dispersion forces were found to be responsible for the loose host – guest interactions. For the toluene molecule however, it was found that stronger interactions are responsible for the geometry adopted by the guest molecule during the interaction, in particular the methyl group of the side chain is found to point toward the center of the aromatic ring at a relative small distance of 3.93 Å between the methyl carbon and the aromatic ring center.

To verify the accuracy of the model, ^{13}C NMR isotropic shielding was calculated for the mPAF material before and after adsorption of the adsorbate. When *n*-hexane is added, no apparent changes were encountered, as expected in the context of a weakly interacting molecule such as *n*-hexane. This is in agreement with the experimental data. However, when the toluene molecule is added to the mPAF model an upfield shift of 2.1 ppm of the methyl carbon is observed, while a downfield shift of 2.3 ppm is observed for the adjacent carbon. This is in apparent contrast with the experimental

data where a downfield shift of 1.6 ppm was observed for the methyl carbon. The disagreement could be explained in terms of the higher number of molecules interacting in the real system upon adsorption of 19 mbar of toluene-d₈ which can cause the shielding effect of toluene on the methyl groups to be overwhelmed by the deshielding of the surrounding molecules⁵. For this reason, the calculations were repeated by adding more toluene molecules. However, the optimization of a structure with many molecules interacting with the framework and among them could be biased by the arbitrary choice of the initial geometries. To avoid this problem and obtain a sound average value of the adsorbate effects, a mixed MD/ab initio procedure was adopted. First, a MD calculation was performed on a cubic periodic box containing the HCP model and 3000 toluene molecules, at constant temperature and pressure (27 °C, 1 atm). After equilibration, 10 snapshots, separated by 5 ps, were selected from the MD file, and from each frame a model was extracted, including the HCP and the two toluene molecules closest to each side chain methyl group. Then ¹³C isotropic shieldings were computed at the DFT - GIAO level and compared to the values of the bare mPAF model. The resulting NMR shifts associated with the three methyl carbons of the three side chains after toluene addition are reported in Table 4. The average effect is a downfield shift of 1.7 ppm, which is in good agreement with the 1.6 ppm downfield shift of the experimental results [5]. It is interesting to note that even when a higher number of toluene molecules is used in the calculations, some carbons in some snapshots still exhibit an upfield shift, while maintaining an average downfield shift with the exception of snapshot 4 (see Table 4).

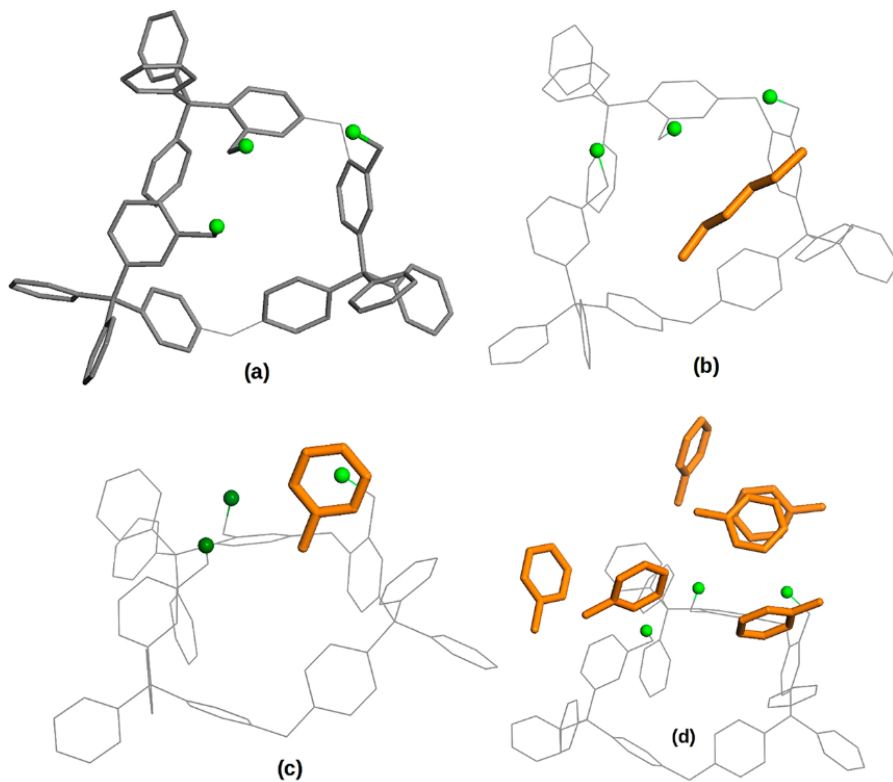


Figure 11. DFT optimized structures of a mPAF material (a), mPAF material with a *n*-hexane guest molecule (b) mPAF material with a guest toluene molecule (c) mPAF material with a toluene guest molecule which is interacting with a methyl carbon via CH/ π interactions (light green) and (d) example of one of the MD snapshots representing the mPAF material and closest toluene molecules.

Table 4. Variation of the methyl ^{13}C isotropic shielding (ppm) with respect to the bare mPAF model, after addition of some toluene molecules (the two molecules closest to each methyl carbon atom). Positive numbers indicate a down-field shift while negative numbers indicate an up-field shift upon toluene addition. 10 snapshots were extracted from MD.

Snapshot number	Methyl carbon 1	Methyl carbon 2	Methyl carbon 3	Average on carbon atoms
1	1.5	1.3	4.5	<i>2.43</i>
2	0.4	4.0	3.3	<i>2.57</i>
3	-0.2	3.2	4.6	<i>2.53</i>
4	-1.2	0.9	-0.9	<i>-0.40</i>
5	0.7	1.1	1.8	<i>1.2</i>
6	-0.4	1.2	0.2	<i>0.33</i>
7	0.3	2.3	1.5	<i>1.37</i>
8	0.9	5.9	0.8	<i>2.53</i>
9	5.3	3.7	-1.4	<i>2.53</i>
10	0.1	3.2	2.8	<i>1.03</i>
Average on snapshots	<i>0.74</i>	<i>2.68</i>	<i>1.72</i>	<i>1.71</i>

4.6 Conclusions

In this chapter, the toluene adsorption capacities of mPAF materials were assessed via volumetric approach. mPAF-1/16 showed the higher toluene uptake with a 154 Q[%] followed by mPAF-1/9 with a 135 Q[%] and finally mPAF-1/30 with a 99 Q[%]. These data were compared to the ones of a well established silica – based adsorbent, namely HSZ-Y which showed a 21 Q[%]. The differences in adsorption capacities were explained in terms of higher affinity of the polymeric framework with the aromatic species which resulted in the swelling of the polymeric framework itself, thus conferring additional volume for the retention of toluene molecules.

The adsorption process was then investigated via a spectroscopic approach, namely FT-IR and SS-NMR. FT-IR spectroscopy was used to study the adsorption of toluene- d_8 on all mPAF materials. The data showed the formation of a liquid – like state of the adsorbed toluene- d_8 within the material's framework in addition to small signs of weak interactions established between the methyl groups of the polymeric framework's alkyl side chains and the interacting toluene- d_8 molecules. SS-NMR spectroscopy was used to gain deeper insights into the nature of the interactions between aromatic species of the BTX family and the mPAF-1/16 framework. The data were compared to the ones obtained for an aliphatic adsorbent, namely *n*-hexane. From the ^{13}C CPMAS NMR data it was observed a downfield shift associated with methyl carbons upon adsorption of 19 mbar of toluene- d_8 while an upfield shift was observed for the protons of the methyl carbons for the ^1H spin-echo NMR data. These effects were also observed for benzene and *p*-xylene but not for *n*-hexane which was interpreted as additional confirmations of the presence of CH/ π interactions between the aromatic guest molecules and the polymeric framework. To shed light on the nature of the different magnetic environment experienced by the two nuclei MD and *ab initio* calculations were performed on a simple HCP model,

at first with one adsorbed molecule, namely *n*-hexane and toluene. This scenario was proven to be ineffective in reproducing the experimental data since an upfield shift was observed for both carbon and proton upon adsorption of toluene. The interaction between *n*-hexane and the HCP framework results in no apparent changes in the NMR polymeric resonances, in agreement with experiments. When the number of adsorbed toluene molecules was increased, the model successfully reproduced the experimental findings, showing an upfield shift associated with the protons of the interacting methyl group, while an average downfield shift was observed for the carbons of both the interacting methyl group and the close methyl carbons. This allows for a better understanding of the dynamics of the adsorption process, showing how magnetic effects of the surrounding aromatic guest molecules induce changes in the magnetic environment of the interacting guest species.

4.7 References

[1] Hypercrosslinked porous polymer materials: design, synthesis, and applications. Tan, L.; Tan, B. *Chem. Soc. Rev.* 2017. 46, 3322 — 3356.

[2] Hypercrosslinked Polymers: A Review. Jing Huang, J.; Turner, S. R. *Polymer Reviews.* 2018. 58, 1, 1 – 41.

[3] A New Strategy to Microporous Polymers: Knitting Rigid Aromatic Building Blocks by External Cross-Linker. Li, B.; Gong, R.; Wang, W.; Huang, X.; Zhang, W.; Li, H.; Hu, C.; Tan, B. *Macromolecules.* 2011. 44, 8, 2410 – 2414.

[4] Synthesis of novel hyper-cross-linked polymers as adsorbent for removing organic pollutants from humid streams. Wang, W.-Q.; Wang, J.; Chen, J. G.; Fan, X.-S.; Liu, Z.-T.; Liu, Z.-W.; Jiang, J.; Hao, Z. *Chem. Eng. J.* 2015. 281 34 – 41.

[5] Hyper-Cross-Linked Polymers for the Capture of Aromatic Volatile Compounds. Paul, G.; Begni, F.; Melicchio, A.; Golemme, G.; Bisio, C.; Marchi, D.; Cossi, M.; Marchese, L.; Gatti, G. *ACS Appl. Polym. Mater.* 2020. 2, 647 – 658.

[6] Thommes, M.; Kaneko, K.; Neimark, A. V.; Olivier, J. P.; Rodriguez-Reinoso, F.; Rouquerol, J.; Sing, K. S. W. *Physisorption of Gases, with Special Reference to the Evaluation of Surface Area and Pore Size Distribution (IUPAC Technical Report).* *Pure Appl. Chem.* 2015. 87 (9–10), 1051–1069.

[7] Interpretation of Infrared Spectra, A Practical Approach, John Coates, Coates Consulting, Newtown, USA, Encyclopedia of Analytical Chemistry, R.A. Meyers (Ed.) Copyright John Wiley & Sons Ltd.

[8] Infrared and Raman Characteristic Group Frequencies: Tables and Charts, 3rd Edition. Socrates, G. Wiley. 2004. ISBN: 978-0-470-09307-8.

[9] Nature and physical origin of CH/p interaction: significant difference from conventional hydrogen bonds. Tsuzuki, S.; Fujiib, A. Phys. Chem. Chem. Phys., 2008, 10, 2584–2594.

[10] Modern Physical Organic Chemistry. Anslyn, E. V.; Dougherty, D. A. University Science Books. 2006. ISBN: 978-1-891389-31-3.

[11] The Hydrogen Bond in the Solid State. Steiner, T. Angew. Chem. Int. Ed. 2002, 41, 48 – 76.

[12] Errahali, M.; Gatti, G.; Tei, L.; Canti, L.; Fraccarollo, A.; Cossi, M.; Marchese, L. Understanding Methane Adsorption in Porous Aromatic Frameworks: An FTIR, Raman, and Theoretical Combined Study. J. Phys. Chem. C 2014. 118 (19), 10053–10060.

[13] Origin of the Attraction in Aliphatic C-H/ δ Interactions: Infrared Spectroscopic and Theoretical Characterization of Gas-Phase Clusters of Aromatics with Methane. Morita, S.; Fujii, A.; Mikami, N.; Seiji Tsuzuki, S. *J. Phys. Chem. A* 2006, 110, 10583-10590.

[14] Interactions of Toluene and n-Hexane on High Silica Zeolites: An Experimental and Computational Model Study. Sacchetto, V.; Bisio, C.; Olivera, D. F. O.; Paul, G.; Gatti, G.; Braschi, I.; Berlier, G.; Cossi, M.; Marchese, L. *J. Phys. Chem. C* 2015, 119, 44, 24875–24886.

[15] Fuson, N.; Garrigou-Lagrange, C.; Josien, M. L. Spectre infrarouge et attribution des vibrations des toluènes C₆H₅CH₃, C₆H₅CD₃ et C₆D₅CD₃. *Spectrochim. Acta* 1960, 16 (1–2), 106–127

[16] Swellable, Water- and Acid-Tolerant Polymer Sponges for Chemoselective Carbon Dioxide Capture. Woodward, R. T.; Stevens, L. A.; Dawson, R.; Vijayaraghavan, M.; Hasell, T.; Silverwood, I. P.; Ewing, A. V.; Ratvijitvech, T.; Exley, J. D.; Chong, S. Y.; Blanc, F.; Adams, D. J.; Kazarian, S. G.; Snape, C. E.; Drage, T. C.; Cooper, A. I. *J. Am. Chem. Soc.* 2014, 136 (25), 9028–9035.

[17] Paul, G.; Steuernagel, S.; Koller, H. Non-Covalent Interactions of a Drug Molecule Encapsulated in a Hybrid Silica Gel. *Chem. Commun.* 2007, 48, 5194–5196.

[18] Induced Paramagnetic Ring Currents. J. A. People, J. A.; Untchl, K. G. J. Am. Chem. Soc. 1996, 88, 21.

Chapter V

Synthetic saponite clays as additives for PIM1 membranes

5.1 Introduction

Gas separation and purification through membrane technology has become a promising candidate as alternative way to CO₂ chemical absorption for carbon capture applications¹. Even though amine-based absorption is still the most employed method for the capturing of CO₂, from both natural and flue gas, ^{1,2} it presents some serious drawbacks. Plant corrosion is usually reported as one of the major issues associated with this type of technology, along with a substantial energetic demand due to regeneration of the liquid phase solvent and environmental concerns on the release of toxic species³. Membrane gas separation is considered a more environment-friendly alternative that exploits the intrinsic ability of permeable materials to selectively separate single components from a gas mixture. The lower costs due to lower energy requirements and the ease of operation give membranes an advantage over other separation technologies⁴. In this respect, polymeric membranes are particularly interesting because of the incredibly diverse landscape of possible synthetic pathways for new materials in combination with simple and relatively cheap production which can result in a more advantageous scale-up for industrial application⁴. Polymers of intrinsic microporosity (PIM) recently have become the

most studied polymeric materials for membrane applications, starting from the first one synthesized, PIM1^{5,6,7}; PIM1 is a glassy and amorphous polymer, soluble in several organic solvents, and can be processed as a gas separation membrane notwithstanding its contorted and barely flexible polymeric chains⁷. The inefficient packing of the PIM1 polymeric chains is the source of both its large internal free volume and of its dramatic and accelerated physical aging, i.e. the fast reduction of free volume^{8,9}. Physical aging is a thermodynamic driven process which manifests as the tendency of glassy polymers to densify reducing the internal free volume, hence resulting in a drop of permeability. This progressive degradation is a thermodynamic driven process which is manifested as the tendency of the polymeric chains to collapse reducing the internal free volume, hence resulting in a progressive drop of the permeation capacities. One way to tackle this problem is the addition of fillers within the polymeric matrix. This strategy has been reported for a wide number of fillers^{10,11,12,13,14,15,16,17}. In particular, the addition of porous polymers (porous aromatic frameworks, PAFs) as fillers has proven to be very effective in reducing physical aging^{12,15} however, their high cost of production prevents an industrial scale implementation. Up to now there have been only a few cases where inexpensive fillers have been used to prevent physical aging^{10,11}. Here we report the use of a synthetic clay named saponite to slow down the physical aging of PIM1 membranes. The synthetic clay is chosen as inexpensive and for the potential to improve the aging behavior of the polymer due to its layered structure. However, given the inorganic nature of these materials, it could be desirable to improve organic affinities via addition of organic moieties through functionalization processes which was performed via a one – pot approach as was reported in Chapter 2.

This chapter is dedicated to the study of the two Mixed Matrix Membranes (MMMs) resulted from the addition of saponite clays to the PIM1 matrix in addition to a pure PIM1 membrane which was used as a comparison. The membranes were characterized via Scanning Electron Microscopy (SEM) and via Transmission

Electron Microscopy (TEM). The permeation data were acquired using a permeation rig whose scheme is reported below (Figure 1). The CO₂ and N₂ were used as single gas for the testing of the permeability performances of the membranes. SS-NMR spectroscopy was used to study the interaction between the fillers and the polymer matrix which was done through inspection of the T1 relaxation times of the carbon atoms associated with the polymeric matrix. The realization of MMMs and the beginning of the corresponding study here presented were performed at the University of Edinburgh in the Chemical Engineering department under the supervision of Prof. Maria – Chiara Ferrari during a three weeks period in June of 2018 and during a three – months period between May and August 2019. The data points outside this time – range were obtained thanks to the help of Dr. Elsa Lasseguette. The membranes permeation performances were analyzed in the course of one year to assess the aging effects.

The findings reported in this section have been published in the journal ACS Applied Polymer Materials with the title Synthetic Saponite Clays as Additives for Reducing Aging Effects in PIM1 Membranes. Begni, F.; Paul, G.; Lasseguette, E.; Mangano, E.; Bisio, C.; Maria-Chiara Ferrari, M-C. Gatti, G.; ACS Appl. Polym. Mater. 2020, 2, 8, 3481–3490.

5.2 Membranes preparation

The procedure for the preparation of PIM1 and 3 wt % (with respect of PIM1 weight) MMMs follows the “solution casting” procedure already reported in the literature ¹⁷. The preparation of the membranes ambient conditions requires the suspension of the filler (6 mg) in 5 mL of CHCl₃ was sonicated with an ultrasound probe for 1 h by using a water bath to maintain the flask at room temperature. Meanwhile, 200 mg of

PIM1 was dissolved in 5 mL of CHCl_3 . After complete dissolution, the PIM1 solution was added to the additive suspension with other 5 mL of CHCl_3 . The mixture was then sonicated again for 2 h at room temperature. The resulting solution was poured into a 5 cm glass Petri dish. The membrane was allowed to form by slow solvent evaporation for 24–36 h under a fume cupboard. Three membranes were obtained, namely a pure PIM1 membrane (PIM1), a MMM composed of PIM1 and SAP110 as a filler (PIM1–SAP110), and finally a MMM composed of PIM1 and SAP-OP (PIM1–SAP-OP). After the drying steps, the thickness of the membranes was determined with a digital micrometer. Before performing permeability measurements, we treated the membranes with methanol by immersion in methanol for 2 h, followed by a drying step under a fume cupboard for an hour and then under vacuum at room temperature overnight before the first measurement. Methanol treatment, in addition to remove any aging – related effects on the PIM1 matrix, allow for the removal of any residual solvent from the casting procedure within the membrane^{18,19}, thus permitting to obtain a comparable starting point regarding membranes performances. In Figure 1, pictures of the obtained PIM1 and MMMs are reported.



Figure 1. Pictures of the PIM1 and MMMs. “e” is the thickness of the corresponding membrane.

5.3 Permeation measurements

The permeation data were acquired at room temperature using a constant volume – variable pressure method in a custom - made time – lag apparatus whose scheme is reported in Figure 2. The permeation cell is composed of three main parts: upstream, permeation cell and downstream. The upstream, or feed side, of the permeation cell is composed of a controlling valve, a pressure gauge, and a volume gas reservoir of 2000 cm³. The sample is positioned in the gas permeation cell. The downstream volume is fixed, and a pressure transducer is used to detect pressure changes. The permeability is obtained from the evolution of pressure of the downstream side. The permeability coefficient, P, was determined from the slope of the pressure *vs* time curve under the steady-state condition using Equation 1.

$$P(G) = \frac{l V_{down}}{A P_{up} RT} \left[\left(\frac{dP_{down}}{dt} \right)_{SS} \right] \quad \text{Equation 1}$$

where *l* is the membrane thickness, *A* is the membrane area, *V_{down}* is the downstream volume, *P_{up}* is the upstream pressure, *P_{down}* is the downstream pressure, *T* is the temperature recorded during analysis, and *R* is the gas constant. The permeability is expressed in barrer defined as 1 barrer = 10⁻¹⁰ $\frac{cm^3_{STP} \cdot cm}{cm^2 \cdot s \cdot cmHg}$ where cm³_{STP} is standard cubic centimeter which is a unit of amount of gas rather than a unit of volume because represents the amount of ideal gas molecules (or moles) that would occupy one cubic centimeter at standard temperature and pressure.

To study aging effects, a comparable initial condition between the PIM1 matrix should be obtained. As reported in the literature^{18,19}, methanol treatments allow for

the complete restoration of permeation performances as if no aging has occurred. For this reason, the permeation data at $t = 0$ (t_0) were acquired right after methanol treatment, which consists of soaking the membrane sample for two hours in methanol under fume cupboard. After methanol treatment the sample was sealed in the permeation cell and left under vacuum over night to allow for the complete desorption of any residue of methanol. Before each experiment, the apparatus is vacuum – degassed and a leak rate is determined from the pressure increase in the downstream part. The ideal selectivity between two gas species i and j is the ratio of the two single-gas permeabilities as reported in Equation 2.

$$\alpha_{ij} = \frac{P(i)}{P(j)} \quad \text{Equation 2}$$

Between every permeation measurement each sample is stored under sealed plastic bag at room temperature.

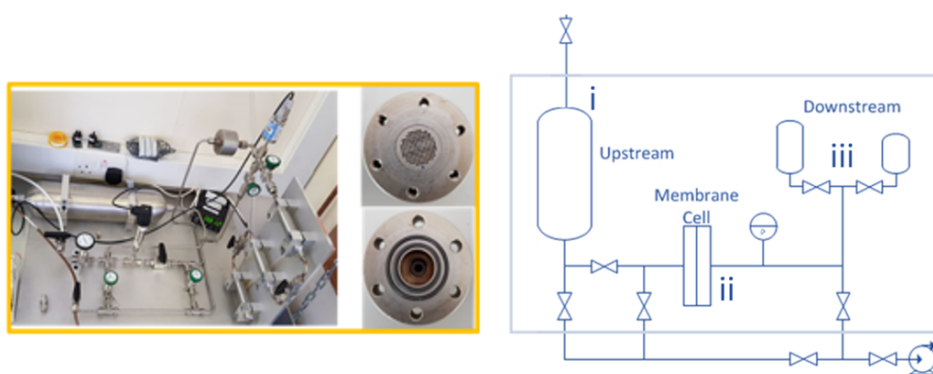


Figure 2. Schematic of the permeation rig (A) and picture of the permeation rig (B).

5.2 Membranes characterization

MMMs appear to be homogeneous at a macroscopic scale (Figure 1), however a deeper inspection of the morphological properties was conducted by means of SEM and TEM microscopies. SEM images are reported in Figure 3. For MMMs the SEM images reveal that the saponite particles are well dispersed within the PIM1 matrix. Particles dimension is heterogeneous and in the range from the hundreds nm to the μm . The surface of the membranes appears non – homogenous due the cutting procedure require for the acquisition of the SEM images.

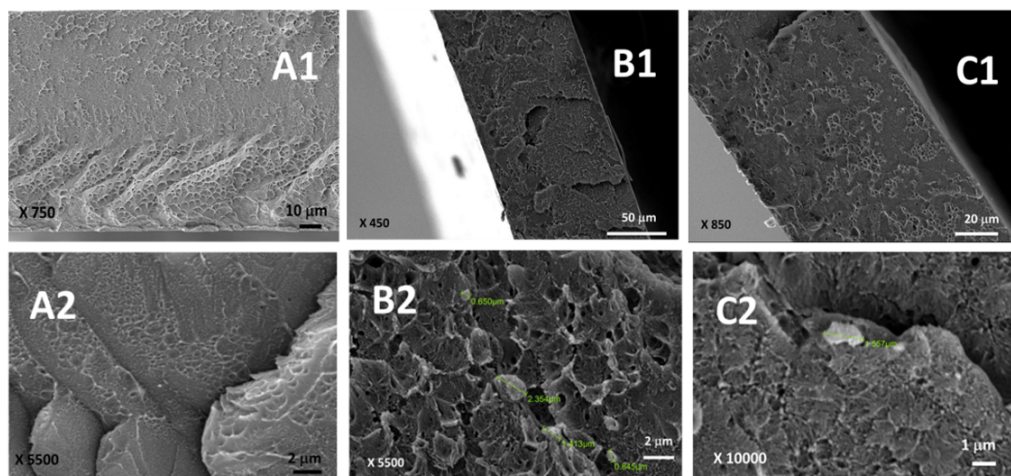


Figure 3. SEM images of membrane samples of pure PIM1 (A) and MMMs PIM1–SAP110 (B) and PIM1–SAP-OP (C) (at two magnifications). Adapted from [20].

In Figure 4 it is reported a TEM micrograph of a section of the PIM1-SAP-OP sample. Here it is seen an aggregate of dimension in the range of the hundreds nm. The layered morphology of the SAP-OP is clearly visible, as the presence of aggregates of few layers of sheet – like crystals.

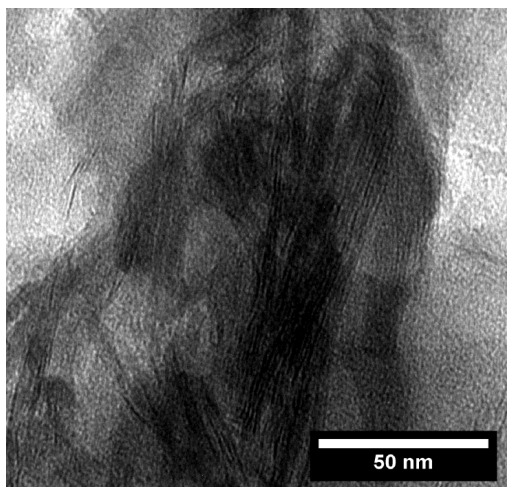


Figure 4. TEM micrograph of a section of the PIM1-SAP-OP sample. Adapted from [20].

In Figure 5 the XRD patterns of both the pure aged PIM1 membrane and aged MMMs are reported. The aging time of all membranes is ≈ 1 year. For pure PIM1, it is seen the typical XRD pattern associated with its amorphous nature, which is also already reported in the literature²¹. Broad bands associated with each reflections are seen, in particular the signals around $13^\circ 2\theta$ is assigned to the inefficiently packed polymeric chains. The band around $18^\circ 2\theta$ is associated with the chain – to – chain distance of efficiently packed polymeric chains and is also linked to the presence of ultramicropores. Finally the signal around $23^\circ 2\theta$ is often found in aromatic systems²¹. For MMMs a closely similar XRD pattern is observed. However, a small shift toward higher 2θ values is observed for all three reflections indicating that the polymeric chains are more close to one another in MMMs, which is interpreted as greater chain – packing²¹.

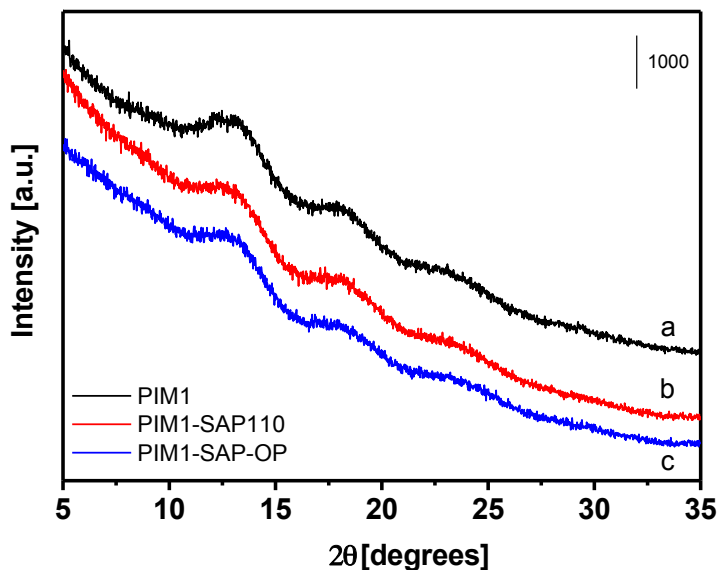


Figure 5. XRD pattern of pure aged PIM1 membrane sample (a), aged PIM1-SAP110 (b) and aged PIM1-SAP-OP (c).

5.3 Membranes permeability measurements

To evaluate the physical aging effects on all membranes samples, permeability measurements were conducted at t_0 and at later times during the course of approximately one year. The time t_0 coincides with the time right after methanol treatment. For permeability measurements this implies approximately 24 h after methanol treatment, since the membrane sample has to be put under vacuum over night in order to allow for the complete desorption of any methanol residue. In Table 1, CO_2 permeability data and CO_2/N_2 selectivity at t_0 are reported.

Table 1. CO₂ permeability data of PIM1, PIM1-SAP110 and PIM1-SAP-OP at t₀. ±5% is the estimated error associated with the CO₂ permeability measurements while ±9% is the estimated error associated with the CO₂/N₂ selectivity.

Sample	Permeability CO₂ [Barrer] (±5%)	Selectivity [CO₂/N₂] (±9%)
PIM1	13400	15
PIM1-SAP110	12300	16
PIM1-SAP-OP	10200	15

As it is seen in Table 1, the CO₂ permeability data and selectivity CO₂/N₂ of pure PIM1 are comparable to the one reported in the literature¹⁵. The addition of the SAP110 and SAP-OP fillers results in a reduced permeability at t₀ by 8 and 24% respectively with respect to pure PIM1. The addition of SAP-OP to the PIM1 matrix preserves the same value of CO₂/N₂ selectivity while a slight increase in selectivity is observed for the PIM1-SAP110 sample from 15 of pure PIM1 to 16. The SSA_{BET} of pure PIM1 (aged) is assessed at 790 cm² while SAP110 and SAP-OP show a SSA_{BET} of respectively 300 and 230 m²/g. When the fillers are added to the polymer matrix the surface area of MMMs is assessed 535 m²/g for PIM1-SAP110 and 486 m²/g for PIM1-SAP-OP for the aged samples. The reduced surface area of MMMs with respect to pure PIM1 is directly linked with the observed lower permeability, because of the lower number of diffusion pathways which characterize MMMs. The MMMs surface area data are obtained from CO₂ adsorption isotherms performed at 0 °C, while the data of the PIM1 sample are obtained from N₂ physisorption at -196.15 °C.

In Figure 6 the CO₂ normalized permeation data acquired in the course of approximately 1 year are reported. For all samples it is seen a sharp drop in the CO₂ permeability within the first 7 days for the MMMs and within the first 15 days for the PIM1 sample. PIM1 shows the typical aging behavior associated with this type of polymer of intrinsic microporosity. This progressive drop in permeability performances is associated with the collapse of internal free volume, which is caused by the thermodynamic process of relaxation of linear polymeric chains⁸. For pure PIM1 it is seen that after approximately 1 year (315 days) the CO₂ permeability has decreased by almost 80%, from 13412 barrer to 2705 barrer while for N₂ the value is only 15% of the t₀ value (891 barrer). The observed PIM1 permeability data are consistent with the ones reported in the literature^{8,15}.

For MMMs the initial drop in permeability performances is quite severe, showing a CO₂ permeation of 57% of the initial value after only 7 days from methanol treatment. However, as time progresses, it is seen that the addition of fillers to the PIM1 matrix indeed results in lower aging rate, as it is clearly visible by the reduced slope of the curves associated with the CO₂ permeation data of MMMs. After 315 days PIM1-SAP110 shows 47% of the initial CO₂ permeability value, namely 5828 barrer, while 41% of the t₀ value is displayed by PIM1-SAP-OP, namely 4140 barrer. One possible explanation for the difference in permeability performances between the two MMMs can be associated with the presence/absence of organic moieties between the filler's T-O-T sheets. SAP-OP is functionalized with a long aliphatic chains (CTA⁺), which is assumed to be positioned parallel to the two planes (above and below) in the interlayer space²². Diffusion of PIM1 polymeric chains within the additives pores is known to happen and has been previously reported for the system PIM1 + PAFs materials^{12,15}. In the case under study it may be possible to account, at least partially, for the recorded difference in aging performances between the MMMs by the presence of organic species between T-O-T sheets in the SAP-OP framework. CTA⁺ moieties can somewhat prevent a fraction of PIM1 polymeric

chains to diffuse in the interlayer space. This is not the case for PIM1-SAP110, because the interlayer space of the filler is free from additional species. The result is that for PIM1-SAP110 the PIM1 polymeric chains are more free to diffuse, to some extent, within T-O-T sheet. The polymeric chains should thus be confined and hindered from further movements, which is consequently seen as a slower aging rate at a macroscopic level²⁰. The small difference in aging rate between the two MMMs samples could be associated with the low content of CTA⁺ in SAP-OP, assessed at 6.3 wt % via TGA analysis, as reported in Chapter 3.

In terms of CO₂/N₂ selectivity for the PIM1 membrane the selectivity has increased from 15 to 19 after 314 days, while for PIM1-SAP110 a small increase is observed from 16 to 17 after 315 days and finally for PIM1-SAP-OP an increase in CO₂/N₂ selectivity is observed at 310 days from 15 to 22.

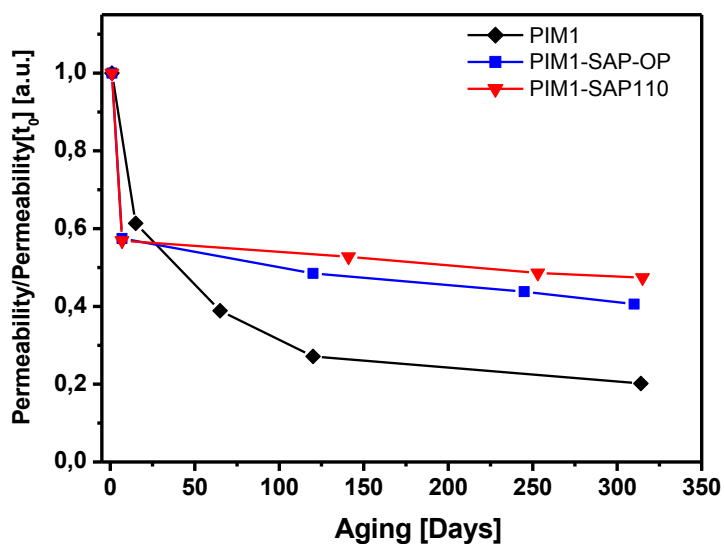


Figure 6. Normalized CO₂ permeation data of PIM1 \blacklozenge , PIM1-SAP110 \blacktriangledown and PIM1-SAP-OP \blacksquare as a function of time. Estimated error: $\pm 5\%$.

In Figure 7 the permeability and selectivity data over time associated with the pure PIM1 and the MMMs are shown in terms of Robeson plots, where the solid black line represents the Robeson upper bound²³.

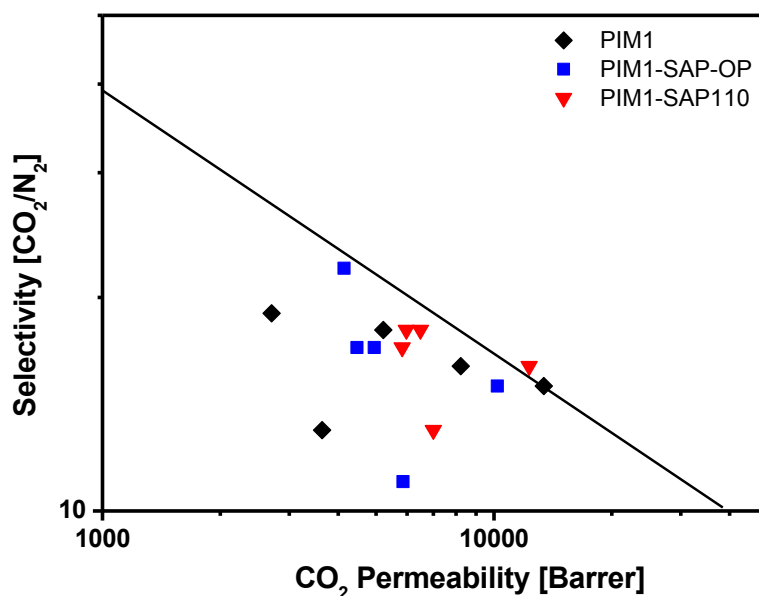


Figure 7. Upper bound correlation for CO₂/N₂ separation of the pure PIM1 membrane \blacklozenge and the two MMMs, PIM1-SAP110 \blacktriangledown and PIM1-SAP-OP \blacksquare .

From the data presented in Figure 7 it can be seen that PIM1-SAP-OP, at t_0 , shows CO₂ permeability and CO₂/N₂ selectivity which are associated with a position in the Robeson plot below the upper bound. For PIM1-SAP110 at t_0 the CO₂ permeability and CO₂/N₂ selectivity allow for the sample to be placed just above the upper bound. The point associated with the pure PIM1 membrane is located right on the upper bound, at t_0 . As aging progresses it is seen, for both MMMs, that the changes in the CO₂ permeability and CO₂/N₂ selectivity result in a departure of the data points from the upper bound. However, for PIM1-SAP110, the points are located farther from the upper bound with respect to the points associated with PIM1-SAP-OP where the

last recorded measurement of CO₂ and N₂ permeability, put this sample closer to the upper bound with respect to the others.

5.4 T1 relaxation times membranes measurements

It is reported in few studies in the literature^{12,15} that measurements of the ¹³C spin – lattice relaxation times (T1) provide information about the dynamics of the polymeric chains in polymer membranes. In particular it is possible to study the change in flexibility of PIM1 polymeric chains as a function of times, that is as physical aging occurs^{12,15}. In addition, for MMMs, T1 values can be used to gain information about the interaction between the filler and the polymer matrix^{12,15}. T1 measurements were performed on all membrane samples by cutting the membranes in small discs which could be then fit into the NMR rotor. T1 curves were obtained by plotting the intensity of the carbon signals versus time. A single - exponential decay was used to fit the data via Equation 3.

$$I_t = I_0 e^{\frac{-t}{T_1}} \quad \text{Equation 3}$$

T1 values were recorded at three different times, namely at t₀ right after methanol treatment, after three months from methanol treatment (t₃) and after almost 1 year after methanol treatment (t₁₂). Relative rate of change of T1 values have been obtained by use of the formula (t_{final} – t_{initial})/t_{initial}, meaning changes in T1 values after three months with respect to t₀ were obtained using the formula (t₃ – t₀)/t₀, while from 3 to 12 months the formula (t₁₂ – t₃)/t₃ was used. In Figure 8 the ¹³C CPMAS NMR spectra of the pure PIM1 membrane and MMMs are reported with the

corresponding assignments while percentage changes in T1 values as a function of time for every assigned carbon are shown in Figure 9.

The ^{13}C resonances are broad because of rigidity of the polymer matrix which results in restricted mobility of the polymeric chains. The resolution and intensities are, however, sufficient for the measurement of relaxation times and chemical shifts. The addition of fillers to the polymeric matrix does not result in visible changes in the spectral profile.

For PIM1, T1 values associated with the carbon of the methyl groups are very short, ≈ 0.3 s, and are not significantly influenced by physical aging, which indicates that they are in high mobile state. Also, the addition of fillers did not induce significant changes. However, the carbons associated with the backbone of the polymeric chains show T1 values of the order of seconds which is related to the rigidity of the polymeric chains. For the PIM1 membrane, as aging occurs, it is seen an increase in T1 values for the carbons A, F and G while a decrease in T1 values is found for the other carbons. T1 values measured in the period between 3 and 12 months are longer for all carbons except H in agreement with the aging behavior of PIM1, as reported in the literature. When physical aging occurs, polymeric chains tend to pack themselves more efficiently thus reducing the internal free volume. Carbons in a more constricted environment show longer spin – lattice relaxation times with respect to carbons in higher mobile state^{12,15}.

For PIM1-SAP110, longer T1 values were recorder at t_3 , indicating an overall aging of the membrane sample. The detection of longer T1 times at t_3 with respect to t_0 correlates well with the CO_2 permeation data which showed a sharp drop of permeability performances in the first period. T1 values measured at t_{12} however, are all shorter with respect to the values measured at t_3 indicating the presence of favorable interactions between the PIM1 matrix and the SAP110 filler. Shorter spin – lattice relaxation times must be associated with higher mobility. A possible

interpretation of the presented data could be the following: in the case of the PIM1 + SAP110 system, partial chain intercalation between saponite T-O-T sheets could result in the preservation of small free volumes which could then result in shorter T1 values as aging progresses. While a fraction of the PIM1 chains diffuses within the saponite interlayer space, it experiences a less hindered environment with respect to the one experienced by the other fraction of PIM1 chains which, as aging occurs, becomes more and more packed. Aging effects should be reduced in longer times as consequence of chains confinement.

A similar situation is seen for PIM1-SAP-OP, even though the extent to which T1 values decrease between t_3 and t_{12} is smaller with respect the one observed for PIM1-SAP110. In the period t_0 - t_3 , the increase in T1 times is also slightly less with respect to the one observed for PIM1-SAP110. PIM1-SAP-OP is composed of an organo - functionalized saponite material and as evidenced before in the context of the permeability measurements, this shouldn't allow chains – diffusion to the extent which is expected for a MMMs with SAP110 as filler. Indeed, the inspection of the rate of change of T1 values for PIM1-SAP-OP is consistent with a scenario in which the PIM1 chains are somewhat more hindered in the process of diffusion within T-O-T sheets, which in turn is reflected in the less pronounced decrease of T1 values from t_3 to t_{12} .

In general, the rate of change of the ^{13}C spin – lattice relaxation times seems to be influenced by the nature of the carbons, namely aromatic groups were slightly more influenced by the addition of saponite fillers. This fact could also support an interpretation of the aging behavior which involves the presence of hydrogen bond – type interactions between the polar groups of the saponite fillers with aromatic groups of the PIM1 chain. This type of interaction could result in lower mobility of the polymeric chains. In addition, if weak interactions are somewhat responsible for the slowdown of the aging effects in MMMs, for PIM1-SAP-OP they should be less intense as T1 values seems to indicate. This is because in PIM1-SAP110 the polar

groups of the PIM1 chains interact with the Na^+ cations which should form stronger interactions with respect to CTA^+ cations of SAP-OP.

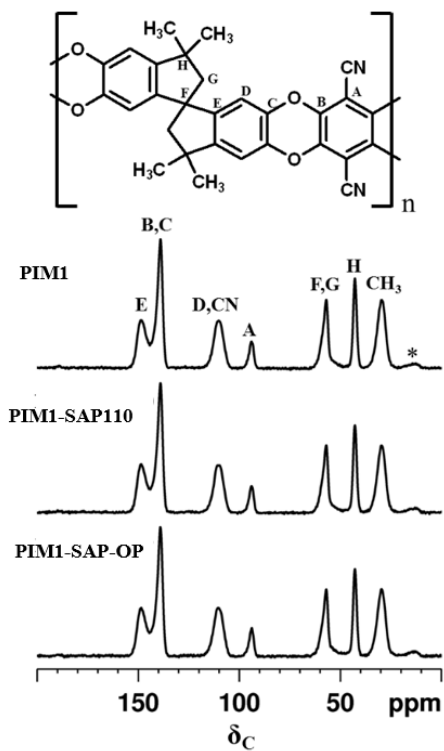


Figure 8. ^{13}C CPMAS NMR spectra of the pure PIM1 membrane and MMMs. * denotes spinning side bands.

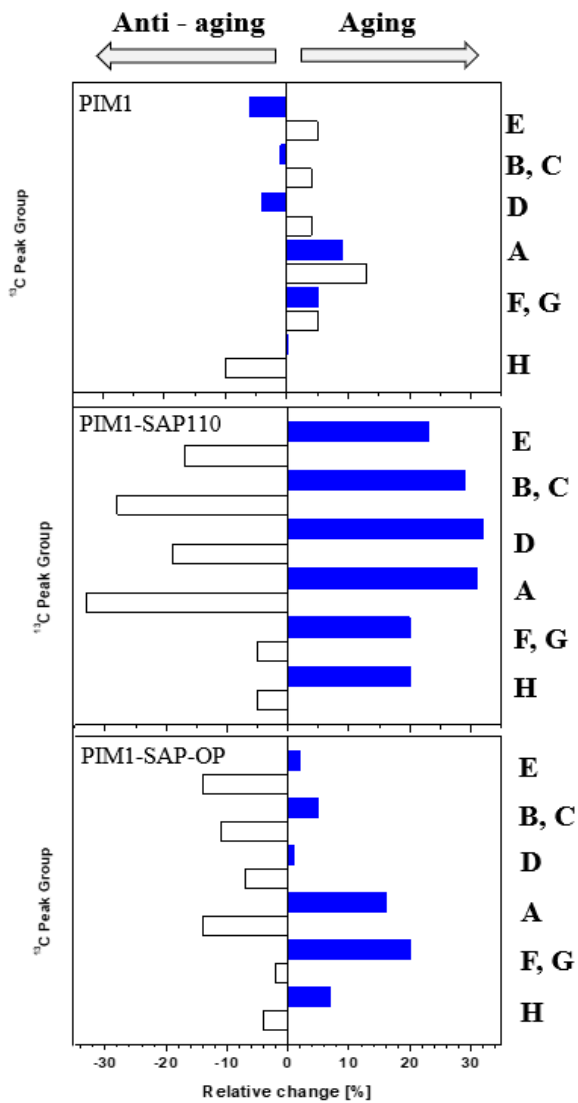


Figure 9. Bar charts representing percentage changes in T1 values for the carbons assigned in panel (A) for $(t_3 - t_0)/t_0$ (■) and for $(t_{12} - t_3)/t_3$ (□).

5.5 Conclusions

Two Mixed Matrix Membranes (MMMs) were obtained via addition to the PIM1 matrix of synthetic saponite clays as fillers. Two MMMs were prepared, namely PIM1-SAP110 and PIM1-SAP-OP. SEM and TEM investigations of the membrane samples revealed that the fillers are indeed well dispersed within the polymer matrix. XRD characterization showed that the presence of fillers induced a slight increase in the packing of the polymeric chains thus resulting in slight increase in densification of the MMMs. CO₂ and N₂ permeability measurements were performed in the laboratories of the Chemical Engineering department of the University of Edinburgh for approximately 1 year. PIM1 permeation data revealed the classical aging behavior associated this type of Polymer of Intrinsic Microporosity. MMMs showed a rapid decrease in the gas permeation rate up to approximately 1 week after methanol treatment, namely a drop of 43% with respect to the initial value for both MMMs samples. After the initial sharp decrease in the CO₂ permeation rate, a further drop of 10 and 16% was observed for PIM1-SAP110 and PIM1-SAP-OP respectively, after approximately 1 year of aging. The final CO₂ permeability is assessed at 20% of the initial value for the pure PIM1 sample, while for PIM-SAP110 and PIM1-SAP-OP is respectively assessed at 47 and 41% of the t_0 value. SS-NMR investigation was conducted on the all the membranes samples via measurements of the ¹³C spin – lattice relaxation times (T1). T1 measurements were performed at t_0 , right after methanol treatment, at t_3 namely after 3 months and at t_{12} namely approximately 1 year after t_0 . For pure PIM1 it was found the classical aging behavior already found in the literature for this of polymers, namely a progressive increase in T1 values associated with almost all the carbons of the polymeric chains. Increase in T1 values is related to the collapse of the internal free volume of PIM1 membranes, which results in reduced permeability performances. For MMMs at t_3 it was also found an increase in T1 values for all the carbons of the PIM1 matrix which is related

to the CO₂ reduced permeability observed in the first days after casting and methanol treatment. However, between t₃ and t₁₂ it is observed a decrease in T1 values for all the carbons for both MMMs samples, even though the effect is more pronounced for PIM1-SAP110. A possible explanation for the observed aging behavior in both CO₂ permeability experiments and T1 measurements could be related to the process of PIM1 chain diffusion, at least partially, within the interlayer space of saponite fillers as aging progresses. For PIM1-SAP110 the space between T-O-T sheets is free hence more prone to accommodate a portion of the polymeric chain which consequently should experience a less crowded environment, thus resulting in shorter T1 values for the associated carbons. However, the interlayer space of SAP-OP is occupied by the CTA⁺ species and consequently it is more difficult for portions of PIM1 chains to diffuse within the interlayer space, which is seen macroscopically as the 6% difference in the observed CO₂ permeation rate of PIM1-SAP-OP.

It is also possible that weak interactions between polar groups of PIM1 and fillers could also result in a slowdown of the aging behavior, namely Na⁺ species could interact with sp² carbons of the PIM1 backbone producing stronger electrostatic interactions with respect to the weaker interactions which could be at play between polar groups with CTA⁺ species in PIM1-SAP-OP

5.6 References

[1] Emerging CO₂ Capture Systems. *Int. J. Greenhouse Gas Control*. Abanades, J. C.; Arias, B.; Lyngfelt, A.; Mattisson, T.; Wiley, D. E.; Li, H.; Ho, M. T.; Mangano, E.; Brandani, S. 2015, 40, 126–166.

[2] CO₂ Removal from Natural Gas by employing amine absorption and membrane technology - A technical and economical analysis. *Peters, L.; Hussain, A.; Follmann, M.; Melin, T.; Hägg, M. B. Chem. Eng. J.* 2011, 172, 952–960.

[3] Pushing the limits of intensified CO₂ post-combustion capture by gas–liquid absorption through a membrane contactor. *Chabanon, E.; Bounaceur, R.; Castel, C.; Rode, S.; Roizard, D.; Favre, E. Chem. Eng. Process.* 2015, 91, 7–22.

[4] Polymers for gas separations: the next decade. *Stern, S. A. J. Membr. Sci.* 1994, 94, 1–65.

[5] Phthalocyaninebased nanoporous network polymers. *McKeown, N. B.; Makhseed, S.; Budd, P. M. Chem. Commun.* 2002, 23, 2780–2781.

[6] Polymers of Intrinsic Microporosity (PIMs): Bridging the Void between Microporous and Polymeric Materials *McKeown, N. B.; Budd, P. M.; Msayib, K. J.; Ghanem, B. S.; Kingston, H. J.; Tattershall, C. E.; Makhseed, S.; Reynolds, K. J.; Fritsch, D.. Chem. - Eur. J.* 2005, 11, 2610–2620.

[7] Polymers of intrinsic microporosity (PIMs): robust, solution processable, organic nanoporous materials. Budd, P. M.; Ghanem, B. S.; Makhseed, S.; McKeown, N. B.; Msayib, K. J.; Carin, E.; Tattershall, C. E. *Chem. Commun.* 2004, 230–231.

[8] Physical aging, CO₂ sorption and plasticization in thin films of polymer with intrinsic microporosity (PIM-1). Tiwari, R. R.; Jin, J.; Freeman, B. D.; Paul, D. R. J. *Membr. Sci.* 2017, 537, 362–371.

[9] Effect of physical aging on the gas transport and sorption in PIM-1 membranes. Bernardo, P.; Bazzarelli, F.; Tasselli, F.; Clarizia, G.; Mason, C. R.; Maynard-Atem, L.; Budd, M.; Lanč, M.; Pilnáček, K.; Vopička, O.; ACS Applied Polymer Materials pubs.acs.org/acsapm Article I Friess, K.; Fritsch, D.; Yampolskii, Y. P.; Shantarovich, V.; Jansen, J. C. *Polymer* 2017, 113, 283–294.

[10] PIM-1 mixed matrix membranes for gas separations using costeffective hypercrosslinked nanoparticle fillers. Mitra, T.; Bhavsar, R. S.; Adams, D. J.; Budd, P. M.; Cooper, A. *ICChem. Commun.* 2016, 52, 5581–5584.

[11] Kinoshita, Y.; Wakimoto, K.; Gibbons, A. H.; Isfahani, A. P.; Kusuda, H.; Sivaniah, E.; Ghalei, B. Enhanced PIM-1 membrane gas separation selectivity through efficient dispersion of functionalized POSS fillers. *J. Membr. Sci.* 2017, 539, 178–186.

[12] Lau, C. H.; Konstas, K.; Thornton, A. W.; Liu, A. C. Y.; Mudie, S.; Kennedy, D. F.; Howard, S. C.; Hill, A. J.; Hill, M. R. Gas- Separation Membranes Loaded with Porous Aromatic Frameworks that Improve with Age. *Angew. Chem., Int. Ed.* 2015, 54, 2669–2673.

[13] Mixed matrix membranes based on MIL-101 metal–organic frameworks in polymer of intrinsic microporosity PIM-1. Khdayyer, M.; Bushell, A. F.; Budd, P. M.; Attfield, M. P.; Jiang, D.; Burrows, A. D.; Esposito, E.; Bernardo, P.; Monteleone, M.; Fuoco, A.; Clarizia, G.; Bazzarelli, F.; Gordano, A.; Jansen, J. C. *Sep. Purif. Technol.* 2019, 212, 545–554.

[14] Alberto, M.; Bhavsar, R.; Luque-Alled, J. M.; Vijayaraghavan, A.; Budd, P. M.; Gorgojo, P. Impeded physical aging in PIM-1 membranes containing graphene-like fillers. *J. Membr. Sci.* 2018, 563, 513–520.

[15] Ending Aging in Super Glassy Polymer Membranes. Lau, C. H.; Nguyen, P. T.; Hill, M. R.; Thornton, A. W.; Konstas, K.; Doherty, C. M.; Mulder, R. J.; Bourgeois, L.; Liu, A. C. Y.; Sprouster, D. J.; Sullivan, J. P.; Bastow, T. J.; Hill, A. J.; Gin, D. L.; Noble, R. D. *Angew. Chem., Int. Ed.* 2014, 53, 5322–5326.

[16] Smith, S. J. D.; Hou, R.; Konstas, K.; Akram, A.; Lau, C. H.; Hill, M. R. Control of Physical Aging in Super-Glassy Polymer Mixed Matrix Membranes. *Acc. Chem. Res.* 2020, 53, 1381.

[17] Hou, R.; Smith, S. J. D.; Wood, C. D.; Mulder, R. J.; Lau, C. H.; Wang, H.; Hill, M. R. Solvation Effects on the Permeation and Aging Performance of PIM-1-Based MMMs for Gas Separation. *ACS Appl. Mater. Interfaces* 2019, 11, 6502–6511.

[18] Solution processed, organophilic membrane derived from a polymer of intrinsic microporosity. Budd, P. M.; Elabas, E. S.; Ghanem, B. S.; Makhseed, S.; McKeown, N. B.; Msayib, K. J.; Tattershall, C. E.; Wang, D. *Adv. Mater.* 2004, 16, 456–459.

[19] Gas permeation parameters and other physicochemical properties of a polymer of intrinsic microporosity: Polybenzodioxane PIM-1. Budd, P. M.; McKeown, N. B.; Ghanem, B. S.; Msayib, K. J.; Fritsch, D.; Starannikova, L.; Belov, N.; Sanfirova, O.; Yampolskii, Y.; Shantarovich, V. J. *Membr. Sci.* 2008, 325, 851–860.

[20] Synthetic Saponite Clays as Additives for Reducing Aging Effects in PIM1 Membranes. Begni, F.; Paul, G.; Lasseuguette, E.; Mangano, E.; Bisio, C.; Maria-Chiara Ferrari, M-C. Gatti, G.; *ACS Appl. Polym. Mater.* 2020, 2, 8, 3481–3490.

[21] Highly Permeable Chemically Modified PIM-1/Matrimid Membranes for Green Hydrogen Purification. Yong, W. F.; Li, F. Y.; Chung, T.-S.; Tong, Y. W. *J. Mater. Chem. A* 2013, 1, 13914.

[22] The effect of synthesis gel dilution on the physico chemical properties of acid saponite clays. Costenaro, D.; Gatti, G.; Carniato, F.; Paul, G.; Bisio, C.; Marchese, L. *Microporous Mesoporous Mater.* 2012, 162, 159–167.

[23] The upper bound revisited. Robeson, L. M. J. *Membr. Sci.* 2008, 320, 390 – 400.

Chapter VI

Hyper cross – linked polymers as additives for PIM1 membranes

6.1 Introduction

Polymers of intrinsic microporosity or PIMs, since their discovery by Prof. Neil McKeown and co-workers in the 1990s¹ have attracted great research interest because of the potential applications in fields such as gas storage and gas separation². In particular, PIMs can be processed in the form of thin membranes, which can be employed for separations applications³. Separation via membrane technologies is usually preferred over liquid absorption on amine – based solvents due to ease of operation, greater plant durability, lower costs of regeneration and lower environmental risks⁴. The tradeoff between the permeability of the gas and the selectivity, namely the difference in the rate of diffusion of two or more gasses, is known as “Robeson upper bound”⁵. Usually, one comes at the expense of the other, however it was soon demonstrated for PIM1 that PIM based membranes shows good performances in both permeability and selectivity^{5,6}. It is essential that permeability performances remain constant over time. PIM are glassy polymers, namely they operate at temperatures lower than their glass transition⁷. As for all glassy materials, aging effects are known to occur over time⁸. In particular for PIM1 it is observed a

drop in permeability which after 1 year is usually assessed at 20% with respect to the initial value^{6,9,10}. This is due to the collapse of the internal free volume because movements of the polymeric chains trying to reach lower energy configurations, that is, aging is a thermodynamic driven process⁶. To slow down aging effects various strategies have been tried in recent years⁶; one of the most effective strategies consists in the addition of porous materials to the PIM1 polymeric matrix^{11,12,13,14,15}. Here a combination of both favorable interactions with the PIM polymeric matrix, in conjunction with the presence of additional gas diffusion pathways offered by the porous structure of the fillers, result in lower aging rates of the PIM matrix⁶. A vast number of fillers have been tried for production of Mixed Matrix Membranes (MMMs), ranging from inorganic to organic materials such as Porous Aromatic Frameworks (PAFs)^{16,17}, which have been demonstrated to remarkably slow down PIM1 aging. However, PAFs are usually very expensive and difficult to produce and for this reason cheaper polymers have also been tried with good results¹⁵. Here we propose the use of novel hyper cross – linked polymers for production of MMMs for CO₂/N₂ gas separations applications. In particular two types of HCPs have been tested as additives, namely ABTs and DIXYT materials. The first are HCPs whose framework is based on tetraphenyl methane units linked together via reaction of 1,3,5-tris(bromomethyl)benzene with AlBr₃ while DIXYT materials are based of diphenyl sulfide monomers linked together via reaction of α,α' -dichloro-p-xylene with TiCl₄. For both types of HCPs two materials were obtained namely ABT01 and DIXYT01 where dichloromethane was used as solvents and the reaction temperature was set to 35 °C and ABT02 and DIXYT02 where dichloroethane was used as solvent and the reaction temperature was set to 80 °C. The details of the synthetic procedure are reported in Chapter 2. MMMs were studied in collaboration with University of Edinburgh at the Chemical Engineering department under the supervision of Prof. Maria – Chiara Ferrari for a period up to more than 1 year for DIXYT additives and for more than two years for ABT materials.

6.2 Membranes preparation

The procedure for the preparation of PIM1 and 3 / 10 wt % (with respect of PIM1 weight) MMMs follows the “solution casting” procedure already reported in the literature¹⁸ and in Chapter V. The preparation of the membranes at ambient conditions requires the suspension of the filler (6 mg for the 3 wt % and 20 mg for the 10 wt %) in 5 mL of CHCl₃ was sonicated with an ultrasound probe for 1 h by using a water bath to maintain the flask at room temperature. Meanwhile, 200 mg of PIM1 was dissolved in 5 mL of CHCl₃. After complete dissolution, the PIM1 solution was added to the additive suspension with other 5 mL of CHCl₃. The mixture was then sonicated again for 2 h at room temperature. The resulting solution was poured into a 5 cm glass Petri dish. The membrane was allowed to form by slow solvent evaporation for 24–36 h under a fume cupboard. Eight membranes were obtained, namely a pure PIM1 membrane (PIM1), seven MMMs composed of: PIM1 and the two ABT fillers at 3 and 10 wt%, namely PIM1-ABT01-3%, PIM1-ABT01-10%, PIM1-ABT02-3% and PIM1-ABT02-10% as a filler (PIM1–SAP110); PIM1 with DIXYT materials with a 3 and 10 wt %, namely PIM1-DIXYT01-3%, PIM1-DIXYT02-10%, PIM1-DIXYT01-10% and PIM1-DIXYT02-10%. After the drying steps, the thickness of the membranes was determined with a digital micrometer. Before performing permeability measurements, we treated the membranes with methanol by immersion in methanol for 2 h, followed by a drying step under a fume cupboard for an hour and then under vacuum at room temperature overnight before the first measurement. Methanol treatment, in addition to remove any aging – related effects on the PIM1 matrix, allow for the removal of any residual solvent from the casting procedure within the membrane^{18,19}, thus permitting to obtain a comparable starting point regarding membranes performances.

6.3 Permeation measurements

Permeation measurements were performed using the same constant volume – variable pressure method in the same custom - made time – lag apparatus used for PIM1 + saponites MMMs, whose scheme is reported in Figure 2 of Chapter V. Before each measurement at t_0 the membrane sample was regenerated in methanol for 2 hours and then sealed in the permeation cell under vacuum over night to allow for the complete desorption of any residue of methanol. The permeability coefficient P was calculated using Equation 1 and the CO_2/N_2 ideal selectivity was calculated using equation 2, both reported in Chapter V.

6.2.1 PIM1 + ABT materials

In Figure 2 the normalized CO_2 permeation data over time are reported for PIM1 and MMMs based on the addition of ABT materials with 3 and 10 wt% load to the PIM1 polymeric matrix. In Table 1 permeability data and the CO_2/N_2 selectivity are reported for PIM1 and MMMs at t_0 .

Table 1. CO₂ permeability data of PIM1, PIM1-ABT01-3%, PIM1-ABT02-3%, PIM1-ABT01-10% and PIM1-ABT02-10% at t₀. ±5% is the estimated error associated with the CO₂ permeability measurements while ±9% is the estimated error associated with the CO₂/N₂ selectivity.

Sample	Permeability CO₂ [Barrer] (±5%)	Selectivity [CO₂/N₂] (±9%)
PIM1	13400	15
PIM1-ABT01-3%	14700	18
PIM1-ABT02-3%	8690	14
PIM1-ABT01-10%	8800	13
PIM1-ABT02-10%	7500	18

As it is seen in Table 1, the CO₂ permeability data and the CO₂/N₂ selectivity of pure PIM1 at t₀ are comparable to those reported in the literature^{19,20}. The addition of ABT01 with a load of 3 wt% results in increased CO₂ permeability and increased CO₂/N₂ selectivity at t₀ with respect to the pure PIM1 membrane. The fact that an higher content of ABT01 within the PIM1 matrix (PIM1-ABT01-10%) results in a lower CO₂ permeability with respect to pure PIM1 (13400 barrer vs 8800) suggests that the textural properties of ABT01 are not the cause of the increased CO₂ permeability for the PIM1-ABT01-3%. For PIM1-ABT02-3% and PIM1-ABT02-10% the CO₂ permeability is respectively assessed at 8690 and 7500 barrer while the CO₂/N₂ selectivity are respectively 14 and 18. In terms of permeability both samples show lower CO₂ permeability with respect to the pure PIM1 membrane while the

selectivity is lower for PIM1-ABT02-3% and higher for PIM1-ABT02-10% with respect to the pure PIM1 membrane at t_0 .

In Figure 1 the CO₂ normalized permeation data are reported. Data were acquired up to: 850 days for PIM1-ABT02-10%, 850 days for PIM1-ABT02-3%, 336 days for PIM1-ABT01-3% and 314 days for the pure PIM1 membrane sample.

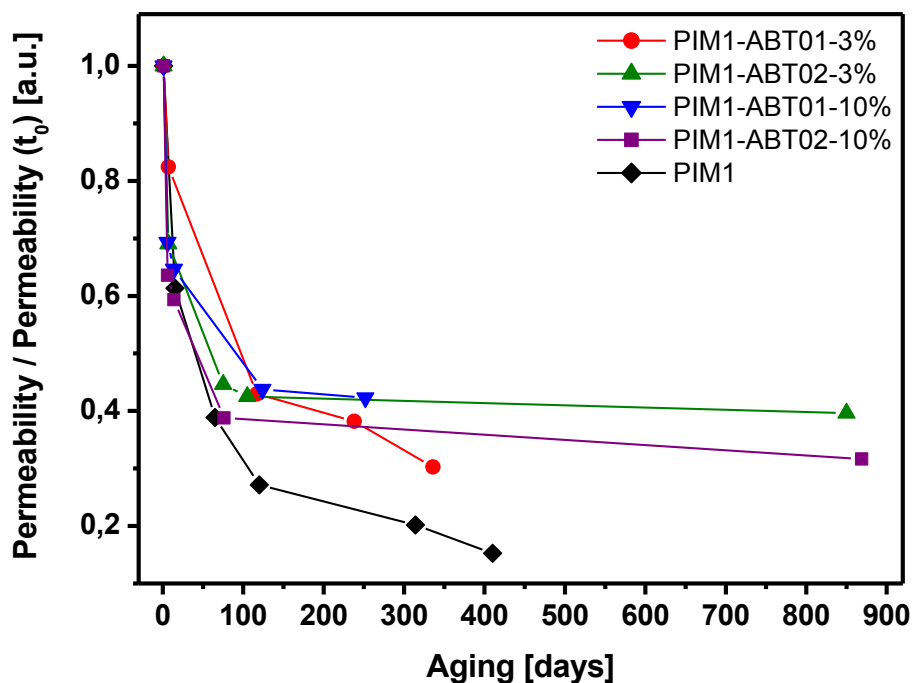


Figure 1. Normalized CO₂ permeation data of PIM1 —◆—, PIM1-ABT01-3% —●—, PIM1-ABT02-3% —▲—, PIM1-ABT01-10% —▼— and PIM1-ABT02-10% —■—. ±5% is the estimated error associated with the CO₂ permeability measurements

PIM1 already shows a sharp drop in CO₂ permeability within the first 15 days which is followed by a progressive decrease up to 410 days. The CO₂ permeability at 410 days is assessed at 2044 barrer, which is approximately 15% of the initial value. This data are in agreement with those found in the literature^{19,20}. The reduced CO₂ permeability is associated with the aging of the polymeric network which results in the collapse of internal free volume thus reducing gas diffusion pathways within the membrane, as already reported in the literature^{6,9,10}.

For all MMM samples it is observed a rapid decrease in the CO₂ permeability up to approximately 70 days when almost half of the initial CO₂ permeability values are observed. For PIM1-ABT01 at 3 and 10 wt% at approximately 130 days the drop in CO₂ permeability slows down reaching for both samples a CO₂ permeability assessed at 43% with respect to the t_0 value. However, a further drop in CO₂ permeability is observed for PIM1-ABT01-3%, namely the CO₂ permeability assessed at 238 and 336 days is respectively 38% and 30% with respect to the initial value. This trend seems to be absent in the case of PIM1-ABT01-10%, for which a CO₂ permeability of 42% with respect to that measured at t_0 is observed at 252 days, thus showing a significant slowdown in the aging rate. A similar trend is displayed by the performances measured for PIM1-ABT02-3%. For this sample the CO₂ permeability value assessed at 105 days, namely 3693 barrer, corresponds to 42% of the initial CO₂ permeability while the permeability measured at 850 days is 3443 barrer, namely 40% of the t_0 value. This shows a clear slowdown in the aging rate since only 2 percentage points are lost in permeability performances in 745 days. For PIM1-ABT02-10% the CO₂ permeability measured at 76 days is 2908 barrer which is 39% with respect to the t_0 value while after 869 days the CO₂ permeability is assessed at 32% of the initial value thus showing a decrease in the aging rate even though less pronounced with respect to the PIM1-ABT02-3% sample.

Neither of the two ABT materials has demonstrated to be a more effective additive. In fact, the two best performing MMMs appear to be the PIM1-ABT02-3% and the

PIM1-ABT01-10%, even though for this last sample measurements performed in the long period are missing. In terms of selectivity, every sample shows an higher CO₂/N₂ selectivity after the aging period and is not surprising since the CO₂/N₂ selectivity is supposed to increase over time as aging progresses^{9,17}. PIM1-ABT01-3% shows a CO₂/N₂ selectivity of 21 after being aged for 336 days while for the other membrane samples a CO₂/N₂ selectivity of 21 is found at longer aging period. The only exception is PIM1-ABT01-10% with a CO₂/N₂ selectivity assessed at 19 with 252 days of aging. The data are summarized in Table 2.

The effectiveness of ABT materials and in general hyper cross – linked polymers, in reducing aging effects in PIM1 could be associated with the presence of π - π interactions with the surface of the HCPs particles. Interactions of this type could result in partial immobilization of the PIM1 chains anchored to the surface of the ABT fillers. Further investigations are needed to confirm the hypothesis.

Table 2. CO₂/N₂ selectivity at t₀ and for the aged membrane samples. (±9%) is the estimated error on the selectivity.

Sample	Selectivity [CO₂/N₂] at t₀ (±9%)	Selectivity [CO₂/N₂] aged samples (±9%)
PIM1	15	21 (410 days)
PIM1-ABT01-3%	18	21 (336 days)
PIM1-ABT02-3%	14	21 (850 days)
PIM1-ABT01-10%	13	19 (252 days)
PIM1-ABT02-10%	18	21 (869 days)

In Figure 2 the upper bound data associated with PIM1 and ABTs – based MMMs are shown.

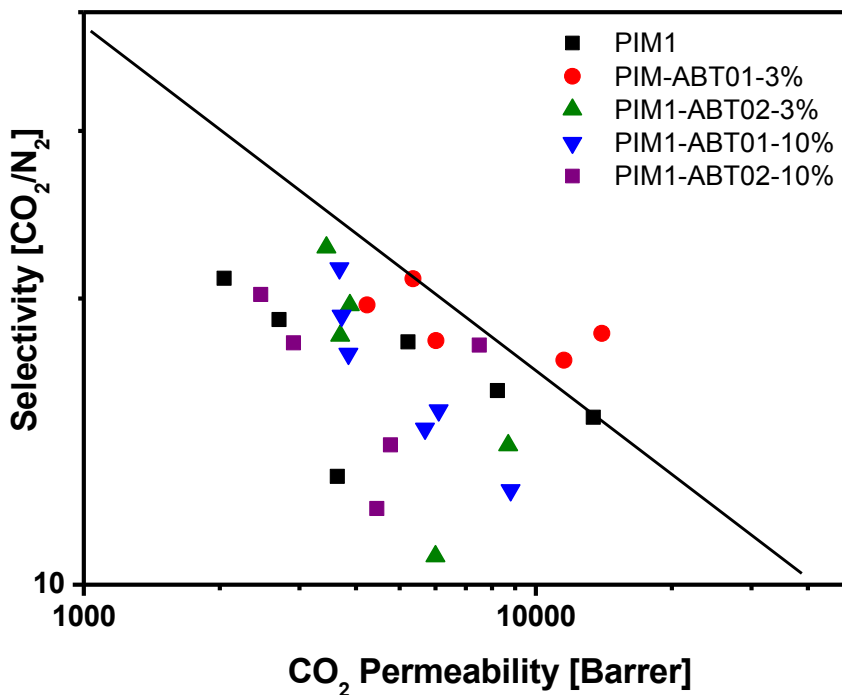


Figure 2. Upper bound correlation for CO₂/N₂ separation of PIM1 ■, PIM1-ABT01-3% ●, PIM1-ABT02-3% ▲, PIM1-ABT01-10% and PIM1-ABT02-10% ◆. The upper bound is referred to the 2008 upper bound⁵.

From the data reported in Figure 2 it is seen that the only sample with data points above the upper bound is PIM1-ABT01-3%. However, as aging progresses, it is seen that the data points drift farther from the upper bound. The data point at t_0 of PIM1-ABT02-10% is also close to the upper bound, however as time passes, data points are progressively found farther with respect to the upper bound. PIM1-ABT02-3% and PIM1-ABT01-10% both show t_0 data points relatively far from the upper bound, however physical aging brings the data points progressively closer to the upper bound.

6.2.2 PIM1 + DIXYT materials

In Figure 3 the normalized CO₂ permeation data over time are reported for PIM1 and MMMs based on the addition of DIXYT materials with 3 and 10 wt% load to the PIM1 polymeric matrix. In Table 3 permeability data and the CO₂/N₂ selectivity are reported for PIM1 and MMMs at t₀.

Table 3. CO₂ permeability data of PIM1, PIM1-DIXYT01-3%, PIM1-DIXYT02-3%, PIM1-DIXYT01-10% and PIM1-DIXYT02-10% at t₀. ±5% is the estimated error associated with the CO₂ permeability measurements while ±9% is the estimated error associated with the CO₂/N₂ selectivity.

Sample	Permeability CO₂ [Barrer] (±5%)	Selectivity [CO₂/N₂] (±9%)
PIM1	13400	15
PIM1-DIXYT01-3%	13982	17
PIM1- DIXYT02-3%	10539	15
PIM1- DIXYT01-10%	14897	18
PIM1- DIXYT02-10%	12839	18

The addition of DIXYT01 at either 3 and 10 wt% to the PIM1 matrix results in higher CO₂ permeabilities at t₀, namely for PIM1 the CO₂ permeability is assessed at 13400 barrer at t₀ while for PIM1-DIXY01-3% and PIM1-DIXYT01-10% is respectively assessed at 13982 and 14897 barrer after methanol treatment. In the case of the DIXYT02 additive at 3 wt% the CO₂ permeability is assessed at 10539 barrer while

for PIM1-DIXYT02-10% is 12839 barrer at t_0 . For all MMMs, comparable or higher CO₂ permeability is measured at t_0 with respect to that observed for pure PIM1. The fact that the SSA of DIXYT materials is much lower with respect to that of PIM1 suggests that one possible explanation for the observed value of CO₂ permeability can be at least partially ascribed to the presence of sulfur based functionalities within the polymeric framework of DIXYT materials. The bridging sulfur atom and the CO₂ molecule can interact via electrostatic attraction generated between the lone pairs of the sulfur atom and the partially positively charged carbon atom of the CO₂ molecule²¹. Additional contributors to the interaction energy could be dipolar interactions, possibly arising due to the polarizabilities of both CO₂ and the sulfur atom^{21,22}. As evidenced in the context of DIXYT material's characterization (see FT-IR and SS-NMR investigation), alongside the bridging sulfur atom, evidences of the presence of -SO₃H groups within DIXYT materials' polymeric framework were also found. The sulfonate group can form relative strong intermolecular interactions via hydrogen bonds thanks to the acidity of the proton, in addition to its capacity to easily rotate around the C-S bond to maximize the magnitude of molecular interactions²¹. Upon interaction with the CO₂ molecule, two main contributors to the interaction energy come into play. One component is due to the electrostatic attraction between the oxygen lone pairs of the S=O bond and the carbon atom of the CO₂ molecule²¹. The second and most stabilizing component is associated with the formation of the -SO₃H...O=C=O hydrogen bond²¹. A smaller contributor is found to be one where the carbon of the CO₂ molecule can form a quadrupole electrostatic interaction with the lone pairs of the oxygen of the sulfonate group while simultaneously forming a weak C(sp²)-H...O=C=O hydrogen bond with an aromatic hydrogen atom²¹. Favorable interactions of the type just described could result in higher CO₂ solubility within the MMMs and since the permability is directly dependent upon the solubility of the gas within the membrane, the overall effect should be the higher CO₂ permeability observed for the MMMs. Higher CO₂ solubility is therefore observed even though a lower number of gas diffusion pathways should be present because of

lower SSA and pore volume of DIXYT additives. It is worth noting that from the SS-NMR analysis it could be seen that the amount of $-SO_3H$ groups is higher for DIXYT01 with respect to DIXYT02 and here the t_0 CO_2 permeability values are higher for the MMMs with DIXYT01 with respect to those with DIXYT02.

As aging progresses, after 7 days it is seen a dramatic drop in CO_2 permeability for the PIM1-DIXYT01-10% membrane, which is assessed at 25% of the initial value. After 379 days the permeability has dropped to 23% of the initial value thus displaying a plateau effect after the first week of aging. The CO_2/N_2 selectivity is 18 after 379 days of aging. A similar behaviour is seen for the other membrane with a 10 wt% load, namely the PIM1-DIXYT02-10%. After the first week of aging the CO_2 permeability is observed to be 43% with respect to the t_0 value. Unfortunately, the membrane broke during permeability measurements and the last point measured was at 28 days of aging when the CO_2 permeability was found to be 5765 barrer (44% with respect to t_0), with a CO_2/N_2 selectivity of 23.

For the two MMMs with a 3 wt% load of DIXYT additives the initial drop in CO_2 permeability is less pronounced with respect to the other membranes and is assessed around 50 days at 59 and 58% with respect to t_0 value for PIM1-DIXYT01-3% and PIM1-DIXYT02-3% respectively. For the MMM obtained with a 3 wt% addition of DIXYT01 the CO_2 permeability is assessed at 49%, with respect to the initial value, after 426 days of aging namely 6803 barrer, with a CO_2/N_2 of 20. For the membrane obtained with a 3 wt% addition of DIXYT02 the CO_2 permeability at 407 days is assessed at 5361 barrer, which is approximately 51% with respect to t_0 value, with a CO_2/N_2 selectivity of 21. A higher CO_2 permeability, in terms of absolute value, is found for the MMM with a 3 wt% of DIXYT01, however a slightly faster aging rate is also observed. Higher selectivities are observed for the MMMs with DIXYT02 as additive, both at 3 and 10 wt%. The CO_2/N_2 selectivity values at t_0 and after the aging period are reported in Table 4.

Interactions with sulfur-based functional groups is likely one of the many contributions to the stabilization of the aging effects in the system PIM1 + DIXYT materials. However, as mentioned in the context of PIM1 + ABT materials, the presence of π - π interactions is expected to play some role in the attenuation of the PIM1 aging effects brought about by the DIXYT fillers.

Table 4. CO₂/N₂ selectivity at t₀ and for the aged membrane samples. ($\pm 9\%$) is the estimated error on the selectivity.

Sample	Selectivity [CO ₂ /N ₂] at t ₀ ($\pm 9\%$)	Selectivity [CO ₂ /N ₂] aged samples ($\pm 9\%$)
PIM1	15	21 (410 days)
PIM1-DIXYT01-3%	17	20 (426 days)
PIM1-DIXYT02-3%	15	21 (407 days)
PIM1-DIXYT01-10%	18	18 (379 days)
PIM1-DIXYT02-10%	18	23 (28 days)

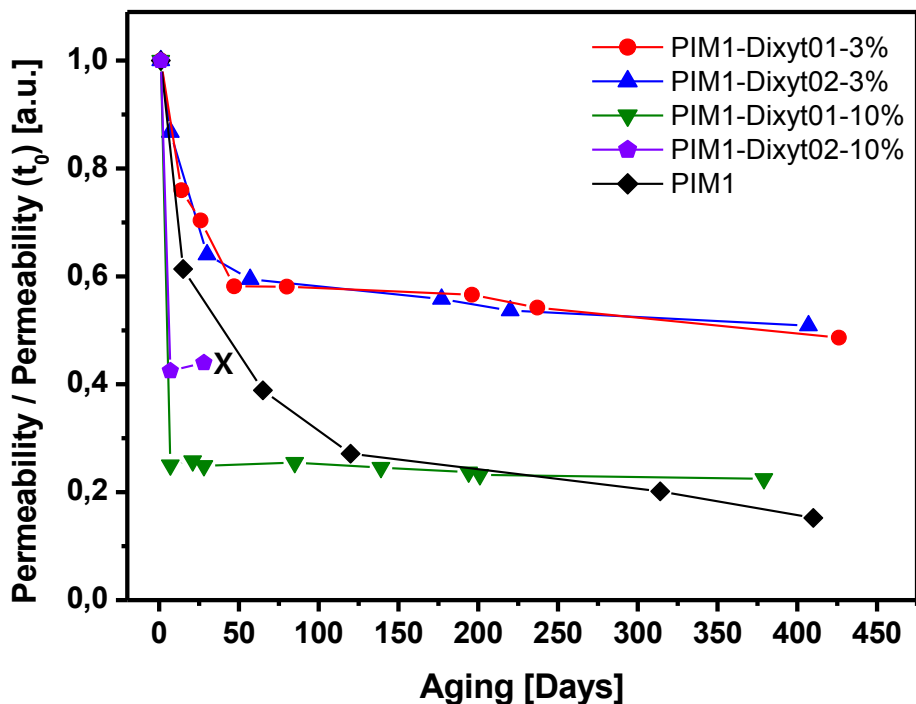


Figure 3. Normalized CO₂ permeation data of PIM1 —◆—, PIM1-DIXYT01-3% —●—, PIM1-DIXYT02-3% —▲—, PIM1-DIXYT01-10% —▼— and PIM1-DIXYT02-10% —■—. The symbol “X” is here used to indicate the breaking of the membrane sample. ±5% is the estimated error associated with the CO₂ permeability measurements.

In Figure 4 the upper bound data associated with PIM1 and ABTs – based MMMs are shown.

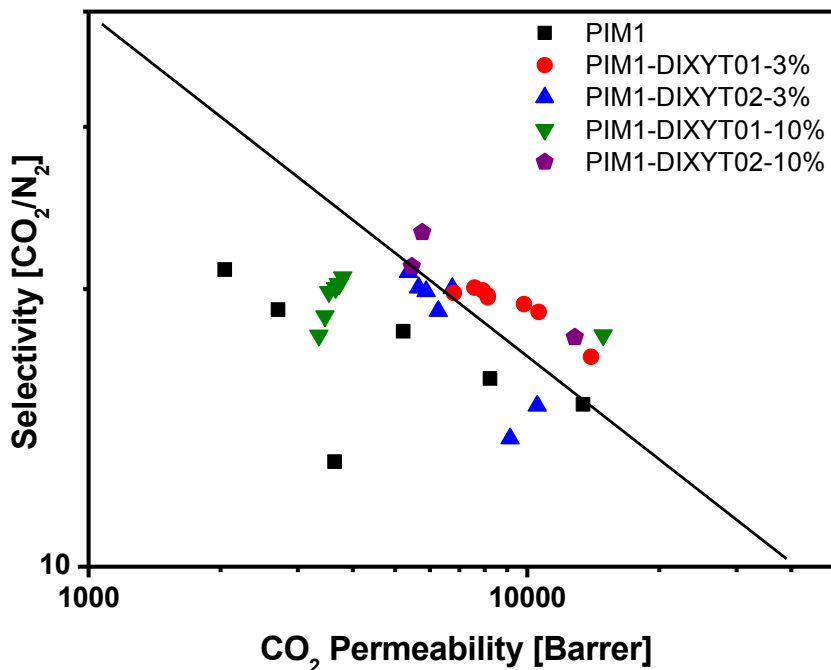


Figure 4. Upper bound correlation for CO₂/N₂ separation of PIM1 ■, PIM1-DIXYT01-3% ●, PIM1-DIXYT02-3% ▲, PIM1-DIXYT01-10% ▼ and PIM1-DIXYT02-10% ◆. The upper bound is referred to the 2008 upper bound⁵.

From the data reported in Figure 4 it is seen that PIM1-DIXYT01-10%, PIM1-DIXYT01-3% and PIM1-DIXYT02-10% are associated with data points at t_0 above the upper bound. As aging progresses the data points associated with PIM1-DIXYT01-10% abruptly shift their position below the upper bound. This effect, as reported in Figure 3, is associated with a sharp drop in permeability performances. PIM1-DIXYT02-10% data points also shift below the upper bound before the membrane broke. All the data points of PIM1-DIXYT01-3% remain above the upper bound even though they progressively approach the upper bound as aging progresses. The t_0 data point associated with PIM1-DIXYT02-3% is located below the upper bound however, as aging progresses, data points gradually approach the upper bound

with the third point located above the upper bound and the last point located on the upper bound.

6.2.3 Comparison between the PIM1 membrane and the best performing MMMs

In this section a comparison between the pure PIM1 membrane and the best performing MMMs is reported in Figure 5 while in Table 5 permeability data and the CO₂/N₂ selectivity are reported for PIM1 and MMMs at t₀.

Table 5. CO₂ permeability data of PIM1, PIM1-SAP110, PIM1-ABT02-3% and PIM1-DIXYT02-3%. ±5% is the estimated error associated with the CO₂ permeability measurements while ±9% is the estimated error associated with the CO₂/N₂ selectivity.

Sample	Permeability CO₂ [Barrer] (±5%)	Selectivity [CO₂/N₂] (±9%)
PIM1	13400	15
PIM1-SAP110	12300	16
PIM1-ABT02-3%	8690	14
PIM1-DIXYT02-3%	10539	15

At t₀ the pure PIM1 membrane is the sample displaying the higher CO₂ permeability, among the selected membrane samples. The CO₂/N₂ selectivity at t₀ is comparable

among all samples. In the first two weeks of aging all membrane samples with exception of PIM1-DIXYT02-3% shows a rapid drop in CO₂ permeability with values assessed at 61, 65 and 55 % with respect to t₀ value for PIM1, PIM1-ABT02-3 and PIM1-SAP110 respectively. PIM1-DIXYT02-3% seems to age at a slightly slower rate, since the CO₂ permeability is found to be 64 % with respect to t₀ at 30 days of aging. As aging progresses PIM1 is found to inevitably loose permeability performances and after 410 days only 15 % of the initial CO₂ permeation rate is found, as already evidenced in previous sections. The addition of 3 wt% of ABT02 to the PIM1 matrix results in a drastic slowdown of the aging rate after 105 days when almost no further decrease in CO₂ permeability is observed, retaining after 850 days of aging 40% of the initial CO₂ permeability. The addition of SAP-110 and DIXYT02 results in a similar aging behavior, that is a slowdown of the aging rate even though a slight downward trend is still observed in the graph for both MMMs for the all aging period. As a result, the CO₂ permeability associated with PIM1-SAP110 is found to be after 315 days of aging 47% of the initial value while for PIM1-DIXYT02-3% is found to be 51% after 407 days. These data seems to indicate that DIXYT02 at 3 wt% results in better performing membranes with respect to membranes obtained with a 3 wt% load of SAP110. The similar textural properties in terms of both SSA and pore volume (see Chapter 3, N₂ physisorption at -196 °C analysis), seem to indicate that one important factor in the better performances displayed by DIXYT additives is the introduction of sulfur – based functionalities, which results in higher solubility of the CO₂ molecule within the MMM. Additional measurements at longer aging times are needed to fully compare the effects on the aging behavior of PIM1 induced by SAP110 and DIXYT fillers, to those induced by the ABT fillers. The CO₂/N₂ selectivity values at t₀ and after the aging period are reported in Table 6. The lower selectivity is found for PIM1-SAP110, assessed at 17 after 1 year of aging while PIM1 + ABT02 and DIXYT02 are both showing a value of 21 after 850 and 379 days of aging respectively.

Table 6. CO₂/N₂ selectivity at t₀ and for the aged membrane samples. (±9%) is the estimated error on the selectivity.

Sample	Selectivity [CO₂/N₂] at t₀ (±9%)	Selectivity [CO₂/N₂] aged samples (±9%)
PIM1	15	21 (410 days)
PIM1-SAP110	16	17 (315 days)
PIM1-ABT02-3%	14	21 (850 days)
PIM1-DIXYT02-3%	15	21 (379 days)

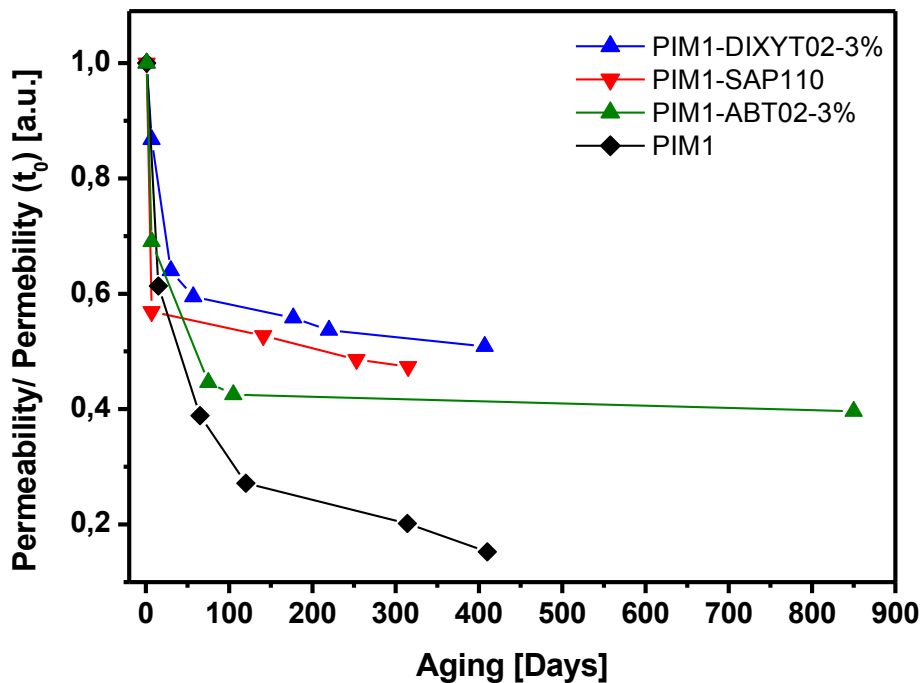


Figure 5. Normalized CO₂ permeation data of PIM1 \blacklozenge , PIM1-DIXY02-3% \blacktriangle , PIM1-SAP110 \blacktriangledown and PIM1-ABT02-3% \blacktriangle . $\pm 5\%$ is the estimated error associated with the CO₂ permeability measurements.

In Figure 6 the upper bound data associated with the best performing membrane samples are shown.

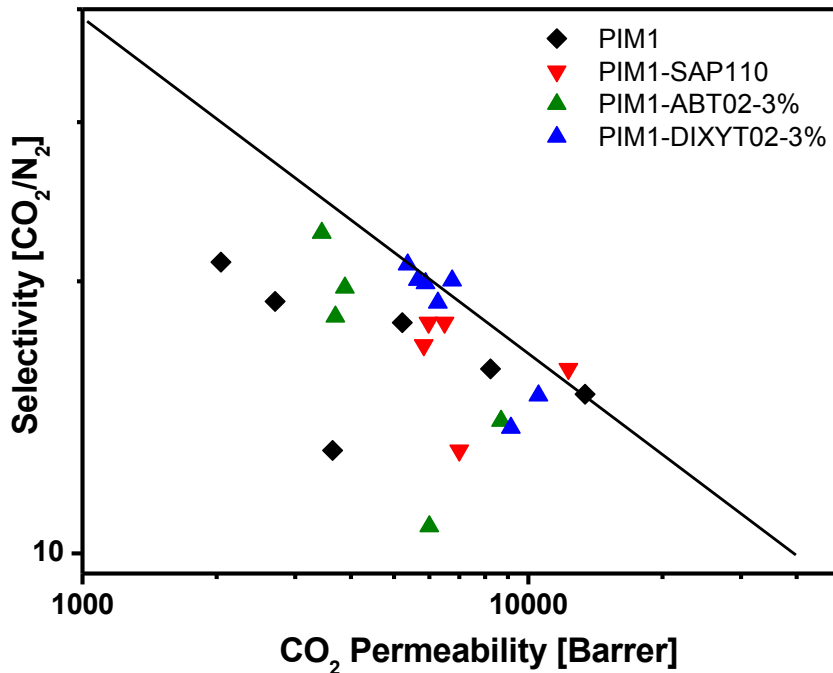


Figure 6. Upper bound correlation for CO₂/N₂ separation of PIM1 \blacksquare , PIM1-SAP110 \blacktriangledown , PIM1-ABT02-3% \blacktriangledown and PIM1-DIXYT02-3% \blacktriangle . The upper bound is referred to the 2008 upper bound⁵.

From the data reported in Figure 6 it is seen that PIM1-DIXYT02-3%, is the MMM sample which is associated with data points that are located closer to the upper bound. Aging effects bring the data point closer to upper bound and the last recorded data point it is located right on the upper bound. PIM1-SAP110 starts with the t_0 data point above the upper bound, however as aging progresses data points shift below the upper bound and slowly farther from the upper bound. PIM1-ABT02-3% shows data points below the upper bound and compared to the other MMMs, farther from the upper bound. PIM1-DIXYT01-3% seems to be best performing MMM among the tested MMMs.

6.4 Conclusions

ABT and DIXYT HCP materials were studied as additives for PIM1 gas separation membranes. A total of eight MMMs were prepared via addition of fillers at 3 and 10 wt% namely, PIM1-ABT01-3%, PIM1-ABT01-10%, PIM1-ABT02-3%, PIM1-ABT02-10%, PIM1-DIXYT01-3%, PIM1-DIXYT01-10%, PIM1-DIXYT02-3% and PIM1-DIXYT02-10%. ABT materials showed a good ability in slowing down aging effects associated with PIM1 polymeric matrix, especially for long period of times. In particular, PIM-ABT02-3% displayed an almost zero aging rate between 105 and 850 days of aging, with a CO₂ permeability assessed at 40% with respect to t_0 at 850 days after methanol treatment. The addition of DIXYT01 at 3 and 10 wt% resulted in higher CO₂ permeability at t_0 with respect to that measured for PIM1. The fact that SSA and the pore volume of DIXYT01 are lower with respect to those of PIM1 may suggest that the presence of -S- and -SO₃H functionalities within the polymeric framework could be one of the sources of the increased CO₂ solubility within the MMMs hence resulting in the observed higher CO₂ permeability. The addition of DIXYT02, with a lower content of -SO₃H functionalities results in lower CO₂ permeabilities at t_0 with respect to MMMs obtained via addition of DIXYT01, however a higher CO₂/N₂ selectivity is observed in the aging samples of MMMs based on DIXYT02 with respect to DIXYT01, namely 21 versus 20 respectively for PIM1-DIXYT02-3% and PIM1-DIXYT01-3% after approximately 400 days of aging and 23 versus 18 after only 28 days of aging for PIM1-DIXYT02-10% and 379 days of aging for PIM1-DIXYT01-10%. After the aging period the two MMM samples with a 3 wt% load of DIXYT materials showed 49 and 51% of the initial CO₂ permeability respectively for PIM1-DIXYT01-3% and PIM1-DIXYT02-3% which seems to indicate a slightly higher effectiveness of DIXYT02 over DIXYT01 in

terms of slowing down the aging rate of the PIM1 matrix. The results are compared to those obtained on saponite additives, in particular a comparison with the PIM1-SAP110 MMM showed that the addition of DIXYT materials at 3% seems to be a more effective strategy to produce better performing MMMs for CO₂ separation. ABT02 at 3 wt%, showed lower CO₂ permeability within the aging period of PIM1-SAP110 and PIM1-DIXY02-3%, however between 105 and 850 days a very slow aging rate was found for PIM1-ABT02-3%. The slightly higher costs of production of ABT materials, with respect to the other fillers, should also be taken into account if further studies are considered.

Upper bound data suggest that PIM1-DIXYT02-3% is the MMM with the best performances in terms of CO₂ permeability with respect to CO₂/N₂ selectivity. PIM1-DIXYT01-3% also shows interesting performances, however as aging progresses it is seen a gradual approach of the data points toward the upper bound, with the last recorded data point located on the upper bound.

6.5 References

[1] Polymers of Intrinsic Microporosity. Neil B. McKeown. ISRN Materials Science. 2012, 1.

[2] Polymers of Intrinsic Microporosity (PIMs) Gas Separation Membranes: A mini Review. Ma, C.; Urban, J. J. Proceedings of the Nature Research Society. 2018. 2, 02002.

[3] Gas separation membranes from polymers of intrinsic microporosity. Budd, P. M.; Msayib, K. J.; Tattershall, C. E.; Ghanem, B. S.; Reynolds, K. J.; McKeown, N. B.; Detlev Fritsch, D. J. Membr. Sci. 2005. 251, 1 – 2, 263 – 269.

[4] Post-combustion CO₂ capture with chemical absorption: A state-of-the-art review. Wanga, M.; Lawal, A.; Stephenson, P.; Sidders, J.; Ramshaw, C. Chem. Eng. Res. Des. 2011. 89, 9, 1609 – 1624.

[5] The upper bound revisited. Robeson, L. M. J. Membr. Sci. 2008, 320, 390 – 400.

[6] Polymers of Intrinsic Microporosity (PIMs) Gas Separation Membranes: A mini Review. Ma, C.; Urban, J. J. Proceedings of the Nature Research Society. 2018. 2, 02002.

[7] First Clear-Cut Experimental Evidence of a Glass Transition in a Polymer with Intrinsic Microporosity: PIM-1. Yin, H.; Chua, Y. Z.; Yang, B.; Schick, C.; Harrison,

W. J.; Budd, P. M.; Böhning, M.; Schönhals, A. J. *Phys. Chem. Lett.* 2018. 9, 8, 2003 – 2008.

[8] On relaxations and aging of various glasses. Amira, A.; Oreg, Y.; Imry, Y. *PNAS.* 2012. 109, 61850 – 1855.

[9] Gas permeation parameters and other physicochemical properties of a polymer of intrinsic microporosity: Polybenzodioxane PIM-1. Budd, P.; McKeown, N.; Ghanem, B.; Msayib, K.; Fritsch, D.; Starannikova, L.; Belov, N.; Sanfirova, O.; Yampolskii, Y.; Shantarovich, V. J. *Membr. Sci.* 2008. 325, 2, 851.

[10] Effect of physical aging on the gas transport and sorption in PIM-1 membranes. Bernardo, P.; Bazzarelli, F.; Tasselli, F.; Clarizia, G.; Mason, C. R.; Maynard-Atem, L.; Budd, P. M.; Lanč, M.; Pilnáček, K.; Vopička, O.; Friess, K.; Fritsch, D.; Yampolskii, Y. P.; Shantarovich, V.; J. C. Jansen, J. C. *Polymer.* 2017. 113, 283.

[11] Gas transport behavior of mixed-matrix membranes composed of silica nanoparticles in a polymer of intrinsic microporosity (PIM-1). Ahn, J.; Chung, W.-J.; Pinnau, I.; Song, J.; Du, N.; Robertson, G. P.; Guiver, M. D. *J. Membr. Sci.* 2010. 346, 2, 280.

[12] Khan, M. M.; Filiz, V.; Bengtson, G.; Shishatskiy, S.; Rahman, M.; Abetz, V. Functionalized carbon nanotubes mixed matrix membranes of polymers of intrinsic microporosity for gas separation. *Nanoscale Res. Lett.* 2014. 9, 7, 504.

[13] Post-synthetic Ti exchanged UiO-66 metal-organic frameworks that deliver exceptional gas permeability in mixed matrix membranes. Smith, S. J.; Ladewig, B. P.; Hill, A. J.; Lau, C. H.; Hill, M. R. *Sci Rep.* 2015. 5, 7823.

[14] Mixed matrix membranes comprising polymers of intrinsic microporosity and covalent organic framework for gas separation. Wu, X.; Tian, Z.; Wang, S.; Peng, D.; Yang, L.; Wu, Y.; Xin, Q.; Wu, H.; Jiang, Z. *J. Membr. Sci.* 2017. 528, 273.

[15] PIM-1 mixed matrix membranes for gas separations using cost-effective hypercrosslinked nanoparticle fillers. Mitra, T.; Bhavsar, R. S.; Adams, D. J.; Budd, P. M.; Cooper, A. I.; *Chem. Commun.* 2016. 52, 5581 – 5584.

[16] Ending Aging in Super Glassy Polymer Membranes. Lau, C. H.; Nguyen, P. T.; Hill, M. R.; Thornton, A. W.; Konstas, K.; Doherty, C. M.; Mulder, R. J.; Bourgeois, L.; Liu, A. C. Y.; Sprouster, D. J.; Sullivan, J. P.; Bastow, T. J.; Hill, A. J.; Gin, D. L.; Noble, R. D. *Angew. Chem., Int. Ed.* 2014, 53, 5322 – 5326.

[17] Gas- Separation Membranes Loaded with Porous Aromatic Frameworks that Improve with Age. Lau, C. H.; Konstas, K.; Thornton, A. W.; Liu, A. C. Y.; Mudie, S.; Kennedy, D. F.; Howard, S. C.; Hill, A. J.; Hill, M. R. *Angew. Chem., Int. Ed.* 2015, 54, 2669 – 2673.

[18] Budd, P. M.; Elabas, E. S.; Ghanem, B. S.; Makhseed, S.; McKeown, N. B.; Msayib, K. J.; Tattershall, C. E.; Wang, D. Solution processed, organophilic membrane derived from a polymer of intrinsic microporosity. *Adv. Mater.* 2004, 16, 456–459.

[19] Budd, P. M.; McKeown, N. B.; Ghanem, B. S.; Msayib, K. J.; Fritsch, D.; Starannikova, L.; Belov, N.; Sanfirova, O.; Yampolskii, Y.; Shantarovich, V. Gas permeation parameters and other physicochemical properties of a polymer of intrinsic microporosity: Polybenzodioxane PIM-1. *J. Membr. Sci.* 2008, 325, 851–860.

[20] McKeown, N. B.; Budd, P. M. Polymers of intrinsic microporosity (PIMs): organic materials for membrane separations, heterogeneous catalysis and hydrogen storage. *Chem. Soc. Rev.* 2006, 35, 675–683.

[21] Impact of ligands on CO₂ adsorption in metal-organic frameworks: First principles study of the interaction of CO₂ with functionalized benzenes. II. Effect of polar and acidic substituents. Torrisi, A.; Mellot-Draznieks, C.; Bell, R. G. *The Journal of Chemical Physics.* 2010. 132, 044705.

[22] Effects of incorporated oxygen and sulfur heteroatoms into ligands for CO₂/N₂ and CO₂/CH₄ separation in metal-organic frameworks: A molecular simulation study. Hu, J.; Liu, Y.; Liu, J.; Gu, C.; Wu, D. *Fuel.* 2018. 226, 591 – 597.

Chapter VII

Experimental techniques

7.1 VOC adsorption on mPAF materials

Toluene adsorption isotherms were obtained at 35 °C on HSZ-Y and mPAF-1/n samples by employing a volumetric analysis of vapor sorption in an Autosorb iQ MP-XR equipped with a cryocooler (Quantachrome Instruments). To remove possible adsorbed species, prior to the adsorption measurements, all samples were outgassed for 30 min at 50 °C, 30 min at 80 °C, 2 h at 120 °C, and 2 h at 150 °C. For the mPAF-1/n a final treatment at 12 h at 220 °C under high-vacuum conditions (final pressure 7×10^{-4} mbar) was adopted. The specific surface area (SSA) was measured by means of nitrogen adsorption at liquid nitrogen temperature (-196 °C) in the pressure range of 1×10^{-6} Torr to 1 P/P₀ by using an Autosorb-1-MP (Quantachrome Instruments). Prior to adsorption, the samples were outgassed for 16 h at 150 °C, (final pressure lower than 10^{-6} Torr). The SSA of the samples was determined by the Brunauer–Emmett– Teller (BET) equation, in a pressure range (0.05–0.15 and 0.005– 0.01 P/P₀ range for mPAF-1/n and HSZ-Y zeolite, respectively) selected to maximize the correlation coefficient of the fitted linear equation. The pore size distribution was calculated by applying the nonlocal density functional theory (NLDFT) method for cylindrical pores.

Infrared spectra were collected on a Thermo Electron Corporation FT Nicolet 5700 spectrometer (resolution 4 cm^{-1}). Pellets were prepared by mixing the prepared materials with KBr (1:10 weight ratio). Pellets were placed into an IR cell with KBr windows permanently connected to a vacuum line (residual pressure: $1.33 \times 10^{-4}\text{ Pa}$, $1\text{ Pa} = 0.01\text{ mbar}$), allowing all treatments and adsorption– desorption experiments to be performed in situ. Before the gas adsorption, mPAF-1/n samples were outgassed at $150\text{ }^{\circ}\text{C}$ with a heating ramp of $5\text{ }^{\circ}\text{C}/\text{min}$ for 2 h, using an oil-free apparatus and grease-free vacuum line.

Solid-state NMR spectra were acquired on a Bruker Avance III 500 spectrometer and a wide bore 11.7 T magnet with operational frequencies for ^1H and ^{13}C of 500.13 and 125.77 MHz, respectively. A 4 mm triple-resonance probe with MAS was employed in all experiments. 19 mbar of toluene- d_8 , toluene, benzene, xylene, and n-hexane were adsorbed directly on a dehydrated powdered sample that was previously packed on a zirconia rotor and inserted in a homemade cell. After waiting for the equilibrium adsorption, we closed the rotor with a zirconia cap using a piston attached to the cell, and later the rotor was extracted from the cell and submitted for solidstate NMR experiments. The zirconia rotor was spun at a MAS rate between 10 and 15 kHz. The magnitude of radio-frequency field was 100 kHz for ^1H MAS NMR, and the relaxation delay, d_1 , between accumulations was 2 s. For the ^{13}C cross-polarization (CP) magic angle spinning (MAS) experiments, the proton radio frequencies (RF) of 55 and 28 kHz were used for initial excitation and decoupling, respectively. During the CP period the ^1H RF field was ramped by using 100 increments, whereas the ^{13}C RF field was maintained at a constant level. During the acquisition, the protons were decoupled from the carbons by using a TPPM decoupling scheme. A moderate ramped RF field of 62 kHz was used for spin locking, while the carbon RF field was matched to obtain optimal signal and CP contact times of 2–10 ms were used. The rotor synchronized spin echo sequence ($\pi/2-\tau-\pi-\tau$ -acquisition) was also applied to record the ^1H NMR spectra with τ

delay time of 4000 μ s. All chemical shifts are reported by using the δ scale and are externally referenced to TMS at 0 ppm.

All the ab initio calculations were performed at the density functional theory (DFT) level using the Gaussian16 program. The hybrid functional B3LYP35 was employed along with the cc-pVDZ basis set. Dispersion energies were included in the model through the semiempirical method and parameters proposed by Grimme, and the NMR chemical shifts were calculated by using the gaugeindependent atomic orbital (GIAO) method. The molecular dynamics (MD) calculations were performed in the NPT ensemble at 300 K and 1 atm using the LAMMPS program.³⁹ Temperature and pressure were controlled through the Nosé–Hoover algorithm; the bond lengths, angles, and dihedrals were kept fixed for the whole run, and long-range nonbonded interactions were computed by using the universal force field (UFF) pairwise parameters. A periodic cubic box containing 3000 toluene molecules was used to simulate a liquid-like environment, as expected inside the material for high adsorbate concentrations; the model of mPAF-1/n material described in the text was then inserted in the box, deleting the overlapping toluene molecules. The equilibration and production times were 10 and 50 ps, respectively.

7.2 Measurements performed on saponites, PIM1 and PIM1 + saponites MMM samples

Scanning Electron Microscopy (SEM). The membranes have been examined with a JSM-IT100 (JEOL, Japan) operating at 10 kV. Before SEM analysis, the samples were fractured in liquid nitrogen and then sputtered with a layer of 9 nm gold to form a conductive surface.

Thermogravimetric Analysis (TGA). TGA was performed on a Setaram SETSYS Evolution instrument under argon (gas flow 20 mL/ min), heating the samples up to 800 °C with a rate of 5 °C/min.

X-ray Diffraction (XRD) Analysis. XRD patterns were obtained on an ARL XTRA48 diffractometer using Cu K α radiation ($\lambda = 1.54062 \text{ \AA}$) at room temperature between 2° and 65° 2 θ with a step size of 0.02 with a rate of 1° 2 θ /min.

Variable Temperature (VT)-IR Analysis. VT-IR analyses were performed on a Fourier transform infrared (FTIR) Nicolet 5700 spectrometer (Thermo Optics) at a resolution of 4 cm⁻¹. The samples were pressed in the form of self-supporting wafers and placed into an IR cell equipped with KBr windows permanently attached to high-vacuum line (residual pressure: 1.0×10^{-6} Torr, 1 Torr = 133.33 Pa). The experimental setup allowed all temperature treatments to be performed in situ and in vacuum conditions. Spectra were collected by heating the samples from room temperature to 500 °C (heating rate of 10 °C/min) under vacuum conditions (residual pressure: 1.0×10^{-6} Torr, 1 Torr = 133.33 Pa).

Transmission Electron Microscopy. High-resolution transmission electron microscope micrographs (HRTEM) images were collected on a Zeiss libra200 FE3010 high-resolution transmission electron microscope operating at 200 kV. The samples were encapsulated in sucrose (2.3 M) and then cut with a Cryo Ultramicrotome Reichert Jung with a diamond knife.

N₂ Physisorption Analysis. Specific surface area analysis of pure PIM and saponite samples has been derived by N₂ physisorption measurements performed at -196 and -186 °C, respectively. N₂ measurements were performed in the relative pressure range from 1×10^{-6} to 1 P/P₀ by using a Quantachrome Autosorb 1MP/TCD instrument. Prior to the saponite samples analysis the samples were outgassed at 150 °C for 3 h (residual pressure lower than 10⁻⁶ Torr). PIM1 was treated at 120 °C overnight. Apparent surface areas were determined by using the

Brunauer–Emmett–Teller equation, in the relative pressure range from 0.01 to 0.1 P/P_0 . Pore size distributions were obtained by applying both the NLDFT method (N_2 silica kernel based on a cylindrical pore model applied to the desorption branch) and the classical BJH method applied to the desorption branch. For the mixed matrix samples CO_2 equilibrium isotherms at 0 °C were measured by using a novel adsorption differential volumetric apparatus (ADVA), custom built at the University of Edinburgh. Differently from conventional volumetric systems, the differential system relies on two symmetric branches, namely the sample and reference side, each comprising their dosing and uptake volume. The experiment is based on following the differential pressure between the sample side (where the sample is placed) and the reference side (where an inert material of the same sample volume is contained). The ADVA system is equipped with a 0–2 bar absolute pressure transducer and a ± 621.3 mbar differential pressure transducer (Rosemount 3051 series). Four thermocouples are used to monitor the temperature of both dosing and uptake volumes in reference and sample side. Volumes of dosing and uptake cells are minimized to allow the use of very small amount of sample. For this study, both uptake cells were temperature controlled by using a thermostatic bath. Prior to the experiment, samples were regenerated in situ overnight at 35 °C. During regeneration, the sample is kept under vacuum by using a high-vacuum turbomolecular pump (Pfeiffer HiCube 80 ECOMVP 015-2).

SS-NMR Spectroscopy. Solid-state NMR spectra were acquired on a Bruker Advance III 500 spectrometer and a wide-bore 11.7 T magnet with operational frequencies for 1H and ^{13}C of 500.13 and 125.77 MHz, respectively. A 4 mm triple-resonance probe in double resonance mode with MAS was employed in all the experiments. The as-cast polymer membranes were cut to small pieces so that it can be packed in a 4 mm zirconia rotor and was spun at a MAS rate of 12 kHz. For the ^{13}C cross-polarization (CP) magic angle spinning (MAS) experiments, the proton radio frequencies (RF) of 55 and 28 kHz were used for initial excitation and

decoupling, respectively. During the CP period the ^1H RF field was ramped using 100 increments, whereas the ^{13}C RF field was maintained at a constant level. During the acquisition, the protons were decoupled from the carbons by using a Spinal-64 decoupling scheme. A moderate ramped RF field of 55 kHz was used for spin locking, while the carbon RF field was matched to obtain optimal signal (40 kHz). T_1 measurements were performed with a CPXT1 pulse sequence using a 10 ms spin-lock of 55 and 40 kHz for ^1H and ^{13}C , respectively, immediately followed by $\pi/2-\tau-\pi/2$ sequence on ^{13}C with variable delay (τ) ranging from 0.1 to 45 s. Spectra were recorded with a spectral width of 42 kHz, and 256 transients were accumulated at 298 K. A line broadening of 50 Hz and zero-filling to 2048 points were used. All chemical shifts are reported using δ scale and are externally referenced to TMS at 0 ppm. Data analysis was performed using Bruker software Dynamics Center, version 2.5.6, and T_1 curves were obtained by plotting the intensity of the carbon signals versus time. A single - exponential decay was used to fit the data via eq

$$I_t = I_0 e^{\frac{-t}{T_1}} \quad \text{Equation 1}$$

7.3 Measurements performed on the synthesized HCPs, PIM1 and PIM1 + HCPs MMM samples

Scanning Electron Microscopy (SEM). The membranes have been examined with a JSM-IT100 (JEOL, Japan) operating at 10 kV. Before SEM analysis, the samples were fractured in liquid nitrogen and then sputtered with a layer of 9 nm gold to form a conductive surface.

Thermogravimetric Analysis (TGA). TGA was performed on a Setaram SETSYS Evolution instrument under argon (gas flow 20 mL/ min), heating the samples up to 800 °C with a rate of 5 °C/min.

N₂ Physisorption Analysis. Specific surface area analysis of HCPs samples has been derived by N₂ physisorption measurements performed at -196 and -186 °C, respectively. N₂ measurements were performed in the relative pressure range from 1×10^{-6} to 1 P/P₀ by using a Quantachrome Autosorb 1MP/TCD instrument. Prior to analysis the samples were outgassed at 150 °C for 3 h (residual pressure lower than 10^{-6} Torr). Apparent surface areas were determined by using the Brunauer–Emmett–Teller equation, in the relative pressure range from 0.01 to 0.1 P/P₀. Pore size distributions were obtained by applying both the NLDFT method (N₂ carbon based on a cylindrical (mPAF, TPMTc, PS-1.3) / slit pore model (DIXYT, ABT) applied to the adsorption branch.

SS-NMR spectra were acquired on a Bruker Advance III 500 spectrometer and a wide bore 11.7 T magnet with operational frequencies for ¹³C of 125.77 MHz. A 4 mm triple-resonance probe with MAS was employed in all the experiments. The samples were packed on a zirconia rotor and spun at a MAS rate of 15 kHz. For the ¹³C{¹H} crosspolarization magic-angle spinning (CPMAS) experiments, the magnetic fields ν_{rf} of 55 and 28 kHz were used for initial excitation and

decoupling, respectively. During the CP period, the ^1H RF field was ramped using 100 increments, whereas the ^{13}C RF field was maintained at a constant level. During the acquisition, the protons are decoupled from the carbons by using a two-pulse phase-modulated (TPPM) decoupling scheme. A moderate ramped RF field of 62 kHz was used for spin locking, while the carbon RF field was matched to obtain optimal signal, and the CP contact time of 2 ms was used. The relaxation delay between accumulations was 1 s, and all chemical shifts are reported using δ scale and are externally referenced to TMS at 0 ppm.

Infrared spectra were collected on a Thermo Electron Corporation FT Nicolet 5700 spectrometer (resolution 4 cm^{-1}). Pellets were prepared by mixing the prepared materials with KBr (1:10 weight ratio). Pellets were placed into an IR cell with KBr windows permanently connected to a vacuum line (residual pressure: $1.33 \times 10^{-4}\text{ Pa}$, $1\text{ Pa} = 0.01\text{ mbar}$), allowing all treatments and adsorption–desorption experiments to be performed in situ. Samples were outgassed at $150\text{ }^\circ\text{C}$ with a heating ramp of $5\text{ }^\circ\text{C}/\text{min}$ for 2 h, using an oil-free apparatus and grease-free vacuum line.

Chapter VIII

Conclusions

The Ph.D. work has focused on the development of porous solids for environmental applications. Two types of porous solids were selected, namely hyper cross – linked polymers (HCPs) and synthetic clays. From the HCPs family, nine materials were obtained among which six were based on the tetraphenyl methane monomer in combination with different cross – linkers and catalysts. Of these six materials three were obtained by employing formaldehyde dimethyl acetal (FDA) as cross – linker and FeCl_3 as catalyst resulting in the production of: mPAF-1/9, mPAF-1/16 and mPAF-1/30. Two other HCPs based on the cross – linker 1,3,5-tris(bromomethyl)benzene and the catalyst AlBr_3 were obtained and named ABT01 and ABT02. Tetraphenyl methane, α,α' -dichloro-*p*-xylene as cross – linker and TiCl_4 catalyst were used to synthesize TPMTc. Of the three remaining HCPs, two were obtained by use of diphenylsulfide as monomer in combination with α,α' -dichloro-*p*-xylene as cross – linker and TiCl_4 as catalyst, resulting in the synthesis of DIXYT01 and DIXYT02. Finally, an HCP obtained from waste product, namely polystyrene chips, was synthesized by dissolution of the chips and subsequent cross – linking with FDA and FeCl_3 . The resulting material was named PS-1.3. Among the aforementioned materials, ABT01 and 02, DIXYT01 and 02 and TPMTc are completely novel materials while the others have been previously discussed in the literature and an optimization of the synthetic procedure has been carried out during the Ph.D. work.

Synthetic clays, specifically saponites, were synthesized with a H₂O / Si ratio of 110, as completely inorganic (SAP110) and as an organo – functionalized saponite (SAP-OP) through a one – pot procedure, resulting in a novel material.

mPAF-1/9, mPAf-1/16 and mPAF-1/30 were selected to be tested for VOC adsorption and toluene was selected as representative of the aromatic VOC family. In particular toluene adsorption capacities of mPAF materials were measured via a volumetric approach and compared to those of a well - established silica – based adsorbent, namely zeolite-Y (HSZ-Y). From the volumetric adsorption experiments, mPAFs showed much higher adsorption capacities with respect to HSZ-Y, resulting in the case of mPAF-1/16, in 154 wt% of adsorbed toluene with respect to 21 wt% observed for HSZ-Y. Evidence of the swellable nature of the HCPs' polymeric framework were found by inspection of the volumetric adsorption isotherms and found to be in part responsible for the high toluene uptakes. To gain additional information, the toluene adsorption process on mPAF-1/16 was followed via both FT-IR and SS-NMR spectroscopy. In this context, the presence of C-H/ π interactions between the side reactions groups found in the mPAF-1/16 framework and the toluene molecules was confirmed by the infrared red shift of the signal associated with the methyl C-H bonds of the mPAF framework and in the context of SS-NMR analysis, by upfield and downfield shifts associated with the aliphatic carbons and protons. To confirm the presence of C-H/ π interaction, the adsorption of benzene, xylene and *n*-hexane on mPAF-1/16 was also followed via SS-NMR spectroscopy. When *n*-hexane was adsorbed on the HCP no signs of spectral shifts were found, in addition to observing lower adsorbed quantities of the aliphatic pollutant molecule. From the acquired data it was possible to conclude that the chemical nature of the polymeric framework allowed the formation of favorable host – guest interactions resulting in higher affinity for the aromatic pollutants species which in turn resulted in the expansion of the polymeric framework.

Hyper cross – linked polymers and synthetic clays were also tested as additives for the production of Mixed Matrix Membranes (MMMs) based on the polymer of intrinsic microporosity PIM1, to be tested for gas separation applications. PIM1 is known to experience severe reduction in gas permeability over time because of the collapse of the internal free volume as a consequence of physical aging. The addition of porous solids as additives has been proven in recent years to be effective in slowing down the PIM1 physical aging. MMMs were obtained via addition of 3 wt% of SAP110 and SAP-OP to the PIM1 matrix resulting in the MMMs PIM1-SAP110 and PIM1-SAP-OP. The membranes were characterized via SEM, TEM, XRD and SS-NMR spectroscopy. CO₂ and N₂ permeability performances were tested for the two MMMs in addition to a pure PIM1 membrane. The CO₂ permeation rate after 1 year of aging was found to be approximately 20% of the initial value for the PIM1 membrane while for PIM1-SAP110 47 and 41% of the initial value was found. The aging rate for the two MMMs was thus found to be reduced with respect to the pure PIM1 membrane. The CO₂/N₂ selectivity was also found to increase for all membranes during aging and the values 19, 17 and 22 were found respectively for PIM1, PIM1-SAP110 and PIM1-SAP-OP. In order to gain additional information on the molecular level dynamics of the aging process in both pure PIM1 and saponite clays – based MMMs, ¹³C spin – lattice relaxation times (T₁) values were measured for all samples. T₁ values were recorded at t₀, right after regeneration of the membrane in methanol, after three months of aging (t₃) and after twelve months of aging (t₁₂). In the first three months, T₁ values were found on average to increase as a consequence of the higher packing density of polymeric chains induced by the collapse of the internal free volume within the PIM1 matrix. However, between t₃ and t₁₂ a decrease on average of T₁ values was found for PIM1-SAP110 and to lower extent to PIM1-SAP-OP, which reflected the measured CO₂ permeation rates. PIM1 polymeric chains diffusion within the interlayer space of saponite particles was proposed to explain the reduced aging behavior thanks to confinement effects hindering further chain movements.

MMMs were also produced via addition of HCPs to the PIM1 matrix. In particular ABT01, ABT02, DIXYT01 and DIXYT02 were used as additives with a load of 3 and 10 wt%. PIM1-ABT02 at 3 and 10 wt% were tested for more than 800 days. An initial decrease in the CO₂ permeation rate was found for both membranes in the first aging period, namely from t₀ up to approximately 100 days where the CO₂ permeability was assessed at 49 and 45% with respect to t₀ values for PIM1-ABT01 and 02 respectively. However, between 80 and 800 days a further drop of 2 percentage points for PIM1-ABT02-3% was found, while for the 10 wt% sample a further drop of 7 percentage points was found. ABT01 with a 3 wt% load was found to not efficiently reduce the aging rate of PIM1, being the CO₂ permeability of PIM1-ABT01-3% after 336 days found to be only 30% of the initial value. However, increasing the loading of ABT01 to 10 wt% seems to result in a slower aging rate having PIM1-ABT01-10% a CO₂ permeability assessed at 42% after 252 days of aging.

MMMs obtained from the addition of DIXYT materials were tested for CO₂ and N₂ permeation up to approximately 1 year. From the acquired data associated with CO₂ and N₂ permeation it was found that the MMMs prepared with a 3 wt% load of additives resulted in higher CO₂ permeation. Around 60 days of aging the CO₂ permeability for PIM1-DIXY01-3% and PIM1-DIXYT02-3% is around 60% with respect to t₀ values. For PIM1-DIXYT02-3% after 407 days of aging the CO₂ permeability is assessed at 51% with respect to the t₀ value while for PIM1-DIXY01-3% the CO₂ permeability is assessed at 49% with respect to the t₀ value after 426 days of aging. For PIM1-DIXYT01-10% a sharp drop in permeability was observed after only 7 days when the CO₂ permeability was assessed at only 25% with respect to the initial value. A similar trend was observed for PIM1-DIXYT02-10%, however the membrane broke during testing at 28 days of aging when the CO₂ permeability was assessed at 44% with respect to t₀ value. The higher CO₂ permeability observed for MMMs obtained via addition of DIXYT materials at 3% was ascribed to the

presence of sulfur - based functionalities within the DIXYTs' polymeric framework allowing stronger interactions with the CO₂ molecules thus increasing the gas solubility within the polymeric matrix hence resulting in higher permeation. Further studies aiming to gain information on the interactions between DIXYT materials' framework and the CO₂ molecule and the kinetic of diffusion will be carried out in the future.

Acknowledgements

First, I would like to express my special thanks to the Director of the department Prof. Leonardo Marchese who gave me the opportunity to work on this wonderful project.

A big thank you to my supervisor, Prof. Giorgio Gatti who provided invaluable guidance throughout this research. His insights and teachings helped me in all the time of the research work and at the same time he thought me the importance of being self – sufficient. Thank you!

To Prof. Chiara Bisio my deep and sincere gratitude for your endless help, your wisdom, your kind heart and your sense of humor. It has been a real pleasure working with you. You made me feel a true part of this group. Thank you!

To Prof. Maria – Chiara Ferrari a big thank you for welcoming me in the laboratories of the University of Edinburgh. Your help and guidance have allowed me to acquire precious knowledge and your sunny and cheerful nature made my stay even more pleasant. Thank you!

To Elsa Lasseguette, a big thank you for your help in the lab, for your patience and for the laughs we shared during my stay in Edinburgh.

To my fellow lab mates Chiara, Stefano and Vanessa a big thank you for your support and thank you for being such good companions during the days of work. Not only we do the best job in the world, but it is truly priceless to being able to do that in good company. Thank you!

To Valeria, a simple thank you is not nearly enough. Your love and support clearly deserve more than a few words at the end of a thesis. I truly am one lucky man.

A special thank you to my sister Irene, for always being there and for being one of the wisest person I know. Thank you for everything!

Last but not least, thank you to my lovely parents Giuliana and Gianfranco who deserve every bit of gratitude a son can give. They valued my instruction above all else and they taught me the value of education. I am proud to be your son.